KONSTANTINOS VASILAKOS

ROLE OF SOLUTE CHEMISTRY ON MEMBRANE CRYSTALLISATION OF INORGANIC SALTS

SCHOOL OF WATER, ENERGY AND ENVIRONMENT

PhD

Academic Year: 2018 – 2024

Primary Supervisor: Dr Ewan McAdam

Associate Supervisor: Dr Pablo Campo-Moreno

July 2024

SCHOOL OF WATER, ENERGY AND ENVIRONMENT

PhD

Academic Year 2018 – 2024

KONSTANTINOS VASILAKOS

ROLE OF SOLUTE CHEMISTRY ON MEMBRANE CRYSTALLISATION OF INORGANIC SALTS

Primary Supervisor: Dr Ewan McAdam
Associate Supervisor: Dr Pablo Campo-Moreno
July 2024

This thesis is submitted in partial fulfilment of the requirements for the degree of PhD

© Cranfield University 2024. All rights reserved. No part of this publication may be reproduced without the written permission of the copyright owner.

ACADEMIC INTEGRITY DECLARATION

I declare that:

- the thesis submitted has been written by me alone.
- the thesis submitted has not been previously submitted to this university or any other.
- that all content, including primary and/or secondary data, is true to the best of my knowledge.
- that all quotations and references have been duly acknowledged according to the requirements of academic research.

I understand that to knowingly submit work in violation of the above statement will be considered by examiners as academic misconduct.

Abstract

Membrane distillation crystallisation (MDCr) is a process developed to recover valuable salts from salt-rich solutions like sea water, brackish water, waste and others for the promotion of zero liquid discharge (ZLD). The chemistry of the crystallised salts is characterised by their different crystal-liquid interfacial energy derived from their solubility. Various studies have evidenced the importance of the interfacial energy in the nucleation process through Gibbs energy but it has never previously used to determine the scaling, nucleation and crystal growth kinetics of membrane distillation crystallisation. Using a combination of a backscatter technique and digital microscopy to detect bulk and scaling induction, this work provides a precise determination of scaling and bulk induction and metastable zone width (MSZW), resulting into a critical differentiation of heterogeneous adhesive growth for low interfacial energy salt and homogeneous bulk deposition for high interfacial energy growth. After understanding that the membrane is not playing as much role as previously thought in MDCr for high interfacial energy salts, another crucial component of the chemistry of the salt and its solubility, is the solubility–temperature dependence. It was found that even in low interfacial energy salts, the dominant factor of scaling is temperature polarisation and not heterogeneous nucleation as previously assumed. To confirm the less critical role of the membrane in MDCr, three membranes comprised of distinctive properties were compare through the use of a neutral solubility–temperature dependent salt. The results demonstrate how both scaling and crystal growth are kinetically controlled rather than thermodynamically dependent upon the material properties to initiate nucleation. To enhance the dependency of the membrane for nucleation within a kinetically controlled environment, K_2SO_4 was studied which exhibits a sharp positive solubility–temperature dependency. The modification of the solubility limit due to temperature polarisation, modifies the thermodynamic barrier of the MSZW which increase scaling, the extent of which is evidenced to directly inform the nucleation kinetics within the bulk solution. This thesis collectively describes and relates solute chemistry to both scaling and nucleation, enabling enhanced crystallisation strategies to be developed for MDC.

Keywords: crystallisation, membrane crystallisation, membrane fouling, membrane scaling, salt solubility, metastable zone width, nucleation kinetics, heterogeneous nucleation, homogeneous nucleation, surface free energy, interfacial energy

Acknowledgments

At Cranfield, I would like to thank Dr Ewan McAdam, for not only his academic supervision but also his personal support and his motivation, without which I would not be able to deliver this thesis. I would like to thank Dr Pablo Campo – Moreno for his useful and input. Last but not least, I would like to thank the whole membrane crystallisation team. To name a few, Dr Mehrez Hermassi, for his tutoring and patience in the lab, Dr Navya Thomas for her precious help, and my fellow PhD researchers Alaa Ouda, Aphiwe Jikazana and Ben Luqmani not only for their cooperation but mostly their friendship outside the lab.

Outside of the university, I would like to thank my parents for their emotional support and of course my wife Catarina Gomes Seidi. Without her unconditional patience and support none of these would ever be possible.

Table of Contents

ACADEMIC INTEGRITY DECLARATION i
Abstract ii
Acknowledgments iii
List of Figures vii
List of Figures for Appendices xiii
List of Tables xv
List of Equations xvi
List of Abbreviations xix
1 Introduction 1
1.1 Water scarcity and desalination 1
1.2 Zero liquid discharge 2
1.3 Membrane distillation and crystallisation 5
1.4 The role of the membrane surface in membrane crystallisation 8
1.5 Membrane Fouling 10
1.6 Aims and Objectives 10
1.7 Thesis structure 11
1.8 References 13
2 Use of crystal-liquid interfacial energy to predict scaling, nucleation and crystal growth in membrane distillation crystallisation 22
2.1 Introduction 24
2.2 Material and methods 29
2.2.1 Experimental setup 29
2.2.2 Analytical procedures 32
2.2.3 Mass and heat transfer analysis 34
2.3 Results and discussion 36
2.3.1 The role of interfacial energy on mass transfer and concentrating rate 36
2.3.2 The role of crystal-liquid interfacial energy in determining scaling 41
2.3.3 The role of interfacial energy in determining nucleation and growth kinetics 45
2.4 Conclusions 48
2.5 Acknowledgements 49
2.6 Appendices 50
2.6.1 Appendix A – Surface free energy analysis 50
2.6.2 Appendix B – Characterisation of the recovered crystal phase 55
3 Temperature polarisation controls nucleation kinetics in membrane distillation crystallisation 61
3.1 Introduction 63

3.2 Materials and methods 66
3.2.1 Experimental setup 66
3.2.2 Analytical methods 67
3.2.3 Heat and mass transfer characterisation 69
3.2.4 Nucleation kinetics characterisation 70
3.3 Results and discussion 73
3.3.1 Determining mass and heat transfer processes for each aqueous salt 73
3.3.2 Scaling is dependent on supersaturation and solubility-temperature dependency 73
3.3.3 Boundary layer supersaturation determines primary nucleation kinetics in the bulk 80
3.4 Conclusions 85
3.5 Acknowledgements 86
3.6 Appendices 87
3.6.1 Appendix A – Primary Flux data 87
3.6.2 Appendix B – Primary Scaling Images 89
3.6.3 Appendix C – Characterisation of nucleation rate based on concentrating rate 90
3.6.4 Appendix D – Comparison of crystal size distribution at equivalent residence times 90
3.6.5 Appendix E – SEM characterisation of Na_2SO_4 deposited on the membrane 91
3.7 References 92
4 Effect of the membrane material on the nucleation kinetics of crystallisation in membrane distillation crystallisation of sodium chloride 96
4.1 Introduction 98
4.2 Materials and methods 102
4.2.1 Experimental setup 102
4.2.2 Analytical methods 105
4.2.3 Characterisation of heat and mass transfer 107
4.2.4 Characterisation of nucleation kinetics 109
4.3 Results and Discussion 110
4.3.1 Introduction to membrane properties, water vapour flux and particle count 110
4.3.2 Characterisation of nucleation kinetics in the bulk solution 113
4.3.3 Characterisation of scaling including relating to mass and heat transfer mechanisms 118
4.3.4 Relating scaling mitigation to the nucleation kinetics of the bulk crystal phase 122
4.4 Conclusion 127

4.5 Acknowledgements 128
4.6 Appendix 129
References 130
5 Solubility-temperature dependency of salts reduces nucleation kinetics in membrane distillation crystallisation 135
5.1 Introduction 137
5.2 Material and methods 139
5.2.1 Experimental Setup 139
5.2.2 Analytical methods 142
5.2.3 Characterisation of heat and mass transfer 144
5.2.4 Characterisation of heat and mass transfer 146
5.3 Results and discussion 146
5.3.1 Relating water vapour flux to nucleation kinetics of the bulk crystal phase 146
5.3.2 The role of boundary layer properties in initiating scaling 152
5.3.3 Determining how scaling informs the probability and nucleation kinetics of bulk crystals 160
5.4 Conclusions 165
5.5 Acknowledgements 166
5.6 References 167
6 Discussion 169
6.1 How thermodynamic properties relate to crystallisation mechanisms in MDCr 169
6.2 How kinetics relate to crystallisation in MDCr 171
6.3 Implications for application of MDCr to real brines 172
6.4 Exploiting understanding for MDCr design 174
6.5 References 176
7 Conclusions and future work 179
7.1 Conclusions 179
7.2 Future work 180

List of Figures

Figure 2.1 ΔG as the minimum free energy value needed for the formation of crystals (a)The representation of the critical energy free barrier (ΔG) and how it is calculated through the difference of the volumetric (ΔGv) and surface (ΔGs) Gibbs free energy. (b) The highest point of the ΔG is the critical nucleus size on which a crystal that is created can stabilise and remain in solid form. The highest the critical nucleus size the more energy it takes to create a stable crystal form that will survive the adhesion forces of the system. (c) The higher the critical nucleus size the higher the ΔGv of the salt-solution-membrane (W132) which translates to lower propensity to nucleation thus scaling. 25

Figure 2.2 Experimental set-up diagram 28

Figure 2.3 Membrane distillation crystallisation data for five salts that exhibit different interfacial energies: (a) membrane flux data, operating conditions (Bulk): T, 44.3±0.5°C; ∆T 13.9±2.5°C; and (b) in-situ particle characterisation determines the first point at which bulk crystals are formed (FBRM set to primary count (<10) for sensitive detection of induction and nucleation rate. 36

Figure 2.4 Demonstrating how interfacial energy decouples supersaturation from concentrating rate. Operating conditions (Bulk): T, 44.3±0.55°C; ∆T 13.9±2.5°C. ... 38

Figure 2.5 Quantifying the extent of scaling based on: (a) time and (b) supersaturation. Direct observation also permits the differentiation between adhesive growth (classical scaling, open shapes) and deposition (following homogeneous nucleation in the bulk solution, closed circles). Operating conditions (Bulk): T, 44.3±0.5°C; ∆T 13.9±2.5°C. 39

Figure 2.6 Demonstrating how interfacial energy: (a) determines the transition from heterogeneous to homogeneous nucleation (above dashed line (unity), bulk nucleation precedes membrane scaling; and (b) how the extent of membrane scaling at bulk induction relates relates to the work of formation. Operating conditions (Bulk): T, 44.3±0.5°C; ∆T 13.9±2.5°C. 41

Figure 2.7 The onset (induction) of scaling observed on the PTFE membrane before induction in the bulk (homogeneous crystallisation) for NaCl (a) but not for silver sulphate (b). Using non-invasive direct observation, real-time data collection can be used to determine the rate and progression of scaling. Operating conditions (Bulk): T, 44.3±0.5°C; ∆T 13.9±2.5°C. 42

Figure 2.8 Nucleation rate (measured using FBRM and normalised using volumetric hold-up): (a) increases under the same membrane operating conditions, due to interfacial energy; and (b) conforms to a similar trend for other aqueous salts (Mersmann and Kind, 1988). Operating conditions (Bulk): T, 44.3±0.5°C; ∆T 13.9±2.5°C. 44

Figure 2.9 The impact of interfacial energy on crystal size: (a) size distributions measured by FBRM; and (b) crystal size (data presented as median (L50) related to supersaturation at induction and compared to literature crystal size data from a range of aqueous salts (Mersmann and Kind, 1988). Inset to provide greater clarity of the reduction in crystal size with relative supersaturation. Operating conditions (Bulk): T, 44.3±0.5°C; ∆T 13.9±2.5°C. 45

Figure 2.10 Framework to describe the relative importance of heterogeneous primary nucleation (membrane scaling) based on the interfacial energy of the solute which sets the relative supersaturation required to initiate nucleation (building upon the early work of Mersmann and Kind, 1988. 47

Figure 3.1 Experimental set-up diagram. 69

Figure 3.2 Demonstrating the effect of the (a) concentrating rate of each salt at scaling induction of each salt where even though the concentrating rate is kept relatively the same, there are big differences in induction time. This change is mainly promoted by (b) the difference in the boundary layer temperature, where the higher the temperature – solubility dependence, the higher the change in the relative supersaturation at scaling induction as the boundary layer temperature decreases. 77

Figure 3.3 Quantifying the extent of scaling based on time for the different TPCs using the positive solubility-temperature dependence salt (α) $KClO_4$ and the almost neutral solubility-temperature dependence salt (b) NaCl. Direct observation also permits the differentiation between adhesive growth and deposition (c) for the different TPCs. . 79

Figure 3.4 Characterisation of (α) $KClO_4$ and (b) NaCl scale formed using Scanning Electron Microscopy (SEM). In these pictures we can the epitaxial growth model is dominating the crystal growth of these crystals. 80

Figure 3.5 Close-up high-quality images of the generated bulk crystals (homogeneous nucleation) through the Scanning Electron Microscope method (SEM) for all the three salts used (a) $KClO_4$, (b) NaCl, (c) Na_2SO_4..... 81

Figure 3.6 In-situ particle characterisation which determines the first point at which bulk (α) $KClO_4$, (b) NaCl, (c) Na_2SO_4 crystals are formed in the different TPCs (FBRM set to primary count (<10)) for sensitive direction of induction and nucleation rate. 83

Figure 3.7 The differentiation between the tendencies of the heterogeneous and homogeneous salts and how they affect bulk and scaling induction time. As seen in (α) the heterogeneous salts are above y = x as scaling occurs first, while the opposite is happening for the homogeneous salts and (b) the effect of the different TPCs in the supersaturation during induction..... 84

Figure 3.8 (a) Supersaturation and relative supersaturation at comparable TPC (Na_2SO_4, 0.48±0.001; NaCl, 0.49±0.001; $KClO_4$, 0.48±0.007); (b) comparison of nucleation rate normalised for volumetric holdup, where the increase in boundary layer temperature is due to the modification of Re. 85

Figure 4.1 Kinetically controlled nucleation can reduce the free energy barrier by adjusting supersaturation. 101

Figure 4.2 Experimental set-up 103

Figure 4.3 SEM and AFM images of virgin (α) PTFE, (b) PVDF and (c) PP membranes. 110

Figure 4.4 Membrane distillation crystallisation data using four different temperature differences (15ºC – 20ºC – 25ºC -30ºC) over time: membrane flux data on (a) PTFE, (b) PVDF, (c) PP flat sheet membranes. 112

Figure 4.5 In-situ particle characterisation which determines the first point at which bulk crystals are formed under the (α) PTFE, (b) PVDF, (c) PP membranes (FBRM set to primary count (<10) for sensitive direction of induction and nucleation rate)..... 113

Figure 4.6 Demonstrating the effect of the concentrating rate of the PTFE, PVDF and PP membranes (a) on the boundary layer concentration and the (b) supersaturation at homogeneous nucleation induction. The increase in the boundary layer concentration thus the increase of the saturation level of the boundary layer during the nucleation induction keeps increasing no matter the membrane used. It must be noted that the bulk concentration during nucleation remains steady no matter the concentrating rate and the membrane. 115

Figure 4.7 Demonstrating the effect of the concentrating rate of the PTFE, PVDF and PP membranes (a) on the boundary layer concentration and the (b) supersaturation at homogeneous nucleation induction. The increase in the boundary layer concentration thus the increase of the saturation level of the boundary layer during the nucleation induction keeps increasing no matter the membrane used. It must be noted that the bulk concentration during nucleation remains steady no matter the concentrating rate and the membrane. 116

Figure 4.8 Characterisation of the bulk crystals through Scanning Electron Microscopy (SEM) created by the (a) PTFE, (b) PVDF and (c) PP membrane crystallisation experiments where rough model is dominating the crystal growth creating a linear crystal growth rate. 117

Figure 4.9 Time series of NaCl scaling on the PTFE membrane. The feed and the permeate flow are counter current and the feed flow direction is from left to right. The feed temperature is 54^{o}C while the temperature difference stands on 25^{o}C. The image on the 50th minute is where the induction of the membrane scaling begins. After the 50th minute the scaling continues to grow without having yet bulk crystallisation. The bulk crystallisation induction is happening on the 86th minute. After that, we can see the effect of the deposited crystals coming from the bulk and create intense scaling. 119

Figure 4.10 Quantifying the extent of scaling based on time for the different temperature differences using (a) polytetrafluoroethylene (PTFE), (b) polyvinylidene fluoride (PVDF), (c) polypropylene (PP) flat sheet membranes. Direct observation also permits the differentiation between adhesive growth (classical, scaling, open shapes) and deposition (following homogeneous nucleation in the bulk solution, closed circles). 120

Figure 4.11 Demonstrating the effect of the concentrating rate of the PTFE, PVDF and PP membranes (a) on the TPC and CPC as well as the (b) boundary layer concentration and the relative supersaturation at scaling induction. The membranes seem to have no effect on the concentrating rate as the experiments seem to follow a constant trend no matter the membrane. 121

Figure 4.12 Demonstrating the effect of the concentrating rate of the PTFE, PVDF and PP membranes (a) on the TPC and CPC as well as the (b) boundary layer concentration and the relative supersaturation at scaling induction. The membranes

seem to have no effect on the concentrating rate as the experiments seem to follow a constant trend no matter the membrane. Figure 8. The effect of the concentrating rate (a) in the saturation level of the scaling induction according to the boundary layer and (b) the difference between the bulk and the boundary layer concentrations. 123

Figure 4.13 The effect of the temperature-solubility dependence can be seen as the difference between the bulk and the boundary layer concentration increases while the concentration in the bulk decreases as the membrane concentration increases no matter the membrane used. 123

Figure 4.14 (α) Demonstrating the effect of the supersaturation of the boundary layer on the onset of bulk induction with the extend of membrane scaling. (b) As bulk induction is pushed back, the concentration on the boundary layer of the membrane is getting higher, extending the growth of the membrane scaling. 124

Figure 4.15 Characterisation of scale formed on each membrane using Scanning Electron Microscopy (SEM): (a) PTFE; (b) PVDF; and (c) PP. Experimental conditions: Feed temperature, 54°C; ΔT, 30ºC. Crystals produced through sacrificial experiments to ensure analysis prior to bulk nucleation. 125

Figure 5.1 Diagram of the full experimental setup. 145

Figure 5.2 Membrane distillation crystallisation data using four different temperature differences (15ºC – 20ºC – 25ºC -30ºC) over time: membrane flux data on (a) PTFE, (b) PVDF, (c) PP flat sheet membranes. 152

Figure 5.3 In-situ particle characterisation with FBRM to determine both induction time (the first point at which bulk crystals are formed) and nucleation rate for crystallisation in the bulk under the (α) PTFE, (b) PVDF, (c) PP membranes (FBRM set to primary count (<10) for sensitive direction of induction and nucleation rate)..... 153

Figure 5.4 The effect of the concentrating rate (a) in the saturation level of the homogeneous nucleation induction according to the boundary layer and (b) the difference between the bulk and the boundary layer concentrations. The effect of the temperature-solubility dependence can be seen as the difference between the bulk and the boundary layer concentration increases while the concentration in the bulk remains steady during nucleation no matter the membrane used. 155

Figure 5.5 Bulk crystals (α) PTFE - 15ºC, (b) PVDF - 15ºC, (c) PP - 15ºC..... 156

Figure 5.6 Typical habit of potassium sulphate grown in aqueous solution at low supersaturation, with Miller indices noted. 157

Figure 5.7 The onset (induction of scaling observed on the (a) PTFE, (b) PVDF and (c) PP membranes before induction in the bulk (homogeneous crystallisation) for K_2SO_4, using non-invasive direct observation, real-time data collection can be used to determine the rate and progression of scaling. Operating conditions ΔT, 15°C. 158

Figure 5.8 Extent of scaling for each ΔT and membrane: (a) polytetrafluoroethylene (PTFE), (b) polyvinylidene fluoride (PVDF), (c) polypropylene (PP) flat sheet membranes. Direct observation also permits the differentiation between adhesive growth (classical, scaling, open shapes) and deposition (following homogeneous nucleation in the bulk solution, closed circles). 160

Figure 5.9 Uncoupling and demonstrating the effect of the: (a) concentration polarisation coefficient and the boundary layer concentration as well as the (b) temperature polarisation coefficient and the boundary layer solubility in the concentrating rate of the experiments. 161

Figure 5.10 Time to nucleation where the boxes represents median (50th percentile, centre line), 25th and 75th percentiles, whereas whiskers represent minimum and maximum times recorded. 164

Figure 5.11 Membrane crystals resulted from scaling for (a) PTFE 15°C (b) PVDF 15°C (c) PP 15°C 165

Figure 5.12 The evolution of the scaling growth rate due to the progressive concentration of the feed solution in the different temperature where bulk nucleation does not occur for (α) PTFE (b) PVDF and (c) combined for the temperature where nucleation occurs but prior to it..... 167

Figure 5.13 Correlation between the membrane scaling coverage at induction against (α) the concentrating rate at bulk nucleation where no corelation is observed and (b) the boundary layer solubility coefficient at bulk nucleation where the lowering c* increases the probability for nucleation, leading to longer times to facilitate growth. 168

Figure 5.14 Nucleation rate (measured using FBRM): (a) increases as the boundary layer coefficient increases due to the homogeneous nucleation moving to higher saturation levels and (b) decreases as the surface scaling is more intensive where the

temperature difference is higher and it consumes most of the salt, leaving less salt available for the bulk. 170

Figure 6.1 Connection between membrane-salt interfacial energy and metastable zone width of the solution..... 179

Figure 6.2 Proposed batch MDCR system 181

Figure 6.3 Proposed continuous MDCR system 181

List of Figures for Appendices

Figure 2.A1 The overall work of adhesion is dependent on W_{23}, the crystal-liquid work of adhesion. This is illustrated by observing the transient in Lifshitz-van der Waals and polar base components as aqueous salts become less soluble. The hydrophobic membrane possesses a minimal acid polar energy contribution, and as such the overall work of adhesion is dependent on the Lifshitz-van der Waals component and the polar base component, whose ratio indicates the probability for adhesion (based on a positive W_{132})..... 52

Figure 2.B1 Illustrative crystal size distributions for each aqueous salt based on square weighted chord size distributions…….54

Figure 2.B2 XRD spectra of calcium sulphate provided for illustration. Red peaks are reference spectra, and black peaks are the sample..... 55

Figure 3.A1. Membrane distillation crystallisation data for all the different TPCs used over time: membrane flux data on (α) $KClO_4$, (b) Na_2SO_4, (c) NaCl…….87

Figure 3.A 2. Reynolds number used to maintain similar CPCs during the experimental procedures. 88

Figure 3.B1. (a) raw image captured at 218 minutes for NaCl; (b) processed image using contrasting to aid surface area quantification…….88

Figure 3.C1. Demonstrating the effect of the concentrating rate of the salts nucleation rate based on volumetric hold-up. The increase in the concentration rate pushes to higher supersaturation rates and as a result increasing the nucleation rate……....89

Figure 3.D1. Crystal size distributions measured for similar residence times (RT, 3-6 mins) when produced with an equivalent temperature polarisation coefficient (TPC: Na_2SO_4, 0.48±0.001; NaCl, 0.49±0.001; $KClO_4$, 0.48±0.007)…….89

Figure 3.E1. Na_2SO_4 crystals observed on the membrane at the end of the experiment. Scaling was not observed for Na_2SO_4 during the experiments, until bulk nucleation was observed. After bulk nucleation, deposition occurs where crystals settle out of the crossflow onto the membrane. Consequently, the crystal population observed within this scanning electron microscopy (SEM) image of the membrane surface is characteristic of that formed within the bulk solution……90

Figure 4.A1 Evidencing the reversible connection between the longer times and the shorter induction……...128

List of Tables

Table 2.1. Physicochemical characteristics of the salts and the membrane..... 27

Table 2.2. Experimental design 30

Table 3.1 Physical properties of salt solutions…….73

Table 4.1 Characterisation of membrane properties…….103

Table 4.A1 Surface tension and apparent contact angles of the different feed solutions on the on the PTFE membrane……..128

Table 5.1 Characteristics of the membranes used in this work.……140

Table 5.2 Comparison at equivalent concentrating rates where crystals were either observed or not observed with different membranes. 157

List of Equations

(*Eq. 2.1*)..... 24
(*Eq. 2.2*)..... 30
(Eq. 2.3)..... 30
(Eq. 2.4)..... 30
(*Eq. 2.5*) 31
(*Eq. 2.6*) 32
(*Eq.2.7*) 32
(*Eq. 2.8*) 32
(*Eq. 2.9*) 32
(*Eq. 2.10*)..... 32
(Eq. 2.11) 32
(*Eq. 2.12*) 32
(*Eq. 2.13*) 32
(*Eq. 2.14*) 32
(*Eq. 2.15*) 33
(*Eq. 2.16*) 33
(*Eq. 2.17*) 33
(*Eq. 2.18*) 33
(*Eq. 2.19*) 33
(*Eq. 2.20*) 33
(*Eq. 2.21*) 33
(*Eq. 2.22*) 34
(*Eq. 2.23*) 34
(*Eq. 2.24*) 34
(*Eq. 2.25*) 34
(*Eq. 2.26*) 34
(*Eq. 2.27*) 34
(*Eq. 2.A1*) 52
(*Eq. 2.A2*).....52
(*Eq. 3.1*).....69
(*Eq. 3.2*).....70
(*Eq. 3.3*).....70
(*Eq. 3.4*) 70
(*Eq. 3.5*) 71
(*Eq. 3.6*) 71
(*Eq. 3.7*) 72

(*Eq. 3.8*) 72
(*Eq. 3.9*) 72
(*Eq. 3.10*) 72
(*Eq. 3.11*) 72
(*Eq. 3.12*) 72
(*Eq. 3.13*) 72
(*Eq. 3.14*) 72
(*Eq. 3.15*) 72
(*Eq. 3.16*) 73
(*Eq. 3.17*) 73
(*Eq. 3.18*) 73
(*Eq. 3.19*) 73
(*Eq. 3.20*) 73
(*Eq. 3.21*) 73
(*Eq. 3.22*) 73
(*Eq. 3.23*) 74
(*Eq. 3.24*) 74
(*Eq. 3.25*) 74
(*Eq. 3.26*) 74
(*Eq. 3.27*) 74
(*Eq. 4.1*).....105
(*Eq. 4.2*).....105
(*Eq. 4.3*).....105
(*Eq. 4.4*).....106
(*Eq. 4.5*).....106
(*Eq. 4.6*).....107
(*Eq. 4.7*).....108
(*Eq. 4.8*).....108
(*Eq. 4.9*).....108
(*Eq. 4.10*).....108
(*Eq. 4.11*).....108
(*Eq. 4.12*).....108
(*Eq. 4.13*).....109
(*Eq. 4.14*).....109
(*Eq. 4.15*).....109
(*Eq. 4.16*).....109
(*Eq. 4.17*).....109

(*Eq. 4.18*)....109
(*Eq. 4.19*)....109
(*Eq. 5.1*).... 147
(*Eq. 5.2*).... 147
(*Eq. 5.3*).... 147
(*Eq. 5.4*).... 148
(*Eq. 5.5*).... 148
(*Eq. 5.6*).... 149
(*Eq. 5.7*).... 149
(*Eq. 5.8*).... 150
(*Eq. 5.9*).... 150
(*Eq. 5.10*)....150
(*Eq. 5.11*)....150
(*Eq. 5.12*)....150
(*Eq. 5.13*)....150
(*Eq. 5.14*)....150
(*Eq. 5.15*)....150
(*Eq. 5.16*)....150
(*Eq. 5.17*)....150
(*Eq. 5.18*)....151
(*Eq. 5.19*)....151
(*Eq. 5.20*)....151
(*Eq. 5.21*)....165

List of Abbreviations

A	Pre-exponential factor	-
A_{hetero}	Heterogeneous substrate	-
B	Nucleation rate	$m^{-3}\ s^{-1}$
B_0	Volumetric Nucleation rate	$m^{-3}\ s^{-1}$
C_m	Membrane permeability	$m\ s^{-1}$
C_b	Solute concentration in the bulk	$kg\ m^{-3}$
C	Solute concentration	$kg\ m^{-3}$
C*	Equilibrium solubility concentration	$kg\ m^{-3}$
C_h	Number of channels in FBRM	-
$C_{i,A}$	Geometric average length of the i_{th} channel	-
c_L	Molar concentration of the solution	$mol\ m^{-3}$
c_S	Molar concentration of the crystal	$mol\ m^{-3}$
C_w	Solute concentration on the membrane wall	$kg\ m^{-3}$
D	Diffusion coefficient	$m^2\ s^{-1}$
dh	Hydraulic diameter of the cell	m^2
D_p	Laser penetration depth of the FBRM	m
ΔC_w	Maximum metastable zone on membrane surface	$mg\ g^{-1}$ solution
ΔH_v	Latent heat of vapourisation	$J\ kg^{-1}$
ΔT	Temperature difference	^oC
ΔP	Vapor pressure difference	kPa
D_p	Laser penetration depth of the FBRM	m
ΔG^*	Critical Gibbs free energy	$kJ\ mol^{-1}$
ΔG	Gibbs free energy barrier	$kJ\ mol^{-1}$
ΔG_{het}	Gibbs free energy for heterogeneous nucleation	$kJ\ mol^{-1}$
ΔG_{hom}	Gibbs free energy for homogeneous nucleation	$kJ\ mol^{-1}$
ΔG_s	Surface formation free energy	$kJ\ mol^{-1}$
ΔG_v	Volume formation free energy	$kJ\ mol^{-1}$
F_p	Permeate flow rate	$kg\ h^{-1}$
f_s	Surface fraction in contact with the liquid droplet	-
G	Crystal growth rate	$m\ s^{-1}$
G_c	Crystal Gibbs free energy	$kJ\ mol^{-1}$
G_l	Liquid Gibbs free energy	$kJ\ mol^{-1}$
G_v	Volume Gibbs free energy	$kJ\ mol^{-1}$
h_c	Membrane heat transfer coefficient	$W\ m^{-2}\ K^{-1}$
h_f	Feed solution heat transfer coefficient	$W\ m^{-2}\ K^{-1}$

h_p	Permeate solution heat transfer coefficient	W m^{-2} K^{-1}
h_v	Vapour heat transfer coefficient	W m^{-2} K^{-1}
J	Water vapour flux	kg m^{-2} h^{-1}
J_{hetero}	Heterogeneous nucleation rate	m^{-3} s^{-1}
K	Mass transfer coefficient	m s^{-1}
K_G	Crystal growth coefficient	m^2 min^{-1}
k	Boltzmann constant	-
k_f	Thermal conductivity of feed solution	W m^{-1} K^{-1}
k_p	Thermal conductivity of permeate solution	W m^{-1} K^{-1}
k_w	Thermal conductivity of solution on the membrane wall	W m^{-1} K^{-1}
L	Length of crystal chords	µm
M	Molar mass of the salt	kg $kmol^{-1}$
m_0	Initial mass feed solution	kg
n*	Crystal nuclear size	m
N_A	Avogadro number	l mol^{-1}
$N_{ch,i}$	Number of counts measured in an ith channel	-
N_i	Number of n-weighted chord counts in the ith channel	µm s^{-1}
$N_{i,o}$	Raw unweighted chord count in the ith channel	s^{-1}
Nu	Nusselt number	-
Ø	Volumetric hold up factor	-
Pr	Prandtl number	-
Q_f	Feed solution flow	ml min^{-1}
Q_p	Permeate solution flow	ml min^{-1}
R_a	Roughness factor	-
R’	Concentration rate of solution	g $100g^{-1}$ h^{-1}
Re	Reynolds number	-
Re_f	Reynolds number for feed solution	-
Re_p	Reynolds number for permeate solution	-
R_G	Crystal growth rate	m^2 min^{-1}
S	Saturation level	-
Sc	Schmidt number	-
Sp	Scan speed of laser	m s^{-1}
t	Time	s
t_{ind}	Induction time	s

T	Temperature	K
T_f	Temperature of feed in the bulk	K
T_{fm}	Temperature of feed on the membrane	K
T_p	Temperature of permeate in the bulk	K
T_{pm}	Temperature of permeate on the membrane	K
v	Velocity of feed solution	$m\ s^{-1}$
V	Volume of solution	m^3
V_M	Molecular volume	m^3
W_a	Work of adhesion	$mJ\ m^{-2}$
W_{12}	Work of membrane – crystal system	$mJ\ m^{-2}$
W_{13}	Work of membrane – water system	$mJ\ m^{-2}$
W_{23}	Work of salt – water system	$mJ\ m^{-2}$
W_{33}	Work of water – water system	$mJ\ m^{-2}$
W_{132}	Work of adhesion of the total system	$mJ\ m^{-2}$
W^*	Work of formation	$mJ\ m^{-2}$
Wl	Laser diameter of focal point	m

Greek symbols

α	Detectable volume fraction	-
β	Cluster shape factor	-
γ	Crystal-liquid interfacial free energy	$mJ\ m^{-2}$
γ^{AB}	Polar component of surface tension	$mJ\ m^{-2}$
γ_{eff}	Effective interfacial energy	$mJ\ m^{-2}$
γ^{total}	Total interfacial energy	$mJ\ m^{-2}$
γ^{LW}	Dispersive component of surface tension	$mJ\ m^{-2}$
γ^{+}	Positive polar component of surface tension	$mJ\ m^{-2}$
γ^{-}	Negative polar component of surface tension	$mJ\ m^{-2}$
γ^{HEN}	Heterogeneous nucleation interfacial tension	$mJ\ m^{-2}$
ζ	Concentration polarisation coefficient	-
θ	Contact angle	^{o}
μ	Dynamic viscosity	Pa s
$\Delta\mu$	Chemical potential	$J\ kg^{-1}$
ρ^s	Crystal density	$kg\ m^{-3}$
φ	Substrate wetting coefficient	-

Abbreviations

AB	Lewis acid-base interaction energy
BC	Brine concentrator
BCr	Brine crystalliser
CLD	Chord length distribution
CNT	Classical nucleation theory
CPC	Concentration polarisation coefficient
CSD	Crystal size distribution
CV	Coefficient of variation
DCMD	Direct crystallisation and membrane distillation
DWE	Decane, Water, Ethylene glycol
DWF	Decane, Water, Formamide
DWG	Decane, Water, Glycerol
DWS	Decane, Water, Dimethylsulfoxide
EL	Electrostatic interaction energy
ePTFE	Expanded Polytetrafluoroethylene
FBRM	Focused beam reflectance measurement
FO	Forward osmosis
FTIR	Fourier transform infrared spectroscopy
HON	Homogeneous conditions
HPRO	High pressure reverse osmosis
LW	Lifshitz-van der Waals
MD	Membrane distillation
MED	Multi-effect distillation
MDCr	Membrane distillation crystallisation
MSF	Multi-stage flash
MSZW	Metastable zone width
OARO	Osmotically aided reverse osmosis
PP	Polypropylene
PTFE	Polytetrafluoroethylene
PVDF	Polyvinylidene fluoride
RMS	Root mean square roughness
RO	Reverse osmosis
SD	Spray dryer

SEM	Scanning electron microscopy
SFE	Surface free energy
TDS	Total dissolved solids
TPC	Temperature polarisation coefficient
VMD	Vacuum membrane distillation
XRD	X-Ray powder diffraction
ZLD	Zero liquid discharge

Chemical formulae and speciation

Ag_2SO_4	Silver sulphate
Ba^{2+}	Barium
$BaSO_4$	Barium sulphate
Br^-	Bromine
Ca^{2+}	Calcium
$CaCl_2$	Calcium chloride
$CaCO_3$	Calcium carbonate
$CaSO_4$	Calcium sulphate
Cl^-	Chloride
K^+	Potassium
K_2SO_4	Potassium sulphate
$KClO_4$	Potassium perchlorate
Li^+	Lithium
Mg^{2+}	Magnesium
$MgCl_2$	Magnesium chloride
$Mg(OH)_2$	Magnesium hydroxide
Na^+	Sodium
NaCl	Sodium chloride
Na_2SO_4	Sodium sulphate
$(NH_4)_2SO_4$	Ammonium sulphate
Rb^+	Rubidium
SO_4^{2-}	Sulphate

1 Introduction

1.1 Water scarcity and desalination

The increase of water demand due to population growth and anthropogenic activities including agriculture and industrial use have led to the extended use of groundwater and surface waters where overuse has led to environmental consequences, and ultimately depletion of many such sources (Richey et al., 2015). Water scarcity and particularly the security of potable sources of clean water is now a critical issue even in water-rich and economically developed countries (Ashraf et al., 2022). Consequently, alternate water sources have to be considered including seawater, brackish water as well as water reuse from municipal and industrial processes (Ghaffour et al. 2015).

One of the technologies developed for the purpose of finding alternative water sources for direct potable use or regeneration of the groundwater reservoirs, and currently the most used, is desalination (Bundschuh et al., 2021; Ayaz et al., 2022). Through desalination all the dissolved salts, ions, minerals and contaminants can be removed from the seawater or the wastewater. This way we purify the water which we can use in anthropogenic activities and save on fresh water (Ashraf et al., 2022). Approximately 21,000 desalination plants are currently operational around the world, with most of them installed in the places with the biggest water scarcity problems such as Israel, United Arab Emirates, Kingdom of Saudi Arabia, USA, China and other areas with similar problems (Jones et al., 2019; Eke et al., 2020). Currently the only operating water desalination plant in the UK for drinking water production is the Thames Water Beckton plant and others built for construction, such as the temporary desalination plants for Sizewell B and the future Sizewell C, but as water scarcity becomes increasingly difficult to manage, water companies are proposing new desalination plant projects. As a result, UK will expand provision through building four more operating desalination plants with a total daily supply of 143ML d^{-1} by 2050 (GOV.UK, 2024).

Desalination can be achieved in two ways, through thermal desalination and membrane desalination (Shafieian et al., 2020). Thermal desalination refers to the process of evaporating salty water and subsequently condensing the resulting steam to produce salt-free water (Ahmed et al., 2021). Despite the significant thermal energy demand of both multi-stage flash (MSF) and multi-effect distillation (MED) ranging from 8 – 24kWh m^{-3}, thermal desalination was initially favoured in middle-eastern regions with access to heat or cheap forms of thermal energy, due to technological maturity and reliability (Cornejo, et al., 2014; Amy et al., 2017; Ahmed et al. 2019; Nassrullah et al., 2020; Prado de Nicolas et al., 2023). Thermal evaporators were often co-located

with power stations where residual waste heat could be used to deliver some or all of the thermal energy load. Membrane desalination gained commercial viability in the 1960's with the discovery of polymer films for reverse osmosis (RO), and is now generally regarded as the best available technique for water desalting and treatment (Mukiibi and Feathers, 2009; Ahmed et al., 2019). Although it is the preferred solution over thermal desalination, the two technologies share a common problem; the production of a concentrated brine as a by-product of the process, which must be managed and disposed of safely. Brine discharge to sea has been linked to adverse impacts on marine ecology, but is currently the main method of disposal due to the lack of available treatment methods as well as their huge costs (Giwa et al., 2017; Frank et al., 2017; Missimer and Maliva 2018; Panagopoulos and Haralambous, 2020). This has led researchers to investigate alternative solutions to treat brines by revaluing their mineral content for resource recovery through a circular approach, which offers new value, reduce environmental risk and enhances product water recovery (Skuse et al., 2021; Ahmed et al., 2021).

1.2 Zero liquid discharge

1.2.1 Brine disposal options

Brine, whether it comes from seawater or industry, is distinguished by its high salinity, inorganic and organic substances, heavy metals, and pre-treatment chemicals such as coagulants, flocculants, and anti-scalants. As a result, disposing of brine in the marine environment or groundwater is extremely dangerous, even though these methods of disposal are still commonly practiced (Heck et al., 2018; Panagopoulos et al., 2019; Panagopoulos and Giannika, 2022a; Panagopoulos and Giannika, 2022b). As concerns arise over these disposal options, efforts are being made to create technology that address the issue and achieve the reduction of wastewater output. This approach is called zero liquid discharge (ZLD) (Wenten et al., 2017).

1.2.2 Preconcentration methods

ZLD typically involves three stages. Firstly, preconcentration is carried out using membrane technologies to recover water and reduce the volume of the brine. The predominant method used for brine pre-concentration is reverse osmosis (Panagopoulos et al., 2019). Although RO is highly successful in treating both seawater and brackish water, it is mostly used for brines with lower total dissolved solids (TDS) of up to 70,000mg/l. This is because the water recovery rate significantly decreases in greater concentrations, reaching only 50% in brines with 70,000mg/l TDS (Aines et al., 2011). Nevertheless, advanced high pressure reverse osmosis membranes (HPRO) have been created to effectively process TDS concentrations of

up to 130,000mg/l (Saltworks Technologies Inc, 2019). RO is considered one of the least versatile pre-concentration technologies, even when it is operated at high pressure. Forward osmosis (FO) is an increasingly prominent technology that functions using osmotic pressure rather than hydraulic pressure, unlike RO and HPRO. FO utilises a highly concentrated draw solution which is subsequently separated and recycled back into the FO system (Ahmed et al., 2019; Abdullah et al., 2019). FO may effectively treat high TDS brines with concentrations of up to 200,000mg/l and can achieve water recovery ratios higher than RO (Eyvaz et al., 2018). Although this technology may have a lower operational cost compared to RO and HPRO, with a potential cost reduction of 15-20% per m^3 of fresh water produced, the overall cost effectiveness of the FO system diminishes when considering the energy required for draw solution recovery. Consequently, both RO and HPRO systems are more cost effective than FO for desalination directly (Valladares Linares et al., 2016). Simultaneously, there are still unresolved issues related to reverse salt flux and concentration polarisation concerns on the membranes that require further optimisation (Johnson et al., 2018). However, due to the insensitivity to feed conductivity, FO may still be competitive for RO brine concentration. The latest advancement in reverse osmosis technology is osmotically aided reverse osmosis (OARO), which is a pressure-driven RO/FO hybrid system. This hybrid technology allows for the treatment of brines with TDS ranging from 140,000 to 250,000mg/l in single and multi-stage systems, respectively (Bartholomew et al., 2017; Peters and Hankins, 2019). Despite the capability of this technology to manage brines with elevated TDS, its current operational expenses are high due to the technology's immaturity (Bartholomew et al., 2018).

1.2.3 Evaporation methods

Preconcentration of brine is followed by evaporation using mostly thermal processes to concentrate brine and recover the remaining water for zero liquid discharge (Spellman, 2015; Malbrouk and Fath, 2015). A brine concentrator (BC) is a type of vertical film evaporator that uses a heat exchanger to heat the brine to its boiling point. After passing through a deaerator, the brine reaches a concentrator where it is heated through multiple heat exchanging tubes. This additional heating causes the water component of the brine to evaporate and then condense outside of the concentrator. In order to maximise the utilisation of this hot condensed freshwater, it is recycled to heat the incoming brine in the initial heat exchanger (Spellman, 2015). The evaporator is capable of operating in brines with a TDS concentration of up to 250,000mg/l. Additionally, it has a high water recovery rate ranging from 90% to 99% (Panagopoulos et al., 2019). An inherent drawback of BC technology is its exorbitant operational cost,

which can reach up to 26 kWh m^{-3} (Mickey, 2018). Multi-stage flash distillation (MSF) is currently being investigated for its potential application in treating brine. In this configuration, the brine is subjected to an external heating source, raising its temperature to 110 - 120°C. The heated brine is then passed through a series of multiple flash units, where the brine is evaporated, resulting in the production of the concentrated brine. The water that has evaporated from the flash reactor is then condensed and utilised in heat exchangers to warm the entering brine, reducing the reliance on an external heat source for heating. The multi-effect distillation (MED) is a concept similar to the MSF, but it differs in that the heating occurs through heat exchange within the evaporative reactors, and lower temperatures (70 - 75%) are required. Similarly to the MSF, the water that has evaporated is also condensed and utilised in heat exchangers before the brine enters the reactors. This helps to reduce the amount of external heating required. Despite having lower operational costs compared to BC, with MSF and MED at 10-20% respectively, and similar freshwater quality, these techniques have a significant drawback in the form of high capital costs due to the materials required for their construction.

1.2.3 Crystallisation methods

Crystallisation is achieved mostly through brine crystallisers (BCr) and spray dryers (SD), to recover the salts that remain in the brine (Panagopoulos et al., 2019). A BCr is typically a vertical vaporising reactor. Brine is introduced into a heat exchanger, where it is pressurised and heated by recirculating the water produced from the crystalliser's outlet. The brine then enters the crystallizer, where the water evaporates and crystals are formed. Subsequently, the crystals are isolated by the process of centrifugation or filtration, while the hot freshwater is employed to raise the temperature of the incoming brine and then collected (Spellman, 2015). Although the BCr is capable of handling high TDS brine with concentrations of up to 300,000mg/l, its cost is significantly elevated because to the substantial energy consumption of the crystalliser, which ranges from 52 to 70 kWh m^{-3} (Mickey, 2008). SD is a crystallisation technique predominantly employed in the food, chemical, and pharmaceutical sectors. It can transform brine into a powdered form consisting of various salts (Al-Khattawi et al., 2017). This method comprises a vertical spray drying chamber in which brine is subjected to centrifugation by a rotary atomiser and subsequently heated by hot air to produce a dry powder mixture. A bag filter is used to separate the dry powder mix from the hot air (Panagopoulos et al., 2019). Despite the similar high running cost of the system, (52 - 64 kWh m^{-3}), it outperforms the BCr in terms of controlling the size distribution, shape, and bulk density of the generated crystals (Mackey and Seacord, 2008). However, both BCr and SD present high capital costs due to the need of use of

high specfication construction materials (Demirel, 2021; Panagopoulos and Giannika, 2022a).

1.2.4 Zero liquid discharge products

The water generated via ZLD is exceptionally pure, with a recovery rate of up to 99%. This water can be used for various reasons, including process water, irrigation, and even drinking water, after undergoing remineralisation (Panagopoulos and Giannika, 2022a). In addition to the evident and beneficial environmental effects of treating the brine and reusing the water, the primary economic incentive for this process lies in the extraction and utilisation of the salts present in the various brines. Brines can include up to twelve highly concentrated ions, including Ca^{2+}, Na^{+}, K^{+}, Cl^{-}, SO_4^{2-}, Mg^{2+}, and others. Additionally, they may contain smaller concentrations of precious ions such as Li^{+}, Rb^{+}, Br^{-}, Ba^{2+}, and others (Panagopoulos and Haralambous, 2022). These salts can be extracted from the brine using ZLD technology, achieving recovery rates of up to 95%. Due to their high purity, these salts are valuable for a wide range of applications, including fertilisers, pharmaceuticals, electronics, and more which significantly contributes to the economic viability of the process. The salts that can be obtained from highly concentrated ions, such as NaCl, $CaCO_3$, $CaCl_2$, $MgCl_2$, K_2SO_4, and $Mg(OH)_2$, can be sold for prices ranging from $65 to $400 per tonne. In contrast, the valuable metals that can be extracted can be sold for prices ranging from $500 (Boron) to $60,000 (Lithium) to $90,000,000 (Cesium and Rubidium) per tonne (Panagopoulos and Giannika, 2022b).

1.3 Membrane distillation and crystallisation

1.3.1 Brine treatment alternatives

Researchers are trying to find alternatives to brine treatment with main focus in, lower operating energy consumption, mostly by avoiding steam needs for heating and incorporating low grade heating from waste heat recovery, and lower capital costs (Panagopoulos, 2019; Chen et al., 2022; Shah et al., 2022). These new alternatives, have to find a way of introducing the two main operational problems of the existing technologies which are the control of the supersaturation and the scalability of the process (Shah et al., 2022). As BCr is an evaporative crystalliser using high temperatures, it leads to temperature gradiant within the crystalliser causing localised supersaturation which can result in uncontrolled nucleation and uneven crystal growth throughout it. This variability grows as we scale the crystalliser trying to incorporate higher flows due to surface area-to-volume ratio making it more difficult to uniform cooling or heating (Amini et al., 2016). SD operates by atomising a liquid feed into a hot gas stream, causing rapid evaporation. This swift reaction, makes the

supersaturation levels difficult to control, as the solution reaches saturation quickly and precipitates out without sufficient time for controlled nucleation and growth (McDonagh and Tajber, 2020). A way to combat these issues is to develop a process which not only operates at lower temperatures but also has a more precise way of controlling supersaturation. Furthermore, by combining evaporation and crystallisation processes, lower capital costs can be achieved. The process that incorporates all these parameters is membrane distillation and crystallisation (MDCr) (Castro-Munoz et al., 2020; Das et al., 2021; Shah et al., 2022).

Membrane distillation (MD) is a membrane process using an induced temperature difference between the two opposite sides of a hydrophobic membrane. The two sides consist of a high temperature solution on one side and a solution with low vapor pressure, primarily water, on the other side. Due to the disparity in temperature, water undergoes evaporation and subsequently traverses the pores of the hydrophobic membrane via diffusion and convection. Consequently, the solution becomes oversaturated, as the non-volatile salts present in the water are unable to traverse through (Kiss and Kattan Readi, 2018). The potential of MD as a promising technique lies in its ability to operate effectively within a reasonable range of temperatures (30 – 80^{o}C) and atmospheric pressure, (Kiss and Kattan Readi, 2018). Because of this, MD has the potential to be powered by low-grade heat sources such as waste heat streams, as opposed to relying on high pressure steam like traditional brine evaporation processes (Prado de Nicolás et al., 2023). Other advantages of MD can treat highly concentrated saline solutions with TDS of up to 300,000mg/l with a potential water recovery of up to 90% (Edwie and Chung, 2013; Anisi et al., 2017; Panagopoulos et al., 2019; Yadav et al., 2021), all while being more compact and modular than other membrane or thermal processes, as it consists of less process stages (Deshmukh et al., 2018; Panagopoulos et al., 2019; Ahmed et al., 2021; Panagopoulos and Giannika, 2022a; Panagopoulos and Giannika, 2022b).

To successfully complete the ZLD process researchers have successfully manage to integrate crystallisation as the next step after MD (Das et al., 2021; Yadav et al., 2022; Sparenberg et al., 2022). Crystallisation is the mechanism of transforming an undersaturated solution to a saturated solution by crossing the solubility curve. This transform from undersaturated to saturated can be initiated in two ways, solution cooling or solution concentration (Chabanon et al, 2016). This transformation can either occur spontaneously or by seeding (Vedantam and Ranade, 2013). The two identified steps of crystallisation process are the formation of nuclei (nucleation) and the growth of this formed nuclei. Nucleation can be classified as primary nucleation and secondary nucleation (Lenka and Sarkar, 2014). Primary nucleation is a

prerequisite for secondary nucleation as this mechanism can only create crystals due to collision of existing crystals with themselves or other foreign substrates, i.e. stirrers, or when the existing crystals can be used as nucleation sites themselves (Kadam et al., 2011). Primary nucleation can be divided into homogeneous and heterogeneous nucleation. First can only take place in a pure system where no solute or any other impurities can be found, while secondary nucleation happens when a crystalline or any other foreign substrate can be present in the system (Jia et al., 2016; Warsinger et al., 2016). To form a stable crystal through nucleation, its size has to be big enough to sufficiently reduce the Gibbs free energy of the system. This drop of the Gibbs free energy is the critical energy barrier for nucleation (Jia et al., 2016). Crystallisation is primarily driven by the generation of supersaturation in the solution required for crystallisation. The supersaturation is defined as the difference between the concentration of the solute to be crystallised and its saturation concentration. The saturation concentration of the solute is its solubility (Nemdili et al., 2021; Wang et al., 2020). Supersaturation can be generated by evaporation, solution extraction, cooling, or the addition of anti-solvent (Nyvlt, 1985; Lenka and Sarkar, 2014; Wang et al., 2020).

1.3.2 Metastable Zone Width

The operating boundary of the crystallisation process when supersaturation occurs can be defined by the metastable zone width (MSZW). MSZW is the region between the solubility curve and the outbreak of nucleation (Mullin, 2001). Using MSZW, we can get a lot of information that can help us determine nucleation kinetics as well as the point of nucleation of crystallisation process (Titiz-Sargut and Ulrich, 2003; Wang et al., 2020). This information is a precondition for the scale up of the process, as it helps control nucleation, crystal size distribution and shape as well as create crystals with useful quantity and quality (Zhou et al., 2017). MSZW can be calculated using either conventional deterministic or probabilistic stochastic models (Goh et al., 2010; Jiang and ter Horst, 2011; Peters, 2011; Kadam et al., 2012; Maggioni and Mazzoti, 2015; Bhamidi et al., 2017; Shiau, 2021). The point of nucleation can be found through induction time, which is defined as the time passed from the onset of supersaturation to the detection of the first crystal (Mullin, 2001). In principle, nucleation takes place before we eventually detect it, which means that the induction time can vary according to the method of detection (Kadam et al., 2011). Widely used methods of detection are, flux drop detection and direct visual observation including microscopy or bulk video imaging, focus beam reflectance measurement (FBRM), infrared spectroscopy (FTIR), ultrasonic velocity, electrical conductivity and turbidity measurements (Fujiwara et al., 2002; Lyczko et al., 2002; Heath eta l., 2002; Tun et al., 2005; Simon et al., 2009; Simon et al., 2010; Frohberg and Ulrich, 2015; Luo et al., 2017; Numdili

et al., 2018). Hence, it is crucial to employ the most optimal method of crystal detection (Nemdili et al., 2018). The induction time of these crystals depends on various thermodynamic, hydrodynamic and other operating parameters such as stirring rate and fluid dynamics (Hu et al., 2001).

1.3.3 Advantages of the new process

By coupling these two processes, a breakthrough process named membrane distillation crystallisation (MDCr) is developed in order to recover valuable salts present in salt-rich solutions including sea water, brackish water, wastewater and others (Das et al., 2021), with lower reported energy consumption compared to MD (Yadav et al., 2022). MDCr uses the principles of membrane distillation for the control of mass transfer (feed solution concentration) as well as using it as a support site to lower the energy barrier and promote heterogeneous nucleation (Curcio and Drioli, 2005; Choi et al., 2019). This not only enhances the efficiency of the process compared to traditional crystallisation methods, but also facilitates a more homogeneous crystal size distribution improving the stability and reliability of the process (Di Profio et al., 2007; Tsai et al., 2018). By utilising this collaborative technology, the evaporation and crystallisation stages of the ZLD process may be combined into a single phase, hence lowering the number of process steps. This integration simplifies the ZLD process and more importantly making it more cost-effective, especially when alternative sources of heating can be used (Prado de Nicolás et al., 2023).

1.4 The role of the membrane surface in membrane crystallisation

The most unique feature on this technology is lying on the existence of the membrane, which is used as the tool to improve the heat and mass transfer performance which is the heart of the MDCr process (Chabanon et al., 2016). To optimize the process conditions, hydrophobic polymeric materials are employed, (Zaheed and Jachuck et al., 2004; Hubadillah et al., 2018) with the most common of them being polytetrafluoroethylene (PTFE), polyvinylidene fluoride (PVDF) and polypropylene (PP). These membranes can be used in three configurations: flat sheet, hollow fibre and electrospun membranes, with the first two being the most prevalent (Ravi et al., 2020).

Even though the primary role of the membrane is to provide barrier where the vapor pressure between the feed and the permeate side is leading to evaporation and the concentration of the feed solution, its role also extends to the heterogeneous crystallisation of the solutes (Meng et al., 2014). As heterogeneous nucleation can occur in the presence of any other foreign matter, which in the case of MDCr is the membrane surface, the pores of the membrane can be used as nucleation spots that

reduce the free energy barrier, forcing the nucleation to occur in lower supersaturation (Bormashenko and Valtsifer, 2021). Homogeneous nucleation occurs at higher supersaturation, as there are no foreign nucleation spots, making its nucleation rate higher than the one of heterogeneous (Wang et al., 2020). As a result, heterogeneous nucleation is by rule of thumb happening before homogeneous nucleation (Erdemir et al., 2019). Coupled with polarisation phenomena, the membrane results in higher supersaturation than the bulk solution, which not only reduces the activation energy required for the critical nuclei increasing the chance of nucleation locally, but reaches higher supersaturation faster favouring the crystallisation on the membrane (Drioli and Efrem, 2005; Tun et al., 2005; Wang et al., 2014). The membrane features that are crucial in the process of heterogeneous crystallisation are contact angle (hydrophobicity of the membrane), roughness, pore size, porosity, and thickness (Gryta, 2008; Gryta and Barancewicz, 2010; Wong et al., 2011; Goh et al., 2013; Warsinger et al., 2017; Cui et al., 2018; Tong et al., 2019; Kharraz and An, 2020). However, heterogeneous crystallisation of salts is not generally preferred and try to be avoided, as the crystal formation and growth on the membrane leads to rapid fouling and eventually wetting of the membrane causing the termination of the process (Shirazi et al., 2010; Meng et al., 2015).

1.5 Thermodynamics of crystal nucleation

To be able to form a crystal, detect it, and reach the induction time, the nuclei has to reach a certain critical size. Reaching this critical size, the nuclei manage to avoid the dissolution and remain stable, resulting into growth (Roelands et al., 2005; Erdemir et al., 2019). The Gibbs free energy needed to develop a crystal of critical size (ΔG^*), is the sum of the positive surface formation free energy (ΔG_s), which favours dissolution, and the negative volume formation free energy which favours growth (ΔG_v) (Erdemir et al., 2019; Bormashenko and Valtsifer, 2021). When the energy difference reaches maximum, its appointed value or radius is the critical size (n^*). After that, total free energy starts decreasing, favouring the growth of the generated nuclei (Erdemir et al., 2019; Bormashenko and Valtsifer, 2021).

A very important characteristic property of ΔG^*, as can be seen by its cubic contribution, is the interfacial energy (Roelands et al., 2005; Torrens-Serra et al., 2009; Erdemir et al., 2019). This is the work needed for the formation of a crystal in the solvent-solute-membrane interaction (Baidakov and Tipeev, 2012), which shows that the higher the interfacial energy of the system, the more energy is needed to crystallise the solute (Shiau and Wang, 2016). Söhnel (1971), was the first to link interfacial energy with the solubility of the aqueous inorganic salts, with more research duplicating

and verifying these results (Söhnel, 1982; Mersmann and Kind, 1988; Bennema and Söhnel, 1990). As the low solubility increases the interfacial energy, ΔG* is increasing and there is a need of higher levels of supersaturation to overcome this energy barrier. Combining it with the lower molecular collision probability of the low solubility salts (Erdemir et al., 2019), there is a preference towards homogeneous nucleation, while the higher solubility salts will tend more towards the heterogeneous nucleation (Mersmann and Kind, 1988).

1.6 Membrane Fouling

In MDCr, membrane fouling is the accumulation of unwanted materials on the membrane surface or inside its pores, causing the flux to decline and eventually terminate the process (Alkhatib et al., 2021; Razmavar et al., 2022). Membrane fouling is typically categorised according to the feed source as biological fouling, organic fouling and inorganic fouling, and according to its generation as deposition (homogeneous nucleation), or scaling (heterogeneous nucleation) (Gryta, 2009; Gryta, 2012; Warsinger et al., 2015; Alkhatib et al., 2021). In order to improve the efficacy of the MDCr process, it is imperative to identify strategies that may effectively reduce or minimize fouling formation and offset its adverse impact on the performance of the process (Tijing et al., 2015).

The fouling cannot only minimised by manipulating the membrane properties, through membrane alterations and the creation of superhydrophobic membranes, but also through manipulation of the thermodynamic and hydrodynamic conditions (Tijing et al., 2015; Goh et al., 2018). The aforementiond conditions significantly influence the chemistry of the inorganic salts, which in turn impact the fouling of the membrane (Alklaibi and Lior, 2005; He et al., 2008; Warsinger et al., 2015). The primary chemical determinant of membrane fouling is solubility, wherein the prevailing scalants are often low solubility salts like $CaSO_4$ and $CaCO_3$ (Darton et al., 2004; He et al., 2008; Rezai et al., 2018; Alkhatib et al., 2021). The severity of the fouling due to the inorganic salts is heavily influenced by the supersaturation and the crystallisation kinetics (Antony et al., 2011).

1.7 Aims and Objectives

The aim of this thesis is to understand the role of the chemistry of the inorganic salts and identify the most suitable thermodynamic, hydrodynamic conditions and membrane properties, to enhance the operation of the membrane crystallisation process. In doing so, we will be able to get a deeper understanding of the fouling

mechanisms of membrane crystallisation and create a more energetically and economically efficient and viable process, while getting high quality inorganic product.

To address these aims, we have developed the following framework:

a. Determine and compare the onset of heterogeneous and homogeneous nucleation of different aqueous inorganic salts, through direct observation of induction time on both bulk and membrane surface, and how interfacial energy can be used to predict it.
b. Identify the influence of the polarisation phenomena on the solute chemistry of three salts with different solubility-temperature dependence, and their effects on the induction time as well as the nucleation mechanism.
c. Decouple the effect of the membrane material from the transmembrane flux to identify the specific mechanisms governing nucleation during membrane distillation, by using an inorganic salt with almost neutral solubility-temperature dependence against three different membranes.
d. Once decoupled the membrane effect, understand the extension of the salt chemistry in crystallisation, by using an inorganic salt with high solubility-temperature dependence.

1.8 Thesis structure

The thesis is consisted of four technical chapters (Chapters 2, 3, 4 & 5), which address the aims of the thesis. Each chapter has been written in the format of a journal paper. Chapter 2, “Use of crystal-liquid interfacial energy to predict scaling, nucleation and crystal growth in membrane distillation crystallisation” establishes a direct connection between the interfacial energy and the nucleation mechanism of the process. Chapter 3, “Temperature polarisation controls nucleation kinetics in membrane distillation crystallisation” identifies the effect of the polarisation phenomena and how we can manipulate the onset of the nucleation as well as the nucleation mechanism by changing the hydrodynamic conditions of the process. Chapter 4, “Effect of the membrane material on the nucleation kinetics of crystallisation in membrane distillation crystallisation of sodium chloride” understands that the membrane material and its properties have no actual effect in the membrane distillation process outside of the transmembrane flux. Chapter 5 “Solubility-temperature dependency of salts reduces nucleation kinetics in membrane distillation crystallisation” extends the effect of the salt chemistry in crystallisation and shows how the nucleation mechanisms can be manipulated by changing the thermodynamics of the process.

The lead author of this thesis including all the submissions was Konstantinos Vasilakos, and they were edited by Dr Ewan McAdam and Dr Pablo Campo-Moreno as supervisors. Data collection in Chapter 2, 3, 4 and 5 were supported by Dr Mehrez Hermassi and Dr Navya Thomas. Chapter 6 & 7 is an overall discussion of the thesis, together with the overall conclusions and proposed future work.

1.9 References

F.E. Ahmed, R. Hashaikeh, N.I. Hilal, Solar powered desalination – technology energy and future outlook, Desalination. 453 (2019) 54 – 76.

F.E. Ahmed, A. Khalil, N. Hilal, Emerging desalination technologies: Current status, challenges and future trends, Desalination. 517 (2021) 115183.

A. M. Alklaibi, N. Lior, Membrane-distillation desalination: status and potential, Desalination. 171(2) (2005) 111 – 131.

A. Alkhatib, M. A. Ayari, A. H. Hawari, Fouling mitigation strategies for different foulants in membrane distillation, Chem. Eng. Proc. – Proc. Intens. 167 (2021) 108517.

Y. Amini, M. B. Gerdroodbary, M. R. Pishvaie, R. Moradi, S. M. Monfared, Optimal control of batch cooling crystallizers by using genetic algorithm, Case Studies in Thermal Engineering, 8 (2016) 300 – 310.

G. Amy, N. Ghaffour, Z. Li, L. Francis, R.V. Linares, T. Missimer, S. Lattemann, Membrane-based seawater desalination: present and future prospects, Desalination. 401 (2017) 16 – 21.

F. Anisi, K.M. Thomas, H.J.M. Kramer, Membrane-assisted crystallisation: membrane characterization, modelling and experiments, Chem. Eng. Sci. 158 (2016) 277 – 286.

A. Antony, J. H. Low, S. Gray, A. E. Childress, P. Le-Clech, G. Leslie, Scale formation and control in high pressure membrane water treatment systems: a review, J. Membr. Sci. 383(1-2) (2011) 1 – 16.

H. M. Ashraf, S.A. Al-Sobhi, M.H. El-Naas, Mapping the desalination journal: A systematic bibliometric study over 54 years, Desalination. 526 (2022) 115535.

M. Ayaz, M.A. Namazi, M. Ammad ud Din, M.I. Mohamed Ershath, A. Mansour, E-H. M. Aggoune, Sustainable seawater desalination: Current status, environmental implications and future expectations, Desalination. 540 (2022) 116022.

V.G. Baidakov, A.O. Tipeev, Crystal nucleation and the soli-liquid interfacial free energy, J. Chem. Phys. 136 (2012) 074510.'

P. Bennema, O. Söhnel, Intefacial surface tension for crystallisation and precipitation from aqueous solutions, J. Cryst. Growth. 102 (1990) 547 – 556.

V. Bhamidi, P.J.A. Kenis, C.F. Zukoski, Probability of nucleation in a metastable zone: cooling crystallisation and polythermal method, Cryst. Growth Des. 17 (2017) 5823 – 5837.

C. Boo, S. Hong, M. Elimelech, Relating organic fouling in membrane distillation to intermolecular adhesion forces and interfacial surface energies, Environ. Sci. Technol. 52 (2018) 14198 – 14207.

E. Bormashenko, V. Valtsifer, Interfacial crystallisation at the intersection of thermodynamic and geometry, Adv. Colloid Int. Sci. 296 (2021) 102510.

L.P.M. Brendel, V.M. Shah, E.A. Groll, J.E. Braun, A methodology for analyzing renewable energy opportunities for desalination and its application to Aruba, Desalination. 493 (2020) 114613.

J. Bundschuh, M. Kaczmarczyk, N. Ghaffour, B. Tomaszewska, State-of-the-art of renewable energy sources using in water desalination: Present and future prospects, Desalination. 508 (2021) 115035.

R. Castro-Munoz, E. Diaz-Montes, A. Cassano, E. Gontarek, Membrane separation processes for the extraction and purification of steviol glycosides: an overview, Crit. Rev. Food Sci. Nutr. (2020) 1 – 23.

E. Chabanon, D. Mangin, C. Charcosset, Membranes and crystallisation processes: state of the art and prospects, J. Membr. Sci. 509 (2016) 57 – 67.

Q. Chen, M. Burhan, M. W. Shahzad, D. Ybyraiymkul, F. H. Akhtar, Y. Li, K. Choon Ng, A zero liquid discharge system integrating multi-effect distillation and evaporative crystallisation for desalination brine treatment, Desalination. 502 (2021) 114928.

Y. Choi, G. Naidu, L.D. Nghiem, S. Lee, S. Vigneswaran, Membrane distillation crystallisation for brine mining and zero liquid discharge: opportunities, challenges, and recent progress, Environ. Sci. Water Res. Technol. (2019) 1202 – 1221.

P.K. Cornejo, M.V. Santana, D.R. Hokanson, J.R. Mihelcic, Q. Zhang, Carbon footprint of water reuse and desalination: a review of greenhouse gas emissions and estimation tools, J. Water Reuse Desal. 4(4) (2014) 238 – 252.

Z. Cui, X. Li, Y. Zhang, Z. Wang, A. Gugliuzza, F. Militano, E. Drioli, F. Macedonio, Testing of three different PVDF membranes in membrane assisted-crystallisation process: Influence of membrane structural-properties on process performance, Desalination. 440 (2018) 68 – 77.

E. Curcio, G. Di Profio, E. Drioli, Membrane crystallisation of macromolecular solutions, Desalination. 145 (2002) 173 – 177.

E. Curcio, E. Drioli, Membrane distillation and related operations – a review, Sep. Purif. Rev. 34 (2005) 25 – 86.

T. Darton, U. Annunziata, F. del Vigo Pisano, S. Gallego, Membrane autopsy helps to provide solutions to operational problems, Desalination. 167(0) (2004) 239 – 245.

P. Das, S. Dutta, K.K.K. Singh, S. Maity, Energy saving integrated membrane crystallisation: a sustainable technology solution, Sep. Purif. Technol. 228 (2019) 115722.

P. Das, S. Dutta, K.K. Singh, Insights into membrane crystallisation: A sustainable tool for value added product recovery from effluent streams, Sep. and Purif. Technol. 257 (2021) 117666.

Y. Demirel, Energy Conversion, Green Energy and Technology, CRC press., 2021.

A. Deshmukh, C. Boo, V. Karanikola, S. Lin, A.P. Straub, T. Dong, D.M. Warsinger, M. Elimelech, Membrane distillation at the water-energy nexus: limits opportunities, and challenges, Energy Environ. Sci. 11 (2018) 1177 – 1196.

G. Di Profio, S. Tucci, E. Curcio, E. Drioli, Controlling polymorphism with membrane-based crystallizers: application to form I and II of paracetamol, Chem. Mater. 5 (2007) 2386 – 2388.

E. Drioli, C. Efrem, Membrane crystallisation in “Membrane Conactors: Fundamentals, Applications and Potentialities”, Membrane Science and Technology. 11 (2005) 254 – 272.

E. Drioli, G. Di Profio, E. Curcio, Progress in membrane crystallisation, Curr. Opin. Chem. Eng. 1(2) (2012) 178 – 182.

F. Edwie, T.S. Chung, Development of simultaneous membrane distillation-crystallisation (SMDCr) technology for treatment of saturated brine, Chem. Eng. Sci. 98 (2013) 160 – 172.

J. Eke, A. Yusuf, A. Giwa, A. Sodiq, The global status of desalination: an assessment of current desalination technologies, plants and capacity, Desalination. 495 (2020) 114633.

M. Elimelech, W.A. Phillip, The future of seawater desalination: Energy, technology, and the environment, Science. 80, 333 (2011) 712 – 717.

K. Elsaid, E.T. Sayed, B.A.A. Yousef, M.K.H. Rabaia, M.A. Abdelkareem, A.G. Olabi, Recent progress on the itilization of waste heat for desalination: A review, Energy Conv. and Manag. 221 (2020) 113105.

D. Erdemir, A. Lee, A. Myerson, Handbook of Industrial Crystallisation, Cambridge: Cambridge University Press, Chapter 3 (2019) 76 – 114.

L. Eykens, K. de Sitter, C. Dotremont, L. Pinoy, B. van der Bruggen, How to optimize the membrane properties for membrane distillation: A review, Ind. Eng. Chem. Res. 55(35) (2016) 9333 – 9343.

H. Frank, E. Rahav, E. Bar-Zeev, Short-term effects of SWRO desalination brine on benthic heterotrophic microbial communities, Desalination. 417 (2017) 52 – 59.

P. Frohberg, J. Ulrich, Single-frequency ultrasonic crystallisation monitoring (UCM): Innovative technique for in-line analyzing of industrial crystallisation processes, Org. Process Res. Dev. 19 (2015) 84 – 88.

M. Fujiwara, P.S. Chow, D.L. Ma, R.D. Braatz, Paracetamol crystallisation using lased backscattering and ATR-FTIR spectroscopy: metastability, agglomeration, and control, Crystl. Growth Des. 2 (2002) 363 – 370.

N. Ghaffour, J. Bundschuh, H. Mahmioudi, M.F.A. Goosen, Renewable energy-driven desalination technologies: a comprehensive review on challenges and potential application of integrated systems, Desalination. 356 (2015) 94 – 114.

A. Giwa, V. Dufour, F. Al Marzooqi, M. Al Kaabi, S.W. Hasan, Brine management methods: recent innovations and current status, Desalination. 407 (2017) 1 – 23.

S. Goh, J. Zhang, Y. Liu, A.G. Fane, Fouling and wetting in membrane distillation (MD) and MD-bioreactor (MDBR) for wastewater reclamation, Desalination. 323 (2013) 39 – 47.

P. S. Goh, W. J. Lau, M. H. D. Othman, A. F. Ismail. Membrane fouling in desalination and its mitigation strategies, Desalination. 425 (2016) 130 – 155.

L. Goth, K. Chen, V. Bhamidi, G. He, N.C.S. Kee, P.J.A. Kenis, C.F. Zukoski, R.D. Braatz, A stochastic model for nucleation kinetics determination in droplet-based microfluidic systems, Cryst. Growth Des. 10(6) (2010) 2515 – 2521.

GOV.UK. (2024, April 24). Research and analysis *Appendix C: Revised draft water resources management plans supply options***.** Environment Agency. https://www.gov.uk/government/publications/a-review-of-englands-draft-regional-and-water-resources-management-plans/appendix-c-draft-water-resources-management-plans-supply-options#contents

M. Gryta, Fouling in direct contact membrane distillation process, J. Membr. Sci. 325 (2008) 383 – 394.

M. Gryta, Calcium sulphate scaling in membrane distaillation process, Chem. Pap. 63 (2) (2009).

M. Gryta, M. Barancewicz, Influence of morphology of PVDF capillary membranes on the performance of direct contact membrane distillation, J. Membr. Sci. 358 (2010) 158 – 167.

M. Gryta, Polyphosphates used for membrane scaling inhibition during water desalination by membrane distillation, Desalination 285 (2012) 170 – 176.

F. He, H. Lee, L. Song, K. K. Sirkar, Potential for scaling by sparingly soluble salts in crossflow DCMD, J. Membr. Sci. 311(1-2) (2008) 68 – 80.

A.R. Heath, P.D. Fawell, P.A. Bahri, J.D. Swift, Estimating average particle size by focused beam reflectance measurement (FBRM), Part. Part. Syst. Charact. 19 (2002) 84 – 95.

H. Hu, T. Hale, X. Yang, L.J. Wilson, A spectrocphotometer-based method for crystallisation induction time period measurement, J. Cryst. Growth. 232 (2001) 86 – 92.

S.K. Hubadillah, M.H.D. Othman, T. Matsuura, M.A. Rahman, J. Jaafar, A.F. Ismail, S.Z.M. Amin, Green silica-based ceramic hollow fiber membrane for seawater

desalination via direct contact membrane distillation, Sep. Purif. Technol. 205 (2018) 22 – 31.

F. Jia, D. Zhao, M. Wang, Selective nucleation and self-organized crystallisation, Prog. Cryst. Growth Charact. Mat. 62 (2016) 252 – 272.

S. Jiang, J.H. ter Horst, Crystal nucleation rates from probability distributions of induction times, Crystl. Growth Des. 11(1) (2011) 256 – 261.

X. Jiang, Y. Shao, L. Sheng, P. Li, G. He, Membrane Crystallisation for Process Intensification and Control: A Review, Engineering. 7 (2012) 50 – 62.

E. Jones, M. Qadir, M.T.H. van Vliet, V. Smakhtin, S. mu Kang, The state of desalination and brine production: a global outlook, Sci. Tot. Environ. 657 (2019) 1343 – 1356.

S.S. Kadam, H.J.M. Kramer, J.H. ter Horst, Combination of a Single Primary Nucleation Event and Secondary Nucleation in Crystallisation Processes, Cryst. Growth Des. 11 (2011) 1271 – 1277.

S.S. Kadam, S.A. Kulkarni, R.C. Colona Ribera, A.I. Stankiwicz, J.H. ter Horst, H.J.M. Kramer, Crystal nucleation kinetics from induction times and metastable zone widths, Chem. Eng. Sci. 72 (2012) 10 – 19.

J.A. Kharraz, A.K. An, Patterned superhydrophobic polyvinylidene fluoride (PVDF) membranes for membrane distillation: Enhanced flux with improved fouling and wetting resistance, J. Membr. Sci. 595 (2020) 117596.

A.A. Kiss, O.M. Kattan Readi, An industrial perspective on membrane distillation processes, J. Chem. Technol. Biotechnol. 93 (2018) 2047 – 2055.

M. Lenka, D. Sarkar, Determination of metastable zone width, induction period and primary nucleation kinetics for cooling crystallisation of L-asparaginenohydrate, J. Cryst. Growth. 408 (2014) 85 – 90.

L. Liu, F. Shen, X. Chen, J. Luo, Y. Su, H. Wu, A novel plasma-induced surface hydrophobization strategy for membrane distillation: Etching, dipping and grafting, J. Membr. Sci. 499 (2016) 544 – 554.

M. Luo, C. Liu, J. Xue, P. Li, J Yu, Determination of metastable zone width of potassium sulphate in aqueous solution by ultrasonic sensor and FBRM, J. Cryst. Growth. 469 (2017) 144 – 153.

N. Lyczko, F. Espitalier, O. Louisnard, J. Schwartzentruber, Effect of ultrasound on the induction time and the metastable zone widths of potassium sulphate, J. Chem. Eng. 86 (2002) 233 – 241.

G.M. Maggioni, M. Mazzotti, Modelling the stochastic behaviour of primary nucleation, Faraday Discuss. 179 (2015) 359 – 382.

A. F. McDonagh, L. Tajber, The control of paracetamol particle size and surface morphology through crystallisation in a spray dryer, Adv. Pow. Technol. 31 (2020) 287 – 299.

S. Meng, Y. Ye, J. Mansouri, V. Chen, Fouling and crystallisation behaviour of superhydrophobic nano-composite PVDF membranes in direct contact membrane distillation, J. Membr. Sci. 463 (2014) 102 – 112.

S. Meng, Y. Ye, J. Mansouri, V. Chen, Crystallisation behaviour of salts during membrane distillation with hydrophobic and superhydrophobic capillary membranes, J. Membr. Sci. 473 (2015) 165 – 176.

A. Mersmann, M. Kind, Chemical Engineering Aspects of Precipitation from Solution, Chem. Eng. Technol. 11 (1988) 264 – 276.

T.M. Missimer, R.G. Maliva, Environmental issues in seawater reverse osmosis desalination: intakes and outfalls, Desalination. 434 (2018) 198 – 215.

M. Mukiibi, R. Feathers, Membrane Technology: A Break Through in Water Treatment – WCP Online, Water Cond. Purif. Mag. 2009 (assessed 27 March 2023).

J.W. Mullin, Crystallisation, Fourth ed. Butterworth -Heinemman, Oxford, (2001) 201.

H. Nassrullah, S.F. Anis, R. Hashaikeh, N. Hilal, Energy for desalination: a state-of-the-art review, Desalination. 491 (2020), 114569.

L. Nemdili, O. Koutchoukali, F. Mameri, I. Gouaou, M.S. Koutchoukali, J. Ulrich, Crystallisation study of potassium sulphate-water system, metastable zone width and induction time measurements using ultrasonic, turbidity and 3D-ORM techniques, J. Cryst. Growth. 500 (2018) 44 – 51.

A.E. Nielsen, O. Söhnel, Interfacial tensions electrolyte crystal-aqueous solution, from nucleation data, J. Cryst. Growth. 11 (1971) 233 – 242.

J. Nyvlt, The kinetics of Industrial Crystallisation, Elsevier, USA, 1985.

A. Panagopoulos, K-J. Haralambous, Environmental impacts of desalination and brine treatment – Challenges and mitigation measures, Mar. Pollut. Bull. 161 (Part B) (2020) 111773.

B. Peters, Supersaturation rates and schedules: Nucleation kinetics from isothermal metastable zone widths, J. Cryst. Growth. 317 (2011) 79 – 83.

M. Polino, C.A.M. Portugal, G. Di Profio, I.M. Coelhoso, J.G. Crespo, Protein crystallisation by membrane-assisted technology, Cryst. Growth Des. 19(8) (2019) 4871 – 4883.

J. Ravi, M.H.D. Othman, T. Matsuura, M. Ro'il Bilad, T.H. El-badawy, F. Aziz, A.F. Ismail, M.A. Rahman, J. Jaafar, Polymeric membranes for desalination using membrane distillation: A review, Desalination. 490 (2020) 114530.

A. Razmavar, G. Annadurai, A. Olufade, C. J. Simonson, A model for predicting the effect of crystallisation fouling on moisture transfer in membrane energy exchangers, Int. J. Heat and Mass Trans. 191 (2022) 122844.

M. Rezaei, D. M. Warsinger, J. H. Lienhard V, M. C. Duke, T. Matsuura, W. M. Samhaber, Wetting phenomena in membrane distillation: mechanisms, reversal, and prevention, Water Res. 139 (2018) 329 – 352.

A.S. Richey, B.F. Thomas, M.H. Lo, J.T. Reager, J.S. Famiglietti, K. Voss, S. Swenson, M. Rodell, Quantifying renewable groundwater stress with GRACE, Water Resour. Res. 51 (2015) 5217 – 5237.

C.P.M. Roelands, J.H. ter Hoorst, H.J.M. Kramer, P.J. Jansens, Analysis of Nucleation Rate Measurements in Precipitation Processes, Cryst. Growth Des. 6 (2006) 1380 – 1392.

M.M. Seckler, Crystallisation in Fluidized Bed Reactors: From Fundamental Knowledge to Full-Scale Applications, Crystals. 12 (2022) 1541.

A. Shafieian, M. Rizwan Ashar, M. Khiadani, T. Kanti Sen, Performance of thermal-driven membrane-based solar desalination systems using nanofluid in the feed stream, Sustain. Energy Technol. Assess. 39 (2020) 100715.

K. M. Shah, I. H. Billinge, X. Chen, H. Fan, Y. Huang, R. K. Winton, N. Y. Yip, Drivers, challenges, and emerging technologies for desalination of high-salinity brines: A critical review, Desalination. 538 (2022) 115827.

L.D. Shiau, A linearized integral odel for determining the n ucleation parameters from metastable zone with data, J. Cryst. Growth. 564 (2021) 126115.

S. Shirazi, C.-J. Lin, D. Chen, Inorganic fouling of pressure-driven membrane processes – a critical review, Desalination. 250(1) (2010) 236 – 248.

K.H.L.L. Simon, Z.K. Nagy, Endoscopy based in-siteu bulk video imaging of batch crystallisation processes, Org. Process Res. Dev. 13 (2009) 1254 – 1261.

L.L. Simon, K. Abbou Oucherif, Z.K. Nagy, K. Hungerbuhler, Bulk video imaging multivariate image analysis, process control chart and acoustic signal assisted nucleation detection, Chem. Eng. Sci. 65 (2010) 4983 – 4995.

C. Skuse, A. Gallego-Schmid, A. Azapagic, P. Gorgojo, Can emerging membrane-based desalination technologies replace reverse osmosis?, Desalination. 500 (2021) 114844.

O. Söhnel, Electrolyte crystal-aqueous solution interfacial tensions from crystallisation data, J. Cryst. Growth. 57 (1982) 101 – 108.

M.-C. Sparenberg, S. Chergaoui, V.S. Sefidi, P. Luis, Crystallisation control via membrane distillation-crystallisation: A review, Desalination. 519 (2022) 115315.

M. Tian, X. Li, Y. Yin, T. He, J. Liu, Preparation of superhydrophobic membranes and their application in membrane distillation, Prog. Chem. 27 (2015) 1033 – 1041.
L.D. Tijing, Y.C. Woo, J-S. Choi, S. Lee, S-H. Kim, H. K. Shon, Fouling and its control in membrane distillation – A review, J. Membr. Sci. 475 (2015) 215 – 244.
S. Titiz-Sargut, J. Ulrich, Application of a protected ultrasound sensor for the determination of the width of the metastable zone, Chem. Eng. Process. Proc. Intens.. 42 (2003) 841 – 846.
T. Tong, A.F. Wallace, S. Zhao, Z. Wang, Mineral scaling in membrane desalination: mechanisms, mitigation strategies, and feasibility of scaling-resistant membranes, J. Membr. Sci. 579 (2019) 52 – 69.
J.-H. Tsai, M.L. Perrotta, A. Gugliuzza, F. Macedonio, L. Giorno, E. Drioli, K.-L. Tung, E. Tocci, Membrane-assisted crystallisation: a molecular view of NaCl nucleation and growth, Appl. Sci. 8 (2018) 2145.
C.M. Tun, A.G. Fane, J.T. Matheickal, R. Sheikholeslami, Membrane distillation crystallisation of concentrated salts-flux and crystal formation, J. Membr. Sci. 257 (2005) 144 – 155.
S. Vedantam, V.V. Ranade, Crystallisation: key thermodynamic, kinetic and hydrodynamic aspects, Sadhana – Acad. Proc. Eng. Sci. 38(6) (2013) 1287 – 1337.
L. Wang, B. Li, X. Gao, Q. Wang, J. Lu, Y. Wang, S. Wang, Study of membrane fouling in cross-flow vacuum membrane distillation, Sep. Purif. Technol. 122 (2014) 133 – 143.
S. Wang, M. Feng, H. Du, J.J. Weigand, Y. Zhang, X. Wang, Determination of metastable zone width, induction time and primary nucleation kinetics for cooling crystallisation of sodium orthovanadate from NaOH solution, J. Cryst. Growth. 545 (2020) 125721.
D. M. Warsinger, J. Swaminathan, E. Guillen-Burrieza, H. A. Arafat, J. H. Lienhard V, Scaling and fouling in membrane distillation for desalination applications: A review, Desalination. 356 (2015) 294 – 313.
D.M. Warsinger, A. Servi, S. Van Belleghem, J. Gonzalez, J. Swaminathan, J. Kharraz, H.W. Chung, H.A. Arafat, K.K. Gleason, J.H. Lienhard V, Combining air recharging and membrane superhydrophobicity for fouling prevention in membrane distillation, J. Mem. Sci. 505 (2016) 241 – 252.
D.M. Warsinger, E.W. Tow, J. Swaminathan, J.H. Lienhard V, Theoretical framework for predicting inorganic fouling in membrane distillation and experimental validation with calcium sulphate, J. Membr. Sci. 528 (2017) 381 – 390.
T.S. Wong, S.H. Kang, S.K. Tank, E.J. Smythe, B.D. Hatton, A. Grinthal, J. Aizenberg, Bioinspired self-repairing slippery surfaces with pressure-stable omniphobicity, Nature. 477 (2011) 443 – 447.

A. Yadav, P.K. Labhasetwar, V.K. Shahi, Membrane distillation using low-grade energy for desalination: a review, J. Environ. Chem. Eng. 9 (2021) 105818.
A. Yadav, P.K. Labhasetwar, V.K. Shahi, Membrane distillation crystallisation technology for zero liquid discharge and resource recovery: Opportunities, challenges and futuristic perspectives, Sci. Tot. Environ. 806 (2022) 150692.
L. Zaheed, R.J.J. Jachuck, Review of polymer compact heat exchangers, with special emphasis on a polymer film unit, Appl. Therm. Eng. 24 (2004) 2323 – 2358.
L. Zhou, Z. Wang, M. Zhang, M. Guo, S. Xu, Q. Yin Determination of metastable zone and induction time of analgin for cooling crystallisation, Chi. J. Chem. Eng. 25 (2017) 313 – 318.

2 Use of crystal-liquid interfacial energy to predict scaling, nucleation and crystal growth in membrane distillation crystallisation

Use of crystal-liquid interfacial energy to predict scaling, nucleation and crystal growth in membrane distillation crystallisation

K. Vasilakos, N. Thomas, M. Hermassi, P. Campo, E. McAdam[a]

Cranfield Water Science Institute, Cranfield University, Cranfield, MK43 0AL

[a]corresponding author: e.mcadam@cranfield.ac.uk

Abstract

Crystal-liquid interfacial energy (γ) is the excess free energy that is needed to create a stable interface between a crystal and a liquid and it is inversely related to the solubility of the aqueous salts. Previous studies have evidenced the importance of this property in the nucleation process by its cubic contribution to Gibbs energy (ΔG*), which is the energy that needs to be exceeded to form a stable nucleus. We therefore introduce high-definition imaging for the detection of induction time and use this crucial characteristic property of the salt to seek its role in the kinetics of scaling, nucleation and crystal growth in membrane distillation crystallisation. To examine this effect, five solutions with five different γ were used ($(NH_4)_2SO_4$, K_2SO_4, NaCl, Ag_2SO_4 and $CaSO_4$). Increasing the γ of the solution lead to higher concentration rates of the solute in the solution pushing the induction to higher supersaturation levels. This resulted to higher nucleation rates for the high γ salts which were pushed towards the homogeneous nucleation pathway, reducing the nucleation's dependency on the membrane which is acting as the heterogeneous substrate on membrane distillation crystallisation. As a result, the scaling due to heterogeneous nucleation was declining as the γ of the solution was increasing, with no scaling observed on the Ag_2SO_4 and $CaSO_4$ solutions prior to bulk induction. Even though this complies with classical nucleation theory it contradicts the MDCr literature, where researchers try to operate in lower supersaturation to avoid scaling. This study provides a critical differentiation of heterogeneous scaling adhesive growth and homogeneous bulk deposition which can be used in order to develop scaling mitigation strategies for the design of a more sustainable MDCr process.

Keywords: membrane distillation crystallisation; crystal-liquid interfacial energy; scaling; fouling; homogeneous nucleation, heterogeneous nucleation

2.1 Introduction

Membrane distillation (MD) is a viable alternative to reverse osmosis for enhancing water recovery from hypersaline wastewater (Horseman et al., 2021). Solvent evaporation through the micropores of a hydrophobic membrane yields a high quality permeate, while concentrating the feed solution to reduce the brine volume for disposal. Once the feed concentration exceeds the solubility limit of the solute, crystallisation can occur, which can be beneficial for enabling resource recovery, and for reducing the cost of brine management (Curcio and Drioli, 2005). The membrane interfacial area introduces well defined mass and heat transfer characteristics that deliver a homogeneous solvent removal rate which is important for the regulation of supersaturation. It is the precise regulation of solvent removal rate that creates a unique advantage for membrane distillation versus classical crystallisers, which incur difficulties in the control of supersaturation due to complex mixing phenomena and poorly defined interfacial area for evaporation, which result from the decoupling of mass and heat transfer in design. This leads to poor control of size, size distribution and quality of the final crystal product (Di Profio et al., 2010; Jiang et al., 2015, 2017.

It is also thought that the membrane contact angle contributes to reducing the Gibbs free energy barrier for nucleation (ΔG) (Di Profio et al., 2010; Ruiz Salmón & Luis, 2018) through modifying the crystal-liquid interfacial free energy (ΔG_s). This effect is proposed to arise by improving molecular orientation through substrate-molecule interactions, which lowers the activation energy for nucleation (Mullin, 2001; Di Profio et al., 2010). In principle, this *heterogeneous* primary nucleation mechanism presents an advantage to MDCr (membrane distillation crystallisation) as this can shorten induction time. However, in practice this mechanism is comparable to membrane scaling, which will reduce control over supersaturation due to the loss in flux, potentially leading to eventual process failure (Choi et al., 2019; Elcik et al., 2020; Gryta, 2008). While scaling has been observed with numerous aqueous salts in membrane distillation (Warsinger et al., 2015; Abdel-Karim et al., 2021), Warsinger et al. (2015b) showed that introducing filtration within the bulk solution, sufficiently reduced the quantity of crystals visible on the membrane to sustain flux during crystallisation. Consequently, it is proposed that scaling proceeds by one of two distinct mechanisms: (i) adhesive growth in which crystallisation manifests as scaling on the membrane surface (*heterogeneous* primary nucleation) (Zepeda-Ruiz and Gilmer, 2015); or (ii) deposition of crystals following formation in the bulk solution via a *homogeneous*

primary nucleation mechanism (Warsinger et al., 2017). However, the reason why and when each of these mechanisms may be favoured has yet to be understood.

Classical nucleation theory (CNT) can be used to describe the mechanisms for both scaling and crystallisation (Horseman et al., 2019). For a thermodynamically stable nucleus to form, the critical Gibbs free energy barrier for nucleation (ΔG*) must be exceeded. The height of the nucleation barrier is dependent upon the *volume* Gibbs free energy (ΔG_v), which is the difference in Gibbs free energy between the liquid and crystal ($\Delta G_v = G_l - G_c$), and the *surface* Gibbs free energy (G_s) which is determined by the crystal-liquid interfacial free energy (γ):

$$\Delta G^* = \Delta G_s + \Delta G_v \qquad (Eq.\ 2.1)$$

As the size of the nucleus (n*) increases, there is competition between ΔG_s which favours dissolution, and ΔG_v which favours growth (Figure 1a) (Erdemir et al., 2019). A critical size is reached once ΔG* approaches a limit that is energetically favourable for crystallisation. Interfacial energy is an important characteristic property of the crystallising substance in the nucleation process, as illustrated by its cubic contribution to ΔG* (Torrens-Serra et al., 2009). The interfacial energy of aqueous inorganic salts is inversely related to their solubility (Mersmann, 1990). Therefore, for sparingly soluble salts, considerably greater ΔG_v must be reached to negate ΔG_s, which requires a high level of supersaturation to provide the needed chemical potential ($\Delta\mu$) (Figure 2.1b). Supersaturation represents the thermodynamic driving force for crystallisation (Roelands et al., 2006). Consequently, Mersmann and Kind (1988) concluded that sparingly soluble salts would favour homogeneous primary nucleation due to the considerable supersaturation requirement which imbues high nucleation rates. In contrast, more soluble salts that are characterised by a low γ, sustain a relatively small Gibbs free energy difference between the liquid and crystal (ΔG_v) which corresponds to generating relatively little supersaturation. This increases the dependency on solute-solvent-solids interactions to overcome the critical energy barrier for nucleation (Mersmann and Kind, 1988, Zhou et al., 2017; Zhou et al., 2021). Accordingly, higher solubility salts (e.g. NaCl) are more likely to depend on the membrane to reduce the interfacial free energy contribution, with primary nucleation therefore proceeding via a heterogeneous mechanism, resulting in lower nucleation rates and in increased propensity for scaling (adhesive growth) due to the reduced chemical potential. We therefore propose that the primary nucleation mechanism can be foreseen through characterisation of solute interfacial energy which can provide a basis with which to control scaling, nucleation and crystal growth in membrane crystallisation.

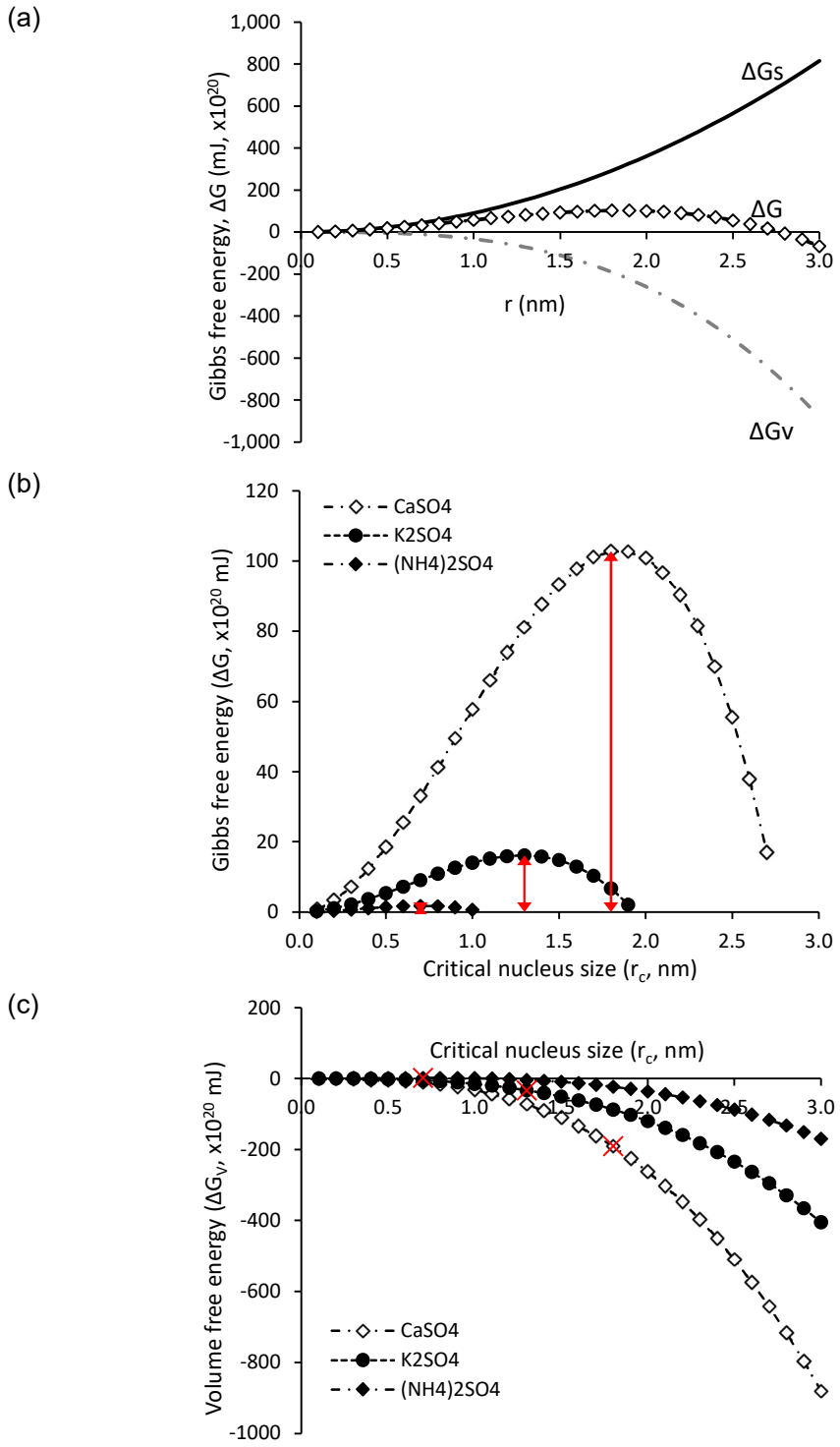

Figure 2.1 ΔG as the minimum free energy value needed for the formation of crystals (a)The representation of the critical energy free barrier (ΔG) and how it is calculated through the difference of the volumetric (ΔG_v) and surface (ΔGs) Gibbs free energy. (b) The highest point of the ΔG is the critical nucleus size on which a crystal that is created can stabilise and remain in solid form. The highest the critical nucleus size the more energy it takes to create a stable crystal form that will survive the adhesion forces of the system. (c) The higher the critical nucleus size the higher the ΔG_v of the salt-solution-membrane (W_{132}) which translates to lower propensity to nucleation thus scaling.

In this study, we therefore seek to establish the role of crystal-liquid interfacial energy in determining the kinetics of scaling, nucleation and crystal growth in membrane distillation crystallisation, as a basis on which to develop scaling mitigation strategies, and to advance control of nucleation and crystal growth. A range of aqueous inorganic salts have therefore been purposefully selected for examination that possess interfacial energies over a two order of magnitude range (Table 2.1). Their investigation is to be complemented with the use of techniques for the characterisation of induction time which are rarely used in MD, and yet are critical for the accurate characterisation of nucleation kinetics (Horseman et al., 2021). Ouda et al. (2023) introduced backscatter technique into the bulk flow which provided for the precise detection of induction in the bulk solution in MD. Jikazana et al. (2023) employed a digital microscope for the determination of induction time for scaling. We propose to combine and employ comparable techniques that enable distinction between homogeneous and heterogeneous primary nucleation mechanisms, while electing to use Focused Beam Reflectance Measurement (FBRM) as the backscatter technique, which also permits counting and sizing of the particle population to precisely estimate nucleation and crystal growth properties of the bulk crystal population, that can be directly related to the crystal-liquid interfacial energy. The objectives are to: (i) characterise induction time for bulk (homogeneous) nucleation of aqueous inorganic salts with different interfacial energies to define the concentrating rate (the driving force for supersaturation); (ii) determine and compare the onset of surface nucleation to bulk nucleation, to establish how interfacial energy can be used to forecast the probability for the type of nucleation mechanism that prevails; and (iii) relate nucleation rate and crystal growth of the bulk crystal phase to evidence how interfacial energy governs properties of the recoverable crystalline phase, thus providing a deterministic characteristic with which to estimate kinetics within MDCr.

Table 2.1. Physicochemical characteristics of the salts and the membrane

Salt	Solubility (g kg^{-1})[a,b]	M.W. (g mol^{-1})[b]	Dyn. Viscosity (Pa s)[b]	Density (kg m^{-3})[b]	Initial Sat. of the exp. (%)[c]	Concentration (mol L^{-1})[c]	Surface tension (mN m^{-1})[c]	Contact angle (°C)[c]	Interfacial energy (mJ m^{-2})[d]
$(NH4)_2SO_4$	812	132.13	0.00106	1191	75	3.16	66 ± 1	142.0 ± 0.9	8.33
K_2SO_4	148	174.26	0.00174	1086	75	0.60	55 ± 3	139.5 ± 0.8	23.12
NaCl	364	58.44	0.00103	1174	75	4.00	68 ± 3	139.8 ± 1.9	27.60
Ag_2SO_4	9.95	311.79	0.00068	1001	75	0.02	66 ± 1	139.7 ± 0.7	54.47
$CaSO_4$	2.11	136.14	0.00061	989	90	0.01	71 ± 1	140.3 ± 0.6	72.06

[a] Solubility at 40°C, [b] Values taken by the literature, [c] Values calculated experimentally, [d] Calculated through Mersmann, 1990

2.2 Material and methods

2.2.1 Experimental setup

The reactor used for the introduction of the solution was a 500ml Reactor Ready™ (Radleys, Essex, UK), equipped with a 4-blade impeller with 45° pitch. The membrane distillation cell was constructed of acrylic with an active membrane area of 140cm^2 (Figure 2.2). The length, width and height of the feed channel were 145, 95 and 2mm respectively. An ePTFE flat sheet membrane with a nominal pore size of 0.1 µm and thickness of 50±20µm was used in this study (Cobetter Filtration, Hangzhou, China), and was supported by a stainless-steel shim. The membrane was operated in direct contact mode with feed-side and permeate operating in counter-current mode with flow rates set to provide Reynolds numbers (*Re*) in the feed and permeate channels of 416±16 and 290±7 respectively (Table 2.2). Feed and permeate temperatures were maintained at 44.3±0.5 and 30.4±1.9°C for the bulk hot and cold solutions respectively, providing an overall average temperature difference (ΔT) of 13.9±2.5°C (LT ecocool 150, Grant, UK). Thermocouples were also positioned upstream and downstream of the membrane cell on both the feed and permeate sides to characterise the overall heat balance (T7-Pro, LabJack, USA). Permeate flux was characterised through collecting the additional permeate mass on a precision balance (Symmetry PR 410, Cole-Palmer, UK). Conductivity was constantly measured in the feed and permeate (Seven2Go Pro, Mettler Toledo, UK).

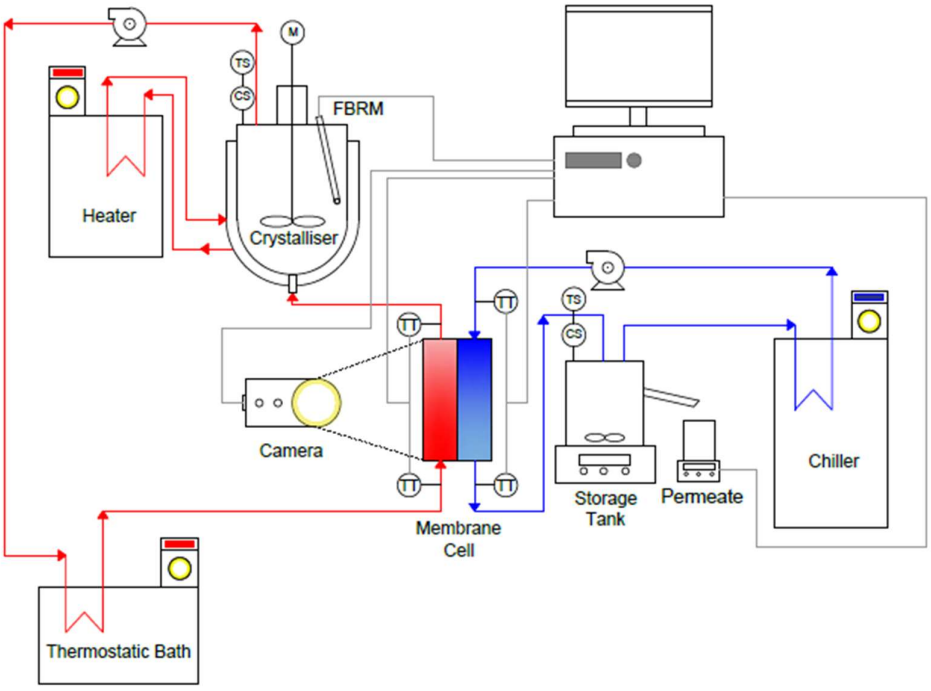

Figure 2.2 Experimental set-up diagram

Table 2.2. Experimental design

Salt	Bulk Hot Temp. (°C)	Bulk Cold Temp. (°C)	ΔTemp (°C)	Q_f (ml min^{-1})	Q_p (ml min^{-1})	Re_f (-)	Re_p (-)	TPC (-)	CPC (-)
$(NH_4)^2SO_4$	44.68 ± 0.13	29.10 ± 0.10	15.6 ± 0.03	1729 ± 7	1072 ± 1	412 ± 2	302 ± 0.5	0.4263 ± 0.0002	1.1580 ± 0.0013
K_2SO_4	44.44 ± 0.11	32.25 ± 0.06	12.2 ± 0.06	1762 ± 49	1058 ± 8	420 ± 12	298 ± 2	0.3754 ± 0.0031	1.3614 ± 0.0345
NaCl	44.41 ± 0.09	29.67 ± 0.28	14.8 ± 0.19	1621 ± 6	1056 ± 4	417 ± 2	291 ± 1	0.4553 ± 0.0003	1.1238 ± 0.0013
Ag_2SO_4	43.70 ± 0.15	30.55 ± 0.47	13.1 ± 0.32	1262 ± 10	1069 ± 1	417 ±3	295 ± 0	0.3480 ± 0.0006	1.6531 ± 0.0104
$CaSO_4$	44.32 ± 0.16	30.65 ± 0.26	13.7 ± 0.10	1143 ± 3	1063 ± 12	415 ± 1	296 ± 3	0.3762 ± 0.0014	1.8443 ± 0.0170

2.2.2 Analytical procedures

2.2.2.1 FBRM

Induction time was estimated using Focused Beam Reflectance Measurement (FBRM) which is a widely used characterisation tool for the development of crystalline materials (ParticleTrack G400, Mettler Toledo, UK) (Heath et al., 2002). The probe was positioned at a 60° incline into the reactor to assure good contact with the particle suspension. The FBRM probe directs a 780nm laser through a beam splitter scanning at a velocity of 2 m s^{-1} which is intersected by the particles to produce a pulse of backscattered light. The duration of the pulse is directly proportional to the width of the particle and recorded as a chord length, within a size range of 0.5 to 2000μm. The Chord Length Distribution (CLD) provides an overall size distribution. The cumulative number of the chord length measurements is obtained in total counts s^{-1} (Kim et al., 2013):

$$total\ counts\ s^{-1} = \sum_{i=1}^{Ch} N_{Ch,i} \qquad (Eq.\ 2.2)$$

where C_h in the number of channels in FBRM and $N_{Ch,I}$ is the number of counts measured in an i^{th} channel. The beginning of primary nucleation is indicated by a rapid increase in total counts s^{-1}, and therefore provides for the accurate determination of induction time in the bulk solution, while the total count (counts s^{-1} (Kim et al., 2013)) can be transformed into the volumetric nucleation rate (B, m^{-3} s^{-1}), assuming a measurement volume of:

$$V = S_p W_l D_p \qquad (Eq.\ 2.3)$$

where S_p is scan speed of the laser (2 m s^{-1}), W_l is the laser diameter at the focal point ($5.8x10^{-6}$ m) and D_p the laser penetration depth in solution ($2x10^{-4}$ m), providing a scanning volume of $2.32x10^{-9}$ m^3 s^{-1} (Mitchell et al., 2011). Induction time was determined using the 'primary' chord selection model, which provides an enhanced sensitivity to fines and particle edges. The difference in particle count over time determines the nucleation rate of the experiment:

$$B_i = \frac{(N_{c,i} - N_{c,i-1})}{t_i - t_{i-1}} \qquad (Eq.\ 2.4)$$

where t_i is the time of the measurements (s) and B_i is the nucleation rate (# m^{-3} s^{-1}) of the two consecutive measurements. As the N_c of the experiment was increasing, the individual nucleation rates calculated from these measurements were used in order to calculate the average nucleation rate (B) of the experiment.

For determination of the crystal size distribution as a chord length distribution (CLD), the 'macro' chord selection model was used as this lowers the sensitivity to crystal edges when particles are close to each other. The raw chord length distributions

used for the particle size determinations were weighted. This increases the sensitivity in the coarse particle fraction, by applying length weightings (moments) to the chord distribution (Heath et al., 2002):

$$N_{i,n} = N_{i,o} C_{i,A}^{n} \quad (Eq.\ 2.5)$$

where $N_{i,n}$ is number of n-weighted chord counts in the i^{th} channel ($\mu m^n\ s^{-1}$), $N_{i,o}$ is the raw unweighted chord count in the i^{th} channel (s^{-1}) and $C_{i,A}$ is the geometric average length of the i^{th} channel (μm), which is a product of the upper and lower boundary lengths of the i^{th} channel (μm) $(C_{i,u} \times C_{i,l})^{1/2}$. A square weighted ($n$ = 2) chord distribution has been used since the square-weighting is effectively a cube (volume) weighting, comparable to the volume-based distribution techniques (Heath et al., 2002). A high definition digital microscope was place within a distance of 145mm (UHM350, AmScope, UK) focused on the feed side of the membrane to determine the induction time for scaling, and the nucleation rate for scaling similar to Jikazana (2023). This method described utilises advanced imaging techniques to track the growth of crystals, particularly focusing on observing the rapid formation of stable crystal structures and measuring its extent of surface coverage. This is made possible by employing a combination of features, including a wide-angle lens, a long working distance, a broad range of magnification (x20 – 100), and high-resolution imaging equal to 2μm per pixel. Even though this technique may not be sufficient to determine the actual nucleation moment (nanometer scale), as the growth rates of the crystals are really fast, this technique is allowing for a detailed real-time examination of the crystal growth process and can be even compared to other widely accepted techniques like the backscatter technique (Ouda et al., 2023). Captured images were transformed into binary, 8-bit, black and white images and characterised for surface coverage (ImageJ software, NIH, US).

2.2.2.2 Chemistry used

Solutions of ammonium sulphate ($(NH_4)_2SO_4$), sodium chloride (NaCl), potassium sulphate (K_2SO_4), silver sulphate (Ag_2SO_4) and calcium sulphate ($CaSO_4$) were prepared using stock anhydrous chemicals (99+% Alfa Aesar, Lancashire, UK). Feed solutions were prepared up to 25% below their saturation limit, with respect to the bulk feed temperature within MDCr. The solutions were prepared using ultrapure water (15MΩ cm) (Purelab, Elga, UK) and heated to 55°C overnight on a stirrer plate to ensure dissolution. Prior to use, each solution was filtered using a 0.45μm Whatman filter (Camlab Ltd., Cambridge, UK) to remove any impurities, followed by confirmatory check of the solution conductivity (Seven2Go Pro, Mettler Toledo, UK). At the end of each experiment, the feed solution was filtered through a pre-weighed 0.45μm Whatman filter (Camlab Ltd., Cambridge, UK) and left to dry before measuring the

weight. Each membrane was also removed and left to dry within a dessicator before being subject to image analysis. Crystals were subjected to SEM (Scanning Electron Microscopy, VEGA3, Tescan, Czech Republic) and XRD (X-Ray Diffraction, Bruker, D5005, Germany) to evaluate crystallinity of each sample. The data presented represents an average of replicates undertaken for each set of conditions.

2.2.3 Mass and heat transfer analysis

The water vapour flux (J) is (Tun et al., 2005):

$$J = C_m \Delta P \quad (Eq.\ 2.6)$$

where C_m is the membrane permeability and ΔP is the vapour pressure difference. In MD, there is competition between the convective solute flux and the diffusive flux of rejected solutes which introduces concentration polarisation, where the subsequent solute build up at the membrane surface can be described by the concentration polarisation coefficient (CPC) (Tun et al., 2005):

$$CPC = \frac{c_w}{c_b} = exp^{\left(\frac{J}{\rho K}\right)} \quad (Eq.2.7)$$

where c_w and c_b are the solute concentrations at the feedside membrane wall and bulk respectively. The solute mass transfer coefficient (K, m s^{-1}) is:

$$K = \frac{1.62\ D}{d_h}\left(\frac{v\ {d_h}^2}{0.146\ D}\right)^{0.33} \quad (Eq.\ 2.8)$$

where D is the diffusion coefficient (m^2 s^{-1}), d_h is the hydraulic diameter (m^2) and v is the feed velocity (m s^{-1}). Heat transport across the membrane through conduction and convection must also be described. Due to these phenomena, a temperature difference is instigated at the membrane surface which can be described by the temperature polarisation coefficient (TPC) (Ali et al., 2013).

$$TPC = \frac{T_{fm} - T_{pm}}{T_f - T_p} \quad (Eq.\ 2.9)$$

where T_f and T_p are the average temperatures of hot and cold sides of the membrane (Martinez-Diez and Vazquez-Gonzalez, 1999). The wall temperature must be calculated analytically (Tun et al., 2005):

$$T_{fm} = T_f - (T_f - T_p)\left[\frac{1/h_f}{(1/(h_c + h_v)) + (1/h_f) + (1/h_p)}\right] \quad (Eq.\ 2.10)$$

And

$$T_{pm} = T_p + (T_f - T_p)\left[\frac{1/h_p}{(1/(h_c + h_v)) + (1/h_f) + (1/h_p)}\right] \quad (Eq.\ 2.11)$$

where h is the heat transfer coefficient (W m^{-2} K^{-1}) and can be calculated through the following equations (Tun et al., 2005):

$$h_v = \frac{J\ \Delta H_v}{\Delta T_m} \quad (Eq.\ 2.12)$$

$$h_c = \frac{k_m}{\delta} \quad (Eq.\ 2.13)$$

$$h_f = \frac{Nu\ k_f}{d_h} \quad (Eq.\ 2.14)$$

$$h_p = \frac{Nu\ k_p}{d_h} \quad (Eq.\ 2.15)$$

where k_m, k_f and k_p is the thermal conductivity of the membrane, the feed solution and the permeate solution (W m^{-1} K^{-1}). Nu is the Nusselt number which can be calculated for this study based on laminar conditions (Ali et al., 2013):

$$Nu = 0.13\ Re^{0.64} Pr^{0.38} \quad (Eq.\ 2.16)$$

where Re and Pr are the Reynolds number and Prandtl number respectively.

2.4 Crystallisation analysis

The crystal-liquid interfacial energy for aqueous salts can be approximated by (Mersmann, 1990).

$$\gamma = 0.414kT\left(p_S \frac{N_A}{M}\right)^{2/3} ln\left(\frac{c_S}{c_L}\right) \quad (Eq.\ 2.17)$$

where k is the Boltzmann constant (J K^{-1}), T is the temperature of the solution (K), ρ_S is the density of the salt (kg m^{-3}), N_A is the Avogadro constant (l mol^{-1}), M is the molar mass of the salt (kg $kmol^{-1}$) and c is the molar concentration of the components (mol m^{-3}).

The driving force for crystallisation is the difference of the Gibbs free energy between the system and the equilibrium conditions. For a spherical nucleus, the critical size (n*) and the nucleation work (W*) can be derived from the condition dW/dn = 0 for n=n* (Roelands et al., 2006):

$$n^* = \frac{32\pi v_0^2 \gamma^3}{3(kT)^3 ln^3 S} \quad (Eq.\ 2.18)$$

$$W^* = \frac{16\pi v_0^2 \gamma^3}{3(kT)^2 ln^3 S} = 1/2\, n^* kT lnS \quad (Eq.\ 2.19)$$

To identify the nucleation rate of the system, we can calculate the supersaturation rate on the onset of nucleation (R'). This can also be referred to as the limit of the metastable zone width (MSZW).

The MSZW was calculated by adopting the approach from Nývlt, (1968). It is assumed that the upper limit of MSZW where nucleation occurs, which is given by ΔC_w (mg g^{-1} solution), is linearly related to the supersaturation rate R' (g of salt per 100g solution h^{-1}). Both these correspond to the nucleation rate:

$$J = k\left(\Delta C_{ma\ ,fm}\right)^n = \left(\frac{dc_0}{dT}\right)_T = \frac{F_p\ C_w}{m_0 - \int_0^t F_p dt} \quad (Eq.\ 2.20)$$

$$Ln(R') = \ln\left(\frac{F_p\ C_w}{m_0 - \int F_p.dt}\right) \quad (Eq.\ 2.21)$$

where F_p is the permeate flow rate of the experiment at a specific time (kg h^{-1}), m_0 is the initial mass of feed solution (kg). $F_p.dT$ is the integral of the permeate flow in respect of the time (kg) and C_w is the concentration of the solution on the membrane surface. The main nucleation kinetics (B) of a system can be established by characterising the MSZW (Jiang et al., 2016):

$$B = Ae^{\left(-\frac{\Delta G^*}{kT}\right)} \quad (Eq.\ 2.22)$$

A represents the pre-exponential factor, while ΔG* represents the critical Gibbs free energy for nucleation, measured in joules (J). The nucleation rate of the salt is directly influenced by the volumetric hold-up, which is the total volume of the reactor occupied by the nucleation phase and is continually changing. In Equation 2.22, a constant pre-exponential factor is incorporated:

$$A = A_0 ø \quad (Eq.\ 2.23)$$

$$B_o = A_0 ø e^{\left(-\frac{\Delta G^*}{kT}\right)} \quad (Eq.\ 2.24)$$

The induction time (t_{ind}) can be determined for the bulk crystal phase and for scaling using FBRM and digital microscopy. The induction time (t_{ind}) is a quantitative measure of the degree of metastability of a solution. It specifically refers to the duration required for nucleation (t_n) to occur after the solution has become supersaturated (t_{c/c^*}=1):

$$t_{ind} = t_n - t_{C/C^*=1} \quad (Eq.\ 2.25)$$

where tind, which can also be referred as the inverse of the nucleation rate (t = $1/J_n$), and based on the classical nucleation theory (CNT) can be conveyed us:

$$t_{ind} = \frac{1}{BV} \quad (Eq.\ 2.26)$$

where V is the volume of the solution (m^3). The analysis of the saturation level at which crystallisation was initiated was conducted using the relative supersaturation:

$$S = \frac{C - C^*}{C^*} \quad (Eq.\ 2.27)$$

C representing the concentration of the solution in the solution (kg m^{-3}) while C* is the equilibrium solubility concentration of the solute at a temperature (kg m^{-3}).

2.3 Results and discussion

2.3.1 The role of interfacial energy on mass transfer and concentrating rate

Aqueous salts which convey distinct crystal-liquid interfacial energy were independently evaluated, using bulk feed and permeate temperatures of 44.3±0.5 and 30.4±1.9°C respectively. At steady state, the flux was highest for $CaSO_4$ and Ag_2SO_4, K_2SO_4, NaCl and $(NH_4)_2SO_4$ respectively (Figure 2.3) which is consistent with the order of their interfacial energy (Figure 2.4). As aqueous salts with higher interfacial energy are poorly soluble, they exert a greater vapour pressure than more soluble compounds,

leading to an increase in flux. A dependency is therefore established between vapour pressure and interfacial energy (Figure 2.3). Since MD was operated in batch mode, the water vapour flux declined as the feed became more concentrated due to the progressive reduction in vapour pressure. This effect was more evident for the higher solubility salts (NaCl and $(NH_4)_2SO_4$). The onset of nucleation was determined by the rapid increase in FBRM particle count that was observed for each aqueous salt (Figure 2.3b). A consistent flux was sustained for the higher interfacial energy aqueous salts ($CaSO_4$, Ag_2SO_4) following nucleation, whereas a rapid decline in flux was observed shortly after nucleation for the lower interfacial energy aqueous salts (NaCl, $(NH_4)_2SO_4$). This rapid decline in flux is often used as a surrogate measure to define induction time (Ouda et al., 2023). However, use of backscatter in this study for nucleation detection evidences that bulk nucleation can occur well in advance of the rapid decline in flux, and in the case of the higher interfacial energy aqueous salts ($CaSO_4$, Ag_2SO_4), induction occurs without an apparent decline in flux. Consequently, we suggest that flux decline is not mechanistically related to induction and cannot be used to differentiate between heterogeneous and homogeneous primary nucleation as suggested in previous studies in which it has been used to infer both scaling and deposition (Horseman et al., 2021).

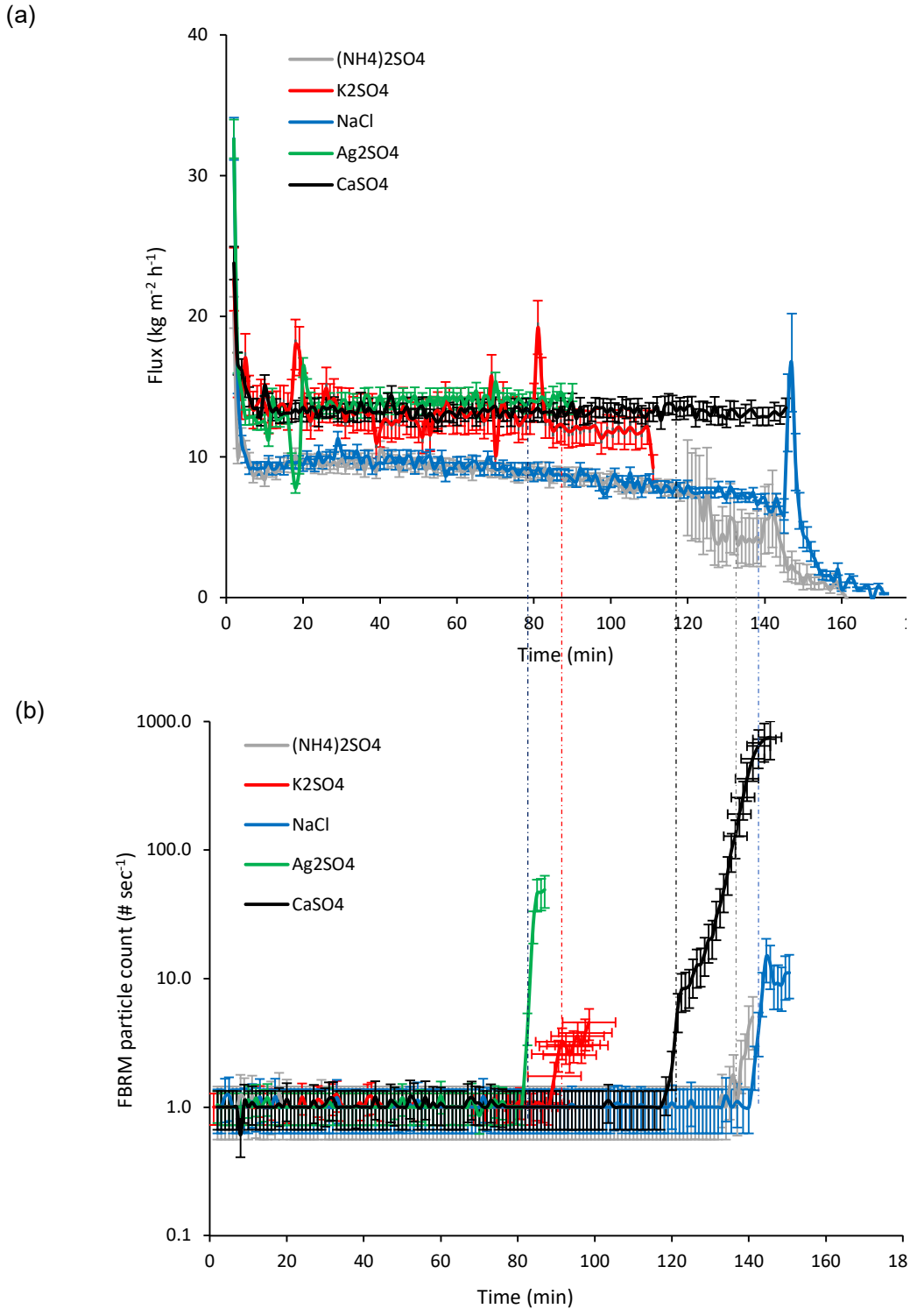

Figure 2.3 Membrane distillation crystallisation data for five salts that exhibit different interfacial energies: (a) membrane flux data, operating conditions (Bulk): T, 44.3±0.5°C; ΔT 13.9±2.5°C; and (b) in-situ particle characterisation determines the first point at which bulk crystals are formed (FBRM set to primary count (<10) for sensitive detection of induction and nucleation rate. Dotted lines indicate the induction times of the different salts.

The concentrating rate (LnR') describes the rate at which solute within the crystallising solution approaches supersaturation (Figure 2.4a). The LnR' can therefore be directly related to the water vapour flux. While the water vapour flux was higher for the aqueous salts that confer a greater interfacial energy, their low solubility result in smaller concentrating rates prior to nucleation (Figure 2.4b). For a specific solute, the maximum metastable zone width is assumed to be proportional to the concentrating rate (LnR') (Ouda et al., 2023). The metastable zone width measured at induction (the onset of nucleation) under the same temperature gradient was therefore wider for NaCl and narrower for $CaSO_4$. When analysing a single aqueous salt, the width of the metastable zone determines the extent of supersaturation and can determine the nucleation rate and induction time (Jikazana et al., 2023). This is the case when the MSZW is kinetically controlled. However, the MSZW measured for aqueous salts in this study are thermodynamically controlled by the transition in crystal-liquid interfacial energy, and so cannot be directly compared in the form of a trend. This can be best illustrated through characterisation of the dimensionless supersaturation ($c\ c^{*-1}$) achieved for each aqueous salt at induction (Figure 2.4c). This demonstrates an inverse trend between supersaturation and crystal-liquid interfacial energy, where greater supersaturation is achieved for relatively sparingly soluble salts. As the less soluble salts there are fewer solute molecules in larger distances are available to form nuclei, higher accumulation of solids in the solute needs to be achieved before nucleation occurs, which leads to higher concentration of the solutes prior to nucleation. Additionally, as higher nucleation rate means lower means slower crystal growth rate, the growing crystals are less efficient due to higher diffusion rate, which causes the crystal to dissolve unless higher supersaturation can be maintained in the solution (Mangin et al., 2009). Supersaturation represents the driving force for nucleation and growth (Mersmann et al., 1992). Consequently, higher nucleation rates are likely to occur for sparingly soluble salts. This requires an increase in supersaturation (G_v) sufficient to compensate for the enhanced crystal-liquid interfacial energy (G_s) component, which may reduce dependency on a heterogeneous substrate to overcome the critical free energy barrier for nucleation.

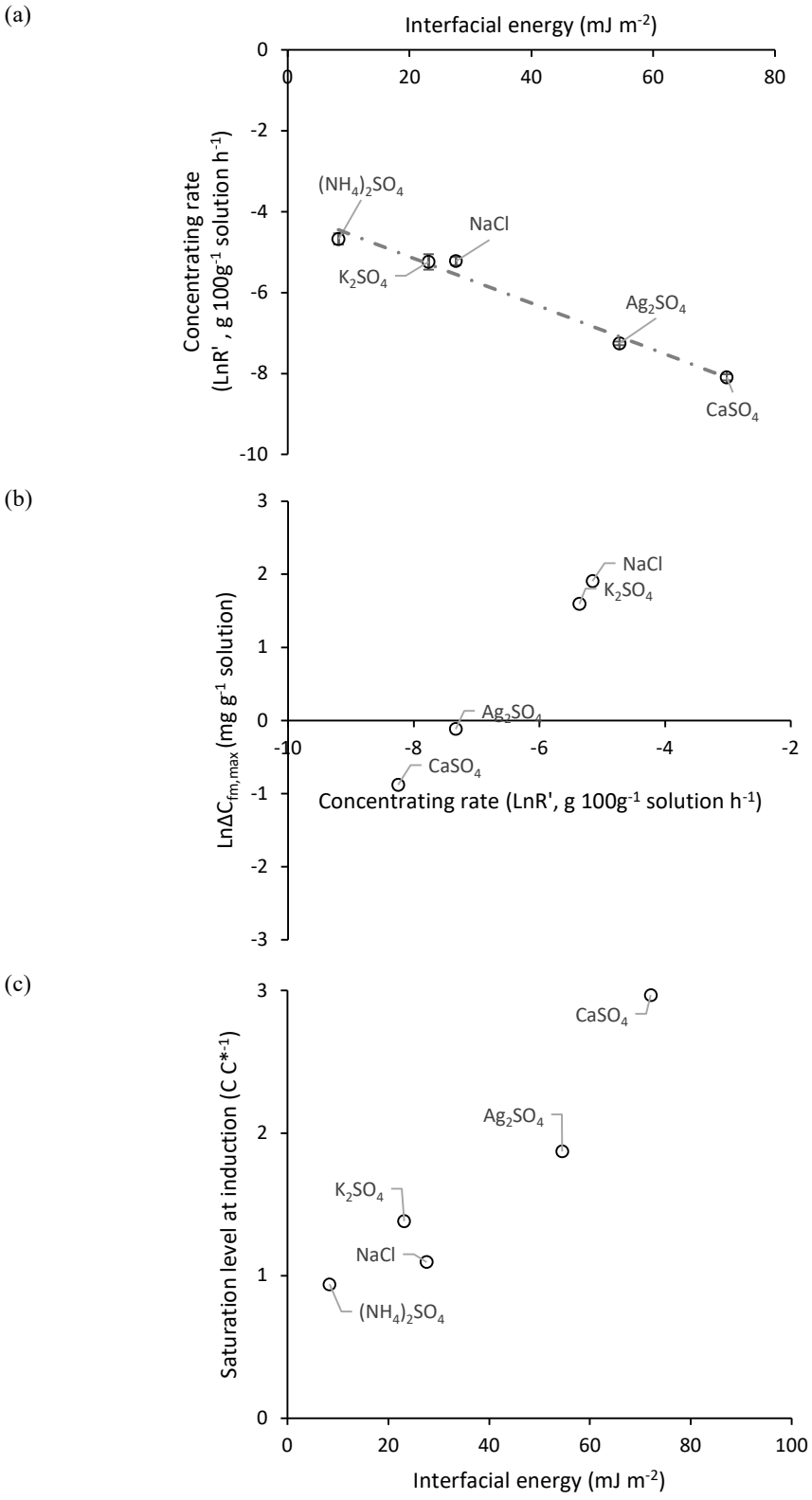

Figure 2.4 Demonstrating how interfacial energy decouples supersaturation from concentrating rate by establishing (a) the linear connection between interfacial energy and concentration rate causing (b) higher concentrations in the low interfacial energy salts, (c) leading to lower saturation levels at induction. Operating conditions (Bulk): T, 44.3±0.55°C; ΔT 13.9±2.5°C.

2.3.2 The role of crystal-liquid interfacial energy in determining scaling

Digital microscopy was used to identify how crystal-liquid interfacial energy modified the onset and extent of surface scaling (Figure 2.5). Two periods of data were described for each aqueous salt: (i) scaling, which was characterised by the progressive growth of crystals on the membrane surface prior to the measurement of crystals in the bulk solution (determined by FBRM); and (ii) deposition, where high numbers of crystals settled onto the membrane following nucleation in the bulk solution. Scaling was greatest for $(NH_4)_2SO_4$ followed by NaCl and K_2SO_4. Following bulk nucleation, substantial deposition was also observed. For Ag_2SO_4 and $CaSO_4$, scaling was not observed prior to bulk induction, but after bulk nucleation, deposition was also observed. Scaling was therefore only noted for aqueous salts where induction occurred at a comparatively low level of supersaturation.

(α)

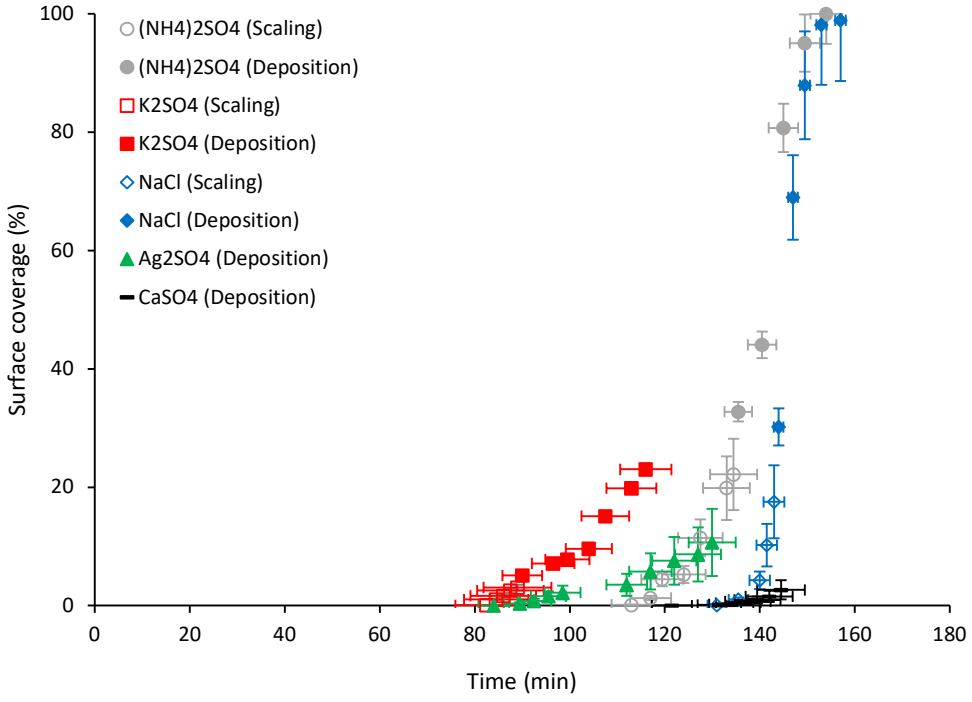

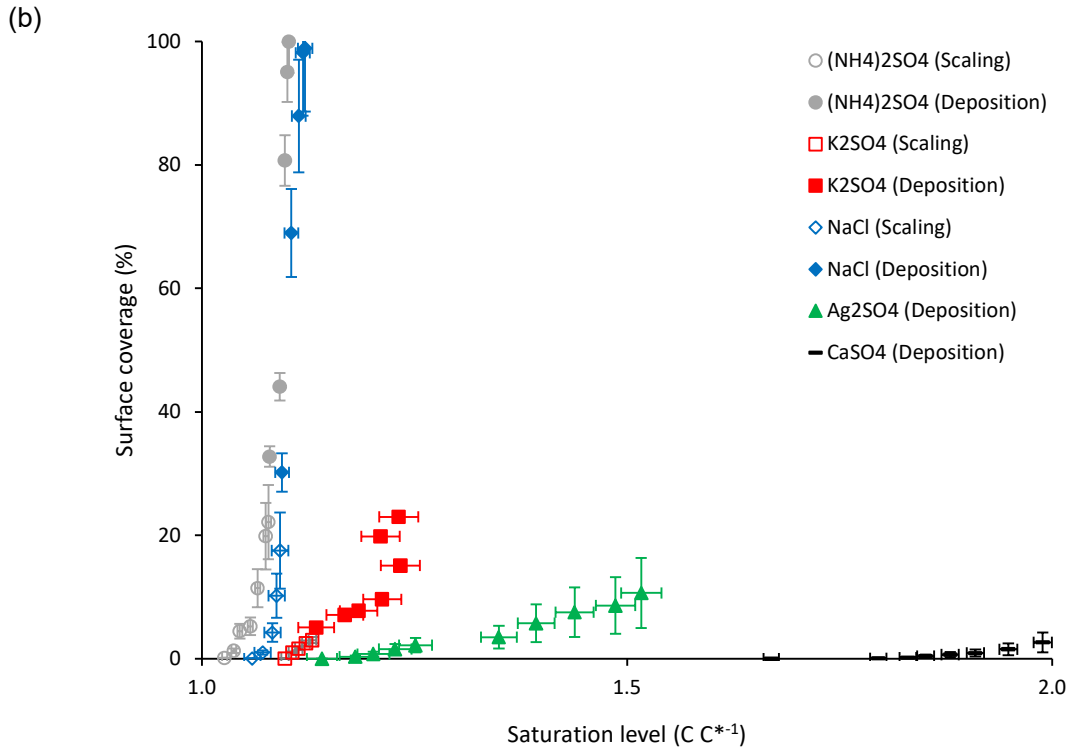

Figure 2.5 Quantifying the extent of scaling based on: (a) time and (b) supersaturation. Direct observation also permits the differentiation between adhesive growth (classical scaling, open shapes) and deposition (following homogeneous nucleation in the bulk solution, closed circles). Operating conditions (Bulk): T, 44.3±0.5°C; ΔT 13.9±2.5°C.

The heterogeneous nucleation pathway presumes that the membrane would instigate formation of a crystal phase in advance of bulk solution (Charcosset et al., 2010; Di Profio et al., 2010). Consequently, the extent to which scaling had propagated across the membrane at the onset of bulk nucleation (induction) was characterised (Figure 2.6a). For this analysis, supersaturation was modified to the *relative* supersaturation form which normalises data for the relative differences in solubility limit between aqueous salts. Scaling reduced to a minimum with an increase in the relative supersaturation achieved at bulk nucleation. The low crystal-liquid interfacial energy exhibited for highly soluble aqueous salts requires a relatively small supersaturation to create the driving force for the formation of a thermodynamically stable critical nucleus. It is this limit in achievable supersaturation for highly soluble salts that increases the dependency on a heterogeneous substrate to initiate nucleation. This is supported by evaluation of the work of formation of the critical nucleus (W*/kT) which illustrates how the greater the energy requirement for nucleation (and therefore the greater the requirement for supersaturation), the lower the dependency on heterogeneous nucleation (Figure 2.6b). Consequently, for poorly soluble aqueous salts (e.g. $CaSO_4$), scaling is most likely to proceed via a deposition mechanism following homogeneous

primary nucleation in the bulk solution, while for more soluble aqueous salts (e.g. NaCl), scaling is mostly likely to proceed via adhesive growth on the membrane which can be described as a heterogeneous nucleation mechanism (Figure 2.7).

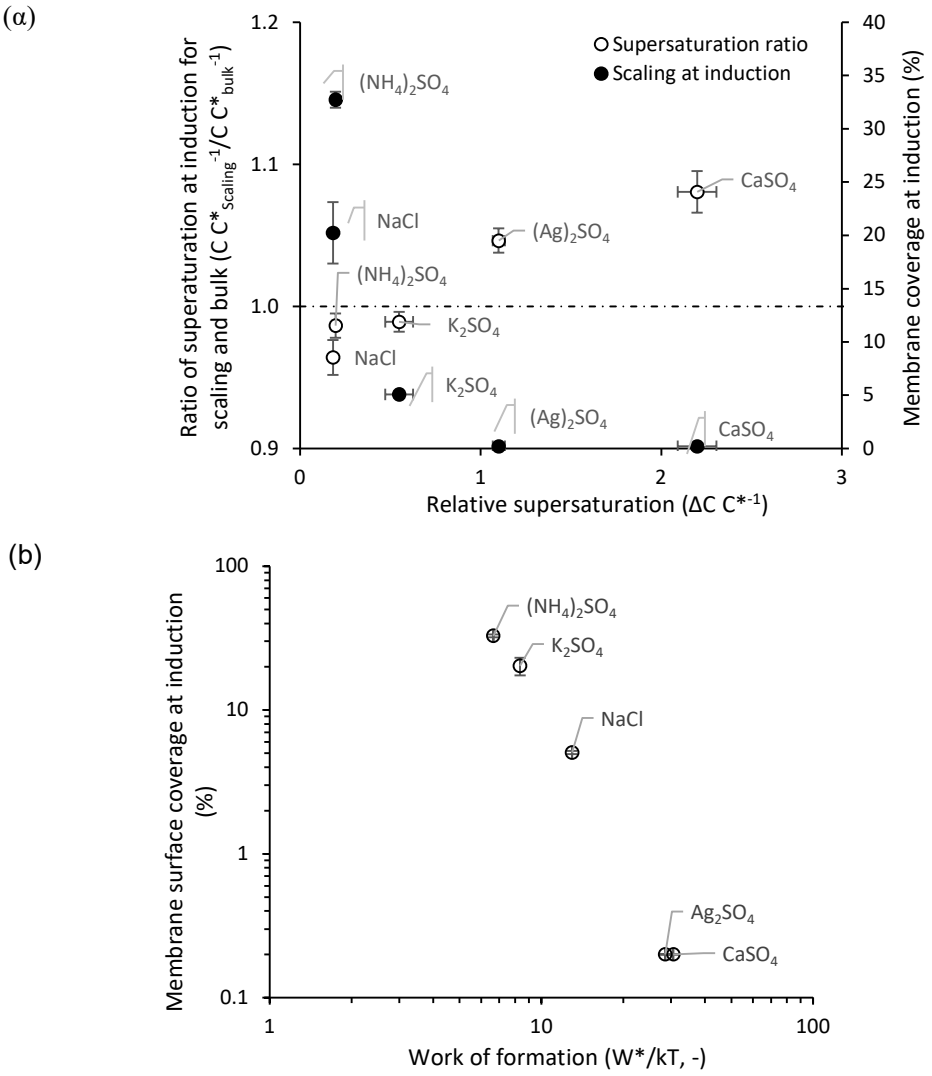

Figure 2.6 Demonstrating how interfacial energy: (a) determines the transition from heterogeneous to homogeneous nucleation (above dashed line (unity), bulk nucleation precedes membrane scaling; and (b) how the extent of membrane scaling at bulk induction relates relates to the work of formation. Operating conditions (Bulk): T, 44.3±0.5°C; ΔT 13.9±2.5°C.

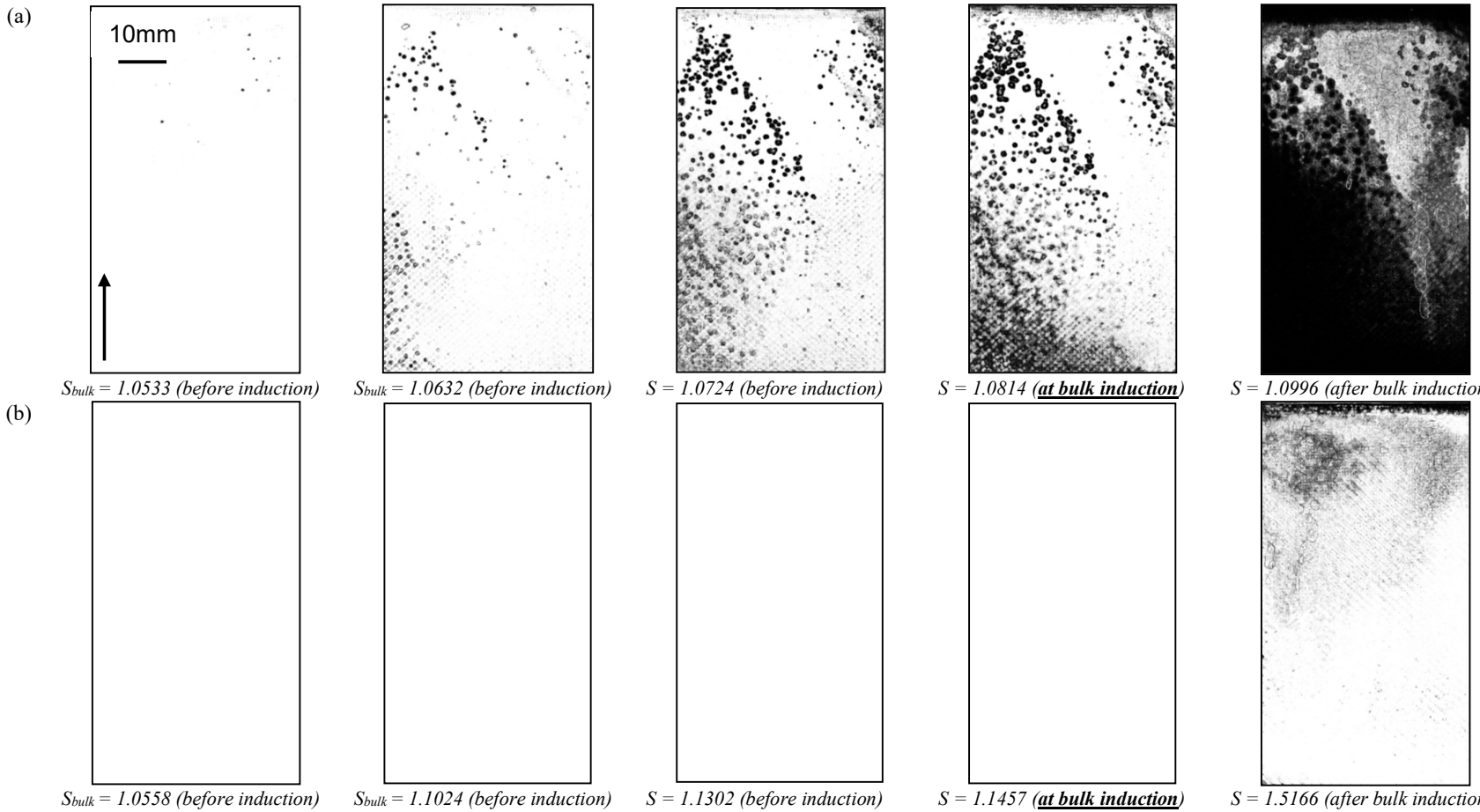

S_{bulk} = 1.0533 (before induction) S_{bulk} = 1.0632 (before induction) S = 1.0724 (before induction) S = 1.0814 (**at bulk induction**) S = 1.0996 (after bulk induction)

S_{bulk} = 1.0558 (before induction) S_{bulk} = 1.1024 (before induction) S = 1.1302 (before induction) S = 1.1457 (**at bulk induction**) S = 1.5166 (after bulk induction)

Figure 2.7 The onset (induction) of scaling observed on the PTFE membrane before induction in the bulk (homogeneous crystallisation) for NaCl (a) but not for silver sulphate (b). Using non-invasive direct observation, real-time data collection can be used to determine the rate and progression of scaling. Operating conditions (Bulk): T, 44.3±0.5°C; ΔT 13.9±2.5°C.

2.3.3 The role of interfacial energy in determining nucleation and growth kinetics

While the extent of scaling was evidenced to be primarily favoured for more soluble aqueous salts, the extent to which the crystal-liquid interfacial energy determines nucleation rate was also investigated using FBRM (Figure 2.8a). The highest nucleation rate of $5x10^{11}$ m^{-3} s^{-1} was recorded for $CaSO_4$. Nucleation rate progressively decreased with the reduction in crystal-liquid interfacial energy to a minimum recorded for $(NH_4)_2SO_4$ of $3x10^7$ m^{-3} s^{-1}. The difference in nucleation rate between aqueous salts can be explained by the critical Gibbs free energy for nucleation having a cubic dependency on the crystal-liquid interfacial energy (Lenka and Sarkar, 2014; Zhou et al., 2017; Li et al., 2020). This necessitates a much greater chemical potential to initiate nucleation ($\Delta\mu = kTlnS$), which at comparable system temperatures is primarily mediated by the solution supersaturation (Figure 2.8b). The increase in nucleation rate with supersaturation is comparable to those prepared by Mersmann and Kind (1988) through the transformation of literature data for a range of aqueous salts. The nucleation rates observed for lower interfacial energy aqueous salts were below those of the reference literature. This may arise from the onset of scaling prior to bulk nucleation for these specific aqueous salts which will desaturate solution, therefore repositioning the system in a lower region of the metastable zone at the point of induction, leading to reduced nucleation rates. While further investigation is required to confirm, scaling not only has implications to the longevity and controllability of nucleation, but may also complicate nucleation kinetic data interpretation in MDCr.

(α)

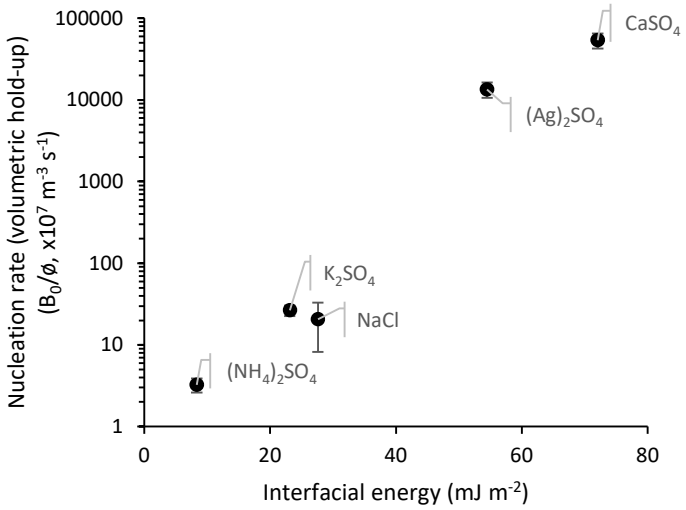

(b)

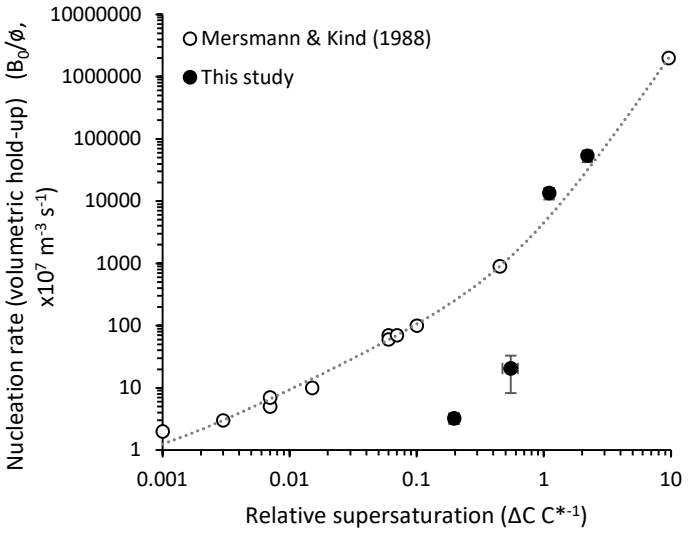

Figure 2.8 Nucleation rate (measured using FBRM and normalised using volumetric hold-up): (a) increases under the same membrane operating conditions, due to interfacial energy; and (b) conforms to a similar trend for other aqueous salts (Mersmann and Kind, 1988). Operating conditions (Bulk): T, 44.3±0.5°C; ΔT 13.9±2.5°C.

Median crystal sizes were also compared to evaluate how thermodynamic properties of the crystallising aqueous salt phase determines the properties of the final crystal product (Figure 2.9). The high supersaturation demanded by the increase in crystal-liquid interfacial energy led to smaller median crystal sizes (L_{50}). This is in accordance with classical nucleation theory where an increase in supersaturation is expected to favour higher nucleation rates and smaller crystal sizes (Lenka and Sarkar, 2014; Zhou et al., 2017). In MDCr, the metastable zone width can be increased for any discrete system by kinetically controlling the supersaturation at induction through an increase in temperature or ΔT (Jikazana et al., 2023). In this study, the bulk temperature and temperature difference were maintained at comparable conditions for each salt and therefore the modification of relative supersaturation at induction is primarily due to the difference in crystal-liquid interfacial energy. The median crystal size range corresponded to those compiled from the literature for a range of aqueous salts (Mersmann and Kind, 1988). Each aqueous salt possesses different surface chemistry, chemical reactivity, surface anisotropy and surface energy that can affect the crystal habit (Erdemir et al., 2019). The crystallinity for each aqueous salt was confirmed through using XRD, where the primary 2θ peaks were compared to a reference sample for confirmation (Appendix B; Fig. 2.B2). Crystal structure (or habit) were confirmed using SEM. The acicular growth of calcium sulphate was analogous to the 'needle-like' scale typically found in water treatment by the precipitation of gypsum

or calcium sulphate dihydrate (Yan et al., 2021). While the crystal habit of NaCl, K_2SO_4 and Ag_2SO_4 were expected, the crystal structure for $(NH_4)_2SO_4$ was more distinctive, but was comparable to that formed using ultrasound assisted crystallisation to reduce the metastable zone width at induction (Mohod and Gogate, 2018). The authors proposed that crystallisation within a lower region of the MSZW improved clarity of surface and edges. In MDCr, the boundary layer may impose comparable benefits by setting conditions for nucleation within a localised region of supersaturation (Jikazana et al., 2023). Determination of the relative supersaturation at induction based on the boundary layer properties, enabled estimation of the median crystal size produced from the crystallisation of aqueous salts in MDCr.

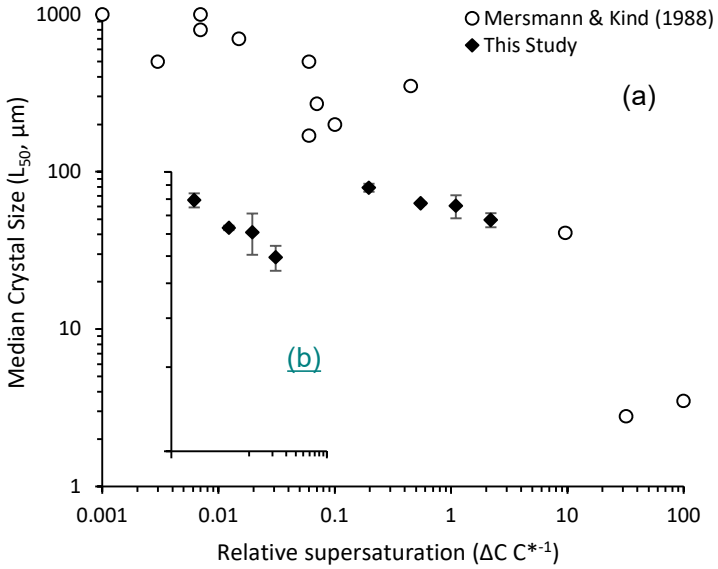

Figure 2.9 The impact of interfacial energy on crystal size: (a) size distributions measured by FBRM; and (b) crystal size (data presented as median (L50) related to supersaturation at induction and compared to literature crystal size data from a range of aqueous salts (Mersmann and Kind, 1988). Inset to provide greater clarity of the reduction in crystal size with relative supersaturation. Operating conditions (Bulk): T, 44.3±0.5°C; ΔT 13.9±2.5°C.

2.4 Conclusions

In this study, detection techniques rarely applied in MD were used in order to provide a framework with which we can predict the scaling, nucleation and crystal growth kinetics, by linking it with the crystal-liquid interfacial energy (Fig. 2.10). To limit the kinetic modification strictly to this, comparable temperatures and Re numbers were used. A tendency where supersaturation and crystal-liquid interfacial energy are inversely correlated with more supersaturation being attained for salts that are more sparingly soluble was observed, with salts that are sparingly soluble resulted in larger nucleation rates. These nucleation rates were demonstrated by the application of FBRM and their crystallinity as well as their crystal structure were confirmed by SEM and XRD. As a result, we managed to observe, differentiate and quantify scaling and deposition, with scaling being the greatest for low crystal-liquid interfacial energy salts, while no scaling was identified prior to bulk induction for Ag_2SO_4 and $CaSO_4$. Even though the measured nucleation rates for the higher crystal-liquid interfacial energy salts were comparable to the literature, the lower ones were not fitting that trend. The reduced nucleation rates may result from the scaling formation prior to the bulk nucleation, which desaturates the solution, creating a low metastable zone system. Moreover, prior studies presume that the use of membranes in MDCr would initiate the heterogeneous nucleation pathway causing formation of scaling prior to bulk nucleation and even try to regulate the crystallisation to lower nucleation rates to minimize scaling. Because of this crystallisation literature regards the high crystal-liquid interfacial salts as scalants. In order to overcome the enhanced free energy barrier for nucleation, an increase in supersaturation (G_v) large enough to offset the elevated interfacial energy (G_s) is required. As the G_v increases, the membrane importance on the system, which in this case is the heterogeneous substrate, becomes lesser to overcome the free energy barrier. Work of formation of the critical nucleus supports that statement, as the greater the energy requirements for nucleation/supersaturation (Table 2A.2), the lower the dependency on heterogeneous nucleation, promoted by the heterogeneous substrate. The threshold of this change has been identified in the supersaturation at induction of scaling/bulk ratio. As the differentiation of the scaling and bulk nucleation formation and their effect have now be separately identified, more effective scaling mitigation strategies can be developed to avoid or minimise scaling of the low crystal-liquid interfacial energy salts and by preventing the deposition of the high crystal-liquid interfacial energy salts formed in the bulk solution to reach the membrane surface.

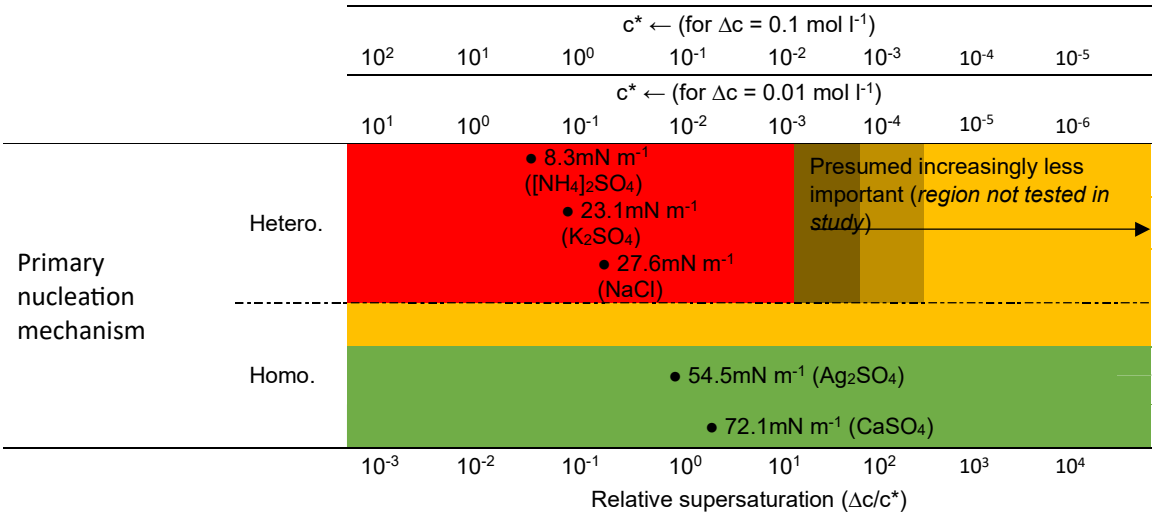

Figure 2.10 Framework to describe the relative importance of heterogeneous primary nucleation (membrane scaling) based on the interfacial energy of the solute which sets the relative supersaturation required to initiate nucleation (building upon the early work of Mersmann and Kind, 1988.

2.5 Acknowledgements

This research was financially supported through European Research Council Starting Grant, 'Sustainable chemical alternatives for reuse in the circular economy' (StG, SCARCE, 714080).

2.6 Appendices

2.6.1 Appendix A – Surface free energy analysis

The probability for scaling is generally studied through the interfacial interactions between the inorganic solute, the solution and the membrane involved in the system (Liu et al., 2018; Lin et al. 2014), which can be facilitated through the work of adhesion (Nguyen et al., 2017; Liu et al., 2017; Signorelli et al., 2019; Nikoo and Malaveri, 2020). Work of adhesion is the amount of work that is required to separate two different surfaces immersed in a medium (W_{132}) (Nguyen et al., 2017) and involves a combination of interaction forces like hydrogen bonding and other forces caused by chemical bonds (Butt et al., 2005). The total interaction energy of the solution-particle-surface system is mainly composed of Lifshitz-van der Waals interaction energy (LW), Lewis acid-base interaction energy (AB) and electrostatic interaction energy (EL) (Zhao et al., 2015; Nguyen et al., 2017; Liu et al., 2017). From these three interaction energies, acid-base and Lifshitz – van der Waals energies are the one who are responsible for the short-range attractive interactions (<3nm), while the electrostatic ones are repulsive and longer range (>3nm). Consequently, the EL contribution is often considered to be negligible, with work of adhesion primarily controlled from the AB and LW interaction energies (Liu et al., 2017; Hou et al., 2020). More specifically, the overall surface energy of work of adhesion is comprised of γ^{LW}, γ^{AB}, γ^{+} (electron acceptor) and γ^{-} (electron donor) (Nguyen et al., 2017; Liu et al., 2017; Hou et al., 2020 (Table 2.A1).

Table 2.A1. Calculated and literature values for Surface Free Energy components (mJ m^{-2}): γ^{LW}, γ^{+}, γ^{-}, γ^{AB}, γ^{total}.

	γ^{LW}	γ^{+}	γ^{-}	γ^{AB}	γ^{total}	$\gamma^{total(theo)a}$	**Ref.**
Crystalline surface free energy components							
Ammonium Sulphate	23.6	2.9	67.8	28.0	51.7	8.3	This study
					79		Tuckermann, 2007
Sodium Chloride	23.8	3.0	67.0	28.3	52.1	27.6	This study
					38		Townsend et al., 2017
Potassium Sulphate	20.0	1.5	85.1	22.5	42.5	23.1	This study
Silver Sulphate[b]	-	-	-	-	-	54.5	
Calcium Sulphate	36.5	3.0	8.6	10.2	46.7	72.1	Hina and Nancullas, 2000
Calcium carbonate	43.8	0.1	29.0	2.8	46.7	139.4	Bargir et al., 2009
Membrane surface free energy components							
PTFE	13.2	0.7	4.5	3.5	16.7		This study
	35.9	3.5	2.3	5.7	41.6		Liu et al., 2017
	20.2	0.1	0.1	0.2	20.3		Janczuk et al., 1999

[a]Calculated using the approach of Mersmann (1990). [b]Crystals were very small and thus contact angle could not be measured.

AB interactions tend to be more dominant than LW interactions, that is why hydrophobic membranes are manufactured in a way to limit these interactions. The hydrophobic PTFE membrane used in this study possessed a high γ^{LW}/γ^{AB} ratio, indicating the Lifshitz–van der Waals to dominate interaction. Hydrophobic membranes are characterised by high contact angles surfaces, and as such generally consist of higher LW interaction energy values than AB (Liu et al., 2017; Signorelli et al., 2019). The electron donor component (γ^-) possessed a minor contribution, while γ^+ tended to zero which is also comparable to earlier literature (Hou et al., 2020). It is therefore generally assumed that hydrophobic membrane interactions are less likely to relate to AB interaction energies (Janczuk et al., 1999), so the lower these contributions, the lower the ΔG contributions towards the free energy barrier for nucleation (Liu et al., 2017). These values are getting bigger and bigger as the membranes suffer scaling, as the inorganic material that is deposited on the membrane possess higher LW and AB interaction energy values and this way they decrease the nucleation energy barrier (Nguyen et al., 2017; Signorelli et al., 2019). Inorganic aqueous salts tend to have high γ^{LW} and γ^{AB} components (Table 2.B1). As the aqueous salts become less soluble, the γ^{LW} and γ^{AB} components increase and decrease respectively. Consequently, aqueous salts of high crystal-liquid interfacial energy (e.g. CaSO4) possess much stronger LW contributions (36.5 mJ m^{-2}), which is also reflected in the collated literature data on a similar range of aqueous salts (Wu et al., 1996; Hina and Nancullas, 2000; Signorelli et al., 2019; Nikoo and Malaveri, 2020). The γ^- contribution is also much lower for aqueous salts of higher crystal-liquid interfacial energy. However, this may be less significant to crystal-membrane interaction since the γ^+ of the PTFE membrane is almost zero.

A positive work of adhesion indicates that scaling is thermodynamically favourable and therefore scale will be difficult to remove, while a negative work of adhesion indicates that scaling is thermodynamically unfavourable and the scale can be more easily displaced (Bargir et al., 2009; Nguyen et al., 2017). The highly soluble aqueous salts characterised by low crystal-liquid interfacial energy, possessed a negative work of adhesion (-12.5 to -7.5 mJ m^{-2}) (Table 2.A2).

Table 2.A2. Calculated W_{12}, W_{13} and W_{132} values (in mJ m^{-2}) of materials using surface free energy components given in Table A2. Subscripts 1, 2 and 3 represent the membrane, crystallite, and water.

Compound	Interfacial Energy $\gamma^{total(theo)a}$ (mJ m^{-2})	Theoretical works of adhesion			
		W_{12}	W_{23}	W_{132}	W_{12}/W_{23}
Ammonium sulphate	8.3	56.2 ± 0.5[a]	145.7 ± 0.1[a]	-7.7 ± 0.4	0.39 ± 0.01
Sodium chloride	27.6	56.3 ± 0.3[a]	145.6 ± 0.1[a]	-7.5 ± 0.4	0.39 ± 0.01
Potassium sulphate	23.1	53.0 ± 2.8[a]	147.3 ± 1.7[a]	-12.5 ± 1.2	0.36 ± 0.01
Silver sulphate[d]	54.5	-	-	-	-
Calcium sulphate	72.1	56.1[b]	103.5[b]	34.4	0.54
Calcium carbonate	139.4	58.1[c]	118.9[c]	21.1	0.49

[a]W_{12} and W_{23} estimated by the author; [b]W_{12} and W_{23} taken by Hina and Nancullas, 2000; [c]W_{12} and W_{23} taken by Bargir et al., 2009; W_{13} is estimated as 63.8 ± 0.5. [d]Could not be directly measured due to the product of small crystals. Four sets of liquid triplets (DWG, DWE, DWF, and DWS) were used to calculate the polar components of SFE.

Due to difficulties in measuring crystalline silver sulphate, calcium carbonate data from the literature was used to supplement crystal-liquid interactions of poorly soluble salts. These poorly soluble aqueous salts (high crystal-liquid interfacial energy) are described by positive W_{132} values (21.1 to 34.4 mJ m-2). The critical factor in this transition toward a positive W_{132} is the reduction in W_{23} which corresponds to the crystal-liquid work of adhesion. This is illustrated by the transition in LW and γ^- contributions to the W_{23} as the aqueous salts become less soluble (Figure 2.A1). The hydrophobic membrane possesses a minimal acid polar energy contribution, and as such the overall work of adhesion is dependent on the Lifshitz-van der Waals component and the polar base component. The increased dominance of the Lifshitz-van der Waals contribution to W_{23} for poorly soluble salts is therefore indicated to increase the probability for adhesion (based on a positive W_{132}).

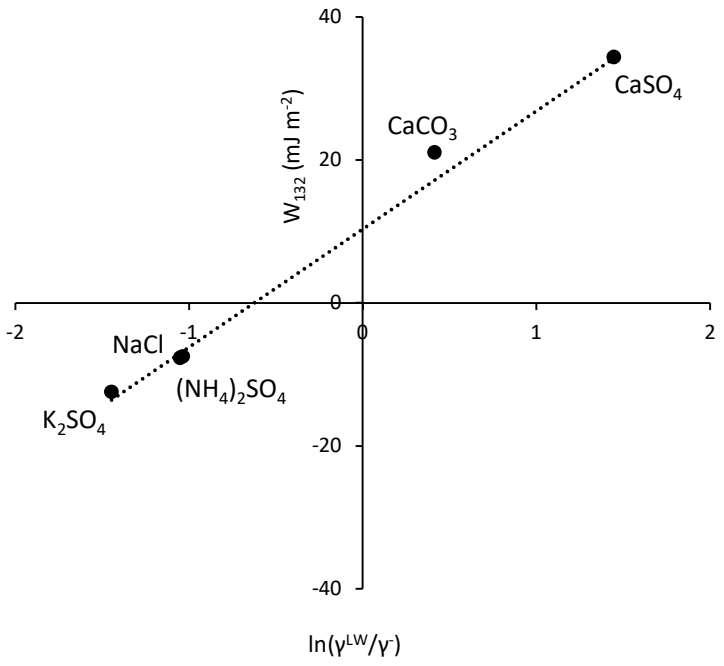

Figure 2.A1 The overall work of adhesion is dependent on W_{23}, the crystal-liquid work of adhesion. This is illustrated by observing the transient in Lifshitz-van der Waals and polar base components as aqueous salts become less soluble. The hydrophobic membrane possesses a minimal acid polar energy contribution, and as such the overall work of adhesion is dependent on the Lifshitz-van der Waals component and the polar base component, whose ratio indicates the probability for adhesion (based on a positive W_{132}).

However, in this study, scaling via an adhesive growth mechanism (or primary heterogeneous nucleation mechanism) approached a minimum for aqueous salts which are theoretically most likely to undergo formation of an adhesive scale based on the calculated work of adhesion (W_{132}). The work of adhesion represents the 'effective' interfacial energy, which is a product of the 'wetting' of the substrate (φ) and the interfacial energy (γ):

$$\gamma_{eff} = \varphi\gamma^3 \qquad (Eq.\ 2.A1)$$

This provides a description of the thermodynamic interaction between crystal, liquid and membrane and represents the surface free energy contribution (ΔG_s) or the work required to produce a nucleus. However, what it fails to consider is the chemical potential ($\mu = kTlnS$) which represents the volume free energy (ΔG_v) contribution that provides the supersaturation (S) driving force for nucleation (J_{hetero}):

$$J_{hetero} = A_{hetero} S e^{\left[-\frac{16\pi\varphi\gamma^3 V_m^2}{3k^3T^3(lnS)^2}\right]} \qquad (Eq.\ 2.A2)$$

Nucleation is less dependent on a heterogeneous substrate when high supersaturations are achieved. High supersaturations are synonymous with poorly soluble aqueous salts due to the low solute concentration which must achieve an

excess of ions to foster sufficient collisions to produce an ordered critical nucleus (Figure 2.A1). Consequently, while aqueous salts that exhibit greater γ^{LW}/γ^{-} may indicate an increased probability for scaling, the high supersaturation requirement for poorly soluble salts is sufficient to favour homogeneous nucleation. In contrast, aqueous salts characterised by high crystal-liquid interfacial energy are extremely soluble, and as such it is difficult to achieve high levels of supersaturation due to the ion density required (Figure 2.A1). Consequently, it is the higher solubility salts that are more likely to scale since the low level of supersaturation increases the dependency on a substrate which was evidenced in this study. The use of work of adhesion is useful for relating how material surface properties may induce interactions for a specific solute, but the role of supersaturation to the initiation of nucleation should not be neglected.

2.6.2 Appendix B – Characterisation of the recovered crystal phase

Crystal size distributions were prepared as square weighted chord length distributions for each aqueous salt (Figure 2.B1). Thousands of chord lengths are counted every second and a precise distribution is reported. Chord lengths are defined for any geometric object.

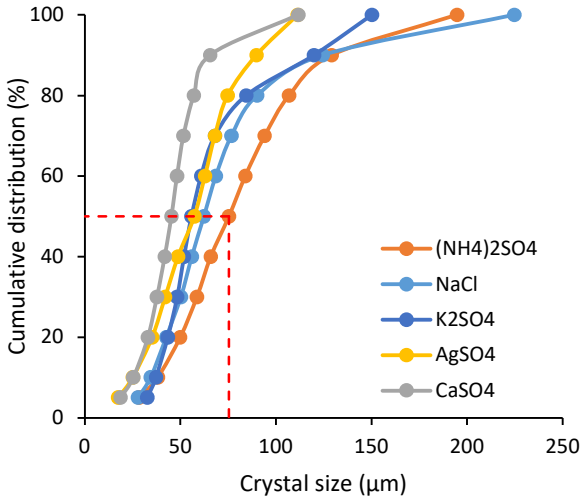

Figure 2.B1 Illustrative crystal size distributions for each aqueous salt based on square weighted chord size distributions.

To compare differences between distributions, percentiles of the distributions were compared and the coefficient of variance calculated (Table 2.B1). The L_{50}, which represents the median of the chord length, is demonstrated to decrease with an increase in crystal-liquid interfacial energy, and is coincident with a decrease in CV.

Table 2.B1. Characterisation of chord length distributions (based on mean of replicates)

Compound	CSD (µm)			CV[a]	Crystal structure	
	L_{10}	L_{50}	L_{90}	(%)	Expected	Observed
$(NH_4)_2SO_4$	43.1	79.3	125.1	21.9	Orthorhombic	Rods & orthorhombic
NaCl	38.5	65.3	125.1	18.7	F-C cubic	F-C cubic
K_2SO_4	31.8	63.1	232.4	12.9	Orthorhombic	Orthorhombic
Ag_2SO_4	30.0	60.7	101.8	3.2	Orthorhombic	Orthorhombic
$CaSO_4$	28.0	48.8	68.6	6.5	Orthorhombic	Acicular

[a] *CV based on:* $CV = \frac{SD}{sample\ mean} x100$*; CSD, Crystal Size Distribution; F-C, Face-centred.*

Crystallography was undertaken to confirm crystal structure for each aqueous salt. Despite differences in observed crystal structure, XRD confirmed that a crystalline phase was produced for each aqueous salt, coincident with the origin of the salt. For example, the 2θ peaks of the calcium sulphate closely matched the reference sample for Gypsum (Figure 2.B2) while $(NH_4)_2SO_4$, NaCl, Ag_2SO_4 and K_2SO_4 closely matched peaks of reference spectra from mascagnite (a form of $(NH_4)_2SO_4$), Halite, Ag_2SO_4 and arcanite respectively.

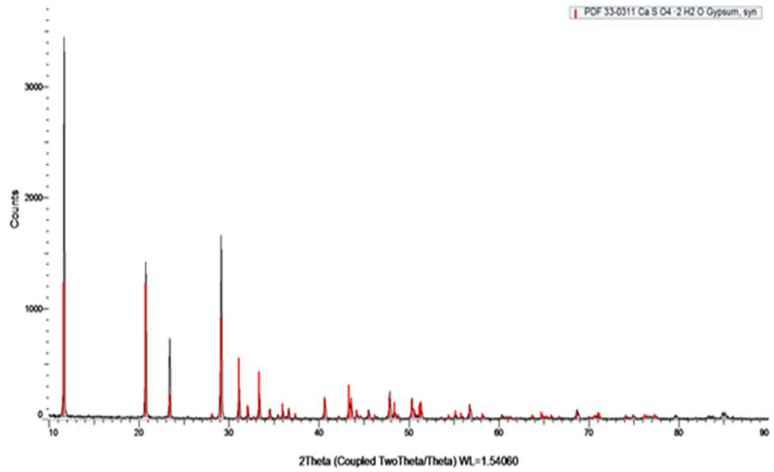

Figure 2.B2 XRD spectra of calcium sulphate provided for illustration. Red peaks are reference spectra, and black peaks are the sample.

References

A. Abdel-Karim, S. Leaper, C. Skuse, G. Zaragoza, M. Gryta, P. Gorgojo, Membrane cleaning and pretreatments in membrane distillation – a review, J. Chem. Eng. 422 (2021) 129696.

N.A. Ahmad, C.P. Leo, A.L. Ahmad, W.K.W. Ramli, Membranes with great hydrophobicity: A review on preparation and characterization, Sep. Pur. Rev. 44 (2015) 109–134.

A. Ali, F. Macedonio, E. Drioli, S. Aljlil, O.A. Alharbi, Experimental and theoretical evaluation of temperature polarization phenomenon in direct contact membrane distillation, Chem. Eng. Res. Des. 91 (2013) 1966 – 1977.

S. Bargir, S. Dunn, B. Jefferson, J. Macadam, S. Parsons, The use of contact angle measurements to estimate the adhesion propensity of calcium carbonate to solid substrates in water, Appl. Surf. Sci. 255 (2009) 4873–4879.

L. de Bartolo, A. Gugliuzza, S. Morelli, B. Cirillo, A. Gordano, E. Drioli, Novel PEEK-WC membranes with low plasma protein affinity related to surface free energy parameters, Journal of Materials Science: Materials in Medicine. 15 (2004) 877–883.

L. de Bartolo, S. Morelli, A. Bader, E. Drioli, The influence of polymeric membrane surface free energy on cell metabolic functions, Journal of Materials Science: Materials in Medicine. 12 (2001) 959–963.

H.J. Butt, B. Cappella, M. Kappl, Force measurements with the atomic force microscope Technique, Interpretation and applications, Surf. Sci. Rep. 59 (2005) 1–152.

C. Charcosset, R. Kieffer, D. Mangin, F. Puel, Coupling between Membrane Processes and Crystallisation Operations, Ind. Eng. Chem. Res. 49 (2010) 5489–5495.

Y. Choi, G. Naidu, L.D. Nghiem, S. Lee, S. Vigneswaran, Membrane distillation crystallisation for brine mining and zero liquid discharge: opportunities, challenges, and recent progress, Env. Sci. Water Res. & Technol. 5 (2019) 1202.

E. Curcio, E. Drioli, Membrane distillation and related operations – A review, Sep Pur. Rev. 34 (2005) 35–86.

G. Di Profio, E. Curcio, E. Drioli, Supersaturation control and heterogeneous nucleation in membrane crystallizaers: facts and perspectives, Ind. Eng. Chem. Res. 49 (2010) 11878–11889.

M.L. Dundon, E. Mack Jr., The solubility and surface energy of calcium sulphate, Journal of the American Chemical Society. 45 (1923) 2479–2485.

H. Elcik, L. Fortunato, A. Alpatova, S. Soukane, J. Orfi, E. Ali, H. Alansary, T. Leiknes, N. Ghaffour, Multi-effect distillation brine treatment by membrane distillation: Effect of antiscalant and antifoaming agents on membrane performance and scaling control, Desalination. 493 (2020) 114653.

D. Erdemir, A. Y. Lee, A. S. Myerson, Handbook of Industrial Crystallisation, Ch. 3, Cambridge University Press. 2019.

M. Gryta, Fouling in direct contact membrane distillation process, J. Membr. Sci., 325 (2008) 383–394.
A.R. Heath, P.D. Fawell, P.A. Bahri, J.D. Swift, Estimating average particle size by focused beam reflectance measurement, Part. Part. Syst. Char. 19 (2002) 84–95.
A. Hina, G.H. Nancollas, Precipitation and dissolution of alkaline earth sulphates: Kinetics and surface energy, Reviews in Mineralogy and Geochemistry. 40 (2000) 276–301.
T. Horseman, C. Su, K. S. S. Christie, S. Lin, Highly effective scaling mitigation in membrane distillation using a superhydrophobic membrane with gas purging, Env. Sci. Technol. Lett. 6 (2019) 423–429.
T. Horseman, Y. Yin, K.S.S. Christie, Z. Wang, T. Tong, S. Lin, Wetting, scaling and fouling in membrane distillation: State-of-the-art insights on fundamental mechanisms and mitigation strategies, ACS EST Eng. 1 (2021) 117–140.
D. Hou, Z. Yuan, M. Tang, K. Wang, J. Wang, Effect and mechanism of an anionic surfactant on membrane performance during direct contact membrane distillation, J. Membr. Sci. 595 (2020) 117495.
B. Janczuk, T. Białopiotrowicz, A. Zdziennicka, Some Remarks on the Components of the Liquid Surface Free Energy, Journal of Colloid and Interface Science. 103 (1999) 96–103. S. Lin, S. Nejati, C. Boo, Y. Hu, C. O. Osuji, M. Elimelech, Omniphobic Membrane for Robust Membrane Distillation, Env. Sci. Technol. Letters. 1 (2014) 443–447.
X. Jiang, X Ruan, W. Xiao, D. Lu, G. He, A novel membrane distillation response technology for nucleation detection, metastable zone width measurement and analysis, Chem. Eng. Sci. 134 (2015) 671–680.
X. Jiang, L. Tuo, D. Lu, B. Hou, W. Chen, G. He, Progress in membrane distillation crystallisation: Process models, crystallisation control and innovative applications, Front. Chem. Sci. Eng. 11 (2017) 647–662.
A. Jikazana, P. Campo, E.J. McAdam, Hydrodynamics (Reynolds number) determine scaling, nucleation and crystal growth kinetics in membrane distillation crystallisation, J. Membr. Sci. 685 (2023) 121909.
J.W. Kim, J. Kim, K.-D. Lee, K.-K. Koo, Evaluation of nucleation rate by in-situ focused beam reflectance measurement in an unseeded batch cooling crystallisation, Crys. Res. Technol. 48 (2013) 1097–1105.
M. Lenka, D. Sarkar, Determination of metastable zone width, induction period and primary nucleation kinetics for cooling crystallisation of L-asparaginenohydrate, J. Crys. Growth. 408 (2014) 85–90.
L. Li, S. Zhao, Z. Xin, S. Zhou, Nucleation kinetics of clopidogrel hydrogen sulphate polymorphs in reactive cyrstallization: Induction period and interfacial tension measurements, J. Cryst. Growth. 538 (2020) 125610.

C. Liu, L. Chen, L. Zhu, Fouling behavior of lysozyme on different membrane surfaces during the MD operation: An especial interest in the interaction energy evaluation, Water Research. 119 (2017) 33–46.
C. Liu, L. Chen, L. Zhu, Fouling mechanism of hydrophobic polytetrafluoroethylene (PTFE) membrane by differently charged organics during direct contact membrane distillation (DCMD) process: An especial interest in the feed properties, J. Membr. Sci. 548 (2018) 125–135.
L.H.T. Lyly, B.S. Ooi, J.K. Lim, C.J.C. Derek, S.C. Low, Correlating the membrane surface energy to the organic fouling and wetting of membrane distillation at elevated temperature, Journal of Environmental Chemical Engineering. 9 (2021) 104627.
D. Mangin, F. Puel, S. Veesler, Polymorphism in Processes of Crystallisation in Solution: A Practical Review, Org. Pro. Res. & Dev. 13 (2009) 1241–1253.
L. Martinez-Diez, M.I. Vazquez-Gonzalez, Temperature and concentration polarization in membrane distillation of aqueous salt solutions, J. Membr. Sci. 156 (1999) 265–273.
A. Mersmann, M. Kind, Chemical Engineering Aspects of precipitation from solution, Chem. Eng. Technol. 11 (1988) 264–276.
A. Mersmann, Calculation of interfacial tensions, J. Crystal Growth 102 (1990) 841–847.
A. Mersmann, M. Angerlhöfer, T. Gutwald, R. Sangl, S. Wang, General prediction of medial crystal sizes, Sep. Technol. 2 (1992) 85–97.
N.A. Mitchell, P.J. Frawley, C.T. Ó'Ciardhá, Nucleation kinetics of paracetamol–ethanol solutions from induction time experiments using Lasentec FBRM®, J. Cryst. Growth. 321 (2011) 91–99.
A.V. Mohod, P.R. Gogate, Improved crystallisation of ammonium sulphate using ultrasound assisted approach with comparison with the conventional approach, Ultrasonics – Sonochemistry, 41 (2018) 310–318.
J. W. Mullin, Crystallisation, Butterworth Heinemann, Oxford. 2001.
D. Nguyen, T. Phan, T.-.P. Hsu, J. Phan, Adhesion and surface energy of shale rocks, Colloids and Surfaces A: Physicochem. Eng. Aspects 520 (2017) 712–721.
A.H. Nikoo, M.R. Malayeri, Incorporation of surface energy properties into general crystallisation fouling model for heat transfer surfaces, Chem. Eng. Sci. 215 (2020) 115461.
J. Nývlt, Kinetics of nucleation in solutions, J. Cryst. Growth. 3-4 (1968) 377–388.
A. Ouda, Y. Bajón Fernández, E. McAdam, Modifying supersaturation rate with membrane area to volume ratio: Scaling reduction and improved crystal growth control in membrane distillation crystallisation, J. Membr. Sci. 683 (2023) 121838.
C.P.M. Roelands, J.H. ter Horst, H.J.M. Kramer, P.J. Jansens, Analysis of nucleation rate measurements in precipitation processes, Cryst. Growth Des., 6 (2006) 1380–1392.
I. Ruiz Salmon, P. Luis, Membrane crystallisation via membrane distillation, Chem. Eng. Process. Process Intensif. 123 (2017) 258–271.

F. Signorelli, M.F.B. Sousa, C.A. Bertran, Interfacial Phenomena on the Inorganic Scaling Prevention, ACS Omega. 4 (2019) 79–85.
N. Subhi, A.R.D. Verliefde, V. Chen, P. Le-Clech, Assessment of physicochemical interactions in hollow fibre ultrafiltration membrane by contact angle analysis, J. Membr. Sci. 403–404 (2012) 32–40.
E.R. Townsend, W.J.P. van Enckevort, J.A.M. Meijer, E. Vlieg, Additive Enhanced Creeping of Sodium Chloride Crystals, Cryst. Growth & Des. 17 (2017) 3107−3115.
J. Torrens-Serra, J. Rodriguez-Viejo, M.T. Clavaguera-Mora, Evaluation of the liquid-solid interfacial energy from crystallisation kinetic data, Scripta Materialia 61 (2009) 879–882.
C.M. Tun, A.G. Fane, J.T. Matheickal, R. Sheikholeslami, Membrane distillation crystallisation of concentrated salts-flux and crystal formation, J. Membr. Sci. 257 (2005) 144–155.
D.M. Warsinger, J. Swaminathan, E. Guillen-Burrieza, H.A. Arafat, J.H. Lienhard V, Scaling and fouling in membrane distillation for desalination applications: A review, Desalination. 356 (2015a) 294–313.
D.M. Warsinger, J. Swaminathan, H.W. Chung, S. Jeong, J.H. Lienhard V., Effect of filtration and particulate fouling in membrane distillation, 2015 International Desalination Association World Congress on Desalination and Water Reuse. (2015b).
D.M. Warsinger, E.W. Tow, J. Swaminathan, J.H. Lienhard V., Theoretical framework for predicting inorganic fouling in membrane distillation and experimental validation with calcium sulphate, J. Membr. Sci. 528 (2017) 381 – 390.
W. Wu, R.F. Giese Jr., C.J. Van Oss, Change in surface properties of solids caused by grinding, Powder Technol. 89 (1996) 129–132.
Y. Yan, T. Yu, H. Zhang, J. Song, C. Qu, J. Li, B. Yang, Co-Deposition Mechanisms of Calcium Sulphate and Calcium Carbonate Scale in Produced Water, Crystals. 11 (2021) 1494.
L.A. Zepeda-Ruiz, G.H. Gilmer, Monte Carlo simulations of crystal growth, Handbook of crystal growth. (2014) 445–475.
F. Zhao, K. Xu, H. Ren, L. Ding, J. Geng, Y. Zhang, Combined effects of organic matter and calcium on biofouling of nanofiltration membranes, J. Mem. Sci. 486 (2015) 177–188.
L. Zhou, Z. Wang, M. Zhang, M. Guo, S. Xu, Q. Yin, Determination of metastable zone and induction time of analgin for cooling crystallisation, Chi. J. Chem. Eng. 25 (2017) 313–318.
T. Zhou, C. Tu, Y. Sun, L. Ji, C. Bian, X. Lu, C. Wang, Determination of the metastable zone and induction time of thiourea for cooling crystallisation, Chi. J. Chem. Eng. 31 (2021) 164–168.

3 Temperature polarisation controls nucleation kinetics in membrane distillation crystallisation

Temperature polarisation controls nucleation kinetics in membrane distillation crystallisation

K. Vasilakos, M. Hermassi, N. Thomas, P. Campo, E. McAdam[a]

Cranfield Water Science Institute, Cranfield University, Cranfield, MK43 0AL

[a]corresponding author: e.mcadam@cranfield.ac.uk

Abstract

As membrane distillation crystallisation (MDCr) operates through temperature difference between the two membrane sides, the arised conductive and convective heat transfer create a temperature gradient throughout the membrane system. Temperature polarisation coefficient (TPC) is the parameter used to measure the heat resistance resulting from the creation of the boundary layer, explaining the temperature gradient across the membrane surface in membrane distillation. At the same time, as vapour transfers through the membrane, its surface concentration is higher than the bulk solution due to concentration polarisation phenomena, measure by the concentration polarisation coefficient (CPC). Even though previous studies have evidenced how increasing TPC is crucial for the delay of scaling as well as the efficiency of the system (Anvari et al., 2020), researchers never really managed to decouple TPC from CPC to find its real impact in the process. Simultaneously, different salts have different solubility – temperature dependences, varying from positive ($KClO_4$) to neutral (NaCl) to negative (Na_2SO_4), leading to different concentration gradient arising from the created temperature gradient. To examine the effect of the TPC in the scaling, nucleation and crystal growth kinetics of MDCr, three salts with different solubility – temperature dependences ($KClO_4$, NaCl and Na_2SO_4) were used in 5 different TPC scenarios each, while the CPC was kept similar through all the experiments. A simultaneous bulk and membrane high-definition imagine techniques were used for the detection of induction time. This resulted in higher scaling at lower TPCs for the positive and neutral solubility – temperature dependence salts, while no scaling prior to bulk nucleation for Na_2SO_4. Even though that contradicts classical nucleation theory (CNT) literature as Na_2SO_4 is a high solubility salt, making it more inclined towards heterogeneous nucleation, temperature polarisation was evidenced to be the dominant factor controlling scaling in MDCr and not heterogeneous nucleation as previously assumed. Therefore, this study offers a comprehensive analysis on the dominant factor controlling scaling, that is temperature polarisation and not heterogeneous nucleation as previously assumed, which can be utilised to develop effective solutions for scaling mitigation in order to enhance the sustainability of the MDCr process.

Keywords: *membrane distillation crystallisation, temperature polarisation, TPC, nucleation kinetics, scaling, temperature difference*

3.1 Introduction

Membrane distillation crystallisation (MDCR) is a solid-liquid separation method that can combine the brine concentration and crystallisation stages of the zero-liquid discharge into a single unit process. In addition to capital savings, less thermal energy is required due to the utilisation of low temperatures and pressures, when compared to multi-effect distillation for example, which is typically recommended for the brine concentration step (Yadav et al., 2021). Membrane distillation enables the treatment of brine solutions exceeding the solubility limit of sodium chloride, which cannot be achieved using conventional separation and purification technologies (Pantoja, 2015). The hydrophobic membrane in MDCr operates by utilising the temperature disparity between the feed and distillate to create a vapour pressure difference, establishing a water vapour flux across them membrane which introduces both conductive and convective heat transfer across the membrane (Alkhudhiri et al., 2012). As the membrane simultaneously controls mass and heat transfer processes, it is possible to strictly regulate supersaturation within MDCr which is the driving force for crystallisation, while the well-defined surface area also simplifies scale-up. Supersaturation control and scale-up are two critical challenges to industrial crystalliser design for brine management. Therefore, process intensification and improved control of solids formation can be achieved by pairing concentration and crystallisation stages within MDCr. However, MDCr is known to generate a temperature gradient across the membrane, which introduces a phenomenon referred to as temperature polarisation (Anvari et al., 2020).

Temperature polarisation refers to the reduction in temperature at the membrane surface of the feed, relative to the bulk solution, due to the combined effect of localised conductive and convective heat transfer. The consequence of this phenomenon is the decrease in vapour pressure at the membrane surface due to the reduction in temperature difference across the membrane (Martinez-Diez and Vazquez-Gonzalez, 1999; Srisurichan, 2006). The temperature polarisation coefficient (TPC) was developed by Schofield et al. (2000) to characterise the heat resistance resulting from the creation of the boundary layer, and ranges in value from 0 to 1, with unity representing a thermally efficient operation (Ali et al., 2013). In addition to reducing the water vapour flux, the reduction in boundary layer temperature will also modify the temperature dependent solubility limit (c^*) of aqueous salts. Dependent upon the solubility-temperature dependency of the salt, this can increase the supersaturation locally at the membrane, which could promote scaling. Therefore, modifying TPC may be critical to delaying or mitigating scaling to facilitate sustained operation of MDCr in concentrated brine management (Anvari et al., 2020).

An increase in temperature or temperature difference raises the vapour pressure which results in a higher water vapour flux that can reduce the TPC (Martinez-Diez and Vazquez-Gonzalez, 1999). At an equivalent temperature, higher feed flow rates can raise the heat

transfer coefficient, leading to an increase in water vapour flux but also results in a greater TPC (Phattaranawik et al., 2003). The role of feed velocity within this range has been shown to offer greater control over the TPC than temperature difference (Manawi et al., 2014). The vapour pressure difference determines the water vapour flux, which in combination with the feed flow rate, also determines the local transport of solute. An accumulation of solute in the boundary layer of the feed channel can be described by the concentration polarisation coefficient (CPC) (Nthunya et al., 2022). The increase in solute concentration (c) can also increase the local supersaturation (S, or c/c^*) driving force for nucleation. Consequently, the increase in inorganic salt concentration near the membrane surface due to concentration polarisation can enhance the likelihood for scale formation, and growth (Chong et al., 2007; Kroiß, et al., 2015; Nthunya et al., 2022). Moreover, the creation of scale leads to a further increase in concentration polarisation known as cake-enhanced concentration polarisation. The reasons for this mechanism is a combination of hindered back-diffusion of salt ions and cross-flow hydrodynamics alterations caused by the generated membrane crystals and this is the phenomenon responsible for the rapid drop in flux and the termination of the process (Hoek and Elimelech, 2003). This work however, is focused on the cake mass after its generation and not the effect of the polarisation phenomena in the nucleation mechanism and its kinetics. In their study, Wang et al. (2014) also demonstrated that crystallisation contributes to the amplification of temperature and concentration polarisation effects, as well as the formation of fouling. However, they were unable to determine the extent to which polarisation phenomena initially influence scaling and fouling. This happened because, this study used single or mixed salt solutions that were based on high crystal-liquid interfacial salts prone to homogeneous nucleation where polarisation phenomena seem to have less effect due to the limited impact of the membrane on the crystallisation process. Moreover, the generated salts had all positive solubility-temperature dependence which encourages the crystal formation on the membrane (Chernysov et al., 2003). This disparity in concentration results in the formation of membrane scaling (Kuang et al., 2019) which can result in a rapid decrease in flux, ultimately leading to the termination of the process (Curcio and Drioli, 2005), something that changes when there is a negative solubility – temperature dependence.

The solubility-temperature dependence of the solute determines the extent to which concentration and temperature polarisation contribute toward the nucleation and growth of scaling. Aqueous salt solubility can exhibit positive, negative, or neutral dependency on temperature. A change in solution temperature can therefore increase or decrease the solubility limit of an aqueous salt. Temperature can therefore increase or decrease the metastable zone width (MSZW, or $\Delta c = c\text{-}c^*$), which is the area between the solubility curve of the solute and the supersaturation at which primary nucleation commences (Choi et al., 2019). The extent of the MSZW determines the driving force available for spontaneous

nucleation and therefore determines induction time and nucleation rate. To understand this, Tun et al. (2005) undertook membrane crystallisation with NaCl and Na_2SO_4, which exhibit neutral and negative solubility-temperature dependencies and demonstrated that salts exhibiting negative solubility – temperature dependence can achieve higher levels of saturation in the bulk due to the favourable influence of polarisation processes, resulting to less scaling as the process is pushed more towards homogeneous nucleation. However, Tun et al. (2005) was unable to demonstrate the extension of the positive solubility-temperature dependence as NaCl has a very slight positive relationship that can be mostly characterised as neutral. At the same time, deposition and scaling are two distinct mechanisms that can be easily confused (Ouda et al., 2023), and the method used for the characterisation of the induction time (flux drop) is not considered best available technique for its determination and can produce more uncertainty, especially for high-interfacial energy salts (CHAPTER 1). Lastly, it is important to note that the study was not able to separate the impact of the solute from the hydrodynamics of the process due to variations in permeate flux across the different experiments, which is known to influence membrane fouling (Mohammadi et al., 2002).

As all the prior studies have been focused on the role of the polarisation phenomena in the scaling process after the generation of crystals, either through deposition or scaling, the focus in this study will be the holistic identification of the impact of the TPC on the chemistry of the solute and their nucleation kinetics prior to scaling as well as how they affect the crystal growth right after. For this reason, three salts with varying solubilities (high and low) and various solubility – temperature dependence (NaCl, $KClO_4$, and Na_2SO_4) were chosen for investigation. Sodium chloride was chosen due to its high solubility and a slight but noticeable increase in solubility with temperature. Potassium perchlorate was chosen for its poor solubility and strong positive solubility – temperature dependence and sodium sulphate for its high solubility and negative solubility – temperature dependence. In order to minimise the effect of concentration polarisation in the system and focus solely on the difference temperature polarisation makes, operating conditions have been employed where the combination of the feed and permeate flows used are always providing similar transmembrane fluxes, resulting into similar CPCs, while TPC is always changing by regulating the temperature. This is how the impact of the hydrodynamics which have been proved to influence membrane found can be completely separated from the effect of the temperature polarisation phenomena (Mohammadi et al., 2002). In addition, despite the intense research of the effect of the TPC in scaling kinetics, the topic has not yet been fully explored using the best available techniques (Tun et al., 2005). This results in a limited comprehension of the relationship between the solute and the polarisation phenomena. By employing an inline Focused Beam Reflectance Measurement (FBRM), which is the industry – standard particle measurement technique positioned within the reactor, along with a high – definition USB digital microscope positioned

in front of the membrane cell, we can obtain a simultaneous, live, high – resolution observation of the system. By adopting this approach, we can obtain significantly more precise data to shape our conclusions.

3.2 Materials and methods

3.2.1 Experimental setup

The direct contact membrane distillation system setup consisted of a Sepa Cell acrylic cross-flow cell (Sterlitech, Washington, USA) with a hold-up volume of $2.8x10^{-5}$ m^3. The channel dimensions was 0.145x0.095m (LxW) with an active membrane area of 0.014m^2. The membrane was an ePTFE flat sheet (Cobetter Filtration, Hangzhou, China), with a pore size of 0.1µm and thickness of 50±20µm. Three different feed solutions were created by adding anhydrous NaCl, $KClO_4$ and Na_2SO_4 crystalline powder (99+% Alfa Aesar, Lancashire, UK) to ultrapure water (15 MΩ cm^{-1}) (Purelab, Elga, UK) to create a concentration equivalent to 75% of the solubility limit at the reference temperature of the feed solution. After completely dissolving the crystalline powder, the solution was filtered using a 0.45µm Whatman filter (Camlab Ltd., Cambridge, UK) to clear any impurities from the initial solution. The solution concentration was confirmed by assessing solution conductivity (Seven2Go Pro, Mettler Toledo, UK). Once ready, the feed solutions were introduced in a 500ml Reactor Ready™, equipped with a 4-blade impeller comprising a 45° pitch (Radley's, Essex, UK). The flow rates for feed and permeate ranged 275 to 3015 ml min^{-1} and 650 – 1629 ml min^{-1} respectively, depending on the salt used (323, Watson Marlow, UK). A heater/chiller (Ministat 230, Huber, UK and LT ecocool 150, Grant, UK) was employed to regulate the temperature on the feed side to around 45°C, and 30°C on the permeate side, providing a ΔT of around 15°C for each salt. Fluid temperatures for feed and permeate were measured using specialist thermometers (T7-Pro, LabJack, USA). The permeate volume was measured using a precision balance (Symmetry PR 410, Cole Palmer, UK) (Figure 3.1).

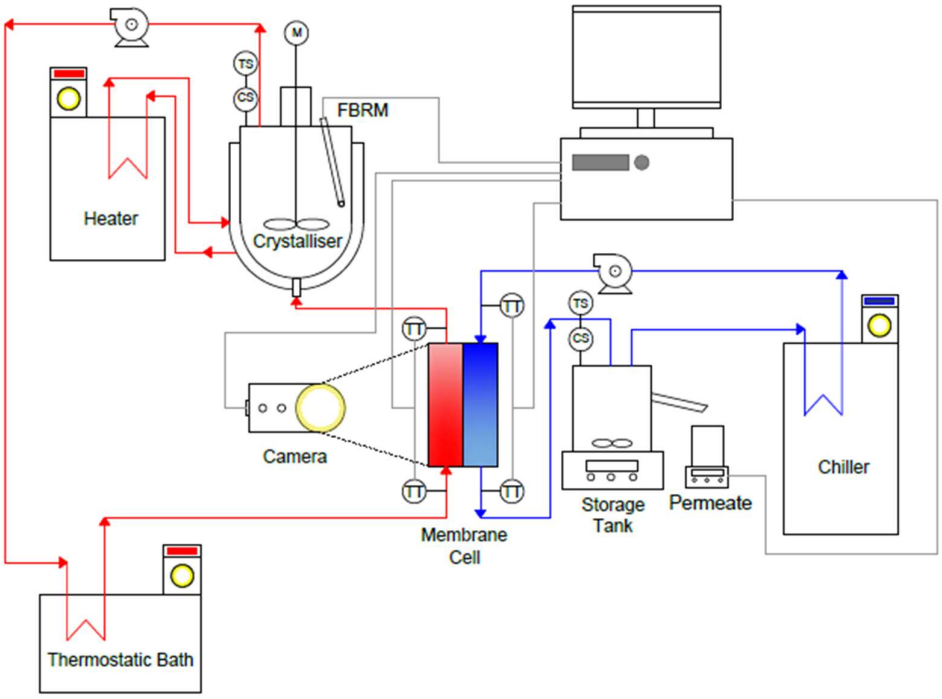

Figure 3.1 Experimental set-up diagram.

3.2.2 Analytical methods

Induction time and nucleation rate of the bulk crystal phase were characterised using Focused Beam Reflectance Measurement (FBRM) (Heath et al., 2002). The FBRM probe uses a 780nm laser that is directed via a beam splitter, scanning at a velocity of 2 m s^{-1}. This laser intersects with the particles, resulting in the production of a pulse of backscattered light and its duration is directly related to the particle's width. This pulse is measured as a chord length with the size range corresponding to between 0.5 to 2000μm. The Chord Length Distribution (CLD) offers a comprehensive representation of the overall size distribution and the total count of chord length measurements is obtained as the cumulative number in s^{-1} (Kim et al., 2013):

$$total\ counts\ s^{-1} = \sum_{i=1}^{Ch} N_{Ch,i} \qquad (Eq.\ 3.1)$$

Ch representing the number of channels in FBRM, while $N_{Ch,I}$ represents the number of counts measured in the i^{th} channel. Once primary nucleation occurs, the total counts per second (s^{-1}) increase rapidly, offering a precise method for determining the induction time in the bulk solution. The instrument used for this purpose consists of a probe positioned at a 60° angle inside the reactor to provide optimal contact with the particle suspension (ParticleTrack G400, Mettler Toledo, UK). Differentiation of the total counts per second (s^{-1}) with time, provides a direct measure of the nucleation rate, where the approximation of the volumetric depth can be used to estimate the volumetric nucleation rate (B, m^{-3} s^{-1}):

$$V = S_p W_l D_p \quad (Eq.\ 3.2)$$

where S_p is the scan speed of the laser (2 m s^{-1}), W_l is the laser diameter at the focal point ($5.8x10^{-6}$ m), and D_p is the laser penetration depth in solution ($2x10^{-4}$ m). The 'primary' selection view was used to determine the induction time. This mode has a narrower measurement zone with precise edge discrimination, allowing for enhanced sensitivity to primary particles and facets. The change in particle count over time is used to calculate the nucleation rate:

$$B_i = \frac{(N_{c,i} - N_{c,i-1})}{t_i - t_{i-1}} \quad (Eq.\ 3.3)$$

t_i representing the time of the measurements in seconds (s), and B_i representing the nucleation rate (# m^{-3} s^{-1}) for two consecutive observations. As the nucleation concentration N_c of the experiment increases, the individual nucleation rates obtained from the two consecutive measurements were utilised to determine the average nucleation rate B of the experiment.

For the crystal size distribution from CLD, the 'macro' mode has been selected, as it uses a wider measurement zone with a macro edge discrimination for crystals and agglomerates. Contrary to the 'primary' selection, this mode is less sensitive to surfaces and facets (Heat et al., 2002).

$$N_{i,n} = N_{i,o} C_{i,A}^n \quad (Eq.\ 3.4)$$

$N_{i,n}$ representing the number of n-weighted chord counts in the i^{th} channel (μm^n s^{-1}). $N_{i,o}$ represents the raw unweighted chord count in the i^{th} channel (s^{-1}), while $C_{i,A}$ is the geometric average length of the i^{th} channel (μm). This is calculated by taking the square root of the product of the upper and lower boundary lengths of the i^{th} channel, measured in μm ($C_{i,u}$ x $C_{i,l}$)$^{1/2}$. A square-weighted (n = 2) chord distribution has been employed to prioritise the coarse end of the distribution, resulting in a more precise depiction of the crystal size. The square-weighting method effectively applies a cube (volume) weighting, similar to volume-based distribution techniques (Heath et al., 2002).

Similarly to the FBRM method, a UHM350 digital microscope (UHM350, AmScope, UK) was used to determine the induction time and surface growth rate for scaling, using direct observations made through the polished Perspex of the crossflow Sepa cell. The digital microscope comprised a wide-angle high-resolution lens (1920px1080p - 2.1MP), with a long working distance and wide magnification range (x20-100). The lens was positioned 145mm from the cell, within the working distance of the microscope, with its focus directed towards the feed side of the membrane. The first detection of the incipient crystal phase was used to determine induction time. This method is comparable to the backscatter technique, where neither are sufficiently sensitive to directly measure newly born nuclei (formation at nanoscale), but since crystal growth quickly proceeds nucleation, the lag-time between nucleation and growth is short, and for the membrane growth is extremely fast due to the elevated supersaturation within the boundary layer due to polarisation (Jikazana et al., 2023).

Consequently, the techniques can be used both to identify the first crystal that has achieved a thermodynamically stable form at the membrane and within the bulk solution. Subsequent to nucleation, imaging was used to monitor the formation and growth of the advancing crystal phase at the membrane, using an elapsed time for image collection of 60 seconds. The generated images were first subject to contrasting using open-source, machine-learning-based image analysis to identify and label the generated crystals with high resolution (Ilastik, GNU General Public License) (Berg et al., 2019). Contrasted images were then transformed into binary, 8-bit, black and white TIF images and uploaded into Image J (ImageJ software, NIH, US) to quantify surface coverage.

The final solutions containing the produced crystallise salts were filtered through a pre-weighted 0.45μm Whatman filter (Camlab Ltd., Cambridge, UK) and left to dry in a dessicator before measuring their final weight. Membrane samples were removed and dried over a dessicant before undergoing image analysis; Prior to drying the membrane, the membrane cell was isolated, and the residual mother liquor drained, to leave only the membrane and crystals found at the membrane. Crystals from the membrane and bulk were analysed using Scanning Electron Microscopy (SEM, VEGA3, Tescan, Czech Republic) and X-Ray Diffraction (XRD, Bruker, D5005, Germany). Experiments for each set of experimental conditions were replicated, and the data provided in the analysis represents the mean of the replicates for each set of conditions.

3.2.3 Heat and mass transfer characterisation

Vapour pressure difference (ΔP) is the driving force behind membrane distillation. This introduces flux (J) across the membrane (Tun et al., 2005):

$$J = C_m \Delta P \qquad (Eq.\ 3.5)$$

where C_m representing the membrane permeability of the membrane (m s^{-1}). The vapour pressure creates a convective flux through the membrane that leads to accumulation of solute, gradually declining the flux, as vapour pressure is reducing (Bhattacharjee, 2017). This accumulation introduces a diffusing flux of solute near the membrane surface opposite to the convective one. This balance is described as concentration polarisation coefficient (CPC) (Tun et al., 2005):

$$CPC = \frac{c_w}{c_b} = exp^{(\frac{J}{\rho K})} \qquad (Eq.\ 3.6)$$

c_w and c_b are the membrane wall and bulk concentration of the feed respectively. K is the solute mass transfer coefficient (m s^{-1}), that needs to be calculated first before CPC.

$$K = \frac{1.62\ D}{d_h}\left(\frac{V\ {d_h}^2}{0.146\ D}\right)^{0.33} \quad (Eq.\ 3.7)$$

where D is representing the diffusion coefficient ($m^2\ s^{-1}$) corrected for temperature, V is the velocity of the feed solution ($m\ s^{-1}$) and d_h the hydraulic diameter of the cell (m^2).

In addition to mass, heat is also conveyed through the membrane not only in convectively but also in conductively (Curcio and Drioli, 2005). This is quantified as temperature polarisation coefficient (TPC), that constitutes the extension of the heat transfer resistance as the ratio between the difference of the temperature on the two sides on the membrane as well as the difference on the two side of the bulk (Ali et al., 2013).

$$TPC = \frac{T_{fm} - T_{pm}}{T_f - T_p} \quad (Eq.\ 3.8)$$

where T_f and T_p are the bulk temperatures at the feed and permeate side respectively. T_{fm} and T_{pm} are the wall temperatures on the feed and permeate side of the membrane respectively. As these two temperatures cannot be measured experimentally, they have to be theoretically calculated through (Tun et al., 2005):

$$T_{fm} = T_f - (T_f - T_p)\left[\frac{1/h_f}{(1/(h_c+h_v))+(1/h_f)+(1/h_p)}\right] \quad (Eq.\ 3.9)$$

and

$$T_{pm} = T_p + (T_f - T_p)\left[\frac{1/h_p}{(1/(h_c+h_v))+(1/h_f)+(1/h_p)}\right] \quad (Eq.\ 3.10)$$

where h is the heat transfer coefficient ($W\ m^{-1}\ K^{-1}$). This coefficient can be calculated through:

$$h_v = \frac{J\ \Delta H_v}{\Delta T_m} \quad (Eq.\ 3.11)$$

$$h_c = \frac{k_m}{\delta} \quad (Eq.\ 3.12)$$

$$h_f = \frac{Nu\ k_f}{d_h} \quad (Eq.\ 3.13)$$

$$h_p = \frac{Nu\ k_p}{d_h} \quad (Eq.\ 3.14)$$

where k_m, k_f and k_p represent the themal conductivities of the membrane ($W\ m^{-1}\ K^{-1}$) for the membrane, feed and permeate solution respectively. N_u is the Nusselt number of the system that for laminar conditions is expressed as (Ali et al., 2013):

$$Nu = 0.13\ Re^{0.64} Pr^{0.38} \quad (Eq.\ 3.15)$$

where Re and Pr are the Reynolds and Prandtl number respectively. Through the CPC and TPC analysis, the real boundary layer and bulk solution supersaturation can be quantified separately and linked to the nucleation kinetics.

3.2.4 Nucleation kinetics characterisation

According to Mersmann (1990), the crystal-liquid interfacial energy for the aqueous salts can be calculated as:

$$\gamma = 0.414kT\left(\rho^S \frac{N_A}{M}\right)^{2/3} ln\left(\frac{c^S}{c^L}\right) \quad (Eq.\ 3.16)$$

where k constitutes the Boltzmann constant (J K^{-1}), T the solution temperature (K), ρ^S is density (kg m^{-3}), N_A is the Avogadro constant (l mol^{-1}), M the molar mass of the salt (kg $kmol^{-1}$) and finally c^S and c^L the molar concentration of the crystal and liquid respectively (mol m^{-3}). The differential Gibbs free energy between the system and the equilibrium state of the nucleus is the driving force of crystallisation. The work needed (W*) to achieve the critical size of the nucleus (n*) and onset the nucleation for a spherical nucleus can be derived from the condition dW/dn = 0 when n = n* (Roelands et al., 2006):

$$n^* = \frac{32\pi v_0^2 \gamma^3}{3(kT)^3 ln^3 S} \quad (Eq.\ 3.17)$$

$$W^* = \frac{16\pi v_0^2 \gamma^3}{3(kT)^2 ln^3 S} = 1/2\, n^* kT lnS \quad (Eq.\ 3.18)$$

where v_0 is the molecular volume, γ is the crystal – liquid interfacial energy, S saturation level where nucleation is induced.

In order to assess the nucleation kinetics, it is necessary to analyse the rate at which nucleation occurs in the system, which at the onset of nucleation (metastable limit) is the supersaturation rate (R'). By doing this action, the boundaries of the metastable zone width (MSZW) of the system can be established (Sangwal, 2021). According to Nývlt (1968), the maximum width of the metastable zone can be reached on the membrane surface. The width of the metastable zone is represented by ΔC_w (mg g^{-1} solution) and is correlated with the concentrating rate of the crystallisation.

$$\Delta C = \left(\frac{dC}{dT}\right)_T R' \quad (Eq.\ 3.19)$$

$$R' = \left(\frac{dC_o}{dt}\right)_t \quad (Eq.\ 3.20)$$

Integrating ΔC_w with the concentration rate R' the following equation arises (Jiang et al., 2016).

$$Ln(R') = \ln\left(\frac{F_p\, C_w}{m_0 - \int F_p.dT}\right) \quad (Eq.\ 3.21)$$

F_p representing the flow rate of the permeate at a time point (kg h^{-1}), m_0 is the mass of the feed solution during the onset of the experiment (kg), C_w is the solution concentration on the membrane surface and F_p,dT is the integral of the permeate flow on a specific time point (kg). Through characterising the MSZW the primary nucleation kinetics (B) of a system can be determined (Jiang et al., 2016):

$$B = Ae^{\left(-\frac{\Delta G^*}{kT}\right)} \quad (Eq.\ 3.22)$$

where A is the pre-exponentinal factor and ΔG* is the critical Gibbs free energy for nucleation (J). As the total volume of the reactor occupied by the nucleation phase is constantly changing, the volumetric hold-up is directly influencing the nucleation rate of the salt. For that, a constant pre-exponential factor is introduced in the Equation 3.22:

$$A = A_0 ø \quad (Eq.\ 3.23)$$

$$B_0 = A_0 ø e^{\left(-\frac{\Delta G^*}{kT}\right)} \quad (Eq.\ 3.24)$$

Using FBRM and digital microscopy, the induction time (t_{ind}) can be estimated for the bulk crystal phase and for scaling respectively. The induction time (t_{ind}) is a measurement of the metastability of the solution, as it represents the time taken to achieve nucleation (t_n) once the solution has reached a supersaturated state ($t_{c/c^*=1}$):

$$t_{ind} = t_n - t_{C/C^*=1} \quad (Eq.\ 3.25)$$

t_{ind} represents the inverse of the nucleation rate (t = 1/B) that in the case of homogeneous nucleation, the induction time based on classical nucleation theory (CNT) can be expressed by:

$$t_{ind} = \frac{1}{BV} \quad (Eq.\ 3.26)$$

where V represents the solution volume (m^3). The saturation level where crystallisation was induced was analysed based on the relative supersaturation:

$$S = \frac{C - C^*}{C^*} \quad (Eq.\ 3.27)$$

where C is the actual concentration of the solute in the solution (kg m^{-3}) and C* is the equilibrium solubility concentration of the solute at a specific temperature (kg m^{-3}).

3.3 Results and discussion

3.3.1 Determining mass and heat transfer processes for each aqueous salt

For each salt studied, the bulk temperature was set to 45°C, and a temperature difference (ΔT) of 15°C was used. To quantify the role of solubility-temperature dependency on nucleation kinetics, the flow rate across the membrane module was modified to alter temperature polarisation for each salt to within a comparable range. The TPC was modified by adjusting Reynolds (*Re*) number, which required slight modification between salts due to differences in solution viscosity and density (Table 3.1). Solubilities of potassium perchlorate ($KClO_4$), sodium sulphate (Na_2SO_4) and sodium chloride (NaCl) relative to the bulk temperature were 45, 366 and 477 g kg^{-1} respectively (Table 3.1). Mean water vapour fluxes of 8.7, 5.7 and 2.9 kg m^{-2} h^{-1} were recorded for $KClO_4$, Na_2SO_4 and NaCl respectively (Appendix Figure 3.A1). The vapour pressure difference across the membrane acts as the driving force for water transport, and as such the higher mean water vapour flux recorded for $KClO_4$ is due to the greater water vapour pressure difference due to the lower solubility of the salt. An increase in *Re* enhances mass and heat transfer processes across the membrane which leads to an increase in flux (Jikazana et al., 2023). However, due to the temperature and ΔT employed, the increase in water vapour flux with *Re* was within a relatively narrow range. A marked modification of temperature and concentration polarisation was observed following an increase in *Re*, which evidences a transition in boundary layer properties that are acknowledged to be important in defining nucleation rate (Jikazana et al., 2025).

Table 3.1 Physical properties of salt solutions.

Salt	MW (g mol^{-1})	Solubility (g kg^{-1})[a]	ΔSol. T^{-1} (% $°C^{-1}$)[b]	Density (g kg^{-1})[c]	Viscosity (N s m^{-2})[c]	Typical crystal morphology
$KClO_4$	138.55	45	4.32	1013	$6.55x10^{-4}$	Rhombohedral[d]
NaCl	58.44	366	0.10	1174	$1.03x10^{-3}$	Cubic
Na_2SO_4	142.04	477	-0.30	1336	$1.74x10^{-3}$	Orthorhombic

[a]At 45 °C. [b]Relative change in solubility following an increase in solution temperature of 1°C, within the range of 40-50°C; [c] [a]At 45 °C.[d]Rhombohedral or trigonal.

3.3.2 Scaling is dependent on supersaturation and solubility-temperature dependency

The concentrating rate (*R'*) describes how solution concentration, concentration polarisation and flux collectively inform on the nucleation kinetics of the system (Ouda et al., 2024). According to the theoretical approach of Nývlt (1968), the concentrating rate can be viewed as an analogy of the nucleation rate (Sangwal, 2009). This was estimated at the onset of nucleation for scaling in this study by determining the time at which the first crystal began to grow at the membrane (Figure 3.2a). A shorter induction time was achieved for higher concentrating rates which conforms with classical nucleation theory (CNT) where induction time is assumed to be inversely proportional to nucleation rate. The induction time is a

measurement of the metastability of a system, describing the lag time between the solution achieving saturation and the time at which a stable crystal phase is formed. The shortest induction time was determined for $KClO_4$ and indicated a greater sensitivity to modification of the concentrating rate by *Re* than the other two salts. Shorter induction times are generally coincident with higher supersaturation levels at induction. This was demonstrated in this study with $KClO_4$ which achieved the highest relative supersaturation at induction (Figure 3.2b). The crystal-liquid interfacial energy (γ) of an aqueous salt determines the minimum supersaturation requirement to overcome the critical Gibbs free energy barrier for nucleation (Mersmann and Kind, 1988). The estimated σ for $KClO_4$, NaCl and Na_2SO_4 are 33.7, 25.7 and 15.9 mJ m^{-2} respectively (Eq. 3.16). Accordingly, the work of formation was greater for $KClO_4$ (*W*/kT*, 18.1) which necessitates a higher level of supersaturation required to form a nucleus (Eq. 3.18). An increase in *Re* increased the TPC for each salt. This increased the boundary layer temperature, which reduced the relative supersaturation at induction due to the modification of the solution solubility limit (c*). The reduction was most evident for $KClO_4$ due to the steep solubility-temperature dependency of the salt (Table 3.1, Δc* 4.32% $°C^{-1}$). Jikazana et al. (2023) illustrated higher supersaturation levels could be achieved when increasing *Re*. The authors explained that supersaturation increases due to modifications within the boundary layer which increased flux; the increase in supersaturation (S = c/c*) within these conditions was therefore dominated by the modification of solute concentration (c). In this study, only small modifications to flux were observed due to the lower temperature and ΔT employed. Consequently, removing large modifications to mass transfer, heat transfer processes dominate the modification in supersaturation through adjustment of c* to provide a clearer observation of temperature polarisation in modulating scaling.

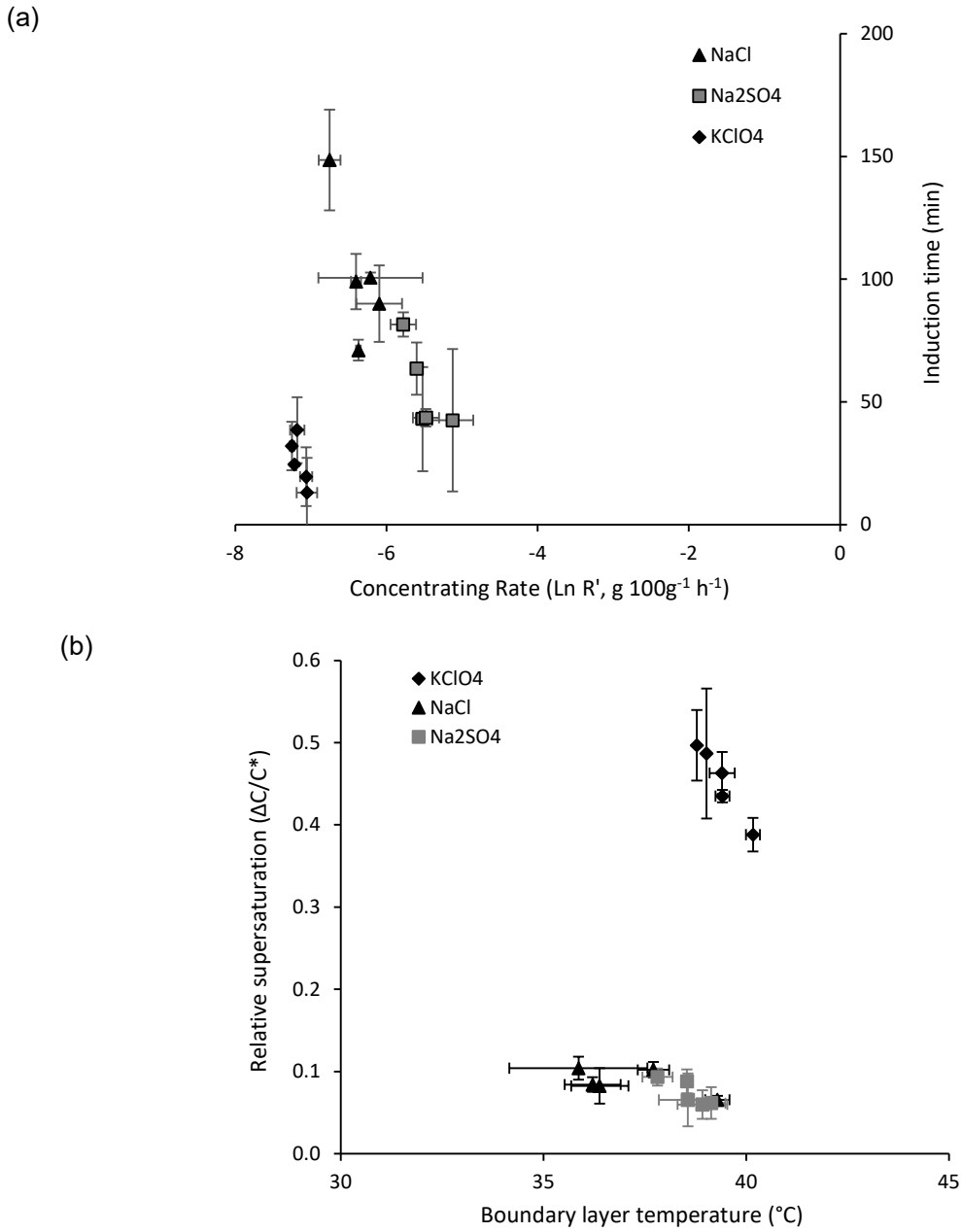

Figure 3.2 Demonstrating the effect of the (a) concentrating rate of each salt at scaling induction of each salt where even though the concentrating rate is kept relatively the same, there are big differences in induction time. This change is mainly promoted by (b) the difference in the boundary layer temperature, where the higher the temperature – solubility dependence, the higher the change in the relative supersaturation at scaling induction as the boundary layer temperature decreases.

Scaling can be characterised by two distinct mechanisms: (i) an initial period in which crystals nucleate, adhere and grow on the membrane; and (ii) a second period following the formation of crystals in the bulk solution in which crystals then deposit on the membrane. The initial period of scaling that precedes the formation of the bulk crystal phase was first characterised for each salt using imaging of the membrane surface (Figure 3.3). Scaling

occurred within the shortest time for $KClO_4$ and began earliest when TPC was at the lowest value (33 mins, TPC 0.33, Figure 3.3a). Once scaling commenced, the membrane surface was quickly covered by scaling, where this rate of coverage was primarily driven by the growth of crystals that had nucleated at the surface of the membrane (Figure 3.4). Even though, the number of initial crystals formulated on the onset of scaling, each crystal grew to a notable size. This happened because the mechanism for the growth of scaling was epitaxial. Epitaxial growth is a heterogeneous nucleation mechanism resulting into high oriented growth with similar lattice constant (Penha et al., 2021). This mechanism is becoming more intense with higher growth rates as the supersaturation gets higher. In this study, this was observed during the lower TPCs (0.33 – 0.45). High epitaxial fits were observed, where scaling promulgated across the membrane (reaching 55% surface coverage) which restricted water vapour flux and crystallisation was not observed in the bulk solution. At the highest TPC (0.48), crystallisation was observed in the bulk solution after 64 mins, following the lowest recorded surface coverage (1%) imposed by the initial phase of adhesive growth (Figure 3.3c). Sodium chloride scaling commenced around 100 minutes later than for $KClO_4$ which is ascribed to the difficulty in developing supersaturation for more soluble salts (characterised by lower γ) (Figure 3.3b).

(a)

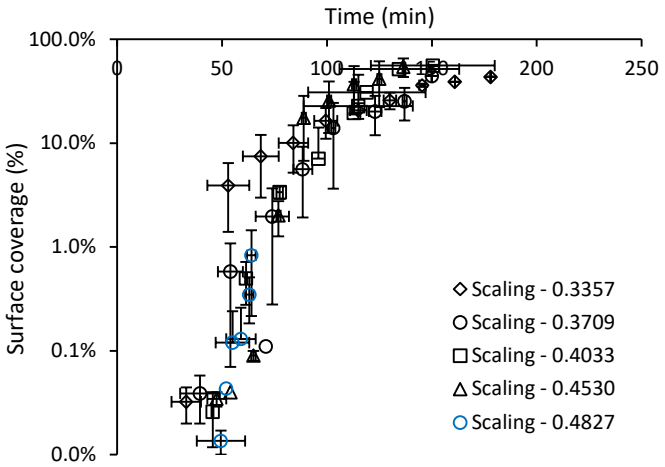

(b)

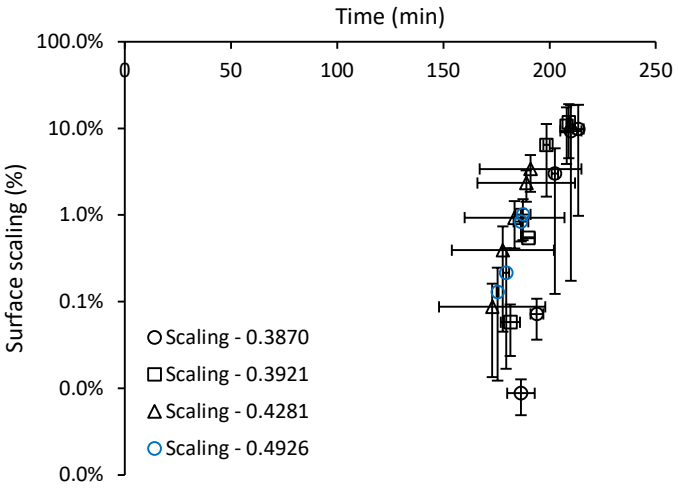

(c)

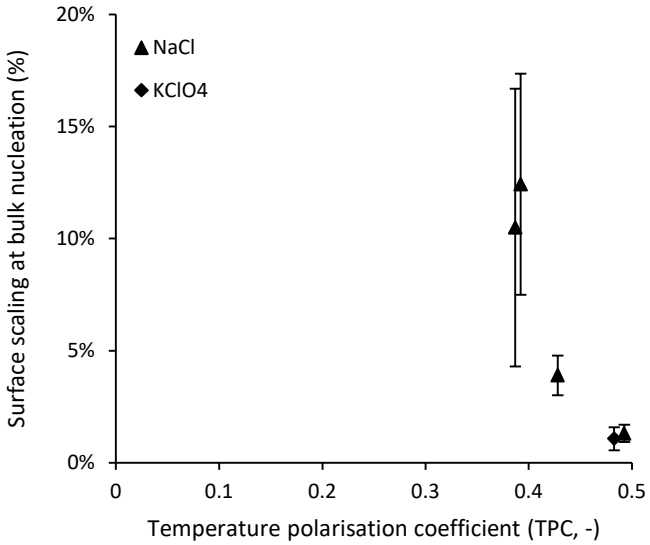

Figure 3.3 Quantifying the extent of scaling based on time for the different TPCs using the positive solubility-temperature dependence salt (α) $KClO_4$ and the almost neutral solubility-temperature dependence salt (b) NaCl. Direct observation also permits the differentiation between adhesive growth and deposition (c) for the different TPCs.

(a)

(b)

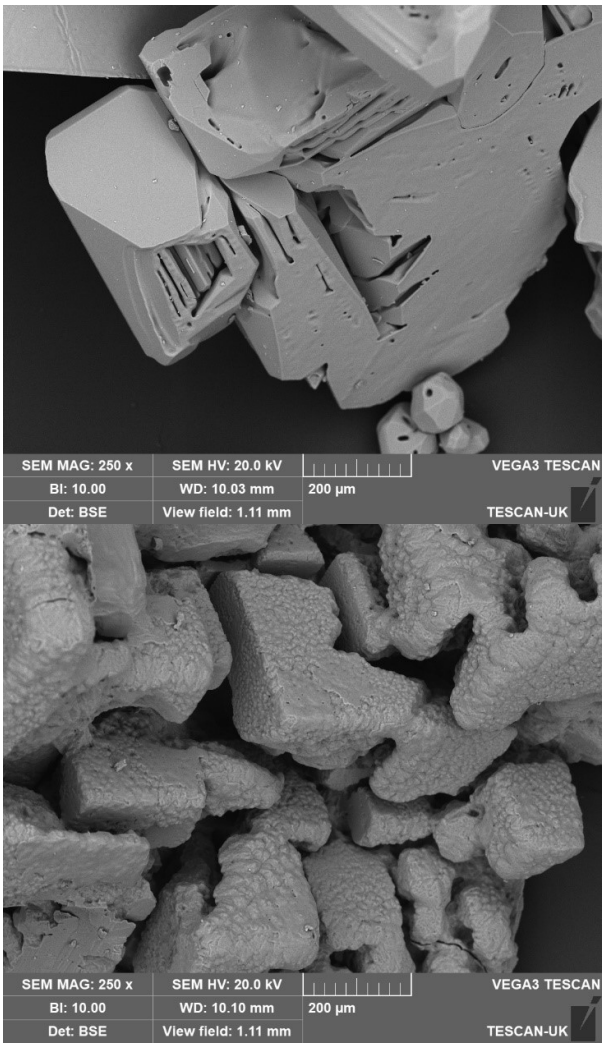

Figure 3.4 Characterisation of (a) $KClO_4$ and (b) NaCl scale formed using Scanning Electron Microscopy (SEM). In these pictures we can the epitaxial growth model is dominating the crystal growth of these crystals.

Crystallisation occurred in the bulk solution at each TPC, where a maximum surface coverage of 12.4% occurred prior to bulk nucleation. In the case of KClO4 a plate-like growth mechanism is observed (Figure 3.6b). Plate-like crystals with large {101} and {210} faces are common in low supersaturation KClO4 crystallisation and tend to grow with flat, often orthorhombic hexagonal or other multigonal faces and can stack together neatly, forming layers or sheets (Patel and Rao, 1977). The extent of scaling that preceded bulk nucleation (an adhesive growth mechanism) was dependent upon the TPC, where an increase in TPC mitigated scaling primarily through the modification of the temperature dependent solubility limit (Figure 3.3c). Consequently, while NaCl is characterised by a relatively flat solubility-temperature dependency, increasing the solubility limit of solution (c*) through adopting higher TPC can help to mitigate scaling. Such sensitivity to TPC is likely to be more observed for crystallising solutions such as NaCl which are characterised by lower γ, as these systems are

frequently limited to lower levels of supersaturation, which increases the probability for heterogeneous primary nucleation (Mersmann and Kind, 1988). In contrast to NaCl and $KClO_4$, no scaling was observed prior to bulk nucleation for Na_2SO_4. This can be accounted for by the negative solubility-temperature dependency of Na_2SO_4 within this prescribed temperature range, where the lower temperature at the membrane wall will increase the solubility limit of solution (Table 3.1). Consequently, there is a higher probability for nucleation to occur at some distance from the wall toward the bulk solution where the higher solution temperature will increase supersaturation by reducing c*. This is exacerbated for more soluble solutes that possess negative solubility-temperature dependencies since only low levels of supersaturation are established before nucleation proceeds (Figure 3.2b), meaning nucleation will be sensitive to only small changes in c*.

(a)

(b)

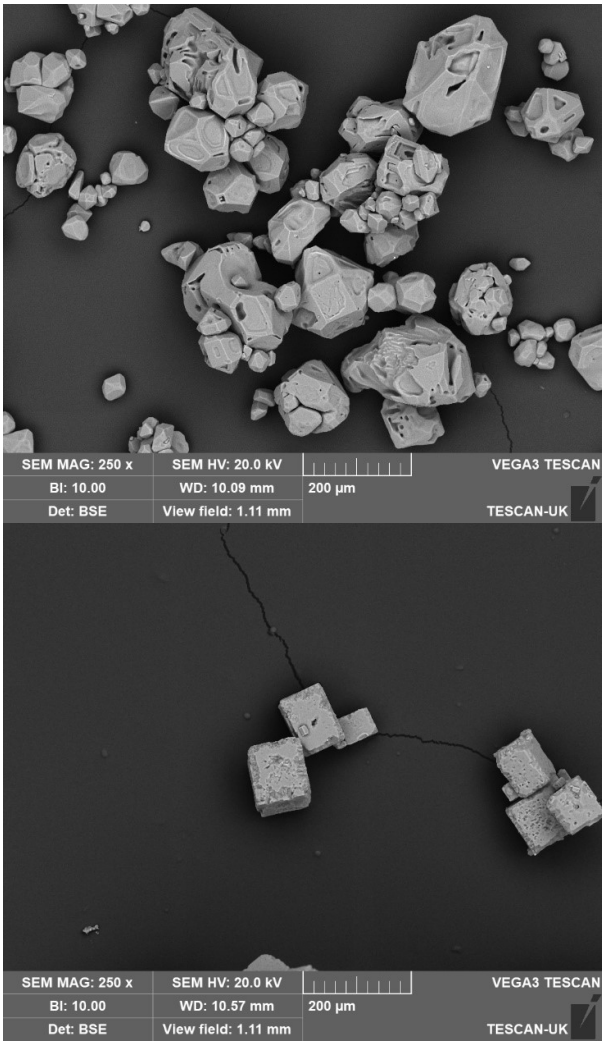

(c)

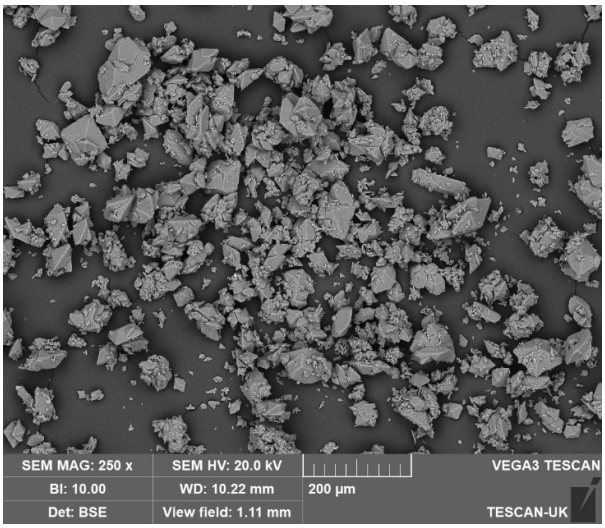

Figure 3.5 Close-up high-quality images of the generated bulk crystals (homogeneous nucleation) through the Scanning Electron Microscope method (SEM) for all the three salts used (a) $KClO_4$, (b) NaCl, (c) Na_2SO_4.

3.3.3 Boundary layer supersaturation determines primary nucleation kinetics in the bulk

The time at which the crystal phase formed within the bulk solution was characterised by FBRM (Figure 3.6). For $KClO_4$, a crystal phase was only detected in the bulk solution at the highest TPC (0.48). Shortly after nucleation was observed in the bulk solution, deposition was observed on the membrane (Figure 3.6a). Deposition occurred for each salt where a crystal phase was first formed in the bulk solution, including Na_2SO_4 which was not subject to an initial phase of scaling prior to bulk nucleation but once deposition began, the membrane surface was quickly covered with crystals. For NaCl and Na_2SO_4, a crystal phase was detected at each *Re* tested, which set TPC in the range 0.32-0.49. For both NaCl and Na_2SO_4, less time was required to reach nucleation in the bulk solution for conditions which coincided with a higher TPC. The primary data was used to estimate induction time and compare this with the induction time (t_{ind}) determined for scaling of the membrane. For each salt, an increase in *Re* reduced t_{ind} (Figure 3.6). For NaCl, bulk t_{ind} was consistently longer than for scaling, and as t_{ind} approached a minimum value at the maximum TPC (0.49), a smaller difference in the t_{ind} for scaling and the bulk crystal phase was observed, as evidenced by proximity to the parity line (x=y). This is comparable to $KClO_4$ where an increase in TPC reduced t_{ind} of scaling to a critical condition where the bulk crystal phase could be subsequently formed. The natural logarithm of induction time is inversely proportional to the square of natural logarithm of supersaturation (Jikazana et al., 2025). Therefore, achieving higher supersaturation at induction leads to a shorter t_{ind}. However, the supersaturation estimated within the boundary layer at induction for bulk crystallisation was within a relatively narrow range (Figure 3.7b), while the relative supersaturation at t_{ind} for scaling reduced with an increase in boundary layer temperature (Figure 3.8).

(a)

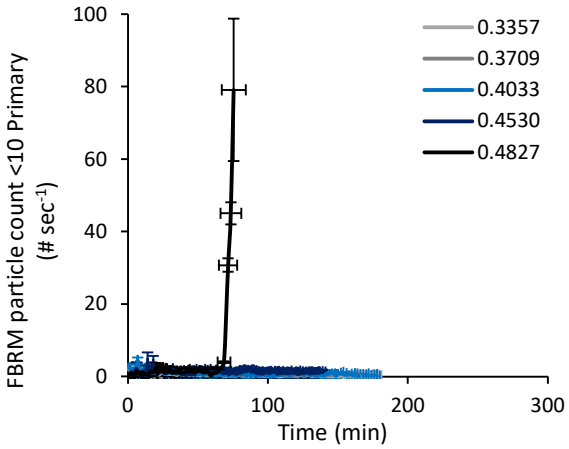

(b)

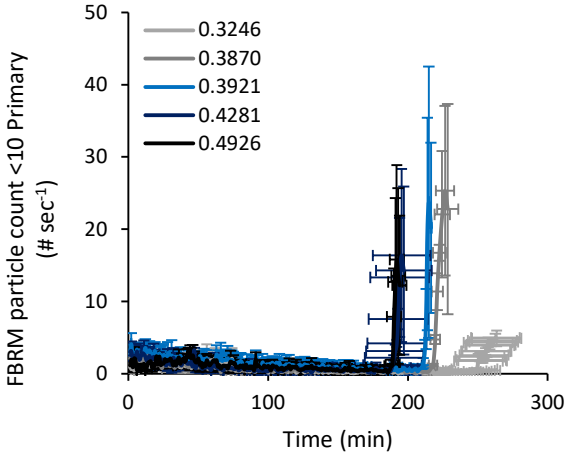

(c)

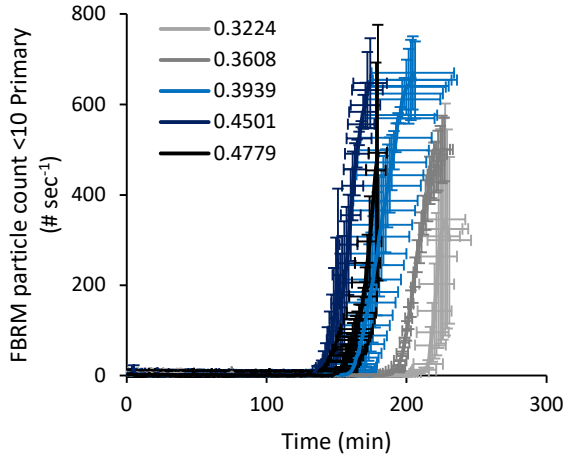

Figure 3.6 In-situ particle characterisation which determines the first point at which bulk (a) $KClO_4$, (b) NaCl, (c) Na_2SO_4 crystals are formed in the different TPCs (FBRM set to primary count (<10)) for sensitive direction of induction and nucleation rate.

(a)

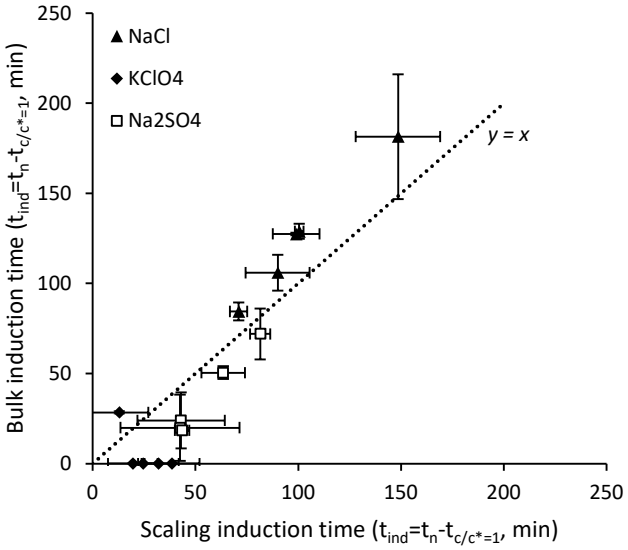

(b)

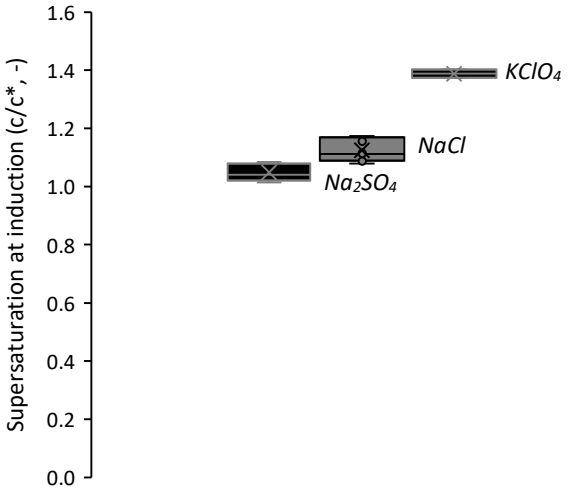

Figure 3.7 The differentiation between the tendencies of the heterogeneous and homogeneous salts and how they affect bulk and scaling induction time. As seen in (α) the heterogeneous salts are above y = x as scaling occurs first, while the opposite is happening for the homogeneous salts and (b) the effect of the different TPCs in the supersaturation during induction.

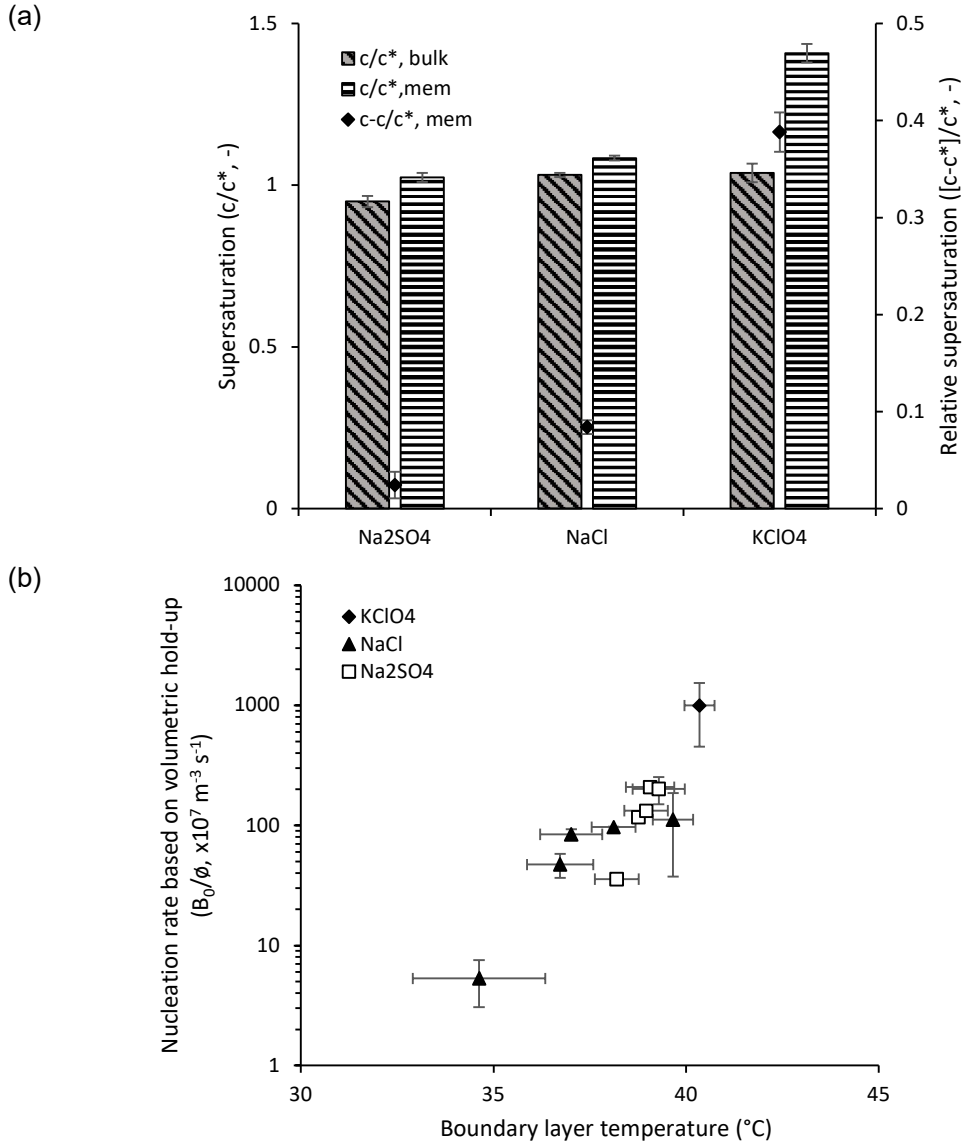

Figure 3.8 (a) Supersaturation and relative supersaturation at comparable TPC (Na_2SO_4, 0.48±0.001; NaCl, 0.49±0.001; $KClO_4$, 0.48±0.007); (b) comparison of nucleation rate normalised for volumetric holdup, where the increase in boundary layer temperature is due to the modification of Re.

The estimation of supersaturation is based on mass balance, where the local supersaturation consumed to initiate nucleation and subsequently the growth of scaling is presently difficult to quantify. Consequently, the role of the TPC is to mitigate scaling and liberate a greater quantity of local supersaturation available to initiate bulk crystallisation at a shorter induction time; the reduction in t_{ind} provides a shorter lag time between t_{ind} for scaling and for bulk crystallisation which also reduces the use of supersaturation for the growth of scaling. A similar trend in the reduction in t_{ind} was observed for Na_2SO_4 where adhesive scaling did not occur. This can be explained by the increase in boundary layer temperature, which reduced the c* to increase the supersaturation at $t_{ind.}$ At the highest TPC, the relative

supersaturation for Na_2SO_4 was just 0.02 (Figure 3.8a). Therefore, even a relatively small reduction in c* can modify supersaturation considerably, and the underlying theory illustrates how the sensitivity of induction time to changes in supersaturation is greater for lower levels of supersaturation. As supersaturation tended toward the lowest value for Na_2SO_4, the difference in t_{ind} when crystals were formed in the bulk (18.5 mins) to when deposition occurred (43.5 mins) reached a maximum (25 mins). This can be accounted for by the higher shear imposed at the greater *Re*, which provided sufficient shear-gradient (or lift) force to sustain crystals in the bulk solution for longer until they reached a critical size for settling.

Nucleation rate is inversely related to induction time (Yang and Florence, 2017) and was illustrated in this study through tracking particle number in real-time using FBRM, in which an increase in nucleation rate (based on volumetric hold-up) was determined for NaCl following an increase in *Re* (which was commensurate with a reduction in t_{ind}). This provides confirmatory evidence for how the mitigation of scaling can increase nucleation rate (and hence recovery) in the bulk solution by providing an increase in available local supersaturation. Due to the high solubility of NaCl, a long time is required to develop the supersaturation required to initiate nucleation. Visual observation of NaCl scaling (Appendix 3.B) can be characterised by a low number of crystals with a high growth rate, which is typical of crystallisation systems with low levels of supersaturation. Consequently, by shortening induction time through increasing boundary layer temperature, nucleation is limited but more critically, less time is provided for crystal growth, leaving more supersaturation available to initiate nucleation in the bulk solution. A small increase in nucleation rate was observed for Na_2SO_4 when exposed to higher TPC. This substantiates induction time observations, illustrating how the nucleation rate of aqueous salts with a negative solubility-temperature dependency are reliant on the solubility limit within the boundary layer to modify local supersaturation. As Na_2SO_4 is extremely soluble (low γ), the chemical potential that serves as the driving force for nucleation in the form of supersaturation is extremely limited (Eq. 3.18). The increase in boundary layer temperature due to a higher TPC may therefore also contribute to a reduction in the Gibbs free energy barrier for nucleation subsequently increasing nucleation rate *(W/kT)*. Nucleation rate was highest for $KClO_4$ which can be accounted for by the higher crystal-liquid interfacial energy which necessitates a greater supersaturation level to overcome the energy barrier for nucleation. This elevated supersaturation leads to greater nucleation rates in the bulk solution but can only occur by minimising the relative supersaturation in the boundary layer to restrict the high growth rates observed for scaling (Figure 3.8b) with salts characterised by a positive solubility-temperature dependency.

3.4 Conclusions

Through this study, the role of temperature polarisation in mediating nucleation kinetics in membrane distillation crystallisation has been established. Non-invasive techniques enabled the independent characterisation of key nucleation properties for scaling and the bulk crystal phase. This exposed an interdependent relationship between the two crystal systems when aqueous salts with a positive or 'flat' (slightly positive) solubility-temperature dependency were subject to a change in temperature polarisation. For both $KClO_4$ and NaCl, the desaturation of solution due to scaling at lower TPC either prevented or restricted bulk nucleation. For NaCl, desaturation can the ascribed to the extended induction time imposed by the low supersaturation, providing time for an extended period of growth. Whereas for $KClO_4$, the larger reduction in solubility limit introduced with a lower TPC enhanced supersaturation local to the membrane leading to high scaling rates. While scaling was found to be critically dependent upon the solubility limit, the crystal-liquid interfacial energy (γ) is also important in defining the supersaturation required to initiate nucleation, where aqueous salts comprising of higher γ will require higher supersaturation. Based on this study, less soluble salts ($\mathrm{higher}\ \gamma$) with a slightly positive solubility-temperature dependency will exhibit a shorter induction time and are likely to be less susceptible to scaling. The literature to date often assumes that nucleation occurs at the membrane, and once a critical crystal size is reached, the crystals are transported to the bulk solution. The evidence provided in this study emphasises how temperature polarisation can be used to mitigate scaling and increase nucleation rate in the bulk solution, therefore challenging the notion of a sequential process. This is exemplified for Na_2SO_4, where no scaling was observed prior to the formation of a crystal phase in the bulk solution due to the negative solubility-temperature dependency. A critical assumption underlying the principle of a sequential process is the role that the membrane is presumed to have in promoting heterogeneous nucleation. Due to its high solubility, sodium sulphate achieved the lowest supersaturation at induction which is most conducive to heterogeneous nucleation as the low supersaturation makes it a challenge to exceed the Gibbs free energy barrier for nucleation. However, no scaling was observed for Na_2SO_4, and scaling was similarly mitigated for NaCl and $KClO_4$ by restricting temperature polarisation. While the membrane may play a role in nucleation, results from this study imply that it is not necessary to form a crystal phase at the membrane to control membrane crystallisation, and the dominant factor controlling scaling is temperature polarisation and not heterogeneous nucleation as previously assumed. While scaling can be mitigated through controlling nucleation, further work is required to impede deposition, which is ubiquitous to all aqueous salts and is primary reason for the dissipation of flux experienced in membrane distillation crystallisation.

3.5 Acknowledgements

The authors are grateful to the European Research Council (ERC) for providing the funding for this research through StG grant 714080, ”Sustainable Chemical Alternatives for Reuse in the Circular Economy (SCARCE)”.

3.6 Appendices

3.6.1 Appendix A – Primary Flux data

(a)

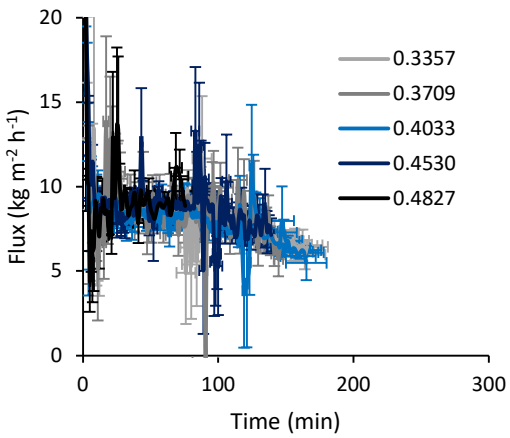

(b)

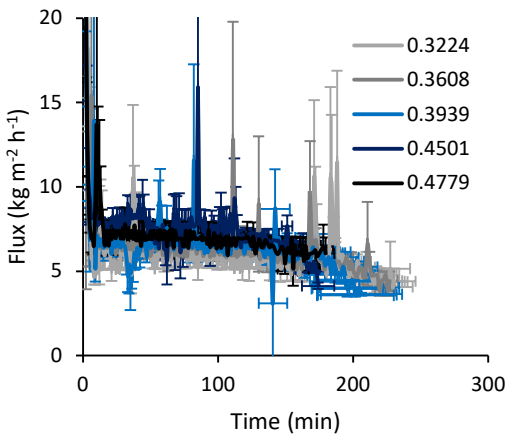

(c)

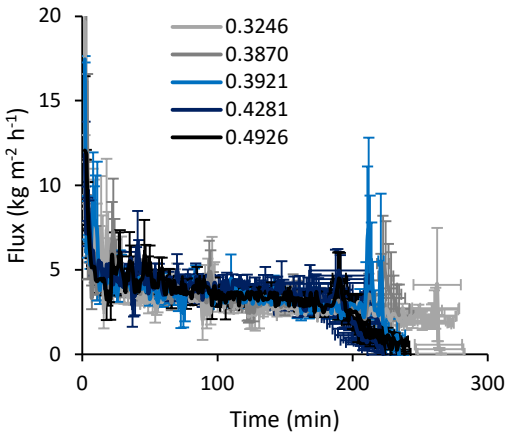

Figure 3.A1. Membrane distillation crystallisation data for all the different TPCs used over time: membrane flux data on (a) $KClO_4$, (b) Na_2SO_4, (c) NaCl

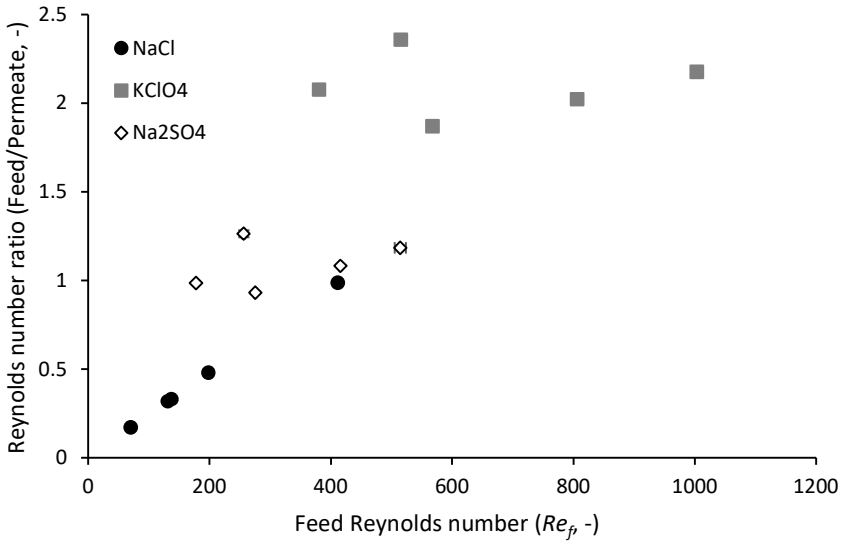

Figure 3.A 2. Reynolds number used to maintain similar CPCs during the experimental procedures.

Table 3.A 1. Reynold numbers and velocities of the duplicated experiments

Salt	Feed Re (-)	Feed Velocity (m s^{-1})	Permeate Re (-)	Permeate Velocity (m s^{-1})	Qf/Qp (-)
NaCl	70	0.0164	404	0.0879	0.17
	71	0.0166	416	0.0905	0.17
	131	0.0305	416	0.0905	0.31
	132	0.0309	409	0.0890	0.32
	139	0.0325	417	0.0909	0.33
	136	0.0319	413	0.0898	0.32
	196	0.0459	417	0.0909	0.47
	201	0.0471	409	0.0891	0.49
	409	0.0956	412	0.0896	0.99
	414	0.0968	421	0.0916	0.98
$KClO_4$	382	0.0659	183	0.0390	2.08
	380	0.0655	184	0.0392	2.06
	517	0.0891	219	0.0466	2.36
	514	0.0887	218	0.0465	2.35
	568	0.0979	303	0.0646	1.87
	567	0.0977	304	0.0648	1.86
	806	0.1390	401	0.0855	2.01
	806	0.1390	396	0.0844	2.03
	1053	0.1815	463	0.0986	2.27
	954	0.1646	459	0.0979	2.07
Na_2SO_4	179	0.0621	182	0.0396	0.98
	177	0.0615	179	0.0391	0.98
	258	0.0895	202	0.0440	1.27
	255	0.0887	204	0.0443	1.25
	277	0.0961	299	0.0651	0.92
	274	0.0952	293	0.0637	0.93
	415	0.1442	383	0.0834	1.08

	417	0.1449	386	0.0841	1.08
	508	0.1766	426	0.0928	1.19
	521	0.1812	443	0.0963	1.17

3.6.2 Appendix B – Primary Scaling Images

(a) (b)

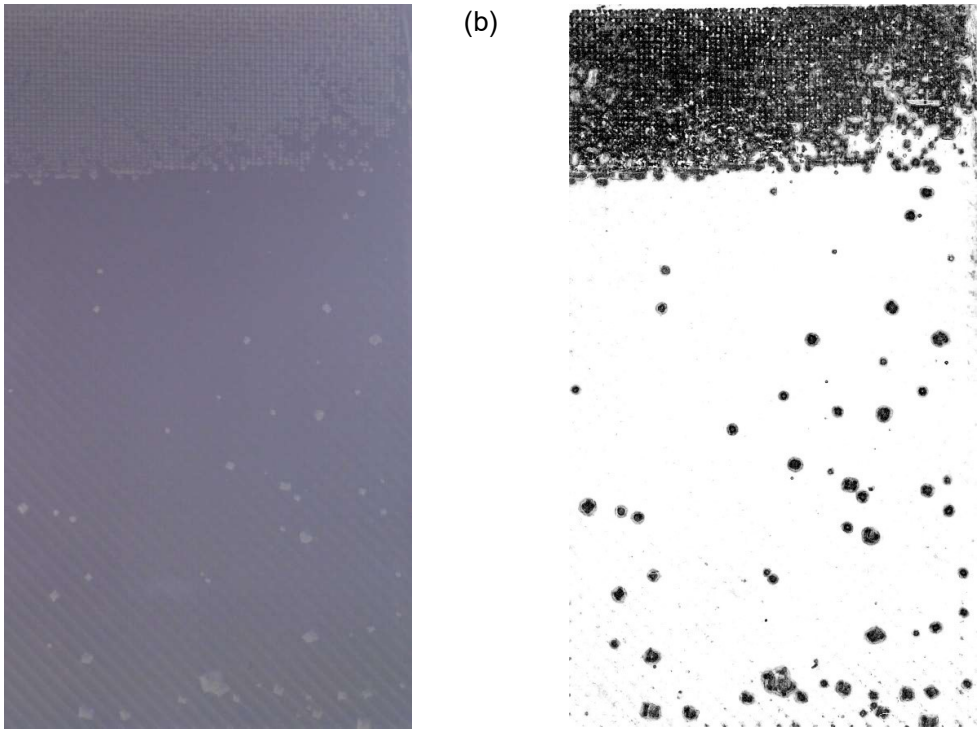

Figure 3.B1. (a) raw image captured at 218 minutes for NaCl; (b) processed image using contrasting to aid surface area quantification.

3.6.3 Appendix C – Characterisation of nucleation rate based on concentrating rate

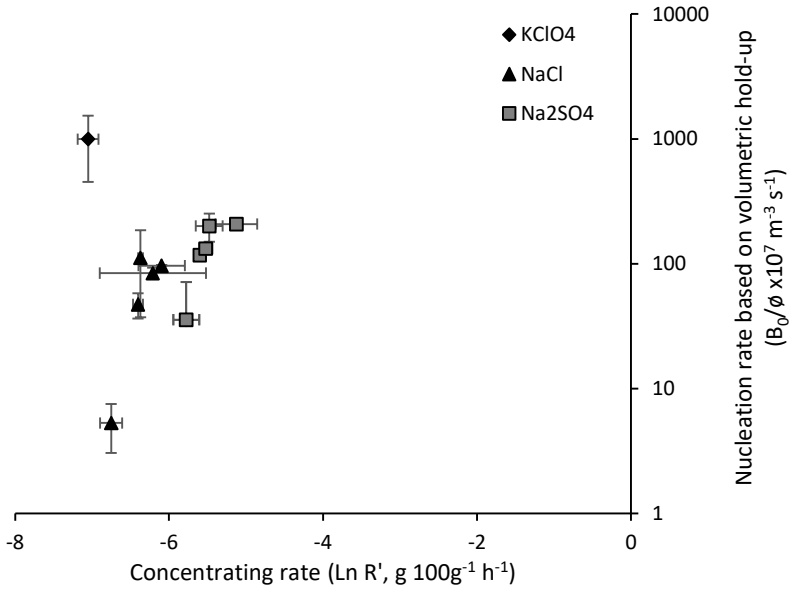

Figure 3.C1. Demonstrating the effect of the concentrating rate of the salts nucleation rate based on volumetric hold-up. The increase in the concentration rate pushes to higher supersaturation rates and as a result increasing the nucleation rate.

3.6.4 Appendix D – Comparison of crystal size distribution at equivalent residence times

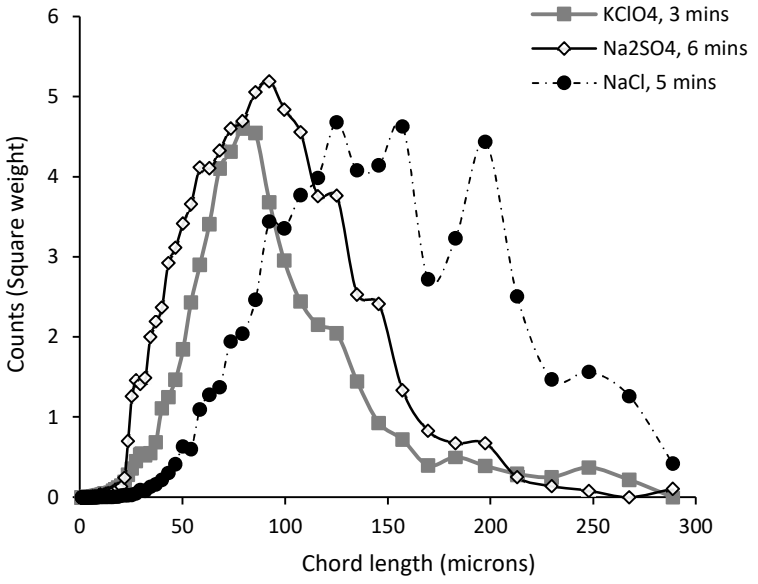

Figure 3.D1. Crystal size distributions measured for similar residence times (RT, 3-6 mins) when produced with an equivalent temperature polarisation coefficient (TPC: Na_2SO_4, 0.48±0.001; NaCl, 0.49±0.001; $KClO_4$, 0.48±0.007).

3.6.5 Appendix E – SEM characterisation of Na_2SO_4 deposited on the membrane

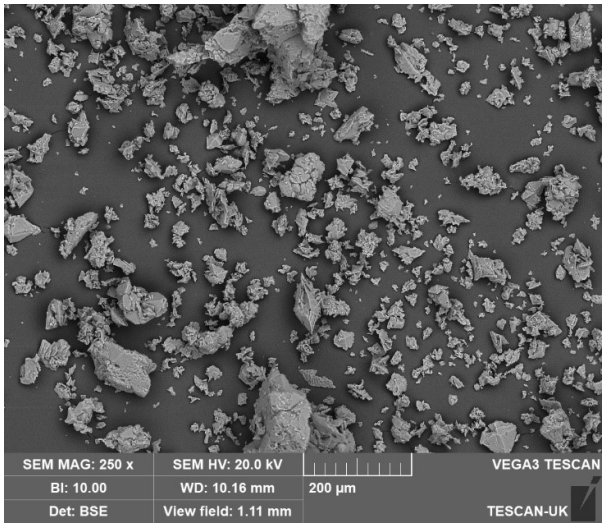

Figure 3.E1. Na_2SO_4 crystals observed on the membrane at the end of the experiment. Scaling was not observed for Na_2SO_4 during the experiments, until bulk nucleation was observed. After bulk nucleation, deposition occurs where crystals settle out of the crossflow onto the membrane. Consequently, the crystal population observed within this scanning electron microscopy (SEM) image of the membrane surface is characteristic of that formed within the bulk solution.

3.7 References

A. Ali, F. Macedonio, E. Drioli, S. Aljlil, O.A. Alharbi, Experimental and theoretical evaluation of temperature polarization phenomenon in direct contact membrane distillation, Chem. Eng. Res. Des. 91 (2013) 1966 – 1977.

A. Alkhudhiri, N. Darwish, N. Hilai, Membrane distillation: a comprehensive review, Desalination. 287 (2012) 2–18.

A. Anvari, A.A. Yancheshme, K.M. Kekre, A. Ronen, State-of-the-art methods for overcoming temperature polarization in membrane distillation process: A review, J. Membr. Sci. 616 (2020) 118413.

S. Bhattacharjee, Concentration polarization: Early theories, Water Planet Inc. 2017.

G. Chen, X. Yang, R. Wang, A.G. Fane, Performance enhancement and scaling control with gas bubbling in direct contact membrane distillation, Desalination. 308 (2013) 47–55.

T.C. Chen, C.D. Ho, H.M. Yeh, Theoretical modelling and experimental analysis of direct membrane distillation, J. Membr. Sci. 330 (2009) 279–287.

M.N. Chernysov, G. W. Meindersma, A. B. de Hann, Modelling temperature and salt concentration distribution in membrane distillation feed channel, Desalination. 157 (2003) 315 – 324.

S.J. Chipera, D.L. Bish, Fitting full X-Ray Diffraction patterns for quantitative analysis: A method for readily quantifying crystalline and disordered phases, Adv. Mat. Phy. Chem. 3 (2013) 47 – 53.

L. Eykens, K. De Sitter, C. Dotremont, L. Pinoy, B. Van Der Bruggen, How to optimize the membrane properties for membrane distillation: a review, Ind. Eng. Chem. Res. 55 (2016) 9333–9343.

A.R. Heath, P.D. Fawell, P.A. Bahri, J.D. Swift, Estimating average particle size by focused beam reflectance measurement, Part. Part. Syst. Charact. 19 (2002) 84-95.

E.M.V. Hoek, M. E., Cake-enhanced concentration polarization: a new fouling mechanism for salt-rejecting membranes, Environ. Sci. Technol. 37 (2003) 5581–5588.

K. Jevons, M. Awe, Economic benefits of membrane technology vs. evaporator, Desalination 250 (2010) 961–963.

X. Jiang, D. Lu, W. Xiao, X. Ruan, J. Fang, G. He, Membrane Assisted Cooling Crystallisation: Process Mode, Nucleation, Metastable Zone and Crystal Size Distribution, AlChe J. 62 (2016) 829–841.

A. Jikazana, P. Moreno Campo, E.J. McAdam (2023). Hydrodynamics (*Reynolds number*) determine scaling, nucleation and crystal growth kinetics in membrane distillation crystallisation, Journal of Membr. Sci. 685, 121909.

A. Jikazana, K. Le Corre Pidou, P. Campo Moreno, E.J. McAdam (2025), The role of mixing on the kinetics of nucleation and crystal growth in membrane crystallisation, Sep. Pur. Technol. 353, Part C, 128533.

S.S. Kadam, S.A. Kulkarni, R.C. Ribera, A.I. Stankiewicz, J.H. ter Horst, H.J.M. Kramer, A new view on the metastable zone width during cooling crystallisation, Chem. Eng. Sci. 72 (2012) 10–19.

A. Katsandri, A theoretical analysis of a spacer filled flat plate membrane distillation modules using CFD: Part I: velocity and shear stress analysis, Desalination. 408 (2017) 145–165.

J.W. Kim, J. Kim, K.-D. Lee, K.-K. Koo, Evaluation of nucleation rate by in-situ focused beam reflectance measurement in an unseeded batch cooling crystallisation, Crys. Res. Technol. 48 (2013) 1097–1105.

Z. Kuang, R. Long, Z. Liu, W. Liu, Analysis of temperature and concentration polarizations for performance improvement in direct contact membrane distillation, International Journal of Heat and Mass Transfer 145 (2019) 118724.

A.E. Lewis, M.M. Seckler, H. Kramer, G. van Rosmalen, Industrial crystallisation: Fundamentals and applications, University Printing House, Cambridge, 2015.

O.R. Lokare, P. Ji, S. Wadekar, G. Dutt, R.D. Vidic, Concentration polarization in membrane distillation: I. Development of a laser-based spectrophotometric method for in-situ characterization, J. Membr. Sci. 581 (2019) 462–471.

Y.M. Manawi, M.A.M.M. Khraisheh, A.K. Fard, F. Benyahia, S. Adham, A predictive model for the assessment od the temperature polarization effect in direct contact membrane distillation desalination of high salinity feed, Desalination. 341 (2015) 38–49.

L. Martinez-Diez, F.J. Florido-Diaz, M.I. Vazquez-Gonzalez, Study of polarization phenomena in membrane distillation of aqueous salt solutions, Sep. Sci. Technol., 35 (2000) 1485 – 1501.

L. Martinez-Diez, M.I. Vazquez-Gonzalez, Temperature and concentration polarization in membrane distillation of aqueous salt solutions, J. Membr. Sci. 156 (1999) 265 – 273.

A. Mersmann, M. Kind, Engineering Aspects of Precipitaion from Solution, Chem. Eng. Technol. 11 (1988) 264 – 276.

T. Mezher, H. Fath, Z. Abbas, A. Khaled, Techno-economic assessment and environmental impacts of desalination technologies, Desalination. 266 (2011) 263–273.

J.W. Mullin, Crystallisation, Butterworth-Heinemann, Oxford. 1997

Y. N. Nariyoshi, C.E. Pantoja, M.M Seckler, Evaluation of sodium chloride crystallisation in membrane distillation crystallisation applied to water desalination, Brazilian J. Chem. Eng. 33 (2016) 675 – 690.

L.N. Nthunya, M.F. Bopape, O.T. Mahlangu, B.B. Mamba, B. Van der Bruggen, C.A. Quist-Jensen, H. Richards, Fouling, performance and costa analysis of membrane-based water desalination technologies: A critical review, J. Env. Man. 301 (2022) 113922.

A. Ouda, Y. Bajón-Fernández, E. McAdam (2024). Methods to modify supersaturation rate in membrane distillation crystallisation: control of nucleation and crystal growth kinetics (including scaling), J. Membr. Sci. 691 122249.

C.E. Pantoja, Y.N. Nariyoshi, M.M. Seckler, Membrane distillation crystallisation applied to brine desalination: a hierarchical design procedure, Ind. Eng. Chem. Res. 55 (2015) 2776–2793.

A. R. Patel, A. V. Rao, Growth of single crystals of KClO4 in silica gels, J. Cryst. Growth. 38 (1977) 288 – 292.

F. M. Penha, F. R. D. Andrade, A. S. Lanzotti, P. F. Moreira Junior, G. P. Zago, M. M. Seckler, In Site Observation of Epitaial Growth during Evaporative Simultaneous Crystallisation from Aqueous Electrolytes in Droplets, Crystals. 11 (2021) 1122.

M. Rabie, M.F. Elkady, A.H. El-Shazly, Effect of channel height on the overall performance of direct contact membrane distillation, Appl. Therm. Eng. 196 (2021) 117262.

C.P.M. Roelands, J.H. ter Horst, H.J.M. Kramer, P.J. Jansens, Analysis of nucleation rate measurements in precipitation processes, Crys. Growth Des. 6 (2006) 1380 – 1392.

K. Sangwal, A novel self-consistent Nývlt-like equation for metastable zone width determined by the polythermal method, Cryst. Res. Technol. 44 (3) (2009) 231–247.

R.W. Schofield, A.G. Fane, C.J.D. Fell, R. Macoun, Factors affecting flux in membrane distillation, Des. 77 (1990) 279 – 294.

S. Srisurichan. R. Jiraratananon, A.G. Fane, Mass transfer mechanism and transport resistances in direct contact membrane distillation process, J. Membr. Sci. 277 (2006) 186–194.

J. Phattaranawik, R. Jiraratananon, A.G. Fane, Effect of pore size distribution and air flux on mass transport in direct contact membrane distillation, J. Membr. Sci. 215 (2003) 75–85.

Y. Taameh, K. Bataineh, Improving the performance of direct contact membrane distillation utilizing spacer-filled channel, Desalination. 408 (2017) 25–35.

P. Termpiyakul, R. Jiraratananon, S. Srisurichan, Heat and mass transfer characteristics of a direct contact membrane distillation process for desalination, Desalination. 177 (2005) 133–141.

G. Tosello, H.N. Hansen, F. Marinello, S. Gasparin, Replication and dimensional quality control of industrial nanoscale using calibrated AFM measurements and SEM image processing, CIRP Annals – Manufacturing Technology. 59 (2010) 563 – 568.

C.M. Tun, A.G. Fane, J.T. Matheickal, R. Sheikholeslami, Membrane distillation crystallisation of concentrated salts-flux and crystal formation, J. Membr. Sci. 257 (2005) 144–155.

K.Y. Wang, S.W. Foo, T.S. Chung, Mixed matrix PVDF hollow fiber membranes with nanoscale pores for desalination through direct contact membrane distillation, Ind. Eng. Chem. Res. 48 (2009) 4474–4483.

L. Wang, B. Li, Z. Gao, Q. Wang, J. Lu, Y, Wang, S. Wang, Study of membrane fouling in cross-flow vacuum membrane distillation, Sep. Pur. Technol. 122 (2014) 133 – 143.

A. Yadav, P.K. Labhasetwar, V.K. Shahi, Membrane distillation crystallisation technology for zero liquid discharge and resource recovery: Opportunities, challenges and futuristic perspectives, Sci. Tot. Environ. 806 (2022) 150692.

H. Yang, A. Florence, Relating induction time and metastable zone, Cryst. Eng. Comm. 19 (2017) 3966 – 3978.

J. Yorston, Why you should use SEM for quality control, Adv. Mat. 2021, Available at: <https://www.thermofisher.com/blog/materials/why-you-should-use-sem-for-quality-control-process/> [Accessed 10 November 2021].

4 Effect of the membrane material on the nucleation kinetics of crystallisation in membrane distillation crystallisation of sodium chloride

Effect of the membrane material on the nucleation kinetics of crystallisation in membrane distillation crystallisation of sodium chloride

K. Vasilakos, N. Thomas, M. Hermassi, P. Campo, E. McAdam[a]

Cranfield Water Science Institute, Cranfield University, Cranfield, MK43 0AL

[a]corresponding author: e.mcadam@cranfield.ac.uk

Abstract

Membrane distillation crystallisation (MDCr) is a novel emerging technology for the recovery of high value products from hypersaline brines. The core of the process is the hydrophobic membrane which separates a heated undersaturated solution from a cold draw solution. While the membrane prevents liquid intrusion, it allows vapour passing through its pores, oversaturating the heated solution. Furthermore, literatures proposes that the membrane plays a role on modifying the energy requirements for nucleation (ΔG_s) through its membrane material and properties like contact angle, surface roughness and porosity. While this can be true, these studies have not managed to decouple membrane material from their role in adjusting flux, which also kinetically controls the nucleation through induction time. At the same time an efficient technique for the measurement of the induction time has not been used, as in previous studies it has mostly been characterised by the rapid decline in water flux (Tun et al., 2005; Jiang et al., 2016; Tong et al., 2019) which is not ideal (Horseman et al., 2021). This leads to a poor cohesion between crystallisation theory and membrane distillation and as a result a poor understanding of the real effect of the membrane on crystallisation kinetics. Consequently, introducing a high-definition imaging for the precise characterisation of the induction time and using three different membranes (PP, PTFE, PVDF) with equivalent pore sizes, we seek to describe how transmembrane flux regulates the nucleation kinetics in MDCr when adjusting membrane material properties. As a result, in this study, the exact point of nucleation was determined and made possible to relate the boundary layer as being the exact site of nucleation. This is reinforced by the excess supersaturation within the boundary layer coupled with its correlation to the concentrating rate. Hence, it is the mass and heat transfer processes through concentration polarisation and temperature polarisation that sets the supersaturation that govern the nucleation in the boundary layer and not the membrane material.

Keywords: *membrane distillation crystallisation, scaling, membranes, nucleation kinetics, crystal growth, sodium chloride*

4.1 Introduction

Membrane distillation crystallisation can enhance product and resource recovery from hypersaline brines for a broad range of applications including desalination (zero liquid discharge) and the mining of high value materials (e.g. magnesium or lithium). The hydrophobic microporous membrane separates a heated undersaturated solvent on the retentate side of the membrane from a cold draw solution on the permeate side (Cui et al., 2018). As the hydrophobic membrane minimises liquid intrusion into the porous structure, the vapour pressure gradient established between the two solutions induces solvent evaporation of the feed solution through the gas-filled pores (Yadav et al., 2022). Since the interfacial area of the membranes is well defined, the pore structure provides numerous points for solvent removal. Membrane distillation therefore achieves precise regulation of the solvent evaporation rate, providing fine control over supersaturation at the membrane-solvent boundary (Phattaranawik et al., 2003; Curcio and Drioli, 2005; Chabanon et al., 2016). This is the key advantage of membrane distillation crystallisation over conventional crystallisers, where poor mixing restricts the regulation of supersaturation, which is the critical parameter for controlling nucleation rate, crystal size, size distribution and purity (Di Profio et al., 2010; Ruiz Salmon and Luis, 2017; Choi et al. 2019).

It has also been proposed that the membrane lowers the surface free energy requirement (ΔG_s) for nucleation, therefore requiring less supersaturation to induce crystallisation and at shorter induction times (Erdemir et al., 2019). This can be important for more complex solutes (e.g., proteins) or highly soluble salts (e.g., sodium chloride, NaCl) which are generally characterised by long induction times and low nucleation rates (Mersmann and Kind, 1988; Di Profio et al., 2010). The membrane contact angle is thought to enhance solute-membrane interactions, reducing the interfacial energy below that of the crystal-liquid system. This enhanced attraction has also been suggested to improve molecular orientation, therefore increasing the probability for molecular aggregation (Curcio and Drioli, 2005). Modification of ΔG_s through membrane properties is generally described as a heterogeneous primary nucleation mechanism. While a conceivable advantage to controlling nucleation kinetics, such intimate interaction between the crystallising solute and the membrane can lead to scaling. Polytetrafluoroethylene (PTFE), polypropylene (PP) and polyvinyldifluoride (PVDF) are commonly used materials for membrane distillation (Curcio et al., 2006). Several studies have indicated PVDF to be more susceptible to scaling, which may relate to the lower material contact angle which could contribute to a greater reduction in the critical free energy requirement for nucleation (Karanikola et a., 2018). It has also been proposed that irregular surface topography may be responsible for promoting heterogeneous nucleation (Di Profio et al., 2010) where cavity structure (Ali et al., 2015), surface roughness (Choi et al., 2019) and

pore structure (Mcleod et al., 2015; Bavarella et al., 2022) can induce solute entrapment, introducing local regions of supersaturation, with a higher probability for nucleation than flat surfaces (Di Profio et al., 2010).

While material properties may contribute to the onset of scaling in membrane distillation (Cui et al., 2018), these factors cannot be easily decoupled from their role in adjusting flux. For example, a change in pore size, porosity, thermal conductivity or contact angle will likely modify transmembrane flux for membranes exposed to the same driving force (Curcio et al., 2006). Transmembrane flux determines the rate at which supersaturation is achieved in the system (the concentrating rate '*R*'). A faster transition across the supersaturated metastable zone will lead to a higher supersaturation level at induction (the onset of nucleation), and a shorter induction time. It is the level of supersaturation at induction that defines the kinetics of nucleation and crystal growth (Ulrich & Strege, 2002). For a defined salt with a fixed crystal-liquid interfacial energy (e.g. NaCl), the surface free energy (ΔG_s) is fixed (Figure 4.1a) while the increase in supersaturation will increase the volume free energy (ΔG_v) (Figure 4.1b) sufficient to lower the critical Gibbs free energy requirement for nucleation (Figure 4.1c). Nucleation can therefore be kinetically controlled through regulating supersaturation with water vapour flux by using modifications to the membrane or the transmembrane temperature difference (ΔT). By raising the supersaturation level at induction, a labile region of the metastable zone width can be entered into where homogeneous primary nucleation is favoured. In principle, this should mitigate scaling as nucleation can occur without requiring a heterogeneous substrate to be present, and as such crystallisation is more likely to proceed in the bulk solution, independent of the membrane. While this strategy reflects the principles set out in classical nucleation theory (CNT), various authors have cited significant scaling at higher transmembrane fluxes, leading to adoption of more conservative operating conditions within MDCr (e.g. lower ΔT) (Tun et al. 2005; Liu et al., 2020).

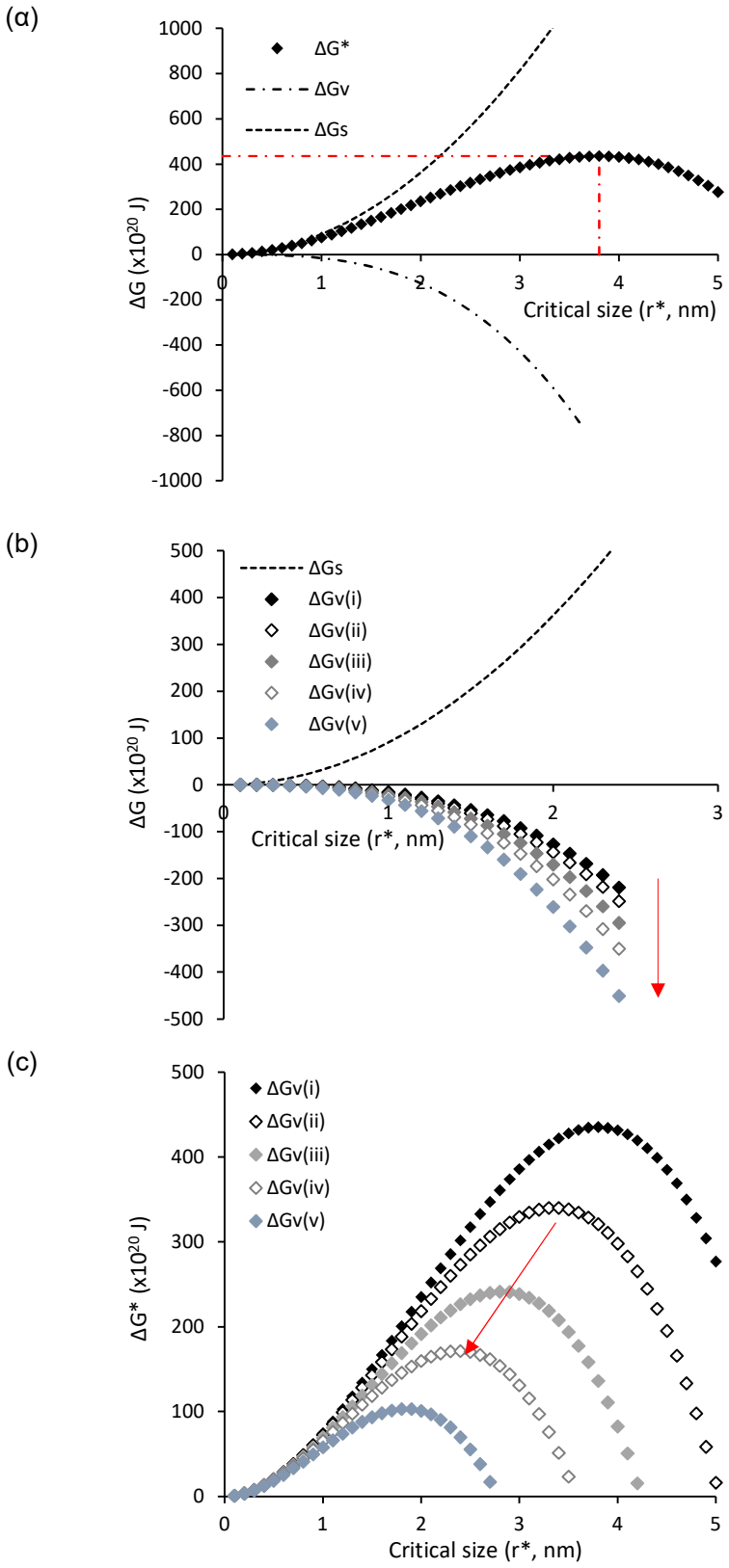

Figure 4.1 Kinetically controlled nucleation can reduce the free energy barrier by adjusting supersaturation.

We propose the poor cohesion between crystallisation theory and membrane distillation literature arises from the paucity of data describing the onset of nucleation in MDCr from which the induction time (a characteristic measurement of metastability, t_{ind}) and metastable zone width (supersaturation driving force, $\Delta C_{,fm}$) can be derived. Without such data, it is not possible to determine how modifications to transmembrane flux by material properties or vapour pressure difference (ΔT) are modifying the kinetics of nucleation in MDCr. The few studies that have characterised induction time, rely on the onset of a rapid decline in water flux as an indirect measurement with which to infer the onset of nucleation (Tun et al., 2005; Jiang et al., 2016; Tong et al., 2019). However, it has been argued that the onset of flux decline and nucleation are phenomenologically distinct, making this a poor surrogate for determining the onset of nucleation (Horseman et al., 2021). Elucidation of the nucleation process is made more complicated by the presence of two induction times within MDCr where primary heterogeneous nucleation (and hence scaling) may occur at the membrane, while a crystal phase is ideally produced under controlled conditions in the bulk solution to form the final crystal product. These mechanisms have been proposed to occur concurrently, sequentially, and independently (Horseman et al., 2021, Jikazana et al., 2023). The deposition of crystals onto the membrane, after formation in the bulk solution, has also been indirectly interpreted as scaling. With no definitive characterisation of the role of these discrete nucleation mechanisms, it is difficult to provide a foundation on which to adequately describe crystallisation within MDCr.

In this study, we therefore propose to describe how transmembrane flux regulates the nucleation kinetics within MDCr when adjusting membrane material properties. Three materials were therefore selected (PP, PTFE and PVDF) of equivalent pore size but offering differences in porosity and thermal conductivity to alter heat and mass transfer characteristics. The membranes also comprised a range of surface roughness and contact angles and were complemented with operation across a range of temperature differences to ascertain the significance of these characteristics to initiating heterogeneous primary nucleation in MDCr when crystallisation is kinetically controlled. Back-scatter and high-definition camera techniques are used *in-situ* to determine the onset of nucleation in the bulk solution and at the membrane respectively therefore enabling discrimination of nucleation mechanisms. This permits amongst the first in-depth characterisations of induction time and metastable zone width, which will be used to construct an analytical framework that can relate nucleation rate to supersaturation. This framework is intended to describe how nucleation kinetics are modified by transmembrane flux, the outcome of which is to foster greater control over crystallisation within MDCr, which includes the mitigation of scaling.

4.2 Materials and methods

4.2.1 Experimental setup

The direct contact membrane distillation system comprised an acrylic cross-flow cell (Model Products, Bedford, UK) with channel dimensions of 0.1x0.04m (LxW) and a hold-up volume of $2x10^{-5}$ m^3 (Figure 4.2). The active membrane area was 0.0004 m^2. The three membrane materials used were PTFE (Membrane Solutions, Auburn, USA), PVDF (Cobetter Filtration, Hangzhou, China) and PP (Sterlitech, Washington, USA). The membranes were selected based on their comparable pore sizes (0.1 μm) while providing differences in porosity, thermal conductivity, surface roughness and contact angle (Table 4.1). A 90% saturated feed solution was prepared by adding NaCl crystalline powder (99+% Alfa Aesar, Lancashire, UK) to ultrapure water (15MΩ cm). After completely dissolving the NaCl, the solution was filtered using a 0.45μm Whatman filter (Camlab Ltd., Cambridge, UK) to remove any impurities. The feed solution was introduced into the cell at a flow rate of 1663±20 mL min^{-1} (Masterflex L/S pump, Cole Palmer, UK), while the permeate flow rate was 1030±24 mL min^{-1} (323, Watson Marlow, UK). The feed side temperature was maintained at approximately 55°C (54.77±0.37) using a heater/chiller assembly (Ministat 230, Huber, UK). Temperature differences of between 15 and 30°C were introduced by adjusting the permeate temperature (ΔT). The temperatures were measured at the inlet and outlet of the cell (T7-Pro, LabJack, USA). Permeate volume was measured with a precision balance (Symmetry PR 410, Cole-Palmer, UK).

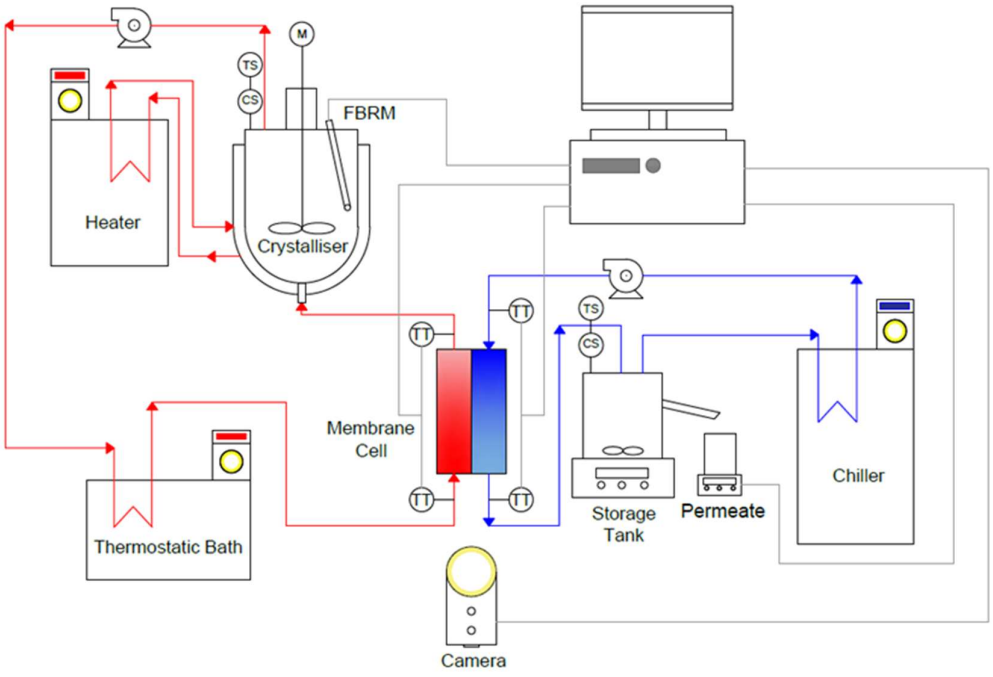

Figure 4.2 Experimental set-up.

Table 4.1 Characterisation of membrane properties.

Membrane	Mean pore size (μm)[a]	Surface porosity (%)[a]	R_a (nm)	RMS (nm)	Membrane thickness (mm)[b]	Contact Angle (°)[c]	Thermal conductivity (W m^{-2} K^{-1})	Heat transfer coefficient (h_c) (W m^{-2} K^{-1})
PTFE	0.30 ± 0.02	9.27 ± 0.6	119	147	0.050 ± 0.005	142.3 ± 0.9	0.055	1010.3
PP	0.31 ± 0.02	5.76 ± 0.3	134	173	0.100 ± 0.010	134.6 ± 0.5	0.070	701.5
PVDF	0.33 ± 0.01	7.09 ± 0.6	45	60.2	0.160 ± 0.010	120.7 ± 0.5	0.075	470.6

[a]Measured by POROMETER using Capillary Flow Porometry (Porolux 1000). These values are taken from the most constricted part of the pore so the selective layer, which have in general lower values than the overall porosity (Agarwal et al., 2022). [b]Given by the manufacturer. [c]Measured with water. R_a - Arithmetic average of profile height deviation (roughness); RMS – Root mean square average of profile height deviation from the mean line (roughness).

4.2.2 Analytical methods

Induction time in the bulk solution was determined using an inline focused beam reflectance measurement (FBRM) (ParticleTrack G400, Mettler Toledo, UK) which uses the backscatter of light from a rotating laser sited within a probe to permit the counting and sizing of crystals in real time (Heath et al., 2002). As the FBRM has a fixed narrow depth of measurement, the position of the FBRM plays a critical role to the measurements taken. Positioned with a 60° incline in the reactor for maximum efficiency, the FBRM probe emits a laser beam in the wavelength of 780nm and a velocity of 2 m s^{-1}. The laser beam, traverses across the reactor and intersects and backscatters when meeting the produced scattered salts within a size range of 0.5 to 2000μm. The duration of this backscattered beam is then translated and corrected by the FBRM software to chord lengths in order to produce a chord length distribution (CLD). The progressive number of the CLD measurements is obtained in total counts s^{-1} (Kim et al., 2013).

$$total\ counts\ s^{-1} = \sum_{i=1}^{Ch} N_{Ch,i} \qquad (Eq.\ 4.1)$$

where C_h is the number of channels in FBRM and $N_{Ch,I}$ is the number of counts measured in an i^{th} channel. The primary nucleation kicks in, the total counts s^{-1} swiftly increase providing an accurate way to determine the induction time in the bulk solution. Using the volumetric depth of measurement of the FBRM, these total counts can also be transformed into the volumetric nucleation rate (B, m^{-3} s^{-1}):

$$V = S_p W_l D_p \qquad (Eq.\ 4.2)$$

where S_p is scan speed of the laser (2 m s^{-1}), W_l is the laser diameter at the focal point (5.8×10^{-6} m) and D_p the laser penetration depth in solution (2×10^{-4} m), providing a scanning volume of 2.32×10^{-9} m^3 s^{-1} (Mitchell et al., 2011). The mode used to determine the induction time was the 'primary' selection view. This mode has a narrower measurement zone with a fine edge discrimination and provides enhanced sensitivity to primary particles and facets. The difference in particle count over time determines the nucleation rate of the experiment:

$$B_i = \frac{(N_{c,i} - N_{c,i-1})}{t_i - t_{i-1}} \qquad (Eq.\ 4.3)$$

where t_i is the time of the measurements (s) and B_i is the nucleation rate (# m^{-3} s^{-1}) of two consecutive measurements. As the N_c of the experiment was increasing, the individual nucleation rates calculated from these measurements were used in order to calculate the average nucleation rate (B) of the experiment.

To determine crystal size distributions from CLD, the mode used is the 'macro' selection view. This mode has a wider measurement zone than primary view with a macro edge discrimination for agglomerates and crystals that is less sensitive to surfaces and facets (Heath et al., 2002):

$$N_{i,n} = N_{i,o} C_{i,A}^{n} \quad (Eq.\ 4.4)$$

where $N_{i,n}$ is the number of n-weighted chord counts in the i^{th} channel ($\mu m^n\ s^{-1}$), $N_{i,o}$ is the raw unweighted chord count in the i^{th} channel (s^{-1}) and $C_{i,A}$ is the geometric average length of the i^{th} channel (μm), which is a product of the upper and lower boundary lengths of the i^{th} channel (μm) ($C_{i,u}$ x $C_{i,l}$)$^{1/2}$. A square weighted (n = 2) chord distribution has been used which emphasizes more in the coarse end of the distribution, we get a more accurate representation of the crystal size, since the square-weighting is effectively a cube (volume) weighting, comparable to the volume-based distribution techniques (Heath et al., 2002).

After each experiment, the probe was cleaned using distilled water and a microfibre cloth to remove the remnant salts. The efficacy of the cleaning was evidenced once the background response (total counts s^{-1}) approached zero.

The crossflow cell was engineered from highly polished Perspex through which a UHM350 digital microscope (UHM350, AmScope, UK). The digital microscope was placed 145mm away from the cell, focused on the feed side of the membrane. capturing images in order to characterise and identify the onset of nucleation at the membrane. In analogy to the backscatter technique, this method is able to identify the formation of the first crystal phase to determine induction time (Jikazana et al., 2023). This method makes use of high definition imaging techniques to track the nucleation and the growth of the crystals first observed on the membrane, as well as their extension of the surface coverage. To make this possible, a digital microscope with specific features was selected. These features include a wide-angle high-resolution lens (1920px1080p – 2.1MP), coupled with long working distance and an extensive magnification range (x20 – 100). Despite the definition is not high enough to determine the actual time of nucleation (nano crystals), the crystal growth is high enough to compensate and allow real-time examination similar to the backscatter techniques (Ouda et al., 2023). The generated salts from the captured images are identified through ilastik software (ilastik, GNU General Public License) and quantified its surface coverage (ImageJ software, NIH, US).

Induction time (t_{ind}) provides a measure of the metastability of solution at the onset of nucleation and can be determined by measuring the difference in time from the point at which the solution achieved saturation ($t_{C\,C^{*-1}} = 1$) to the time at which nucleation first commences (t_n):

$$t_{ind} = t_n - t_{C\,C^{*-1}} \quad (Eq.\ 4.5)$$

Induction time (t_{ind}) is usually expressed as the inverse of the rate of nucleation ($t = 1/B$). In the case of true homogeneous nucleation, and based on classical nucleation theory, the induction time can be given by:

$$t_{ind} = e^{\frac{16\pi\emptyset\gamma_i^3 v^2}{3k^3T^3LnS^2}}$$ (*Eq. 4.6*)

where the critical difference is ø which represents the extent to which the crystal-liquid surface free energy (γ, J mol^{-1}) is reduced by the present of a heterogeneous substrate and the induction time is increasing with the increase of the free energy or the molecular volume (v, m^3 mol^{-1}). Similarly, the induction time is decreasing when the saturation level is increasing (S, C C*$^{-1}$). Consequently, these complementary systems can be used to discriminate between primary nucleation fostered by the membrane (digital imaging) and the bulk solution (FBRM) enabling differentiation between scaling and deposition. Images were taken every 60s to examine the evolution of crystal growth at the membrane. Images were first contrasted (transformed into binary, 8-bit, black and white TIF images) using ilastik software. Ilastik is an open-source, machine-learning-based image analysis software that can easily segment, classify, track and count experimental data with high efficacy (Berg et al., 2019). These identified crystals were then transformed into binary black and white images and quantified its surface coverage through ImageJ software. All experiments were replicated, and the average of these replicates are presented in the analyses. Crystals were separated from solution for further analysis by filtering through a pre-weighed 0.45μm Whatman filter (Camlab Ltd., Cambridge, UK). The membrane was removed from the cell and kept separate from the bulk crystals.

Crystal samples from the bulk and membrane were independently subject to X- Ray Diffraction (XRD, Bruker, D5005, Germany) to confirm their crystallinity and Scanning Electron Microscopy Scanning Electron Microscopy (SEM, VEGA3, Tescan, Czech Republic) to examine their crystal habit. X-rays are widely used in crystallography to characterise crystals, by examining their atoms positioning and spacing (Ali et al., 2022). Additionally, SEM is a robust and analytical imaging technique that can identify and quantify crystals in nanometer scale (Ali et al., 2023). Both these techniques are extensively used in multiple industries ranging from aerospace to pharmaceutical industry.

For the examination of the membranes, AFM (Atomic Force Microscopy, Bruker, AFM D3100, Germany) was used to measure membrane surface roughness. AFM is a powerful high-resolution imaging platform for the mapping of mechanical, thermodynamic and other properties of structures with high precision (Dufrene, et al., 2017). Static contact angle measurements were performed on each membrane with a goniometer (OCA 25, DataPhysics Instruments GmbH, Stuttgart, Germany).

4.2.3 Characterisation of heat and mass transfer

The driving force for membrane distillation is the vapour pressure difference, that introduces a flux (J) across the membrane (Tun et al., 2005):

$$J = C_m \Delta P \quad (Eq.\ 4.7)$$

Where ΔP (Pa) is the vapour pressure difference created between the two sides of the membrane and C_m is the membrane permeability of the membrane used in the system (m s^{-1}). This produces a convective solute flux towards the membrane. This leads to the accumulation of solute which reduces vapour pressure causing a gradual flux decline (Bhattacharjee, 2017). The accumulated solute at the membrane introduces an opposing diffusive flux of solute near the membrane surface, the balance of which is described by the concentration polarisation coefficient (CPC) (Tun et al., 2005):

$$CPC = \frac{c_w}{c_b} = exp^{(\frac{J}{\rho K})} \quad (Eq.\ 4.8)$$

where c_w and c_b are the feed concentration at the membrane wall and bulk respectively. To calculate the CPC, the solute mass transfer coefficient (m s^{-1}) must first be obtained:

$$K = \frac{1.62\ D}{d_h}(\frac{V\ {d_h}^2}{0.146\ D})^{0.33} \quad (Eq.\ 4.9)$$

where D is the diffusion coefficient (corrected for temperature) (m^2 s^{-1}), d_h is the hydraulic diameter of the cell (m^2) and V is the velocity of the feed solution (m s^{-1}).

Heat is also transferred across the membrane in the conductive and convective forms (Curcio and Drioli, 2005). This institutes temperature polarisation coefficient (TPC) which quantifies the extent of the heat transfer resistance, as the ratio between the difference of the temperature on the two sides on the membrane, and the difference of the temperatures of the two sides on the bulk (Ali et al., 2013):

$$TPC = \frac{T_{fm} - T_{pm}}{T_f - T_p} \quad (Eq.\ 4.10)$$

Wall temperatures cannot be measured experimentally, but they can be calculated theoretically (Tun et al., 2005):

$$T_{fm} = T_f - (T_f - T_p)\left[\frac{1/h_f}{(1/(h_c+h_v))+(1/h_f)+(1/h_p)}\right] \quad (Eq.\ 4.11)$$

And

$$T_{pm} = T_p + (T_f - T_p)\left[\frac{1/h_p}{(1/(h_c+h_v))+(1/h_f)+(1/h_p)}\right] \quad (Eq.\ 4.12)$$

where T_f and T_p are the bulk temperatures at the feed and the permeate side respectively, h is the heat transfer coefficient (W m^{-1} K^{-1}) and can be estimated:

$$h_v = \frac{J\,\Delta H_v}{\Delta T_m} \quad (Eq.\ 4.13)$$

$$h_c = \frac{k_m}{\delta} \quad (Eq.\ 4.14)$$

$$h_f = \frac{Nu\,k_f}{d_h} \quad (Eq.\ 4.15)$$

$$h_p = \frac{Nu\,k_p}{d_h} \quad (Eq.\ 4.16)$$

where k_m, k_f and k_p is the thermal conductivity of the membrane (W m^{-1} K^{-1}), the feed solution and the permeate solution respectively and Nu is the Nusselt number which for laminar conditions can be calculated (Ali et al., 2013):

$$Nu = 0.13\,Re^{0.64}Pr^{0.38} \quad (Eq.\ 4.17)$$

where Re and Pr are the Reynolds number and Prandtl number respectively. From this analysis, the supersaturation produced within the boundary layer and bulk solution can be independently quantified and related to the nucleation kinetics.

4.2.4 Characterisation of nucleation kinetics

To determine the nucleation kinetics, the nucleation rate of the system has been evaluated through supersaturation rate (R') on the onset of the crystallisation on the system caused by the flux differences. By doing this, the metastable zone width (MSZW) limits of the system will be defined (Sangwal, 2021). Defining the MSZW and figuring the supersaturation levels at induction, the heterogeneous and homogeneous nucleation zones can be mapped (Ulrich & Strege, 2002).

Following Nývlt, (1968), the MSZW is determined by ΔC_w (mg g^{-1} solution) which is related to the concentrating rate of the crystallisation (Jiang et al., 2016):

$$\Delta C = \left(\frac{dC}{dT}\right)_T \quad (Eq.\ 4.18)$$

Combining it with the supersaturation rate R' the following Equation occurs (Jiang et al., 2015).

$$Ln(R') = \ln\left(\frac{F_p\,C_w}{m_0 - \int F_p.dt}\right) \quad (Eq.\ 4.19)$$

where F_p is the flow rate of the permeate at a time point (kg h^{-1}), C_w is the concentration of the solution on the membrane surface, m_0 is the mass of feed solution in the beginning of the experiment (kg) and F_p.dt is the integral of the permeate flow on a specific moment of time (kg).

4.3 Results and Discussion

4.3.1 Introduction to membrane properties, water vapour flux and particle count

The three hydrophobic membranes comprised water-membrane contact angles of 120.7±0.5, 134.6±0.5 and 142.3±0.9° for the PVDF<PP<PTFE respectively, which is consistent with the order generally observed in the literature of the commercially available membranes (Khaisri et al., 2009). Pore sizes were comparable for each membrane (Table 4.1). Porosity was greatest for the PTFE membrane, followed by the PVDF and PP membranes (Table 4.1). While PVDF possesses the highest thermal conductivity, the heat transfer coefficient was the smallest due to the larger wall thickness (h_c, 470.6 W m^{-2} K^{-1}). Examination of surface topography indicated the order of surface roughness to be PVDF<PTFE<PP (Figure 4.3, Table 4.1).

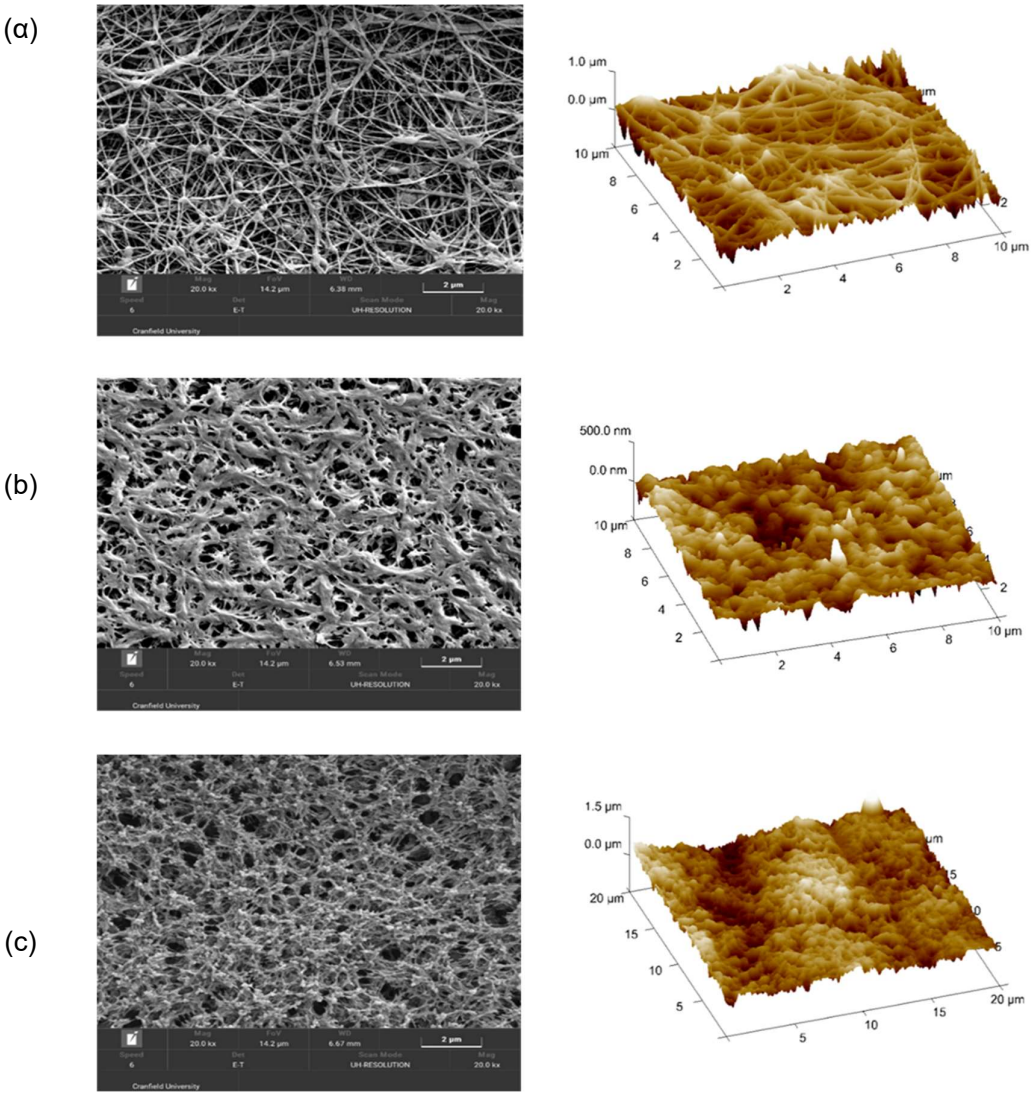

Figure 4.3 SEM and AFM images of virgin (α) PTFE, (b) PVDF and (c) PP membranes.

For each membrane, the feed temperature was fixed (T_f, 54.77±0.37°C), and temperature differences (ΔT) of 15°C, 20°C, 25°C and 30°C were instigated by modification of the permeate temperature (Figure 4.4, a-c). Flux trends for each membrane and temperature difference were characterised by an initial slow decline in flux due to the reduction in vapour pressure instigated by a progressive increase in feed concentration. This was followed by a critical point after which the flux decreased rapidly to zero. The initial flux was greatest for the highest ΔT and resulted in reaching a rapid flux decline more quickly. To illustrate, for the PTFE membrane, flux tended to zero at 86.5, 96.5, 132 and 208 minutes for ΔT of 30, 25, 20 and 15°C respectively. At an equivalent ΔT, permeate flux was highest for the PTFE membrane, followed by the PVDF and PP membranes. This correlates to the order of membrane porosities which may explain the difference in flux observed at an equivalent ΔT. Consequently, at an equivalent ΔT, the transition from a slow to a rapid decline in flux was reached sooner with the PTFE membrane, followed by the PVDF and PP membranes.

(a)

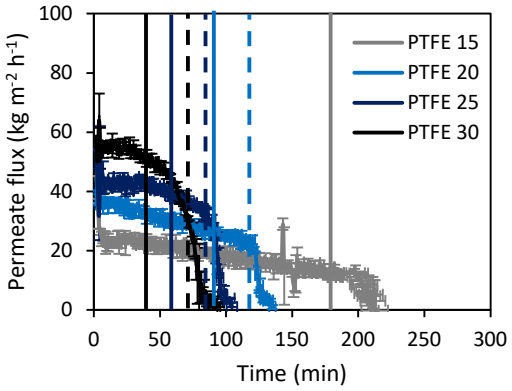

(b)

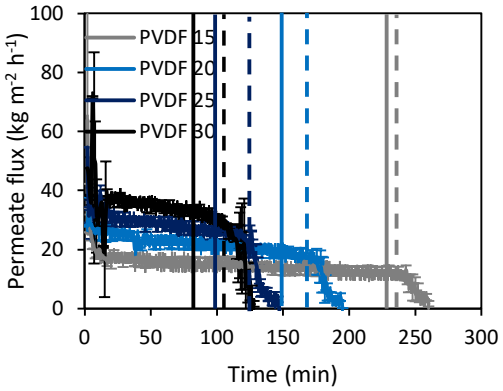

(c)

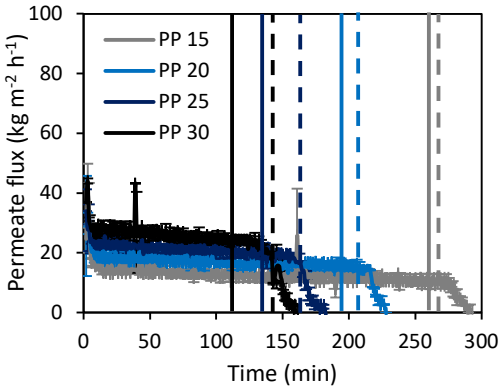

Figure 4.4 Membrane distillation crystallisation data using four different temperature differences (15°C – 20°C – 25°C -30°C) over time: membrane flux data on (a) PTFE, (b) PVDF, (c) PP flat sheet membranes.Solid lines represent the induction of scaling while dotted lines represent the induction of bulk crystallisation.

Use of FBRM permitted the direct determination of the start of nucleation (and hence induction time) in the bulk solution (Figure 4.5, a-c). The start of nucleation was characterised by an increase in particle count (# sec^{-1}). The onset of nucleation was consistently determined first for the highest ΔT of 30°C and was subsequently detected in order of ΔT applied at 25, 20 and finally 15°C respectively. At an equivalent ΔT, nucleation first commenced for the PTFE membrane, followed by the PVDF and PP membranes respectively. This corresponds to the order in which water vapour flux was measured (Figure 4.4, a-c). The onset of bulk nucleation broadly correlated to the transition point from a slow to a rapid decline in flux (indicated by dashed line, Figure 4.3, a-c). This implies that it is the deposition of crystals formed within the bulk solution that is primarily responsible for the rapid loss in flux. Re-evaluation of flux data based on the bulk saturation value (c c^{*-1}) evidenced that bulk nucleation commenced at a saturation value close to c c^{*-1} ~1 and that slightly higher supersaturation values were generally achieved when a greater ΔT was applied (c c^{*-1} 0.93 to 1.05). Supersaturation, specifically the metastable zone width (MSZW, the difference in concentration between the supersaturation at nucleation and the saturation value of solution), represents the driving force for nucleation. Since the bulk supersaturation values correspond closely to the saturation value of solution, it implies that the bulk conditions do not offer sufficient driving force for nucleation. While it is yet to be demonstrated, it has been previously postulated that the supersaturation developed within the boundary layer sets the driving force for nucleation. This study is amongst the first to determine the exact point of nucleation, and therefore makes it possible to relate the supersaturation condition within the boundary layer to the onset of nucleation, which can be correlated to amongst the first measurements of induction time (the lag time to nucleation having achieved saturation in solution) as a further measure of metastability. These collectively provide a framework to describe nucleation kinetics, that can

be used to confirm which region of supersaturation (bulk or boundary layer) ultimately set conditions for nucleation within MDCr.

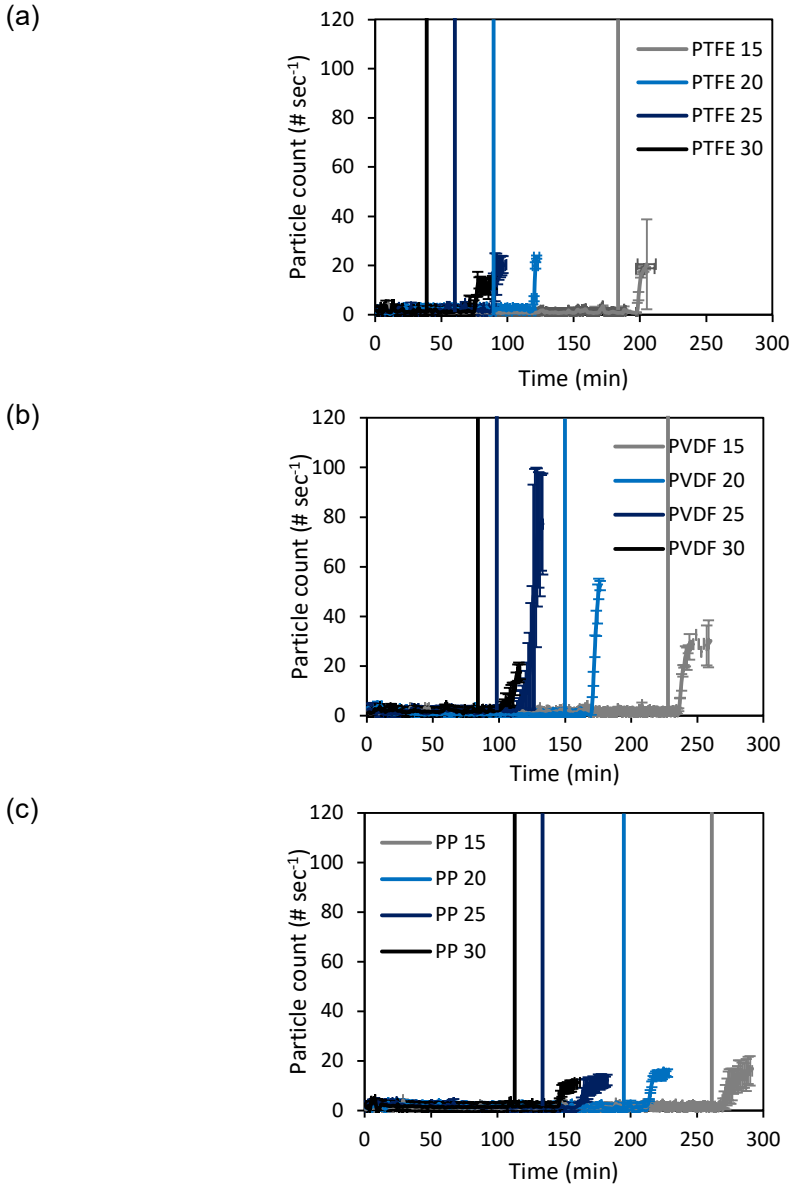

Figure 4.5 In-situ particle characterisation which determines the first point at which bulk crystals are formed under the (α) PTFE, (b) PVDF, (c) PP membranes (FBRM set to primary count (<10) for sensitive direction of induction and nucleation rate).

4.3.2 Characterisation of nucleation kinetics in the bulk solution

The concentrating rate (R' g $100g^{-1}$ h^{-1}) describes the rate at which solute in solution is concentrated and therefore provides a means of normalising flux data produced from different membranes at distinct ΔT for correlation to the nucleation kinetics. In principle, the concentrating rate is proportional to the maximum supersaturation established at induction (the onset of nucleation) (Sangwal, 2010). This was demonstrated in this study by constructing

the correlation between supersaturation rate (LnR′) and the corresponding metastable zone width ($Ln_{\Delta Cmax,fm}$) (Figure 4.6). The maximum supersaturation at the onset of nucleation was characterised within the boundary layer and represents the MSZW ($C_{max,fm}$, g $100g^{-1}$), which takes account of changes to the solubility constant (C*) due to the effects of heat transfer. The lowest MSZW of 0.85 mg_{solute} $g_{solution}^{-1}$ was recorded for the PP membrane (ΔT 15°C) corresponding to LnR' -2.71 g $100g^{-1}$ h^{-1}, whereas the greatest $\Delta C_{max,fm}$ of 2.32 mg g^{-1} was recorded for the PTFE membrane (ΔT 30°C) as LnR' increased to -1.59g 100 g^{-1} h^{-1} . The concentrating rate is considered a direct analogy to the nucleation rate (Sangwal, 2010). Consequently, the nucleation kinetics were ascertained from line fitting to provide a nucleation order n = 1.07 (−) and nucleation constant k = 4.04 No. m^{-3} s^{-1}. The nucleation order and constant are physical parameters that relate the dependency of the MSZW to the concentrating rate, describing the domain in which thermodynamically stable nuclei transform to visible entities (Ouda et al., 2023). Importantly, this correlation represents data from each membrane operated across a broad range of ΔT, which emphasises how it is the supersaturation developed within the boundary layer that determines the nucleation kinetics, with the width of the MSZW being dependent on the supersaturation rate which is consistent with the crystallisation literature (Ouda et al., 2023).

(a)

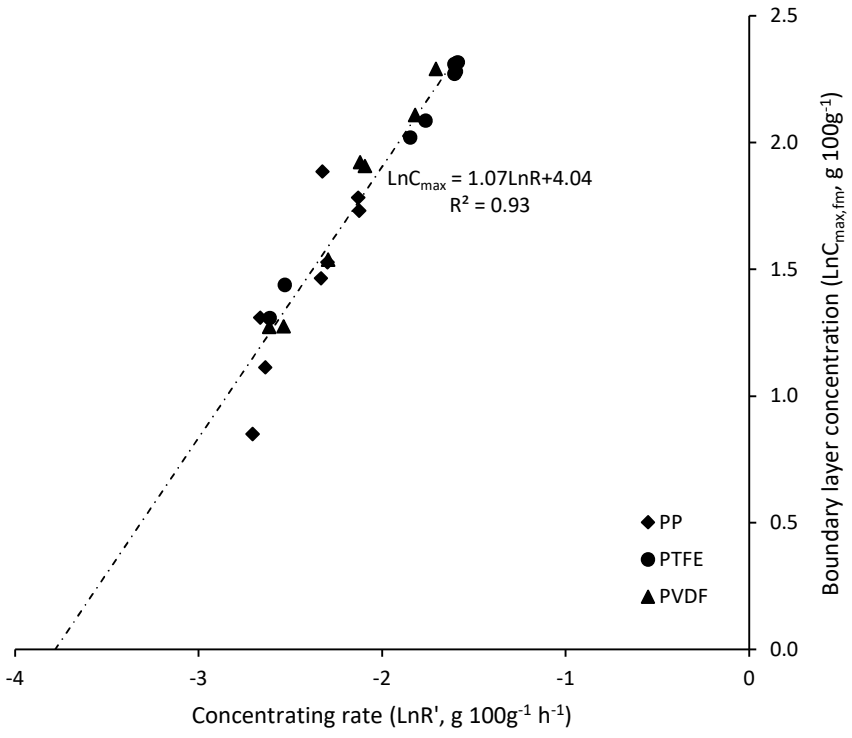

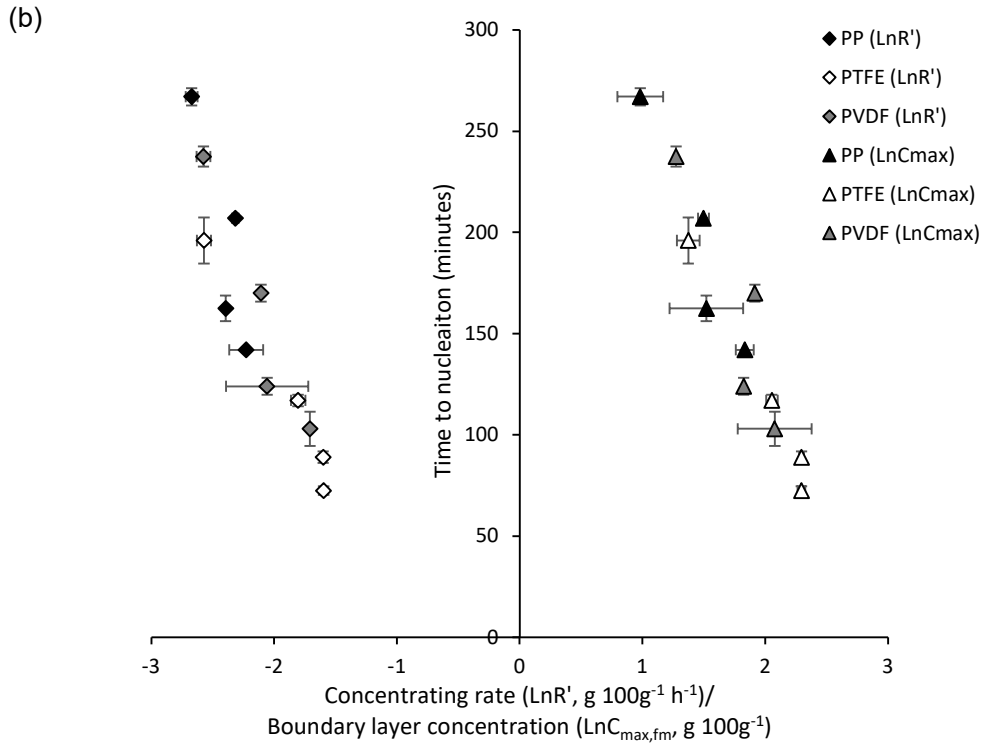

Figure 4.6 Demonstrating the effect of the concentrating rate of the PTFE, PVDF and PP membranes (a) on the boundary layer concentration and the (b) supersaturation at homogeneous nucleation induction. The increase in the boundary layer concentration thus the increase of the saturation level of the boundary layer during the nucleation induction keeps increasing no matter the membrane used. It must be noted that the bulk concentration during nucleation remains steady no matter the concentrating rate and the membrane.

To confirm the role of the boundary layer, the two discrete regions of supersaturation (bulk and boundary layer) were characterised at the onset of nucleation and compared (Figure 4.7). The analysed data comprises of supersaturation measurements for each membrane, operated at ΔT of between 15 and 30°C. For each membrane, higher concentrating rates imposed by an increase in ΔT, raised the maximum supersaturation in the boundary layer at the onset of nucleation. Conversely, supersaturation was consistently close to ~1 in the bulk solution at the onset of nucleation. To enable the formation of a critical nucleus, there must be sufficient excess supersaturation to overcome the Gibbs free energy barrier for nucleation (Figure 4.1). The supersaturation state in the bulk solution being approximately equivalent to the solubility constant (c*) is not sufficient to overcome the nucleation barrier. As the concentrating rate increased, the difference in supersaturation between the boundary layer and bulk solution increased further. The excess supersaturation within the boundary layer, coupled with its correlation to concentrating rate, imply that it is the boundary layer which provides the driving force for nucleation. The nucleation mechanism in MDCr is often described as heterogeneous as the contact angle and porosity can modify the surface free energy contribution (ΔG_s) to reduce the Gibbs free energy barrier for nucleation ((Yadav et al., 2022); Appendix 4.A). This

does not consider the kinetics of nucleation, where an increase is supersaturation generated at higher concentrating rates, will increase the driving force for nucleation by an increase in ΔG_v, which will similarly suppress ΔG^* (Figure 4.1) but will favour homogeneous nucleation due to the excess solute availability. According to the heterogeneous model, the membrane properties in this study can contribute 0.83 to 0.96 $\Delta G_{het}/\Delta G_{hom}$ where the contact angle of the PP membrane (120.7°) facilitates the greatest opportunity for modification. However, the supersaturation developed within the boundary layer at the onset of nucleation was comparable for each membrane when exposed to an equivalent concentrating rate, which would not be the case if the onset of nucleation strongly relied on the distinctive properties of each membrane. Consequently, we propose that when supersaturation is modified by ΔT, it is the mass and heat transfer processes that set the maximum supersaturation threshold within the boundary layer which primarily govern nucleation

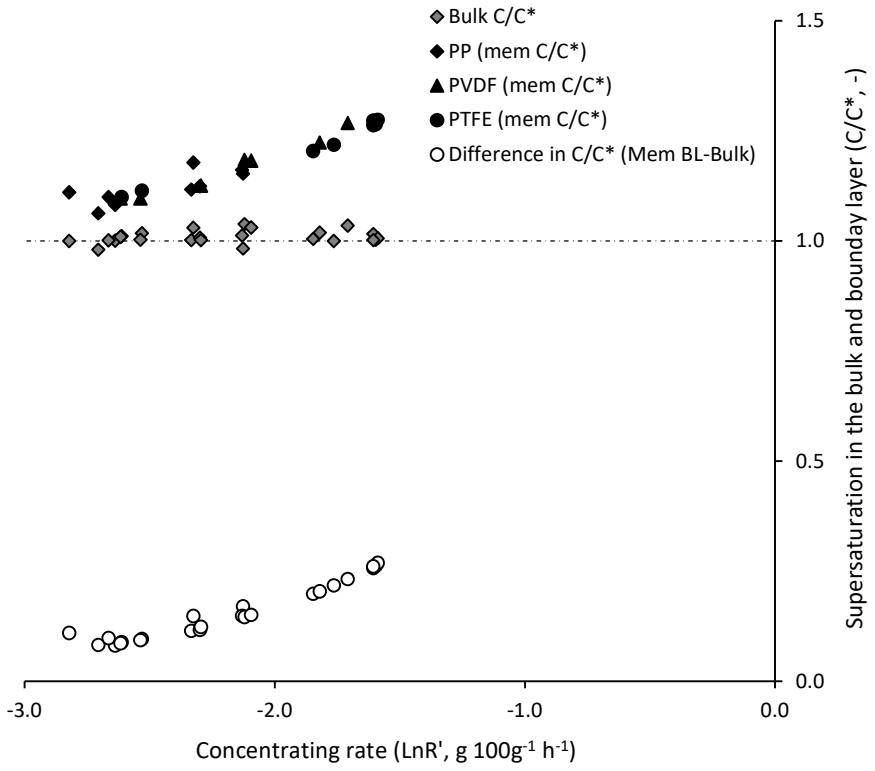

Figure 4.7 Demonstrating the effect of the concentrating rate of the PTFE, PVDF and PP membranes (a) on the boundary layer concentration and the (b) supersaturation at homogeneous nucleation induction. The increase in the boundary layer concentration thus the increase of the saturation level of the boundary layer during the nucleation induction keeps increasing no matter the membrane used. It must be noted that the bulk concentration during nucleation remains steady no matter the concentrating rate and the membrane.

The effect of the kinetic change can be observed on its effect on the type of growth of the nucleated bulk crystals eventually determining their shape. While in low supersaturation levels the generated NaCl crystals has been observed to have their distinct cubic shape (Al-Jibbouri

and Ulrich, 2002; Linnikov, 2006). In this case, the boundary layer is uniformed around the nucleated crystal, causing it to grow symmetrical, leading to flat cubes (Figure 4.8) (Pettit and Fontana, 2019).

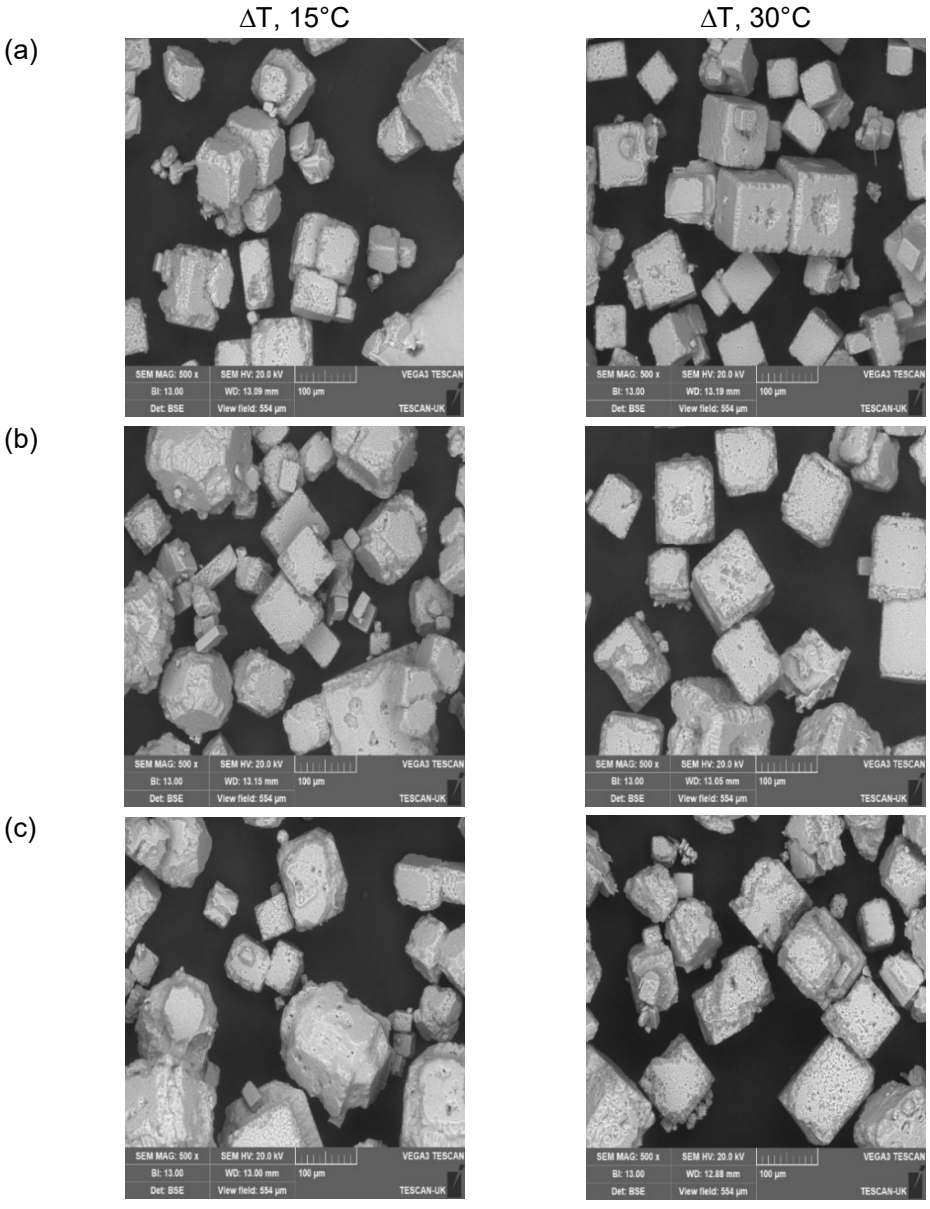

Figure 4.8 Characterisation of the bulk crystals through Scanning Electron Microscopy (SEM) created by the (a) PTFE, (b) PVDF and (c) PP membrane crystallisation experiments where rough model is dominating the crystal growth creating a linear crystal growth rate.

As the induction supersaturation level grows, the crystallisation process generates NaCl hopper crystals, with their peculiar branches to increase as the supersaturation level at induction increases resulting to interconnected crystals (Desarnaud et al., 2018). This change in shape is happening due to the higher growth rate of the crystal resulting from the very high

supersaturation rates. This extra force is mainly imposed on the edges of the crystal, where the ion concentration is higher and are more thermodynamic favorable. making them growing faster than the center (Pettit and Fontana, 2019). As a result, the hopper crystal is highlighted by its pyramid like shape. Following this theory, the generated bulk NaCl crystals from the PTFE, PVDF, PP have a slower growth of the edges in the lower temperature difference experiments while, they have a more complete and distinct cubic shape as the temperature difference is rising towards 30°C. Even though they do not enter the hopper crystal shape, they follow exactly the same pattern as it is described by the theory and proved by the existed literature (Desarnaud et al., 2018).

4.3.3 Characterisation of scaling including relating to mass and heat transfer mechanisms

The nucleation kinetics of scaling was also characterised, to confirm the relevant importance of membrane properties to instigating scaling, further to enabling distinction between scaling and bulk crystal formation mechanisms, that can better inform how to control crystal growth within MDCr. From this analysis, the onset of nucleation could be established, and the extent of surface scaling quantified temporally which can then be compared to the time at which the onset of nucleation was determined within the bulk solution to establish the order in which both mechanisms prevail. From the example primary data provided (PTFE, ΔT 25°C; Figure 4.9), the onset of nucleation (induction time) is typically observed by the formation of a single crystal (50 minutes), after which further crystals are observed to grow at the membrane. While not significant in number density, each crystal grows to a considerable size. At 86 minutes, nucleation was determined in the bulk solution, 36 minutes after scaling commenced. In the minutes immediately following bulk nucleation, a substantive increase in crystal number is observed, and the crystals are considerably smaller in size. Here we presume this rapid increase in crystal number density on the membrane surface is due to the deposition of crystals formed in the bulk solution. Consequently, when quantifying scaling by surface area coverage, we differentiate between scaling, which occurs before bulk nucleation, and deposition which occurs after bulk nucleation has commenced (Figure 4.10). For each membrane, an increase in ΔT from 15 to 30°C, reduced the time to when scaling was first observed. The extent of scaling prior to bulk nucleation (open shapes) was also greatest for higher ΔT. To illustrate, 0.3% of the PTFE membrane surface area was covered due to scaling at the onset of bulk nucleation percentage when ΔT 15°C, whereas 48.6% surface coverage was already completed at the onset of bulk nucleation when ΔT 30°C. Once deposition began (closed shapes), the membrane surface area was quickly covered by a high volume of small crystals, approaching 100% surface coverage due to scaling and deposition. This analysis confirms that it is this rapid deposition of crystals formed within the bulk solution which leads to the rapid reduction in flux (Figure 4.3). For the same ΔT, membrane scaling was greatest

for the PTFE membrane. At ΔT 30°C, the PTFE membrane reached 48.6% surface coverage compared to the PP and PVDF membranes which reached 15.0 and 19.4% surface scaling, by the time bulk nucleation commenced.

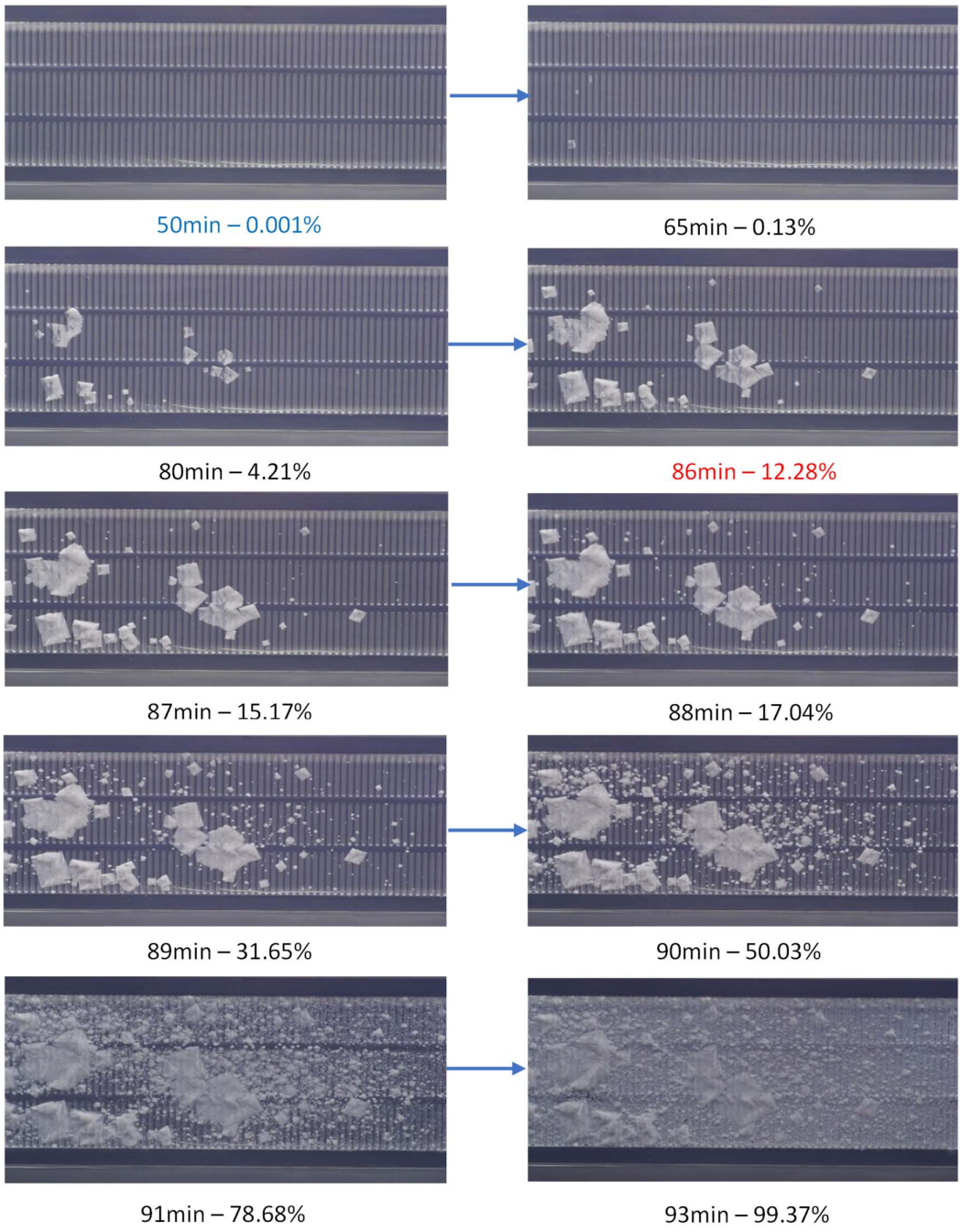

Figure 4.9 Time series of NaCl scaling on the PTFE membrane. The feed and the permeate flow are counter current and the feed flow direction is from left to right. The feed temperature is 54°C while the temperature difference stands on 25°C. The image on the 50th minute is where the induction of the membrane scaling begins. After the 50th minute the scaling continues to grow without having yet bulk crystallisation. The bulk crystallisation induction is happening on the 86th minute. After that, we can see the effect of the deposited crystals coming from the bulk and create intense scaling.

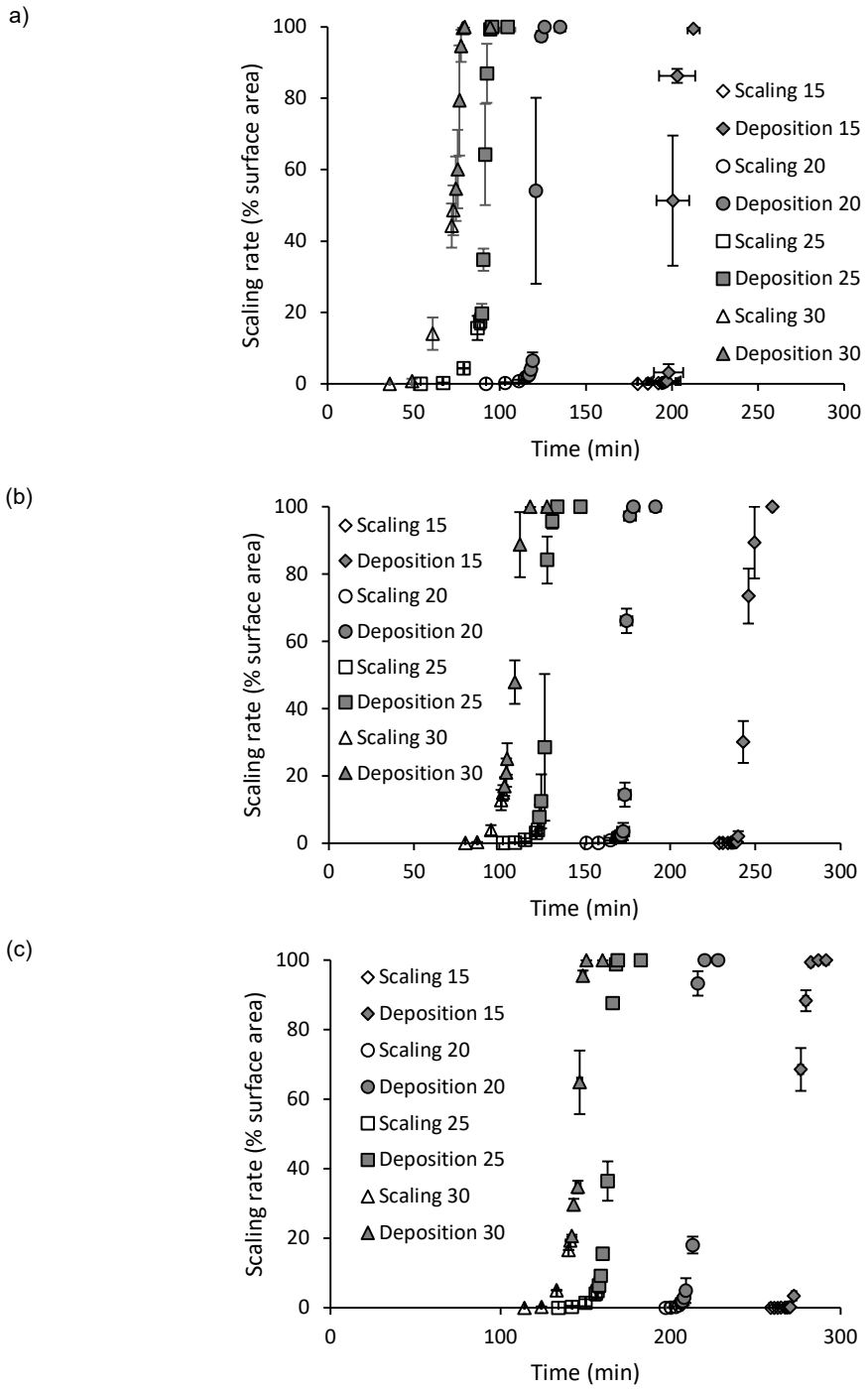

Figure 4.10 Quantifying the extent of scaling based on time for the different temperature differences using (a) polytetrafluoroethylene (PTFE), (b) polyvinylidene fluoride (PVDF), (c) polypropylene (PP) flat sheet membranes. Direct observation also permits the differentiation between adhesive growth (classical, scaling, open shapes) and deposition (following homogeneous nucleation in the bulk solution, closed circles).

To determine how membrane scaling is initiated, the boundary layer properties were characterised for each membrane (Figure 4.11). Higher concentration polarisation was

achieved due to differences in heat and mass transfer fostered through distinctions in membrane properties, and by modifying ΔT. The cumulative effect was an increase in concentrating rate which correlated to a greater CPC which subsequently raises supersaturation within the boundary layer (Table 4.1). However, at an equivalent concentrating rate, the temperature polarisation is distinct for each membrane. The PTFE membrane exhibited the greatest temperature polarisation followed by the PP and PVDF which can be accounted for by the relative heat transfer coefficients ($h_{c,\ PTFE}$, 1010.3 W m^{-2} k^{-1}). The TPC was also reduced for each membrane by the convective heat loss as the concentrating rate increased. However, sodium chloride is characterised by a relatively flat solubility-temperature dependency, and as such the solubility (c*) within the boundary layer was not substantially modified by the difference in TPC measured for each membrane, which ranged 36.98 to 36.75 g $100g^{-1}$ (~0.6% change). Consequently, while an increase in concentrating rate will modify both CPC and TPC, concentration polarisation can be expected to primarily contribute to setting the maximum supersaturation (c c^{*-1}) within the boundary layer.

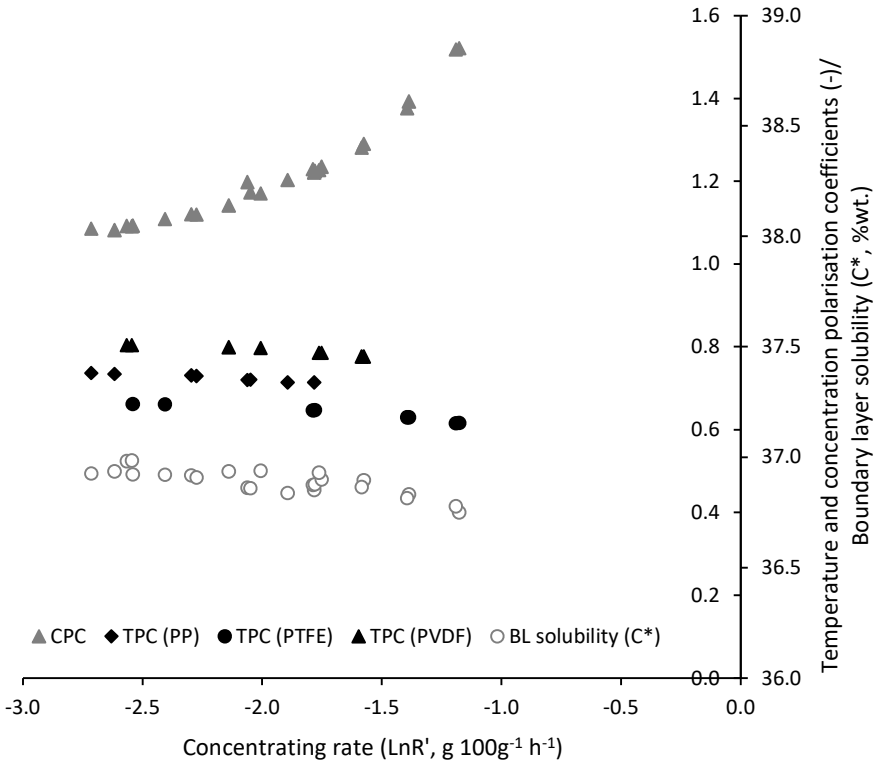

Figure 4.11 Demonstrating the effect of the concentrating rate of the PTFE, PVDF and PP membranes (a) on the TPC and CPC as well as the (b) boundary layer concentration and the relative supersaturation at scaling induction. The membranes seem to have no effect on the concentrating rate as the experiments seem to follow a constant trend no matter the membrane.

4.3.4 Relating scaling mitigation to the nucleation kinetics of the bulk crystal phase

While each membrane provided distinctive mass and heat transfer characteristics, as evidenced by the difference in flux at equivalent temperature differences, by normalising flux through the concentration rates, and presented together, the boundary layer concentration during scaling induction is linear despite the membrane used. Simultaneously, the datapoints generated from the different membranes at different temperature differences are indistinguishable from each other acting as a singular dataset. Similarly to the boundary layer concentration, the boundary layer supersaturation at the point of scaling induction are linearly correlated and increases through the concentrating rates (Figure 4.12a). According to the CNT, the induction time of crystallisation in heterogeneous nucleation is inversely correlated to the saturation level (Eq. 4.3), consequently, the scaling induction is decreasing, as the concentrating rate increases (Figure 4.12b). As the concentration at the induction get higher, the extend of scaling increases (Figure 4.10), leading to local high supersaturation areas on the boundary layer. Consequently, less salt molecules are available in the bulk solution to from nuclei (Mangin et al., 2009), negatively affecting the local bulk supersaturation keeping its level permanently below S = 1 (Figure 4.13). This is more prevalent as the concentration rate is increasing due to the flux increase lead by the increase on the temperature difference forced on the system, causing higher concentration polarisation effect (Schofield et al., 1987; Tun et al., 2005). As a result, bulk nucleation is pushed back, as scaling is increasing and only onsetting after a significant amount of scaling is generated (Figure 4.14a,b).

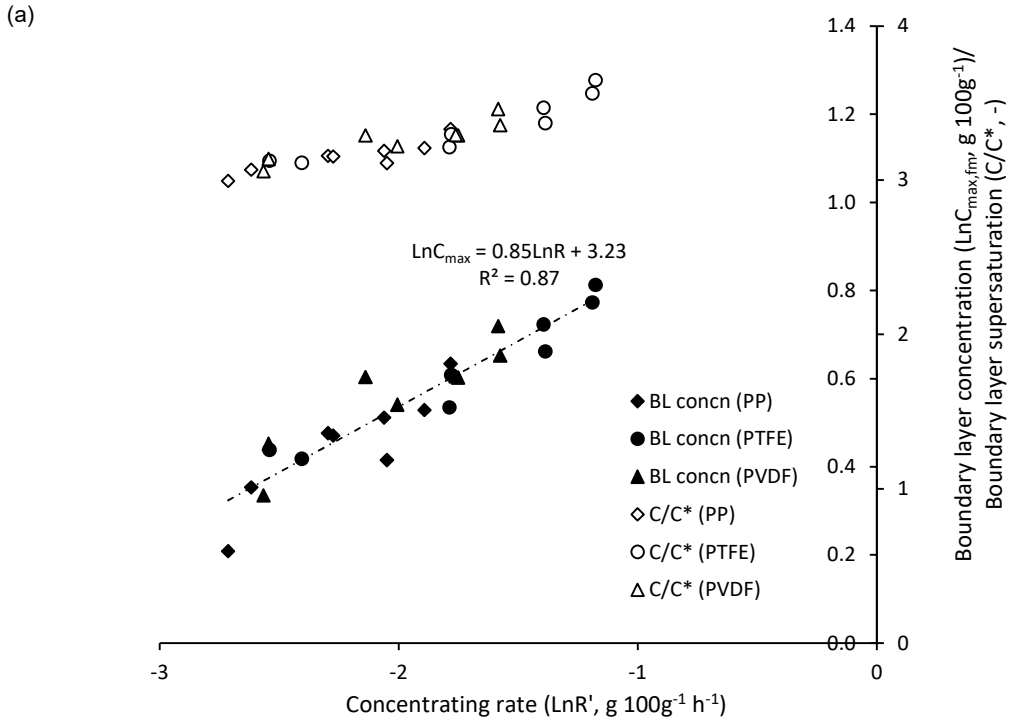

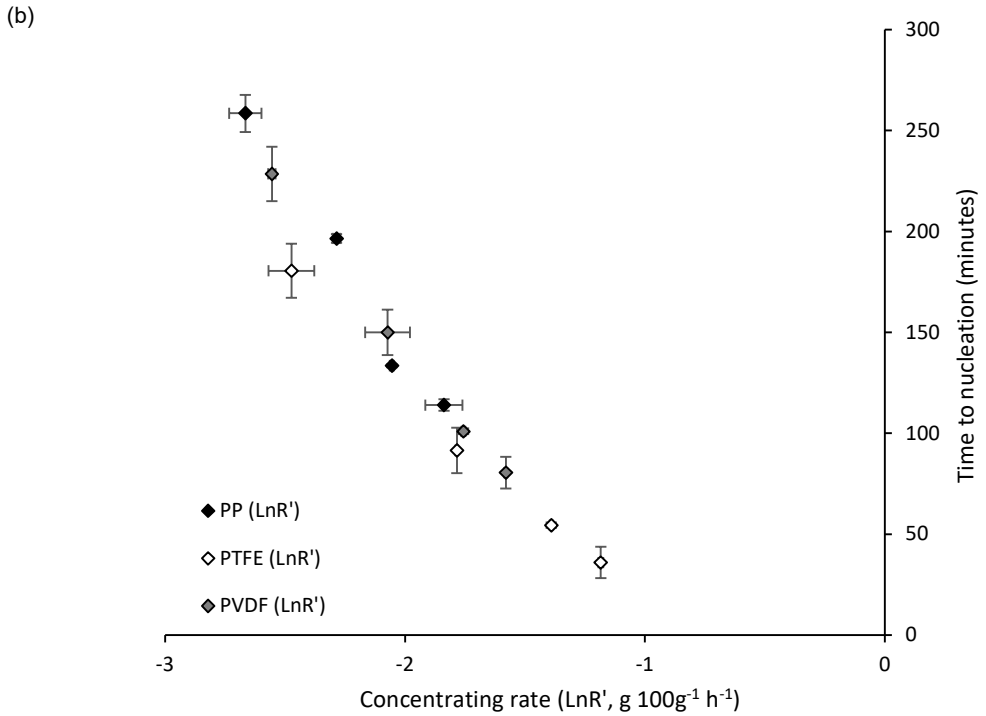

Figure 4.12 Demonstrating the effect of the concentrating rate of the PTFE, PVDF and PP membranes (a) on the TPC and CPC as well as the (b) boundary layer concentration and the relative supersaturation at scaling induction. The membranes seem to have no effect on the concentrating rate as the experiments seem to follow a constant trend no matter the membrane. Figure 1. The effect of the concentrating rate (a) in the saturation level of the scaling induction according to the boundary layer and (b) the difference between the bulk and the boundary layer concentrations.

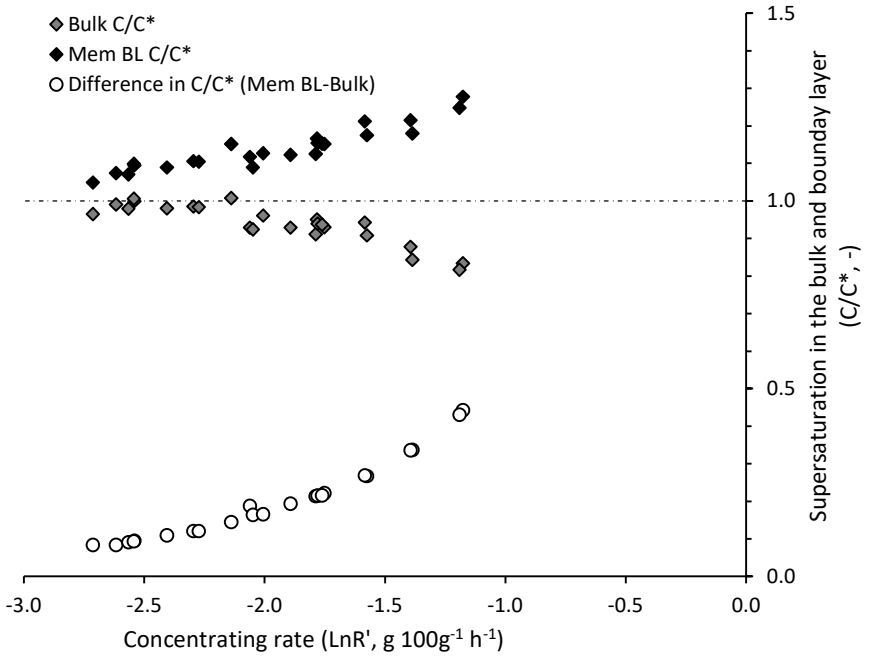

Figure 4.13 The effect of the temperature-solubility dependence can be seen as the difference between the bulk and the boundary layer concentration increases while the concentration in the bulk decreases as the membrane concentration increases no matter the membrane used.

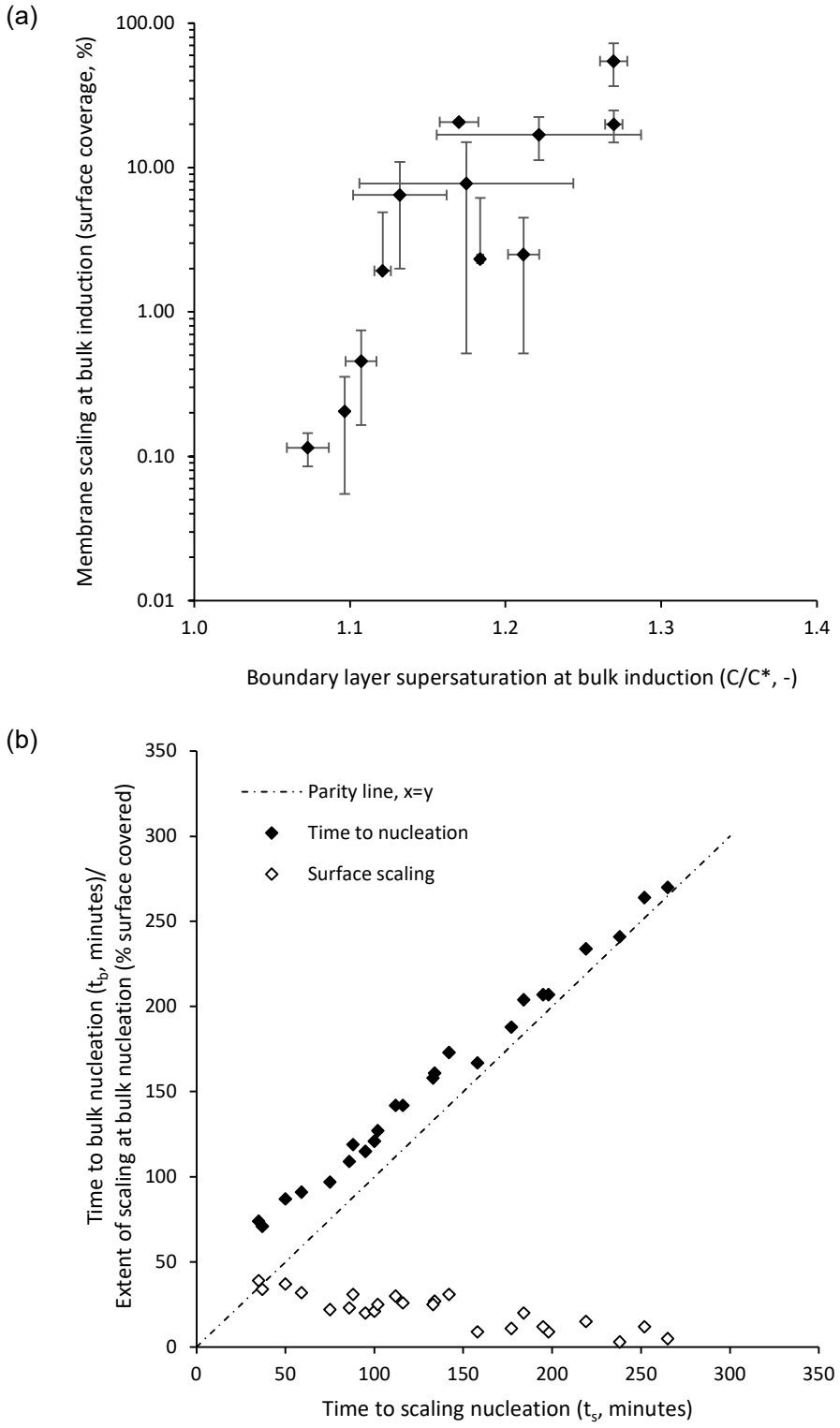

Figure 4.14 (a) Demonstrating the effect of the supersaturation of the boundary layer on the onset of bulk induction with the extend of membrane scaling. (b) As bulk induction is pushed back, the concentration on the boundary layer of the membrane is getting higher, extending the growth of the membrane scaling.

In contrary to the bulk crystal shape, the heterogeneous crystals are formed in much higher saturation levels due to the effect of the concentration polarisation and the temperature polarisation on the membrane. Because of that, the kinetic effect on the membrane crystals is even higher and interconnected hopper crystals are generated (Figure 4.15), spreading from the colder side of the membrane with the smaller ΔT, towards the hotter side of the membrane with the higher ΔT (Figure 4.9) (Desarnaud et al., 20114; Desarnaud et al., 2018).

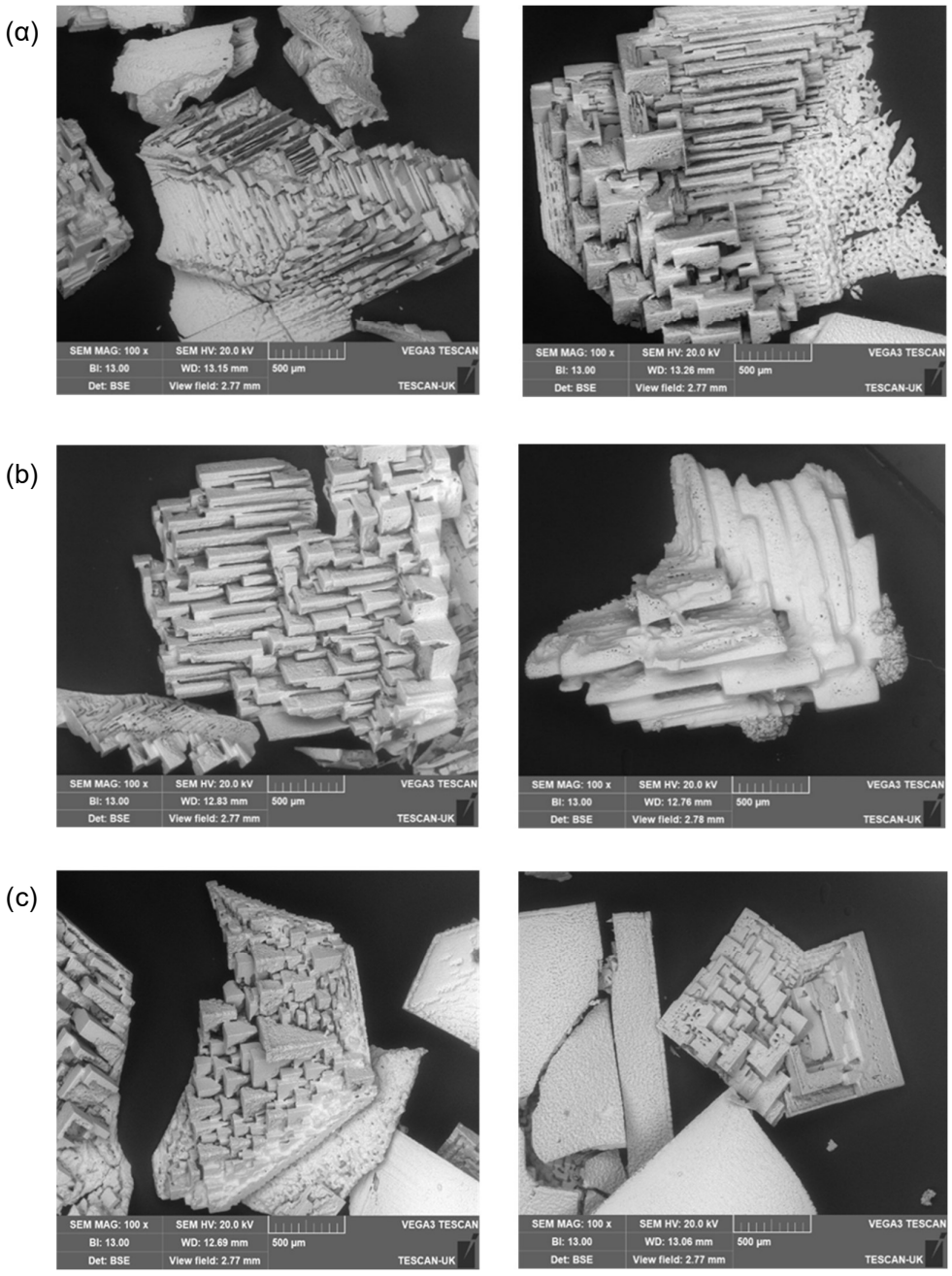

Figure 4.15 Characterisation of scale formed on each membrane using Scanning Electron Microscopy (SEM): (a) PTFE; (b) PVDF; and (c) PP. Experimental conditions: Feed temperature, 54°C; ΔT, 30°C. Crystals produced through sacrificial experiments to ensure analysis prior to bulk nucleation.

Although the boundary layer concentration is linearly related to the concentrating rate of the crystallisation process no matter the membrane used, the extend of the scaling at the point of nucleation seem to have no correlation whatsoever between the three membranes. PTFE has the highest scaling rate, followed by the PVDF and the PP (Figure 4.10). This difference can be explained by the difference in their porosity (Table 4.1). Bigger porosity means more available spots for the crystals to grow, which leads to lower energy needs for heterogeneous nucleation, thus higher scaling possibility (Liu et al, 2021).

Despite we decoupled the thermodynamic flux effect of the process from the membrane material, if we examine the connection between the membrane material through the scope of the surface free energy of the different membranes and the scaling surface coverage at induction through the concentration rate, there is a linear corelation (Appendix 4.A, Table 4.A1). Even though, that sounds contradictory to our point and agree with previous works (Erdemir et al., 2019), this corelation needs a deeper examination.

To estimate surface free energy, the dispersive and the polar acid base components have to be calculated (Appendix Eq. 3, 4, 5), making the liquid-surface contact angle its most important factor (Han et al., 2019; Yao et al., 2020). Even though theoretically there should be a strong correlation between the liquid-surface contact angle and the energy needed for the induction of scaling ($\Delta G_{het}/\Delta G_{hom}$) Appendix 4.A, Fig. 4.A1), the experimental data of induction do not support this theory (PTFE>PVDF>PP instead of PTFE>PP>PVDF).

Surface free energy seems to have a linear relation to the porosity. Porosity plays a major role on the surface topography, thus free energy of the membrane, as the higher porosity means more available spots for solute entrapment, which affects local supersaturation by reducing the energy requirement for crystal formation (ΔG_s) highering the probability for scaling. Concurrently, higher porosity signifies more available openings for flux permeation, resulting to higher concentrating rates, through more intense mass and heat transfer, prolonging the induction time. This leads to extreme supersaturation levels which promote homogeneous bulk nucleation inside the membrane pores (ΔG_v).

As a result, even though the lowering of the ΔG_s is a factor for the promotion of scaling, the manipulation of ΔG_v creates an even bigger kinetic effect which overcomes the effect of the surface free energy (Chapter 1).

4.4 Conclusion

In this study, highly efficient detection techniques, not common in MDCr, were implemented to provide an accurate characterisation of induction time and decouple the effect of the membrane material from the effect of the adjusted flux and as a result, the decoupling of crystallisation from membrane distillation. To achieve this, three different membranes with similar pore sizes but differences in porosity, thermal conductivity, roughness and contact angles were used, operating across a range of temperature differences. To minimise the effect of the chemistry, a salt with minimal solubility-temperature dependence was selected (NaCl). A tendency was noticed, were in the higher temperature differences, more scaling was observed before the onset of nucleation. The induced nucleation was observed, and their rates were quantified through FBRM and their crystal structure was confirmed by SEM. This precision on the estimation of the induction time of heterogeneous scaling as well the homogeneous nucleation, allowed us to get an actual representation of the metastable zone width and identify the exact site of the onset of the nucleation which is the boundary layer of the membrane, as the driving force on the bulk solution is not sufficient for nucleation. The supersaturation rate, thus the MSZW is increasing with the increase of the concentration rate causing lower growing rates. This is confirmed by the differences observed on the crystal structure of the nucleated NaCl, which leads towards a more distinct cubic shape as the temperature difference increases. As the heterogeneous scaling and the homogeneous nucleation causing crystal deposition was differentiated by the use of the detection techniques used, it was confirmed that even though the scaling was increasing with the increase of the ΔT in all the membranes, due to higher CPC and TPC, it is always the crystal deposition causing the rapid reduction in flux which leads to the termination of the process. Furthermore, the supersaturation of the boundary layer at the onset of nucleation is comparable on al the three different membranes at an equivalent concentrating rate. This means that the main driver for nucleation is not the membrane material, but the mass and heat transfer processes which are governed by the transmembrane flux and the temperature difference of the system. Even though prior studies recommend that membranes can reduce ΔG_s and promote heterogeneous nucleation as it seems to be the case also here, ΔG_v seems to create an even bigger kinetic effect overcoming this through the aforementioned mass and heat transfer. As the effect of the membrane has now been decoupled by the effect of the flux, more effective scaling mitigations strategies can be developed focusing more on the control of the transmembrane flux of the process through membrane properties related to that such as porosity and thermal conductivity and not the actual material of the membrane.

4.5 Acknowledgements

This research was financially supported through European Research Council Starting Grant, 'Sustainable chemical alternatives for reuse in the circular economy' (StG, SCARCE, 714080).

4.6 Appendix

Table 4.A1 Surface tension and apparent contact angles of the different feed solutions on the on the PTFE membrane.

	Initial saturation (%)	Concentration (mol/L)	Surface tension (mN/m)	Contact angle (degrees)		
				PVDF	PP	PTFE
NaCl	75	4.00	68 ± 3	121.8 ± 0.9	132.8 ± 1.9	139.8 ± 1.9
DI Water (Ref.)	-	-		120.7 ± 0.5	134.6 ± 0.5	142.3 ± 0.9

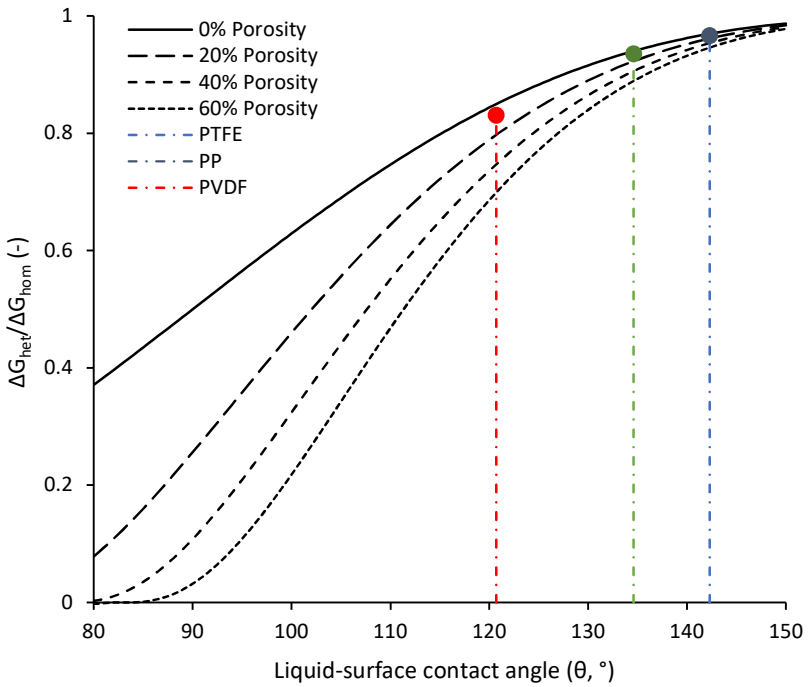

Figure 4.A1 Evidencing the reversible connection between the longer times and the shorter induction.

References

C. Agarwal, S. Das, A. K. Pandey, Study on pore size distributions of microporous polymer membranes having different physical architecture using capillary flow porometry, Materials Today Chemistry. 23 (2022) 100652.

A. Alkhatib, M. A. Ayari, A. H. Hawari, Fouling mitigation strategies for different foulants in membrane distillation, Chem. Eng. Proc. – Proc. Intens. 167 (2021) 108517.

A. Ali, F. Macedonio, E. Drioli, S. Aljlil, O.A. Alharbi, Experimental and theoretical evaluation of temperature polarization phenomenon in direct contact membrane distillation, Chem. Eng. Res. Des. 91 (2013) 1966-1977.

L. de Bartolo, A. Gugliuzza, S. Morelli, B. Cirillo, A. Gordano, E. Drioli, Novel PEEK-WC membranes with low plasma protein affinity related to surface free energy parameters, Journal of Materials Science: Materials in Medicine. 15 (2004) 877–883.

L. de Bartolo, S. Morelli, A. Bader, E. Drioli, The influence of polymeric membrane surface free energy on cell metabolic functions, Journal of Materials Science: Materials in Medicine. 12 (2001) 959–963.

S. Berg, D. Kutra, T. Kroeger, C.N. Strahle, B.X. Kausler, C. Haubold, M. Schiegg, J. Ales, T. Beier, M. Rudy, K. Eren, J.I. Cervantes, B. Xu, F. Beuttenmueller, A. Wolny, C. Zhang, U. Koethe, F.A. Hamprecht, A. Kreshuk, Ilastik: interactive machine learning for (bio)image analysis, Nature Methods. 16 (2019) 1226 – 1232.

S. Bhattacharjee, Concentration polarization: Early theories, Water Planet Inc. 2017.

T. Y. Cath, V. D. Adams, A. E. Childress, Experimental study of desalination using direct contact membrane distillation: a new approach to flux enhancement, J. Membr. Sci. 228 (2004) 5–16.

E. Chabanon, D. Mangin, C. Charcosset, Membranes and crystallisation processes: State of the art and prospects, J. Membr. Sci. 509 (2016) 57–67.

Chemister.ru., Physicochemical properties of substances 2021. [online] Available at: <http://chemister.ru/Database/search-en.php> [Accessed 11 November 2021].

S.J. Chipera, D.L. Bish, Fitting full X-Ray Diffraction patterns for quantitative analysis: A method for readily quantifying crystalline and disordered phases, Adv. Mat. Phy. Chem. 3 (2013) 47 – 53.

Y. Choi, G. Naidu, L.D. Nghiem, S. Lee, S. Vigneswaran, Membrnane distillation crystallisation for brine mining and zero liquid discharge: opportunities, challenges, and recent progress, Env. Sci. Water Res. & Technol. 5 (2019) 1202.

Z. Cui, X. Li, Y. Zhang, Z. Wang, A. Gugliuzza, F. Militano, E. Drioli, F. Macedonio, Testing of three different PVDF membranes in membrane assisted-crystallisation process: Influence of membrane structural-properties on process performance, Desalination. 440 (2018) 68–77.

E. Curcio, E. Drioli, Membrane distillation and related operations – a review, Sep. Purif. Rev. 34 (2005) 35–86.
E. Curcio, E. Fontananova, G. Di Profio, E. Drioli, Influence of the structural properties of poly(vinylidene fluoride) membranes on the heterogeneous nucleation rate of protein crystals, J. Phys. Chem. 110 (2006) 12438–12445.
P. Das, S. Dutta, K.K.K. Singh, S. Maity, Energy saving integrated membrane crystallisation: a sustainable technology solution, Sep. Purif. Technol. 228 (2019) 115722.
P. Das, S. Dutta, K.K. Singh, Insights into membrane crystallisation: A sustainable tool for value added product recovery from effluent streams, Sep. Pur.. Technol. 257 (2021) 117666.
Z. Ding, L. Liu, Z. Liu, R. Ma, Fouling resistance in concentrarting TCM extract by direct contact membrane distillation, J. Membr. Sci. 362 (2010) 317 – 325.
G. Di Profio, E. Curcio, E. Drioli, Supersaturation control and heterogeneous nucleation in membrane crystallizaers: facts and perspectives, Ind. Eng. Chem. Res. 49 (2010) 11878–11889.
E. Drioli, G. Di Profio, E. Curcio, Progress in membrane crystallisation, Curr. Opin. Chem. Eng. 1(2) (2012) 178 – 182.
M.L. Dundon, E. Mack Jr., The solubility and surface energy of calcium sulphate, Journal of the American Chemical Society. 45 (1923) 2479–2485.
H. Groen, K. J. Roberts, An examination of the crystallisation of Urea from supersaturated aqueous and aqueous-methanol solutions as monitored in-process using ATR FTIR spectroscopy. Cryst. Growth Des. 4 (5) (2004) 930–936.
B. Han, X. Wang, J. Zheng, S. Liang, K. Xiao, J. Yu, Z. Qian, X. Huang, Determination of Surface Energy Parameters of Hydrophilic Porous Membranes via a Corrected Contact Angle Approach, Langmuir. 35 (2019) 15009–15016.
B. Han, S. Liang, B. Wang, J. Zheng, X. Xie, K. Xiao, X. Wang, X. Huang, Simultaneous determination of surface energy and roughness of dense membranes by a modified contact angle method, Colloids and Surfaces A. 562 (2019) 370–376.
A.R. Heath, P.D. Fawell, P.A. Bahri, J.D. Swift, Estimating average particle size by focused beam reflectance measurement, Part. Part. Syst. Charact. 19 (2002) 84–95.
A. Hina, G.H. Nancollas, Precipitation and dissolution of alkaline earth sulphates: Kinetics and surface energy, Reviews in Mineralogy and Geochemistry. 40 (2000) 276–301.
T. Horseman, Y. Yin, K.S.S. Christie, Z. Wang, T. Tong, S. Lin, Wetting, scaling and fouling in membrane distillation: State-of-the-art insights on fundamental mechanisms and mitigation strategies, ACS EST Eng. 1 (2021) 117–140.
B. Jan, T. Białopiotrowicz, A. Zdziennicka, Some Remarks on the Components of the Liquid Surface Free Energy, Journal of Colloid and Interface Science. 103 (1999) 96–103.

X. Jiang, X Ruan, W. Xiao, D. Lu, G. He, A novel membrane distillation response technology for nucleation detection, metastable zone width measurement and analysis, Chem. Eng. Sci. 134 (2015) 671–680.

X. Jiang, D. Lu, W. Xiao, X. Ruan, J. Fang, G. He, Membrane assisted cooling crystallisation: process model, nucleation, metastable zone and crystal size distribution J. Al. Che. 62 (2016) 829–841.

X. Jiang, L. Tuo, D. Lu, B. Hou, W. Chen, G. He, Progress in membrane distillation crystallisation: Process models, crystallisation control and innovative applications, Front. Chem. Sci. Eng. 11 (2017) 647–662.

A. Jikazana, P Campo, E.J. McAdam, Hydrodynamics (Reynolds number) determine scaling, nucleation and crystal growth kinetics in membrane distillation crystallisation, J. Membr. Sci. 685 (2023) 121909.

V. Karanikola, C. Boo, J. Rolf, M. Elimelech, Engineered slippery surface to mitigate gypsum scaling in membrane distillation for treatment of hypersaline industrial wastewaters, Environ. Sci. Technol. 52 (2018) 14362–14370.

S.A. Kulkarni, S.S. Kadam, H. Meekes, A.I. Stankiewicz, J.H. ter Horst, Crystal nucleation kinetics from induction times and metastable zone widths, Cryst. Growth Des. 13 (2013) 2435–2440.

M. Lenka, D. Sarkar, Determination of metastable zone width, induction period and primary nucleation kinetics for cooling crystallisation of L-asparaginenohydrate, J. Cryst. Growth. 408 (2014) 85–90.

L. Liu, Z. Xiao, Y. Liu, X. Li, H. Yin, A. Volkov, T. He, Understanding the fouling/scaling resistance f superhydrophobic/omniphobic membranes in membrane distillation (DCMD), Desalination. 499 (2020) 114864.

J. Liu, A. K. Albdoor, W. Lin, F. I. Hai, Z. Ma, Membrane fouling in direct contact membrane distillation for liquid desiccant regeneration: Effects of feed temperature and flow velocity, J. Membr. Sci. 642 (2022) 119936.

Y. Liu, T. Horseman, Z. Wang, H. A. Arafat, H. Yin, S. Lin, T. He, Negative Pressure Membrane Distillation for Excellent Gypsum Scaling Resistance and Flux Enhancement, Environ. Sci. Technol. 56, 2 (2022) 1405–1412.

L.H.T. Lyly, B.S. Ooi, J.K. Lim, C.J.C. Derek, S.C. Low, Correlating the membrane surface energy to the organic fouling and wetting of membrane distillation at elevated temperature, J. Env. Chem. Eng. 9 (2021) 104627.

H. A. Maddah, Simulating fouling impact on the permeate flux in high-pressure membranes, Int. J. Adv. App. Sci. 8 (2021) 1–8.

L. Martinez-Diez, M.I. Vazquez-Gonzalez, Temperature and concentration polarization in membrane distillation of aqueous salt solutions, J. Membr. Sci. 156 (1999) 265–273.

L. Martinez, J.M. Rodriguez-Maroto, Membrane thickness reduction effects on direct contact membrane distillation performance, J. Membr. Sci. 312 (2008) 143–156.
S. Meng, Y. Ye, J. Mansouri, V. Chen, Fouling and crystallisation behaviour of superhydrophobic nano-composite PVDF membranes in direct contact membrane distillation, J. Membr. Sci. 463 (2014) 102–114.
S. Meng, Y. Ye, J. Mansouri, V. Chen, Crystallisation behavior of salts during membrane distillation with hydrophobic and superhydrophobic capillary membranes, J. Membr. Sci. 473 (2015) 165–176.
J. Nývlt, Kinetics of nucleation in solutions, J. Crystal Growth. 3, 4 (1968) 337 – 383.
A. Ouda, Y. Bajón Fernández, E. McAdam, Modifying supersaturation rate with membrane area to volume ratio: Scaling reduction and improved crystal growth control in membrane distillation crystallisation, J. Membr. Sci., 683 (2023) 121838.
J. Phattaranawik, R. Jiraratananon, A.G. Fane, Heat transports and membrane distillation coefficients in direct contact membrane distillation, J. Membr. Sci. 212 (2003) 177–193.
M. Polino, C.A.M. Portugal, G. Di Profio, I.M. Coelhoso, J.G. Crespo, Protein crystallisation by membrane-assisted technology, Cryst. Growth Des. 19(8) (2019) 4871 – 4883.
A. Razmavar, G. Annadurai, A. Olufade, C. J. Simonson, A model for predicting the effect of crystallisation fouling on moisture transfer in membrane energy exchangers, Int. J. Heat and Mass Trans. 191 (2022) 122844.
I. Ruiz Salmon, P. Luis, Membrane crystallisation via membrane distillation, Chem. Eng. Process. Process Intensif. 123 (2017) 258–271.
J.M. Schall, A.S. Myerson, Handbook of Industrial Crystallisation. 1 (2019) 1 – 31.
C.A. Schneider, W.S. Rasband, K.W. Eliceiri, NIH Image to ImageJ: 25 years of image analysis, Nature Methods. 9 (2012) 671 – 675.
L. L. Simon, Z. K. Nagy, K. Hungerbuhler, Comparison of external bulk video imaging with focused beam reflectance measurement and ultra-violet visible spectroscopy for metastable zone identification in food and pharmaceutical crystallisation processes, Chem. Eng. Sci. 64 (14) (2009) 3344–3351.
L. D. Tijing, Y. C. Woo, J-S. Choi, S. Lee, S-H. Kim, H. K. Shon, Fouling and its control in membrane distillation – A review, J. Membr. Sci. 475 (2015) 215–244.
T. Tong, A.F. Wallace, S. Zhao, Z. Wang, Mineral scaling in membrane desalination: Mechanisms, mitigation strategies, and feasibility of scaling-resistant membranes, J. Membr. Sci. 579 (2019) 52–69.
G. Tosello, H.N. Hansen, F. Marinello, S. Gasparin, Replication and dimensional quality control of industrial nanoscale using calibrated AFM measurements and SEM image processing, CIRP Annals – Manufacturing Technology, 59 (2010) 563 – 568.

E.R. Townsend, W.J.P. van Enckevort, J.A.M. Meijer, E. Vlieg, Additive Enhanced Creeping of Sodium Chloride Crystals, Crys. Growth & Des. 17 (2017) 3107−3115.
C.M. Tun, A.G. Fane, J.T. Matheickal, R. Sheikholeslami, Membrane distillation crystallisation of concentrated salts-flux and crystal formation, J. Membrane Science 257 (2005) 144–155.
J. Ulrich, C. Strege, Some aspects of the importance of metastable zone width and nucleation in industrial crystallizers, J. Cryst. Growth. 237 (2002) 2130–2135.
S. Wang, M. Feng, H. Du, J.J. Weigand, Y. Zhang, X. Wang, Determination of metastable zone width, induction time and primary nucleation kinetics for cooling crystallisation of sodium orthovanadate from NaOH solution, J. Cryst. Growth. 545 (2020) 125721.
S. H. Woo, J. Park, B. R. Min, Relationship between permeate flux and surface roughness of membranes with similar water contact angle values, Sep. Pur. Technol. 146 (2015) 187–191.
D. Xu, X. Xiong, D. Xu, Y. Zhong, Z. Wang, Z. Zhang, X. Yang, Experimental determination of solubility and metastable zone width of ammonium dihydrogen phosphate in $(NH_4)_2SO_4$ + water and NH4F + water systems, Fluid Phase Equilibria 468 (2018) 1–8.
A. Yadav, P.K. Labhasetwar, V.K. Shahi, Membrane distillation crystallisation technology for zero liquid discharge and resource recovery: Opportunities, challenges and futuristic perspectives, Sci. Total Env. 806 (2022) 150692.
H. Yang, A. Florence, Relating induction time and metastable zone, Cryst. Eng. Comm, 19 (2017) 3966 – 3978.
M. Yao, L.D. Tijing, G. Naidu, S-H. Kim, H. Matsuyama, A.G. Fane, H.K. Shon, A review of membrane wettability for the treatment of saline water deploying membrane distillation, Desalination. 479 (2020) 114312.
J. Yorston, Why you should use SEM for quality control, Advancing Materials, 2021, Available at: <https://www.thermofisher.com/blog/materials/why-you-should-use-sem-for-quality-control-process/> [Accessed 10 November 2021].

5 Solubility-temperature dependency of salts reduces nucleation kinetics in membrane distillation crystallisation

Solubility-temperature dependency of salts reduces nucleation kinetics in membrane distillation crystallisation

K. Vasilakos, N. Thomas, M. Hermassi, P. Campo, E. McAdam[a]

Cranfield Water Science Institute, Cranfield University, Cranfield, MK43 0AL

[a]corresponding author: e.mcadam@cranfield.ac.uk

Abstract

Membrane distillation and crystallisation (MDCr) is a state of the art rising technology, competitive to the reverse osmosis (RO), for the production of high quality products from brine. So far, the research on MDCr is mainly centered on the crystallisation of NaCl as it is the main salt in brine and is characterized by a relatively flat solubility-temperature dependence, which is not the case through for the rest of the salts concentrated in brine. One of the salts included in brine which follows a stepper of positive solubility – temperature dependence trend, is the potassium sulphate. This is the most common dependence in salts, and can have a more complex effects on the mass and heat transfer mechanisms of MDCr due to the more intense temperature and concentration polarisation phenomena it imposes. Furthermore, these polarisation phenomena may have significant effects on the crystallisation kinetics, based on their effect in saturation. In this study, we managed to differentiate scale formation from bulk crystal deposition on the membrane and understand the role of a steep solubility – temperature dependence on the kinetics of MDCr. This differentiation was possible by using novel high – definition, non – invasive detecting techniques. To decouple the effect of the membrane from the effect of the temperature differences imposed, three different membranes (PP, PTFE, PVDF) with equivalent pore sizes were used. As scaling and bulk crystal nucleation were separately distinguished, it was noticed that both of them are primarily kinetically controlled by the supersaturation (ΔG_v) and not the membrane properties (ΔG_s). Through the changes of the temperature differences of the system, we managed to modify the solubility limit and reduce the thermodynamic barrier of the metastable zone width (MSZW). Hence, we managed to control the extent of scaling occurs before bulk nucleation and identify temperature polarisation an integral mechanism for scaling control. This study shows us that to better control crystallisation, a wider MSZW with a membrane with poor heat transfer can mitigate the controlling effect of scaling by limiting the lag time between scaling and bulk nucleation.

Keywords: *membrane distillation crystallisation, scaling, membranes, nucleation kinetics, crystal growth, potassium sulphate*

5.1 Introduction

Membrane distillation crystallisation (MDCr) offers a competitive solution to reverse osmosis (RO) for the concentration of hypersaline brines, and by simultaneously accommodating crystallisation, the number of unit processes required to achieve zero liquid discharge can be reduced. The hydrophobic membrane ensures minimum liquid intrusion into the pores, and the vapour pressure difference established by the thermal gradient, permits water vapour transport through the gas filled pores. This leads to the production of high quality permeate which can improve net water recovery from desalination, while enabling brine concentrations that exceed osmotic pressures ordinarily applied to RO. The highly porous and well-defined surface area in MDCr also offers more precise control over solvent separation in comparison to conventional thermal crystallisers providing stricter control over supersaturation (Curcio and Drioli, 2005; Chabanon et al., 2016). This is of critical importance to crystallisation as supersaturation is the driving force for both nucleation and crystal growth (Di Profio et al., 2010; Ruiz Salmon and Luis, 2017; Choi et al. 2019).

Membranes typically comprise of polytetrafluoroethylene (PTFE), polyvinyldifluoride (PVDF) or polypropylene (PP) and are largely distinguished by their liquid-solid contact angle. It is proposed that the presence of a foreign substrate with a liquid-solid contact angle <180° can reduce the surface free energy (ΔG_s) requirement for nucleation (Di Profio et al., 2010). This heterogeneous nucleation mechanism can be important for the crystallisation of salts that exhibit low supersaturation and long induction times (e.g. NaCl) (Mersmann and Kind, 1988). However, use of the membrane to lower the Gibbs free energy needed to initiate formation of a ‘critical’ nucleus may also introduce a process risk, due to the potential for scaling (Karanikola et al., 2018). The surface topography might also encourage scaling as the membrane roughness (Choi et al., 2019) and pore structure (Mcleod et al., 2015; Bavarella et al., 2022) can instigate localised regions of supersaturation through solute entrapment (Di Profio et al., 2010). However, membrane porosity and pore size will adjust water vapour flux by enhancing mass transfer. The thermal conductivity of the polymer will also amend heat transfer (specifically the heat transfer coefficient which normalises thermal conductivity for membrane thickness). By modifying mass transfer, the rate at which solute is concentrated in solution will increase (c), while an enhancement in heat transfer will modify the solubility constant (c*). Consequently, it is possible to achieve higher levels of supersaturation (c/c*) at an equivalent temperature and temperature difference by using a polymeric membrane with different properties that extend beyond the contact angle. While these properties are well characterised within the membrane distillation literature in consideration of their adjustment to flux, their role in modifying nucleation kinetics within MDCr has not been critically investigated to date. The rate at which the solution is concentrated will determine the extent of metastability in solution (or supersaturation) at the onset of nucleation, and hence will define the

crystallisation kinetics related to the formation and growth of scaling and of the crystal phase produced in the bulk solution. According to classical nucleation theory (CNT), elevated supersaturation and shorter induction times will increase the probability for nucleation to proceed through a homogeneous mechanism (Ouda et al., 2023). Consequently, these polymeric properties complimented by modification of the thermal gradient (ΔT) may be applied to mitigate scaling, favouring crystallisation in the bulk phase to create a more sustainable process.

To date, the development of MDCr for brine management has largely focused on the crystallisation of sodium chloride (NaCl) which is characterised by a relatively flat solubility-temperature dependency ($\Delta C_{sol\text{-}temp\text{-}nacl}$, 0.038 g $100g^{-1}$ $°C^{-1}$). However, brines comprise a complex matrix of inorganic salts. The simultaneous crystallisation of salts has been investigated for brines using classical evaporation (Penha et al., 2018), while the selective crystallisation of specific salts such as potassium sulphate (K_2SO_4) has also been studied within salt bitterns as an economic circular route for the recovery of high value fertilisers (Marx et al., 2019). Potassium sulphate is amongst a wide range of salts which can be crystallised from seawater brine that is characterised by a considerably steeper solubility-temperature dependency than NaCl ($\Delta C_{sol\text{-}temp}$, 0.168 g $100g^{-1}$ $°C^{-1}$). In MDCr, a steeper solubility-temperature dependency can instigate more complex crystallisation pathways due to temperature and concentration polarisation phenomena that occur from the unique mass and heat transfer mechanisms imposed across the membrane. Consequently, the solubility limit of such salts is likely to be strongly modified by temperature polarisation, where the reduction in saturation (c*) could shorten the time to nucleation and increase supersaturation (c/c*) at the beginning of nucleation. The solubility-temperature dependency of the salt may therefore be significant to controlling the nucleation kinetics of scaling. However, there is also a lag time between scaling and bulk nucleation, where the rate and extent of scaling could also modify the nucleation kinetics of the crystal phase within the bulk solution due to the desaturation of solution originated by the growth of scale, or the increased resistance to mass and heat transfer initiated by scale formation, which will ultimately reduce the supersaturation rate of solution.

This study therefore seeks to discriminate scale formation and formation of the bulk crystal phase to collectively describe the mechanism for how salts with a steep solubility-temperature dependency inform the kinetics of nucleation in MDCr. There is presently only very limited data in the literature on the kinetics of nucleation within MDCr due to the difficulty in precisely determining when nucleation has commenced. This is of critical importance since the quantification of induction time and the metastable zone width (MSZW) provide the basis for the characterisation of nucleation kinetics. Non-invasive techniques using microscopic and turbidimetry have recently been demonstrated that enable the detection of the onset of

nucleation at the membrane and in the bulk solution respectively (Jikazana et al., 2023; Ouda et al. 2023). This enables the disaggregation of the kinetics of scaling from those of the bulk crystal phase, therefore also permitting differentiation of scaling initiated through an adhesive mechanism (heterogeneous primary nucleation mechanism) from the deposition of crystals formed in the bulk solution (homogeneous primary nucleation mechanism). In this study, we employ a similar microscopic technique to previous literature (Jikazana et al., 2023) complemented with an enhanced backscatter technique that provides the measurement of induction time in the bulk solution, and a real-time count of the particle distribution within the bulk solution, from which the nucleation kinetics can be directly ascertained. Specific objectives are to: (i) determine water vapour flux for three discrete polymeric membranes with distinctive heat and mass transfer characteristics during the crystallisation of K_2SO_4 at four comparative ΔT; (ii) relate the rate and extent of scaling to the boundary layer characteristics established at induction; (iii) characterise nucleation kinetics for scaling and the bulk crystal phase; and (iv) determine the extent to which scaling is moderated by polarisation phenomena and how this ultimately informs the nucleation kinetics of the bulk crystal phase.

5.2 Material and methods

5.2.1 Experimental Setup

An acrylic cross-flow cell (Model Products, Bedford, UK) with a hold-up volume of $2x10^{-5}m^3$ and channel dimensions of 0.1x0.04m (LxW) with an active area membrane of $0.0004m^2$, made up the direct contact membrane distillation system setup (Figure 5.1). Three membrane of three different membrane materials were utilised. These membranes were made of PP (Sterlitech, Washington, USA), PVDF (Cobetter Filtration, Hangzhou, China) and PTFE (Membrane Solutions, Auburn, USA). As Table 5.1 shows, the chosen membranes comprised of similar pore diameter (0.1μm) but with variations in porosity, thermal conductivity, surface roughness and contact angle. Ultrapure water (15MΩ cm) was mixed with K_2SO_4 crystalline powder (99.0% minimum, Thermo Fisher Scientific Inc., Massachusetts, USA) to create a 90% saturated feed solution. Following the full dissolution of the K_2SO_4 crystalline powder, the mixture was filtered using a 0.45μm Whatman filter (Camlab Ltd., Cambridge, UK). Once the filtration is complete, any remaining contaminants have been removed from the feed solution. This feed solution was delivered into the cell at a flow rate of 1670±12 ml min^{-1} (Masterflex L/S pump, Cole Palmer, UK), while the permeate was flowing through the cell at a rate of 1018±11 ml min^{-1} (323, Watson Marlow, UK). A heater/chiller combination (Ministat 230, Huber, UK) was used to maintain the feed side temperature at roughly 55°C (54.68±0.55). The permeate temperature was varied from approximately 25 – 40°C to introduce temperature variations (ΔT) ranging from 15 to 30°C. The cell's inlet and outlet temperatures were recorded using

specialised thermometers (T7-Pro, LabJack, USA). Using a precision balance (Symmetry PR 410, Cole Palmer, UK), the permeated volume was determined.

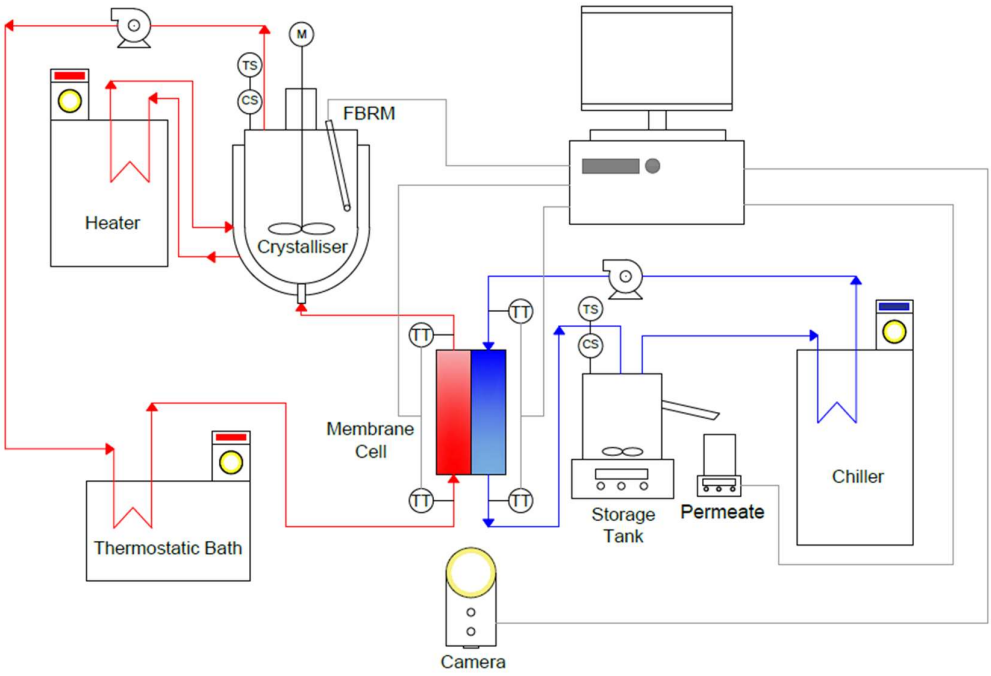

Figure 5.1 Diagram of the full experimental setup.

Table 5.1 Characteristics of the membranes used in this work.

Membrane	Mean pore size (μm)[a]	Surface porosity (%)[a]	R_a (nm)	RMS (nm)	Membrane thickness (mm)[b]	Contact Angle (°)[c]	Thermal conductivity (W m^{-1} K^{-1})	Heat transfer coefficient (h_c) (W m^{-1} K^{-1})
PTFE	0.30 ± 0.02	9.27 ± 0.6	119	147	0.050 ± 0.005	142.3 ± 0.9	0.055	1010.3
PP	0.31 ± 0.02	5.76 ± 0.3	134	173	0.100 ± 0.010	134.6 ± 0.5	0.070	701.5
PVDF	0.33 ± 0.01	7.09 ± 0.6	45	60.2	0.160 ± 0.010	120.7 ± 0.5	0.075	470.6

[a]Measured by POROMETER using Capillary Flow Porometry (Porolux 1000). These values are taken from the most constricted part of the pore so the selective layer, which have in general lower values than the overall porosity. [b]Given by the manufacturer. [c]Measured with water.

5.2.2 Analytical methods

Using an inline focused beam reflectance measurement (FBRM) (ParticleTrack G400, Mettler Toledo, UK) that counts and sizes crystals in real time using the backscatter of light positioned within a probe, the induction time in the bulk solution was ascertained (Heat et al., 2002). The placement of the FBRM is crucial to the crystal measurements as it has a fixed narrow depth of measurement. The FBRM probe, which is positioned inside the reactor at a 60° inclination for optimal efficiency, generates a 780nm laser beam. The laser beam progresses through the reactor at a velocity of 2m s^{-1} encountering scattered salts ranging 0.5 to 2000μm in size. As it is encounters the salts, the beam intersects and backscatters, converting and correcting the received signal into chord lengths in the FBRM software. These chord lengths results into the creation of a chord length distribution (CLD). The growing number of the CLD measurements is derived in total counts s^{-1} (Kim et al., 2013).

$$total\ counts\ s^{-1} = \sum_{i=1}^{Ch} N_{Ch,i} \qquad (Eq.\ 5.1)$$

where C_h is the channels number in FBRM while $N_{Ch,I}$ is the number of counts provided in the i^{th} channel. As soon as the primary nucleation occurs, these total counts rise rapidly, offering a precise mechanism of induction time determination of the bulk solution. The provided total counts can also be converted into the volumetric nucleation rate (B, $m^{-3}\ s^{-1}$), by the utilisation of the volumetric depth of measurement of the FBRM.

$$V = S_p W_l D_p \qquad (Eq.\ 5.2)$$

where S_p is the laser scanning speed (2m s^{-1}), W_l is the diameter of the laser at the focal point ($5.8x10^{-6}$m) and D_p is the penetration depth of the laser into the solution ($2x10^{-4}$m). This results in a scanning volume of $2.32x10^{-9}m^3\ s^{-1}$ (Mitchell et al., 2011). The 'primary' selection view was the mode that was utilised to calculate the induction time. The 'primary' selection view offers augmented sensitivity to particles and facets with a fine edge discrimination, through its narrower measurement zone. The produced experimental nucleation rates are determined by the variation in particle count over time.

$$B_i = \frac{(N_{c,i} - N_{c,i-1})}{t_i - t_{i-1}} \qquad (Eq.\ 5.3)$$

where B^i is the nucleation rate (# $m^{-3}\ s^{-1}$) of two successive measurements and ti is the time point of the measurement (s). The average nucleation rate (B) of the experiment was determined using the individual nucleation rates derived from the individual measurements as the experimental N_c increases.

The 'macro' selection view is the mode used to extract the crystal size distributions from the CLD. Using a macro edge discrimination for agglomerates and crystals that is less

sensitive to surface and facets, this mode has a larger measurement zone than the primary view (Heath et al., 2002).

$$N_{i,n} = N_{i,o} C_{i,A}^{n} \quad (Eq.\ 5.4)$$

where $N_{i,n}$ is the amount of n-weighted chord counts in the i^{th} channel ($\mu m^n\ s^{-1}$), Ni,o is the measured unweighted chord count in the i^{th} channel (s^{-1}) and $C_{i,A}$ is the geometric average length of the i^{th} channel (μm). $C_{i,A}$ is the product of the boundary width of the i^{th} channel (μm) $(C_{i,u} \times C_{i,l})^{1/2}$. Since the square weighting is essentially a cube (volume) weighting, similar to the volume-based distribution techniques, we obtain a more accurate representation of the crystal size when using a square weighted (n = 2) chord distribution, which emphasises more in the coarse end of the distribution (Heath et al., 2002).

The probe was cleaned with distilled water and a microfiber cloth following each experiment to get rid of any leftover salts. The effectiveness of the cleaning was visible as the FBRM counts response turn out to zero.

Highly polished Perspex was used to construct the crossflow cell. This was so that a UHM350 digital microscope (UHM350, AmScope, UK) could be used. UHM350 was positioned 145mm from the feed side of the cell, obtaining images used for the identification of the commencement of the nucleation on the membrane area. This technique, which is directly comparable FBRM's backscatter approach, can detect the time when a crystal phase first forms and can be used to calculate induction time (Jikazana et al., 2023). This methodology tracks the nucleation, growth and the extension of the surface coverage of the crystals that ar first seen on the membrane using high quality imaging techniques. To achieve this, a digital microscope with a long range working distance, a large magnification range (x20 – 100) and a wide-angle lens with coupled with high-resolution (1920px1080p – 2.1MP) was used. Even though the actual time of nucleation cannot be exactly determined, as it is occurs in the nano-scale, the high crystal growth can more than make up for the lack of the imaging definition of the chosen microscope, enabling real-time analysis akin to that of the backscatter method (Ouda et al., 2023).

Ilastik (ilastik, GNU General Public License) was the software that was used to identify the nucleated crystals from the images produced by UHM350. The surface coverage quantification of these crystals was done using ImageJ (ImageJ software, NIH, US).

The determination of the induction time is provided by the time difference of the point where the solution is now supersaturated, until the time where nucleation first kicks in.

$$t_{ind} = t_n - t_{C\,C^{*-1}} \quad (Eq.\ 5.5)$$

where t_{ind} is the induction time of the experiment and is represented as the nucleation rate inverse (t = 1/B), $t_{c\,c^{*-1}}$ is the point where the solution achieves saturation ($t_{c\,c^{*-1}} = 1$) and t_n is the time point at which nucleation kicks in. Using the calculated induction time, we can

measure the metastability of the solution. To examine the real homogeneous nucleation, the induction time according to the CNT can be found by:

$$t_{ind} = Ae^{\frac{\Delta G}{kT}} \quad (Eq.\ 5.6)$$

where A represents the pre-exponential factor (s), ΔG the Gibbs free energy needed for the genereation of the crystals (J), k is the Boltzmann constant (J K^{-1}) and T is the solution temperature (K).

For the heterogeneous nucleation, the induction time can be found through (Yan et al., 2017):

$$t_{ind} = e^{\frac{16\ \emptyset\gamma_l^3 v^2}{3k^3T^3LnS^2}} \quad (Eq.\ 5.7)$$

where the induction time increases with an increase in crystal-liquid surface free energy (γ, J mol^{-1}) or the molecular volume (v, m^3 mol^{-1}) and can be calculated using critical difference ø which indicates the degree to which the presence of a heterogeneous substrate reduces this free energy. In a similar vein, when the saturation level rises (S, C C^{*-1}), the induction time lowers. As a result, by distinguishing primary nucleation promoted by the membrane (digital imaging) from bulk solution (FBRM), scaling and deposition can be differentiated. Every 60 seconds, pictures were captured to track the development of crystal formation on the membrane. Using ilastik software, photos were first converted into binary, 8-bit black and white TIF images, and then the ImageJ software was used to measure the surface coverage at each selected point. Ilastik is a image analysis tool, capable to categorise, sort, monitor and count experimental data with high efficacy (Berg et al., 2019). Every experiment was repeated and the analyses show the average of these repetitions. To use these crystals for further analysis, they were removed through a pre-weighed 0.45μm Whatman filter (Camlab Ltd., Cambridge, UK). After being taken out of the cell, the membrane was stored apart from the bulk crystals.

The produced bulk and membrane crystals underwent separate examinations using XRD (X-Ray Diffraction, Bruker, D5005, Germany) to verify their crystal structure, as well as SEM (Scanning Electron Microscopy, VEGA3, Tescan, Czech Republic) to assess their crystal habit. In crystallography, X-rays are frequently employed to evaluate crystals by analysing the spacing and arrangement of their atoms. (Ali et al., 2022). Furthermore, according to Ali et al., (2023), SEM is a reliable imaging method that can detect and measure crystals at nanoscale. These two methods are widely employed in a variety of sectors, including the pharmaceutical and other high importance industries.

5.2.3 Characterisation of heat and mass transfer

The vapour pressure difference created by the temperature difference between the hot feed and the cold permeate side, introduces a flux through the membrane which is the driver for membrane distillation (Tun et al., 2005):

$$J = C_m \Delta P \quad (Eq.\ 5.8)$$

where C_m is the membrane permeability utilised in the system (m s^{-1}) and ΔP (Pa) is the vapour pressure difference formed between the hot feed and the cold permeate side. As this cause the solute to flow through the membrane, solute builds up and the vapour pressure drops, gradually reducing the flow (Bhattacharjee, 2017). The resulted concentration build-up on the membrane creates an opposing diffusive flux on the membrane surface. This can be described by the concentration polarisation coefficient (CPC) (Tun et al., 2005):

$$CPC = \frac{c_w}{c_b} = exp^{(\frac{J}{\rho K})} \quad (Eq.\ 5.9)$$

where c_w and c_p are the solute concentration on the feed membrane wall and bulk. K is the solute mass transfer coefficient (m s^{-1}) which can be calculated through:

$$K = \frac{1.62\ D}{d_h}(\frac{V\ {d_h}^2}{0.146\ D})^{0.33} \quad (Eq.\ 5.10)$$

where D is the temperature corrected diffusion coefficient (m^2 s^{-1}), d_h the hydraulic diameter of the membrane cell (m^2) and V is the velocity of the feed solution (m s^{-1}).

Additionally, convective and conductive heat transmission occur through the membrane (Curcio and Drioli, 2005). According to Ali et al., (2003), this generates the temperature polarisation coefficient (TPC), which measures the degree of heat transfer resistance as the ratio between the temperature difference of the membrane sides and the temperature difference of the bulk sides:

$$TPC = \frac{T_{fm} - T_{pm}}{T_f - T_p} \quad (Eq.\ 5.11)$$

As the temperatures on the membrane walls cannot be experimentally measured, they are calculated theoretically through (Tun et al., 2005):

$$T_{fm} = T_f - (T_f - T_p)\left[\frac{1/h_f}{(1/(h_c + h_v)) + (1/h_f) + (1/h_p)}\right] \quad (Eq.\ 5.12)$$

And

$$T_{pm} = T_p + (T_f - T_p)\left[\frac{1/h_p}{(1/(h_c + h_v)) + (1/h_f) + (1/h_p)}\right] \quad (Eq.\ 5.13)$$

where T_f and T_p are the feed and the permeate bulk temperatures respectively, while h are the different heat transfer coefficients (W m^{-1} K^{-1}) and can be calculated:

$$h_v = \frac{J\ \Delta H_v}{\Delta T_m} \quad (Eq.\ 5.14)$$

$$h_c = \frac{k_m}{\delta} \quad (Eq.\ 5.15)$$

$$h_f = \frac{Nu\ k_f}{d_h} \quad (Eq.\ 5.16)$$

$$h_p = \frac{Nu\ k_p}{d_h} \quad (Eq.\ 5.17)$$

where ΔHv is the enthalpy of vaporisation, k_m, k_f and k_p are the thermal conductivities of the membrane used, the hot feed solution and the cold permeate solution (W m^{-1} K^{-1}), while Nu is

the Nusselt number. In laminar conditions, the Nusselt number can be calculated (Ali et al., 2013):

$$Nu = 0.13\, Re^{0.64} Pr^{0.38} \quad (Eq.\ 5.18)$$

where Re is the Reynolds number and Pr is the Prandtl number of the feed side. Through this, the supersaturation built inside the boundary layer as well as the feed bulk solution can be evaluated and connect it to the nucleation kinetics.

5.2.4 Characterisation of heat and mass transfer

The nucleation rate of the system must be assessed using the supersaturation rate (R') at the beginning of the system's crystallisation due to flux variations in order to ascertain the nucleation kinetics. This will determine the system's metastable zone width (MSZW) limits (Sangwal, 2021). The heterogeneous and homogeneous nucleation zones can be defined by defining the MSZW and calculating the supersaturation values during induction (Ulrich and Strege, 2002).

According to Nývlt (1968), the MSZW is calculated by the ΔC_w (mg g^{-1} solution) and is correlated with the crystallisation rate through the following equation.

$$\Delta C = \left(\frac{dC}{dT}\right)_T R' \quad (Eq.\ 5.19)$$

The following equation results from combining it with the supersaturation rate R' (Jiang et al., 2015).

$$Ln(R') = \ln\left(\frac{F_p\, C_w}{m_0 - \int F_p . dT}\right) \quad (Eq.\ 5.20)$$

where F_p is the permeate flow rate (kg h^{-1}), C_w is the membrane surface concentration, m_0 is the mass of the feed solution in the commissioning of the experiment (kg) and F_p, dT is the permeate flow integral (kg). All these values are at a specific time point for a specific ln(R').

5.3 Results and discussion

5.3.1 Relating water vapour flux to nucleation kinetics of the bulk crystal phase

Each membrane material was investigated at four temperature differences ranging ΔT 15-30°C (Figure 5.2). At each ΔT, water vapour flux was characterised by an initial period of pseudo steady-state flux, followed by a rapid decline in flux. Initial water vapour flux was greatest at the highest ΔT and reached the rapid flux decline in the shortest time. At an equivalent ΔT water vapour fluxes were greatest for PTFE, followed by the PVDF and PP membranes, which can be accounted for by the difference in porosity (PTFE>PVDF>PP) (Table 5.1). Back-scatter technique permitted the determination of when nucleation occurred through the detection of particles in the bulk solution (Figure 5.3). For all three membranes, nucleation was detected earliest in the bulk solution for the PTFE membrane at ΔT 15°C. At

an equivalent ΔT of 15°C, the order in which nucleation was observed was PTFE>PVDF>PP. Nucleation was not observed in the bulk solution for the PTFE membrane when operated at higher ΔT (20-30°C). Similar observations were made for the PVDF and PP membranes but the ΔT above which nucleation was not observed were >25 and >30°C respectively. This is distinct from the characterisation of NaCl by backscatter measurement, where bulk nucleation was observed at each ΔT (Jikazana et al., 2023; Vasilakos et al., In preparation).

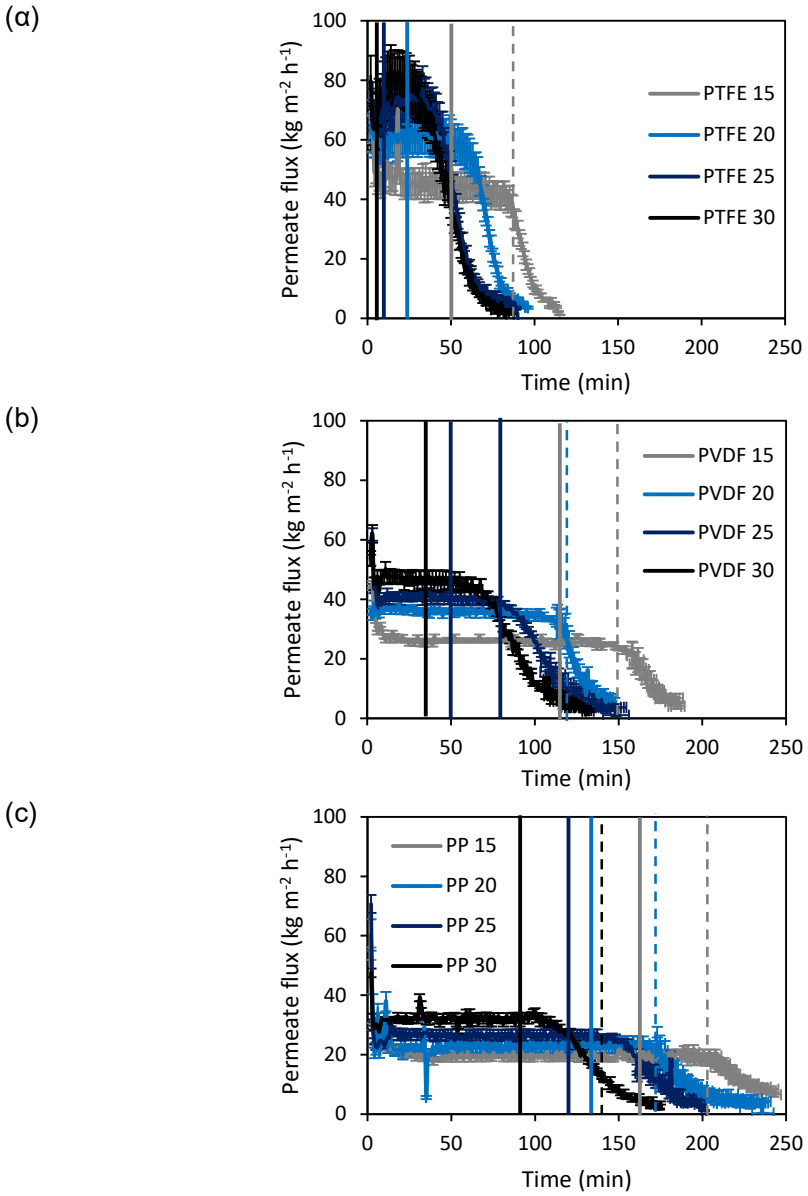

Figure 5.2 Membrane distillation crystallisation data using four different temperature differences (15°C – 20°C – 25°C -30°C) over time: membrane flux data on (a) PTFE, (b) PVDF, (c) PP flat sheet membranes. Solids lines represent scaling induction time while dotted lines represent the induction time of bulk crystallisation.

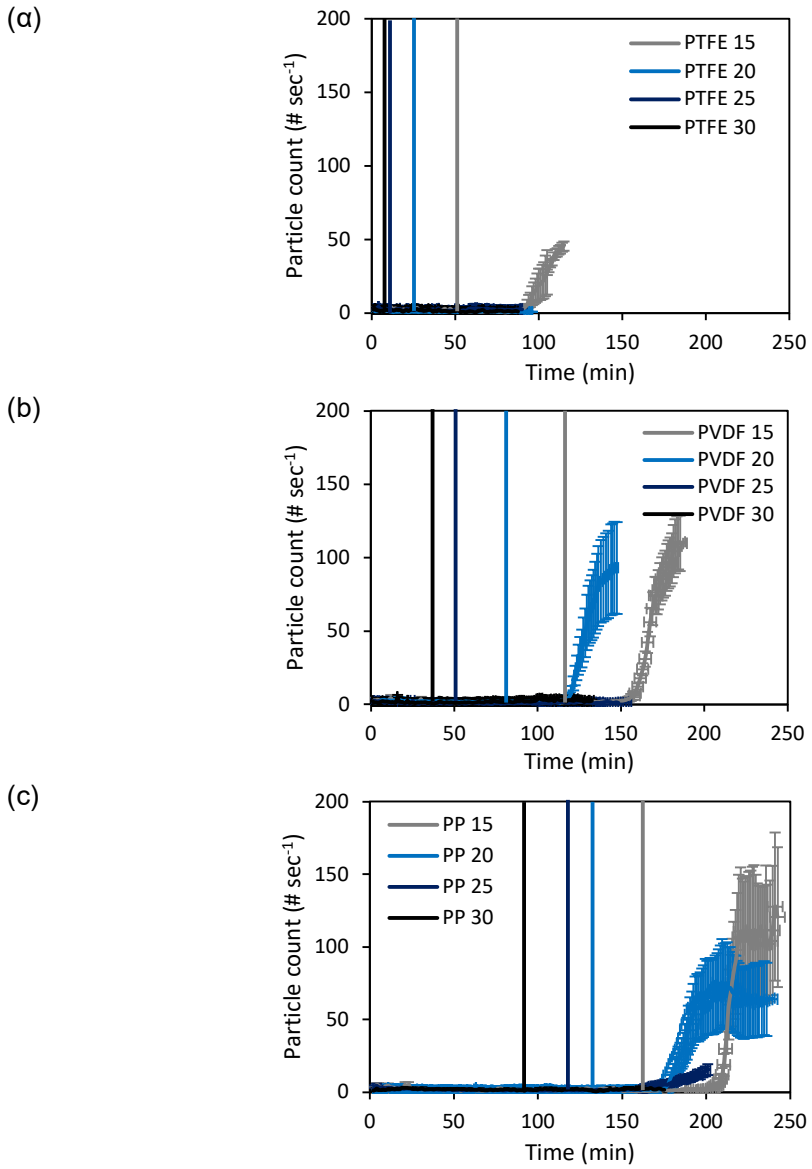

Figure 5.3 In-situ particle characterisation with FBRM to determine both induction time (the first point at which bulk crystals are formed) and nucleation rate for crystallisation in the bulk under the (α) PTFE, (b) PVDF, (c) PP membranes (FBRM set to primary count (<10) for sensitive direction of induction and nucleation rate). Solids lines represent scaling induction time.

To determine how crystallisation is informed by the vapour pressure gradient (set by ΔT and discrete membrane characteristics), supersaturation (ΔC_{max}) was characterised in the boundary layer and bulk solution at the time at which the crystal phase was first observed (Figure 5.4a). Supersaturation is the driving force for nucleation (Equation 5.7). The concentrating rate represents the collective roles of mass and heat transfer, solute concentration and concentration polarisation in determining the rate at which supersaturation is developed in solution. For a greater concentrating rate, it is possible to instigate nucleation within a higher region of the metastable zone width in which primary nucleation is favoured (Ouda et al., 2023). In this analysis, supersaturation data was only included where bulk

nucleation was determined. The greatest supersaturation at bulk nucleation (LnC_{max}, 2.64g $100g^{-1}$) was achieved with the PTFE membrane by setting the highest concentrating rate (ΔT 15°C, LnR' -1.018 g $100g^{-1}$ h^{-1}), whereas the lowest supersaturation (LnC_{max}, 1.86g $100g^{-1}$) was identified with the PP (LnC_{max}, 1.857g $100g^{-1}$) membrane which possessed the lowest concentrating rate (ΔT 15°C, LnR' -1.716g $100g^{-1}$ h^{-1}). A log-linear relationship was identified between the concentrating rate set by the membrane and the supersaturation concentration within the boundary layer at nucleation. This has been described by analogy to the power-law relation between the nucleation rate and the supersaturation (Eq. 5.20), where concentrating rate represents the supersaturation dependent nucleation rate (Sangwal, 2009). Consequently, the nucleation order (m, 0) and nucleation constant (k, 0) can be obtained. From this analysis, it can be inferred that it is the mass and heat transfer processes within the boundary layer which govern the onset of nucleation. This assertion is supported by characterisation of the bulk solution, which consistently approached saturation (c/c*) at nucleation, and therefore does not possess the excess supersaturation required to overcome the Gibbs free energy barrier for nucleation (Figure 5.4b).

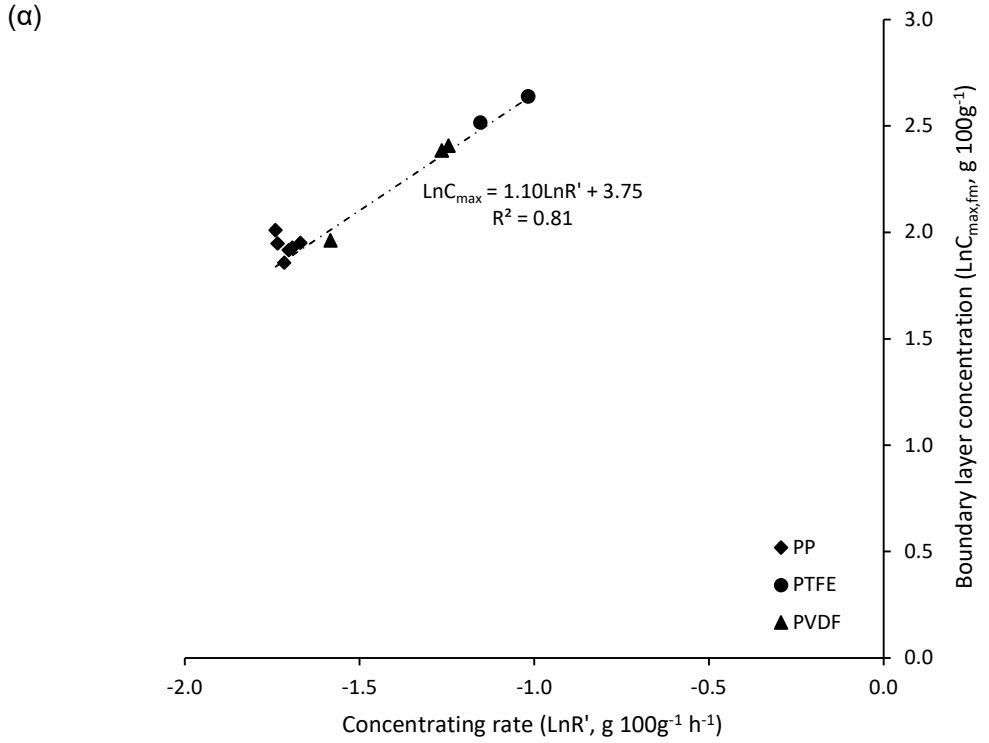

(b)

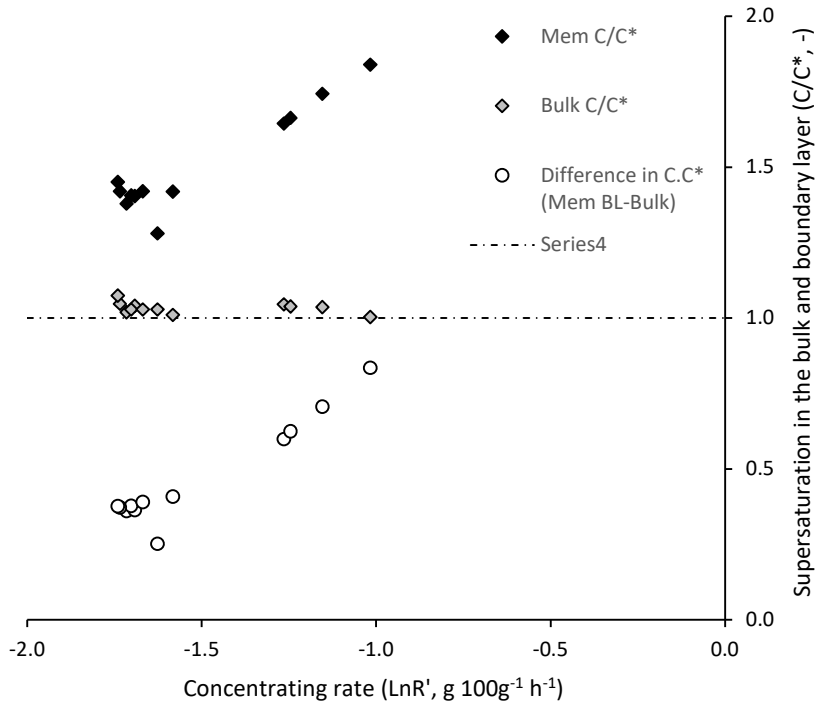

Figure 5.4 The effect of the concentrating rate (a) in the saturation level of the homogeneous nucleation induction according to the boundary layer and (b) the difference between the bulk and the boundary layer concentrations. The effect of the temperature-solubility dependence can be seen as the difference between the bulk and the boundary layer concentration increases while the concentration in the bulk remains steady during nucleation no matter the membrane used.

Crystal morphology of the bulk crystal phase was examined through microscopy (Figure 5.5). At ΔT 15°C, the predominant crystallographic <010> and <021> faces (Figure 5.6) are apparent but a rod like crystal habit was primarily produced using the PTFE membrane which generated the highest supersaturation (C-C*, 0.04 kg kg^{-1}). However, potassium sulphate crystallises in the orthorhombic *space* group, which is more evident at the lower supersaturation levels instigated by the PVDF (C-C*, 0.02 kg kg-1) and PP membranes (C-C*, 0.03 kg kg-1). The excess axial growth observed in the crystal phase produced *by the* PTFE membrane can be explained by the second-order rate kinetics typically observed at the <001> plane when grown within a high concentration driving force (Figure 5.6), whereas the <100> plane is limited to a first-order growth rate (Mullin and Gaska, 1973). At lower concentration driving force (C-C*), linear growth rates in the <001> and <100> planes are comparable, leading to the more granular equidimensional orthorhombic form evidenced with the PVDF and PP membrane. The supersaturation threshold previously described for preferential formation of the orthorhombic habit (C-C* ~0.01 kg kg^{-1}) (Mullin and Gaska, 1973), closely compare to the supersaturation within this study for the PVDF and PP membrane and indicate a critical role for the boundary layer properties in both nucleation and crystal growth.

(α)

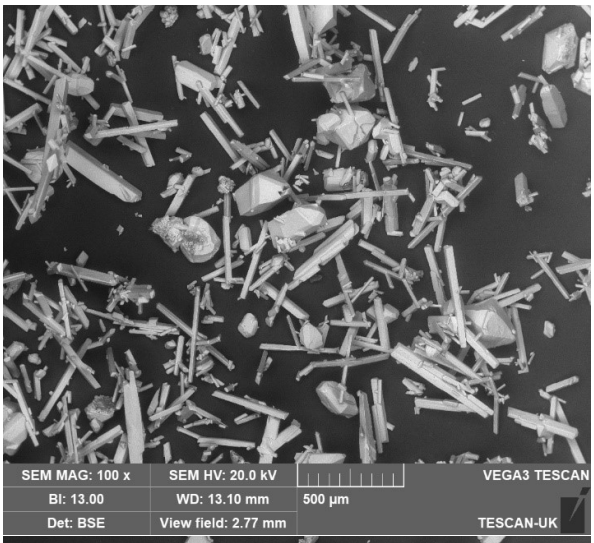

(b)

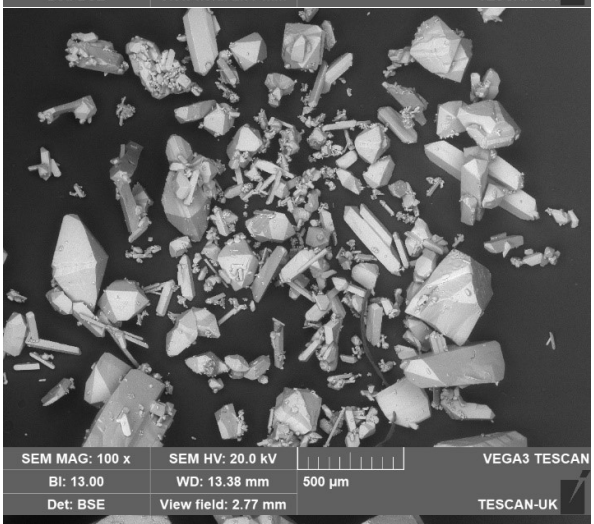

(c)

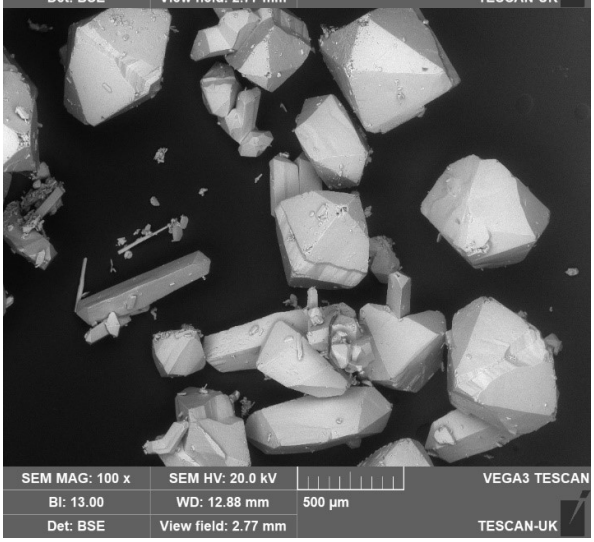

Figure 5.5 Bulk crystals (α) PTFE - 15°C, (b) PVDF - 15°C, (c) PP - 15°C.

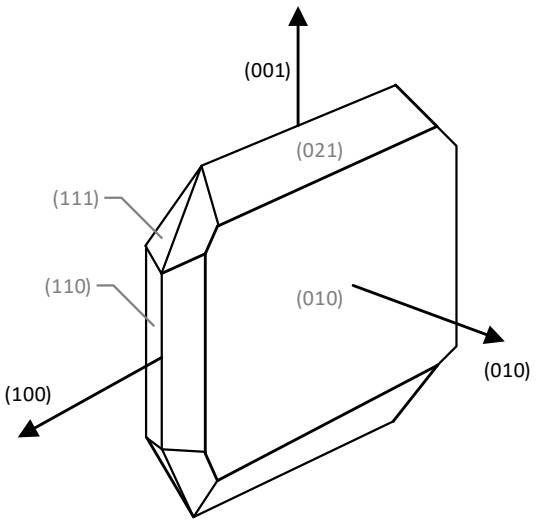

Figure 5.6 Typical habit of potassium sulphate grown in aqueous solution at low supersaturation, with Miller indices noted.

5.3.2 The role of boundary layer properties in initiating scaling

Digital microscopic examination was used to ascertain the time at which scaling commenced and the extent of scaling observed for each membrane (Figure 5.7, and 5.8). Scaling was differentiated into two mechanisms: an adhesive growth mechanism in which scaling is initiated and propagates at the membrane surface prior to bulk nucleation, and a deposition mechanism which involves the settling of crystals onto the membrane following bulk nucleation. The adhesive growth mechanism is generally presumed to represent a heterogeneous primary nucleation pathway, in which the membrane enhances the probability for nucleation at a lower supersaturation threshold (Ouda et al., 2023). Scaling occurred earliest for the PTFE membrane, followed by the PVDF and PP membranes respectively. Scaling proceeded most quickly at the highest ΔT. For each condition where a bulk crystal phase was not produced (PTFE ΔT 20-30°C; PVDF ΔT 25-30°C; PP ΔT 30°C), scaling almost completely covered the membrane. In contrast, crystallisation was observed in the bulk solution in conditions where only partial coverage was noted, and longer operating times were observed. This was illustrated through the deposition of finer particles following their formation in the bulk solution (Figure 5.3), which gradually covered the membrane surface.

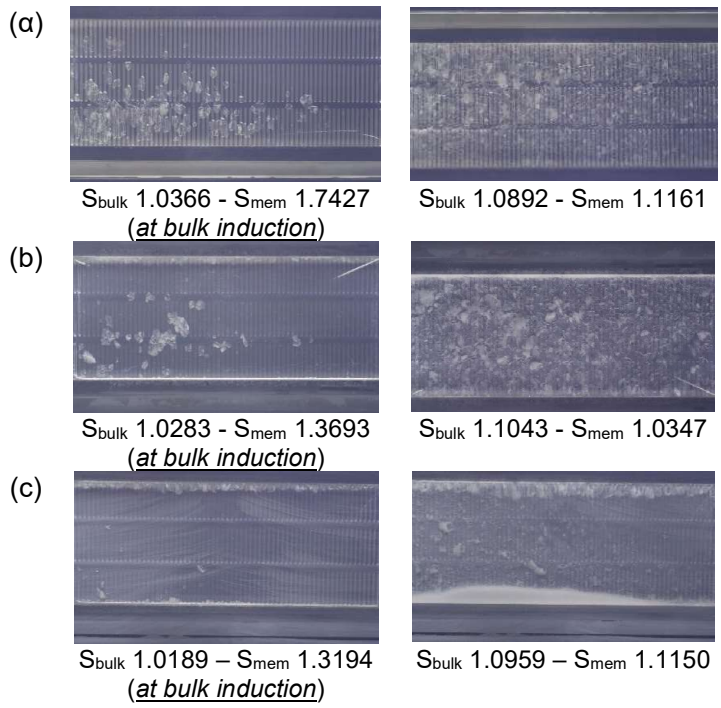

Figure 5. 7 The onset (induction of scaling observed on the (a) PTFE, (b) PVDF and (c) PP membranes before induction in the bulk (homogeneous crystallisation) for K_2SO_4, using non-invasive direct observation, real-time data collection can be used to determine the rate and progression of scaling. Operating conditions ΔT, 15ºC.

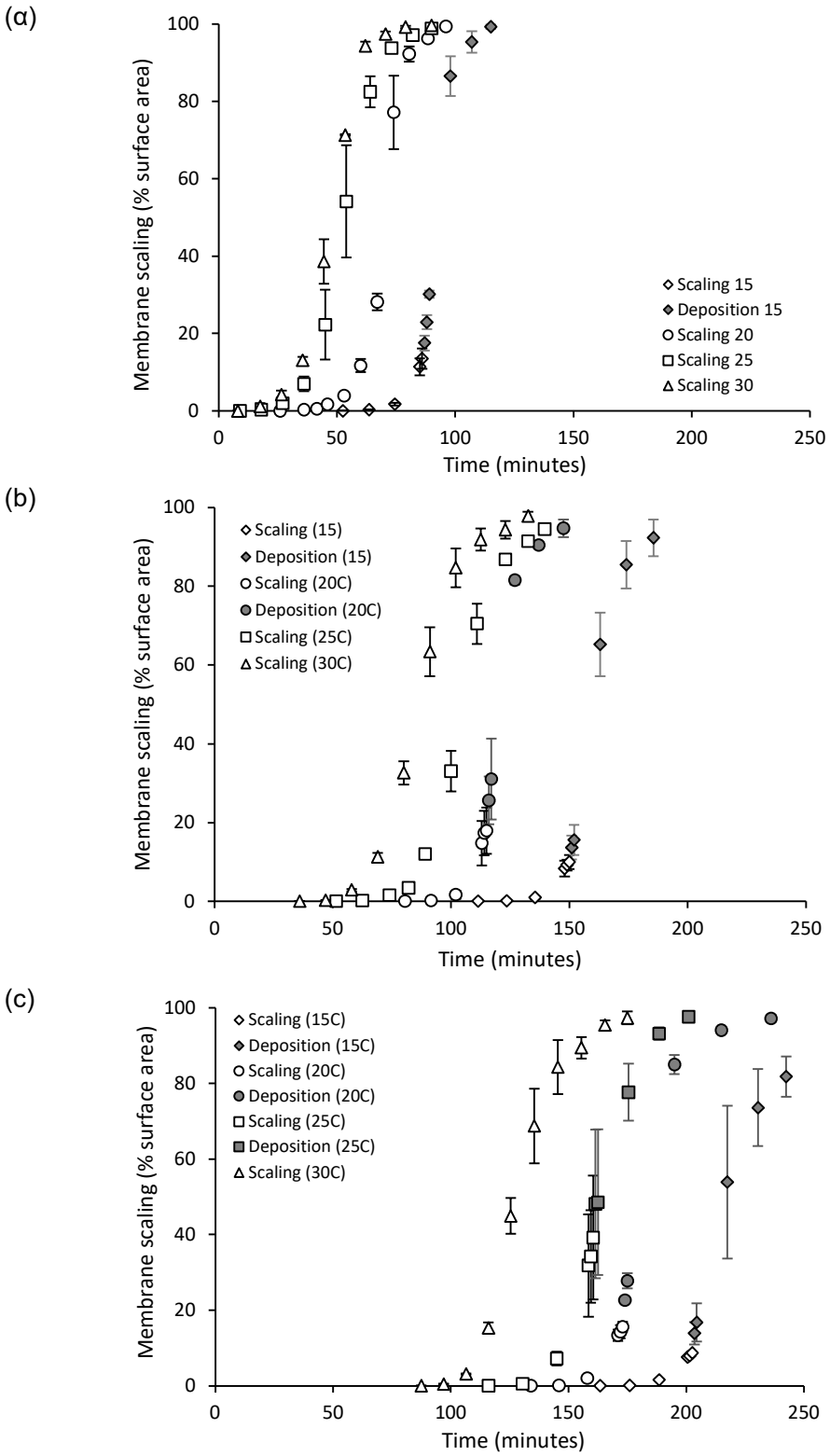

Figure 5.8 Extent of scaling for each ΔT and membrane: (a) polytetrafluoroethylene (PTFE), (b) polyvinylidene fluoride (PVDF), (c) polypropylene (PP) flat sheet membranes. Direct observation also permits the differentiation between adhesive growth (classical, scaling, open shapes) and deposition (following homogeneous nucleation in the bulk solution, closed circles).

The earlier onset of scaling observed with the PTFE membrane can be accounted for by the higher water vapour flux, which set a greater concentrating rate in solution (Figure 5.9). Data are evaluated at the induction time for scaling. The mass and heat transfer experienced by the PTFE membrane due to the larger porosity and h_c, resulted in the greatest concentration and temperature polarisation observed of the three membranes. This was particularly evident from the gradient of the K_2SO_4 boundary layer solubility coefficient which reduced considerably in response to an increase in ΔT. While a higher concentrating rate was instigated by the PVDF membrane in comparison to the PP membrane, which increased concentration polarisation, a higher temperature polarisation was observed. Consequently, a considerably higher K_2SO_4 solubility limit was achieved in the boundary layer for the PVDF membrane at an equivalent concentrating rate. As such, an equivalent supersaturation was established in the boundary layer for the PVDF membrane (ΔT 20°C) and PP membrane (ΔT 30°C) but a crystal phase was only produced in the bulk solution with the PVDF membrane. Similarly, a comparable supersaturation was established between the PVDF (ΔT 30°C) and PTFE (ΔT 15°C) membrane at an equivalent concentrating rate, but a crystal phase was only produced in the bulk solution with the PTFE membrane (Table 5.2).

(α)

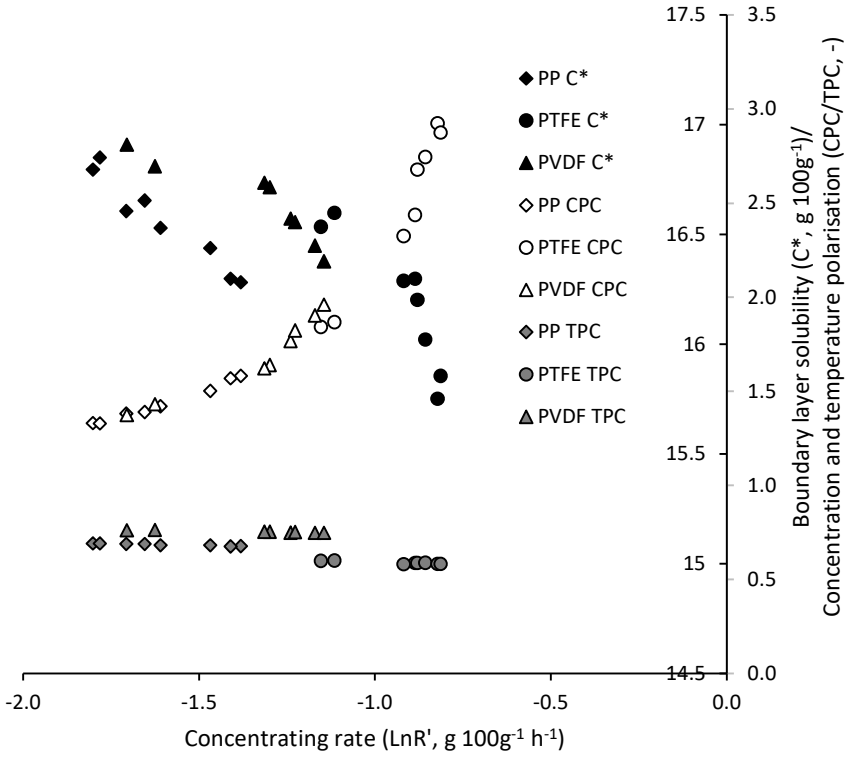

(b)

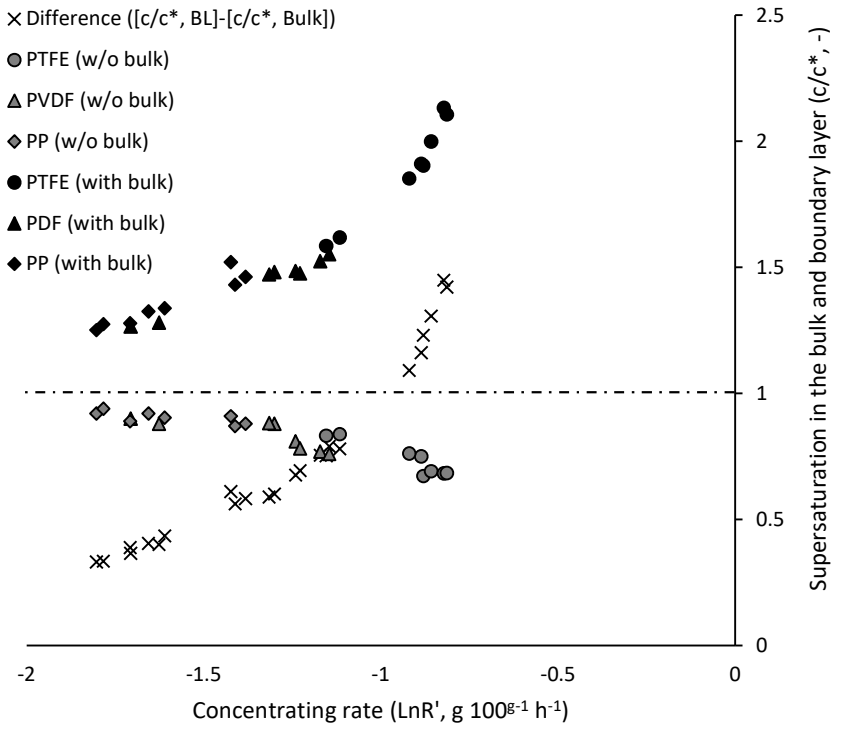

Figure 5.9 Uncoupling and demonstrating the effect of the: (a) concentration polarisation coefficient and the boundary layer concentration as well as the (b) temperature polarisation coefficient and the boundary layer solubility in the concentrating rate of the experiments.

Table 5.2 Comparison at equivalent concentrating rates where crystals were either observed or not observed with different membranes.

Comparison	Material	$Nucl._{bulk}$[a] observed	Scaling at $Nucl._{bulk}$ (%)[b]	dT (°C)	Concentrating rate (LnR', g $100g^{-1}$ h^{-1})	BL Solubility (C*, %wt.)	Comment
Heat transfer coefficient/ Porosity	PP	No	N/a	30	-1.40±0.02	16.29	*PVDF has a 6.4% higher concentrating rate, which shortens induction time, and can sustain a boundary layer solubility 2.7% higher, due to lower conductive loss and higher mass transport*
	PVDF	Yes	21.6	20	-1.31±0.01	16.72	
	Difference				-0.089	0.44	
Porosity	PVDF	No	N/a	30	-1.16±0.02	16.41	*PTFE has a 2.4% higher concentrating rate, and yet sustains a boundary layer solubility that is 0.9% higher, due to the higher porosity which enables higher fluxes, and shorter induction times for bulk crystals*
	PTFE	Yes	18.2	15	-1.14±0.03	16.57	
	Difference				-0.024	0.15	

[a]$Nucl._{bulk}$ – bulk nucleation. [b]Extent of scaling detenced at the onset of bulk nucleation.

With an increase in concentrating rate, the supersaturation in the boundary layer increased and the commensurate supersaturation in solution at the inception of scaling decreased. This is distinct from the induction time for the nucleation of the bulk crystal phase where the bulk solution must achieve saturation (K_2SO_4 concentration equivalent to the solubility limit) before a thermodynamically stable crystal phase can be formed. The increase in supersaturation reduced the time to nucleation To illustrate, the median time to induction for scaling, where a bulk crystal phase was not formed, was 31 minutes and is commensurate with the highest concentrating rates established with each membrane. This corresponds to classical nucleation theory in which a higher supersaturation will shorten induction time and induce a greater nucleation rate. In comparison, the median time to induction for scaling, where formation of a bulk crystal phase followed scaling was 114 minutes. The time lag following scaling to bulk nucleation ranged between 24.5 minutes (PTFE) and 44.5 minutes (PP) (Figure 5.10). Scaling morphology was characterised for each membrane at an equivalent ΔT (Figure 5.11). For each membrane, the predominant crystallographic <010> and <021> faces were absent from the scale, creating a different crystal habit from that of the bulk crystal phase, and the crystal size was markedly higher. Desarnaud et al., (2018) observed how at lower supersaturation levels, the formed crystals scale in a more holistic way, growing with a similar rate in from every face. On the other hand, at higher supersaturation levels, the faces at the edge of the crystal grows faster than the faces in the middle of the crystal. In the potassium sulphate, the faces growing faster in the higher saturation levels are the <001> and <100>, with the crystals resulting in needle shaped crystals. In the lower saturation level <010> faces are also growing as fast, resulting in more pyramid shaped crystals (Figure 5.6) (Mullin and Gaska, 1973). As the supersaturation levels vary between the membranes used, this also results in nucleation rate and growth rate differences as the process moves more towards homogeneous or heterogenous nucleation. Because of this, PTFE has the most and smaller needle shaped crystals, while the PP has the least and bigger pyramid shaped crystals (Figure 5.5) (Roelands et al., 2006). These morphological differences imply distinctive growth mechanisms between the two crystal phases. This is complemented by nucleation kinetic parameters which describe the supersaturation driving force for scaling and the bulk crystal phase as two discrete systems. However, scaling does appear to control the probability for the occurrence of a bulk crystalline phase in the case of K_2SO_4, and the relationship between the nucleation and growth kinetics of scaling and the nucleation kinetics of the bulk crystal phase is therefore further investigated.

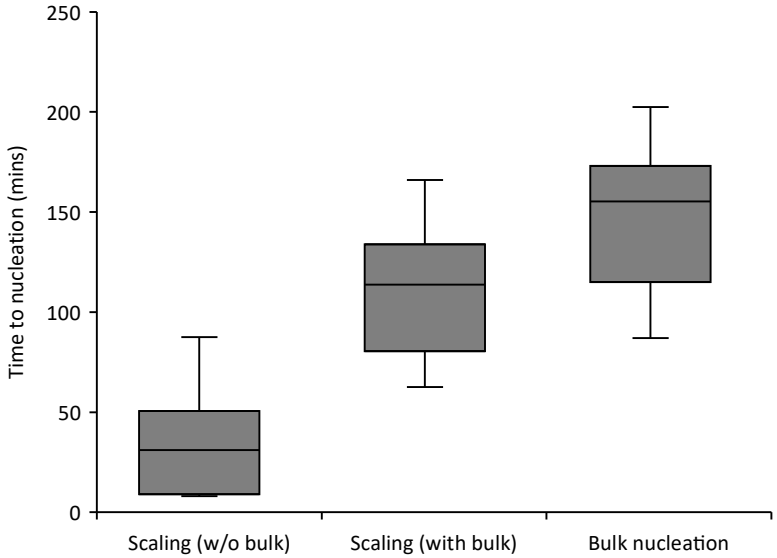

Figure 5.10 Time to nucleation where the boxes represents median (50th percentile, centre line), 25th and 75th percentiles, whereas whiskers represent minimum and maximum times recorded.

(a)

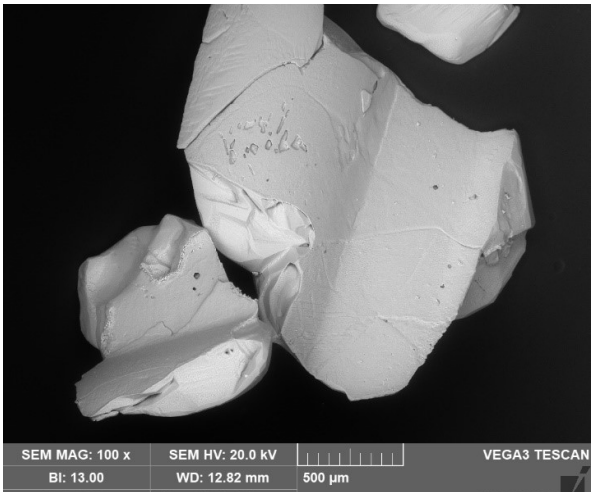

(b)

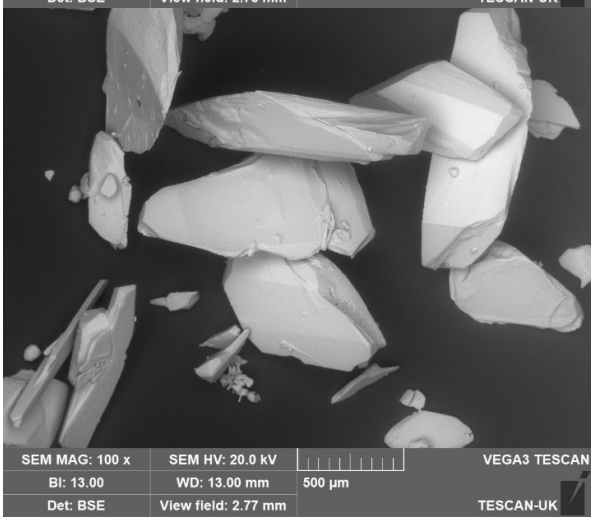

(c)

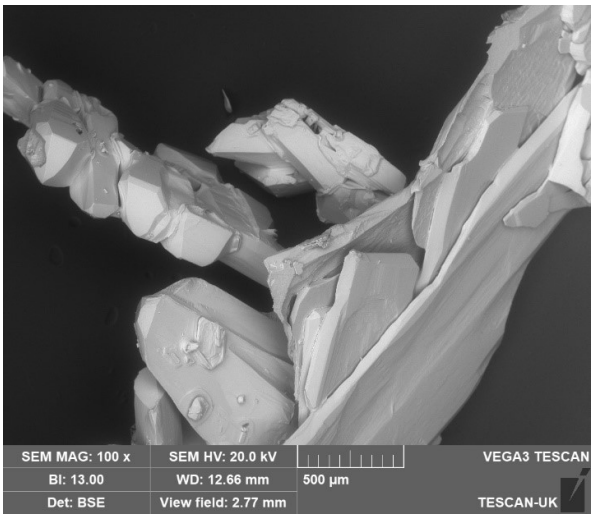

Figure 5.11 Membrane crystals resulted from scaling for (a) PTFE 15°C (b) PVDF 15°C (c) PP 15°C.

5.3.3 Determining how scaling informs the probability and nucleation kinetics of bulk crystals

To establish how scaling impedes the onset of bulk nucleation, the scaling growth rate was characterised (dA/dt, m^2 min^{-1}). Crystal growth rate (R_g) is determined by the concentration driving force (ΔC):

$$R_G = K_G(\Delta C)^g \qquad (Eq.\ 5.21)$$

For conditions where scaling occurred in the absence of bulk nucleation (Figure 5.12a and b), scaling growth rate initially increased with the rise in ΔC (kgK_2SO_4 kgH_2O^{-1}) following the commencement of scaling. This increase in ΔC is due to the progressive concentration of the feed solution due to the withdrawal of water vapour. The extent of the growth rate and ΔC was dependent on the mass and heat transfer processes introduced by the membrane properties and ΔT applied. However, as growth rate increased, a hysteresis was observed where the scaling growth rate decreased as the concentration driving force reduced. The reduction in ΔC can be ascribed to the extent of scaling which suppressed mass and heat transfer mechanisms. For conditions in which a bulk crystal phase was produced, the scaling growth rate increased with an increase in ΔC up to the onset of bulk nucleation and only limited hysteresis was observed prior to bulk nucleation (Figure 5.12c). We suggest the distinction in these two outcomes arises from the high concentrating rates that are commensurate with conditions in which bulk nucleation does not occur. This leads to nucleation for scaling within a much shorter time interval (Figure 5.10), enabling long-term exposure for crystalline growth of the scale within a highly supersaturated boundary layer.

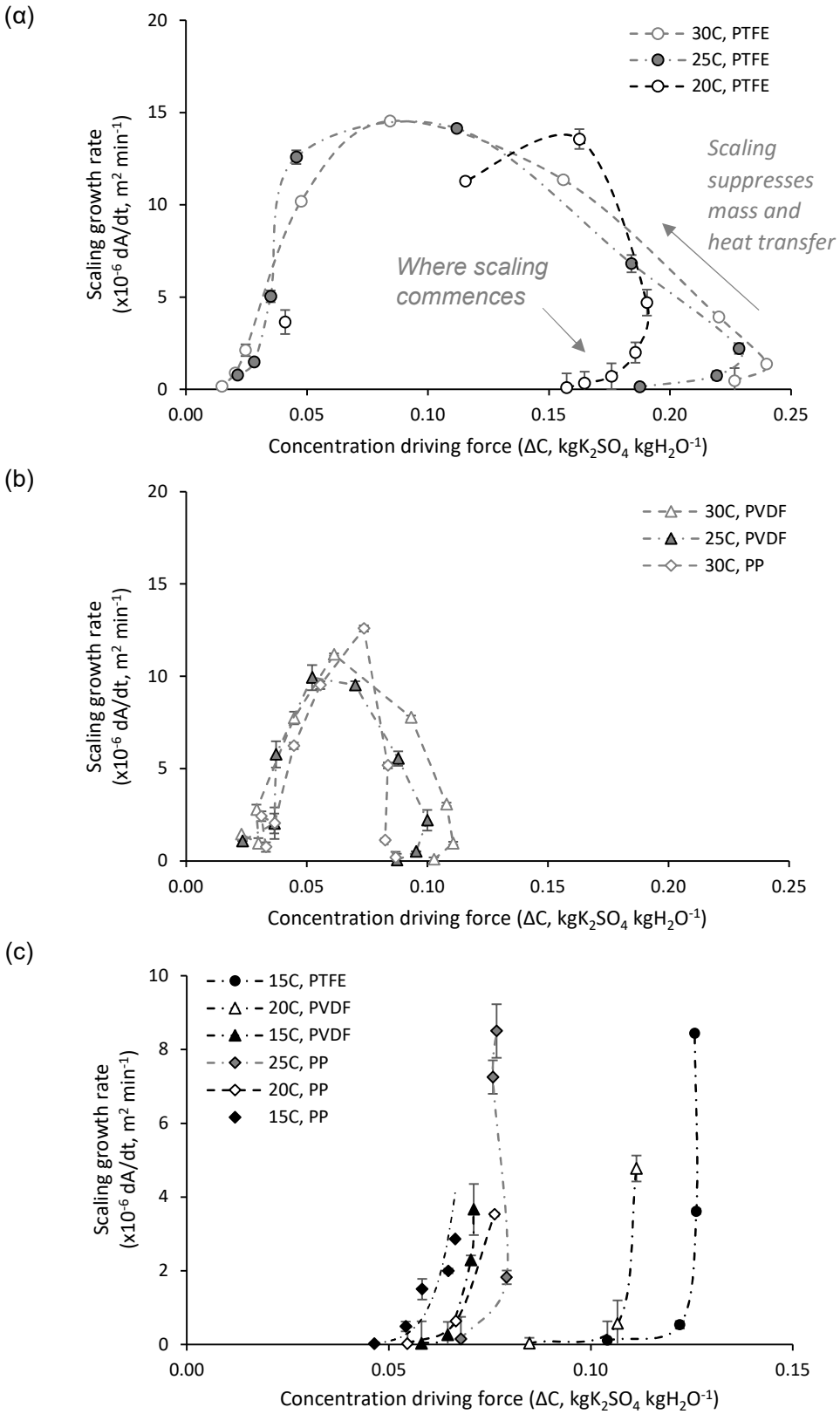

Figure 5.12 The evolution of the scaling growth rate due to the progressive concentration of the feed solution in the different temperature where bulk nucleation does not occur for (α) PTFE (b) PVDF and (c) combined for the temperature where nucleation occurs but prior to it.

The concentrating rate determines the extent of supersaturation that is achieved at induction time, and subsequently represents the driving force for nucleation in the bulk phase (Eq. 5.19, Figure 5.4) and for the nucleation of scaling (Figure 5.9). Supersaturation is therefore kinetically controlled by the mass and heat transfer processes set by the membrane characteristics and ΔT applied. However, scaling (before bulk nucleation) was greatest at the lowest concentrating rate (22.9%; PP, ΔT 25°C) and highest concentrating rate (18.2%; PTFE, ΔT 15°C). The concentrating rate takes account of the increased boundary layer solute concentration and rate of concentration imposed by the higher flux, but the extent of scaling identified at the onset of bulk nucleation, did not correspond to the concentrating rate applied. Simultaneous mass and heat transfer processes also modify the boundary layer solubility coefficient (c*) which helps sets the extent of the supersaturation driving force applied ($\Delta c = c-c^*$). The boundary layer supersaturation also does not explain the extent of membrane scaling observed at the onset of nucleation in the bulk phase (Figure 5.13), but there is good correlation to the boundary layer solubility coefficient explicitly. The solubility coefficient also represents the minimum thermodynamic threshold for the metastable zone width. Consequently, lowering c* reduces the solute concentration (and time) required to facilitate an 'excess' boundary layer supersaturation, which increases the probability for nucleation and can lead to an extended lag time between the nucleation of scaling to the nucleation of the bulk crystal phase, leaving longer dwell times to facilitate scaling growth. This contrasts with the NaCl system, where lower concentrating rates mitigate scaling at induction (Vasilakos et al., In preparation).

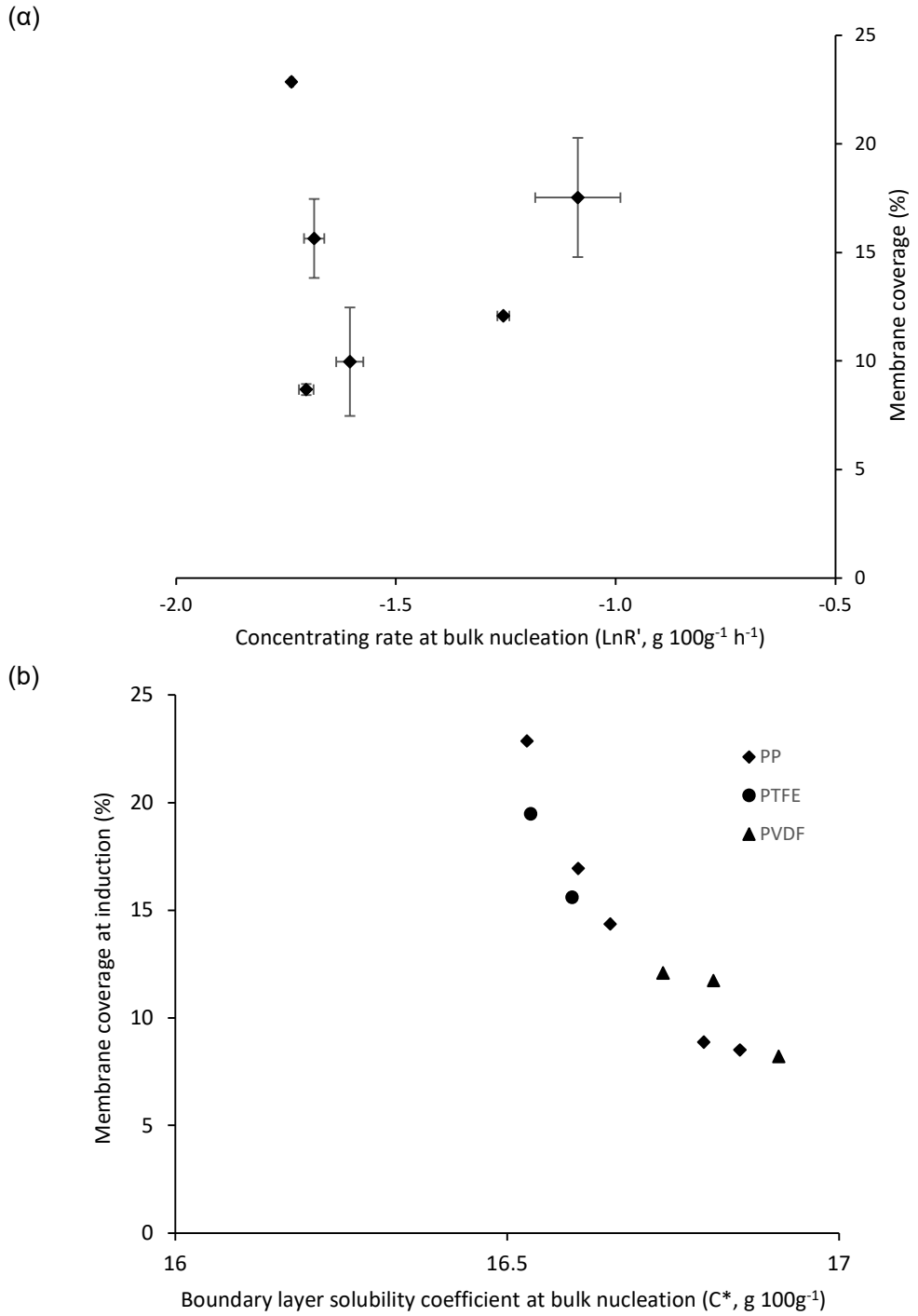

Figure 5.13 Correlation between the membrane scaling coverage at induction against (α) the concentrating rate at bulk nucleation where no corelation is observed and (b) the boundary layer solubility coefficient at bulk nucleation where the lowering c increases the probability for nucleation, leading to longer times to facilitate growth.*

The distinction with the K_2SO_4 crystallising system arises from the sharp solubility-temperature dependency (170mg $100g^{-1}$ $°C^{-1}$) which is substantially reduced by modifications to boundary layer temperature. In this study, the conditions which

facilitated the greatest scaling before bulk nucleation was observed, were responsible for the greatest shift in c*. This was due to an increase in mass transfer based on a higher porosity membrane (18.2%; PTFE, ΔT 15°C) or an increase in dT (22.9%; PP, ΔT 25°C). The nucleation rate for the bulk phase was measured from in-situ particle measurements using FBRM (Figure 5.3). The nucleation rate for the bulk crystal phase was found to be dependent on the boundary layer solubility coefficient (Figure 5.14a). While c* is indirectly related to the extent of supersaturation, it does not directly relate to the kinetics of nucleation. Instead, c* re-establishes the thermodynamic limit that determines the extent of scaling, and it is the extent of scaling, that governs the nucleation kinetics of the crystal phase in the bulk solution. This is explained by the suppression of the concentrating (or supersaturation) rate at induction by the mitigation of heat and mass transfer processes due to scaling, which constrains the rise in nucleation rate following induction by limiting the rate at which solute can be concentrated leading to the desaturation of solution. Consequently, mechanisms to decouple heat and mass transfer systems in MDCr may prove advantageous for enhancing control of crystallisation in the bulk solution. This was evidenced in this study, with the PVDF membrane wherein a higher MSZW was established than for PP, and with less scaling, due to the lower heat transfer coefficient of the polymer, which subsequently fostered higher nucleation rates in the bulk solution due to its effect in the TPC of the solution (Eq. 5.11 – 5.13).

(α)

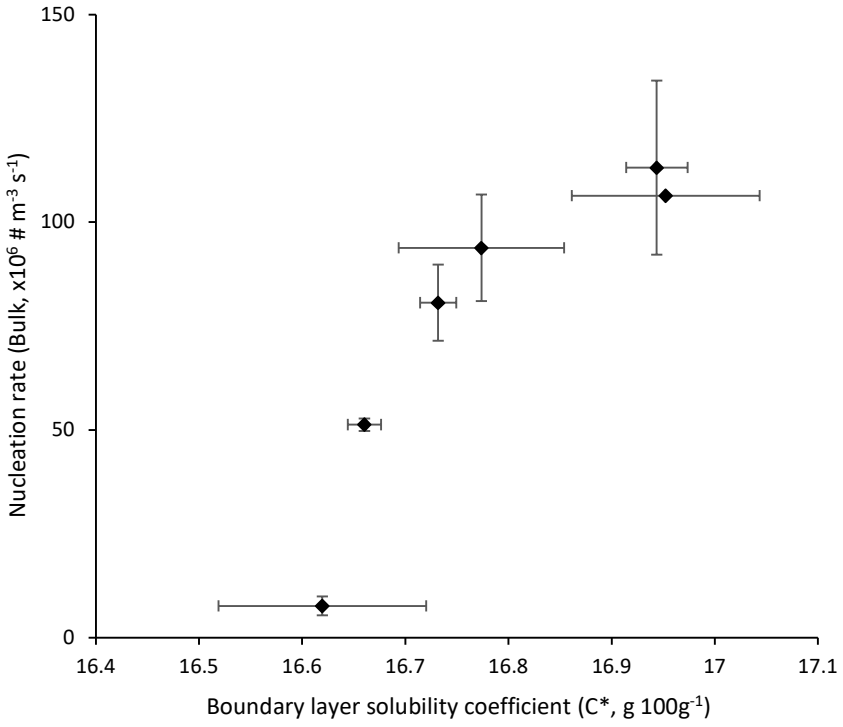

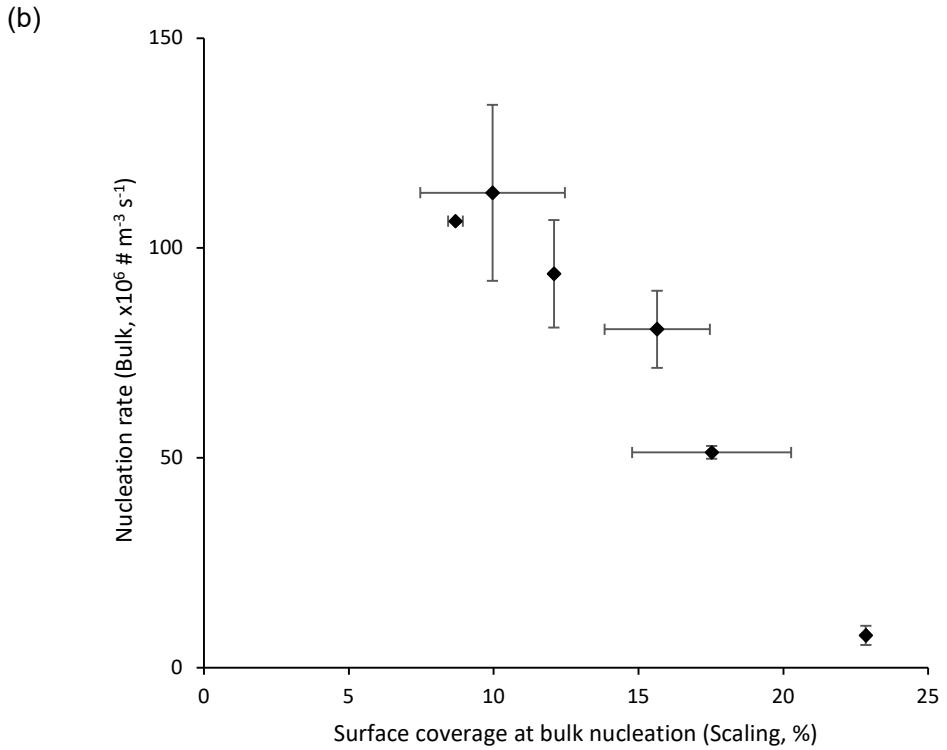

Figure 5.14 Nucleation rate (measured using FBRM): (a) increases as the boundary layer coefficient increases due to the homogeneous nucleation moving to higher saturation levels and (b) decreases as the surface scaling is more intensive where the temperature difference is higher and it consumes most of the salt, leaving less salt available for the bulk.

5.4 Conclusions

The crystallisation mechanisms for salts comprised of a sharp solubility-temperature dependency have been elucidated and related to the mass and heat transfer processes within membrane distillation to enhance the selection of membrane and operational characteristics for improved control over nucleation and crystal growth. While the implications of salts of similar characteristics have been inferred, the consequences to scaling or crystal growth mechanisms have been previously poorly understood. Advanced characterisation tools in this study showed that nucleation was directly correlated the supersaturation driving force that was set by mass and heat transfer processes originating from the membrane properties and thermal difference applied. The correlation between supersaturation and concentrating rate imply that nucleation for scaling and the bulk crystal phase are primarily kinetically controlled by supersaturation (ΔG_v) rather than surface topography and material wettability (ΔG_s) which would have otherwise reduced the supersaturation requirement for induction (ΔG^*). This characterisation also evidences that the nucleation of scaling and the bulk crystal phase can be described as independent mechanisms, which is supported by the formation of uniquely faceted crystal habits. While the onset of scaling nucleation

was directly correlated to supersaturation level, which was kinetically controlled within the boundary layer, modification of the solubility limit also reduced the thermodynamic barrier of the metastable zone width which increases the time the boundary layer exists in a supersaturated state; this enhances the extent of scaling that can occur before bulk nucleation. For brines comprised of salts characterised by sharp solubility-temperature dependencies, temperature polarisation therefore represents an important characteristic for scaling control, wherein polymers that can differentiate mass and heat transfer mechanisms may be preferred (e.g. high porosity and a low heat transfer coefficient), and are potentially distinct from material demands of other membrane distillation applications. While we propose that the nucleation mechanisms of scaling and the bulk crystal phase are distinct, the extent of scaling indirectly controls nucleation rate of the bulk crystal phase through suppressing mass and heat transfer processes following nucleation. To better control crystallisation, development of a broader metastable zone width, using a polymer with a poor heat transfer characteristic can mitigate the controlling effect of scaling by limiting the lag time between scaling and bulk nucleation. However, a broad metastable zone width can also foster more complex crystal habits. A narrower metastable zone width may therefore be sustainably achieved through an alternate driving force (e.g. vacuum) to direct-contact, by mitigating scaling through limiting temperature polarisation.

5.5 Acknowledgements

This research was financially supported through European Research Council Starting Grant, ‘Sustainable chemical alternatives for reuse in the circular economy’ (StG, SCARCE, 714080).

5.6 References

A. Ali, F. Macedonio, E. Drioli, S. Aljlil, O.A. Alharbi, Experimental and theoretical evaluation of temperature polarization phenomenon in direct contact membrane distillation, Chem. Eng. Res. and Des. 91 (2013) 1966-1977.

S. Bavarella, B. Luqmani, N. Thomas, A. Brookes, A. Moore, P. Vale, M. Pidou, E.J. McAdam, CO_2 absorption into aqueous ammonia using membrane contactors: Role of solvent chemistry and pore size on solids formation fow low energy solvent regeneration, Sep. Pur. Technol. 290 (2022) 120786.

S. Berg, D. Kutra, T. Kroeger, C.N. Strahle, B.X. Kausler, C. Haubold, M. Schiegg, J. Ales, T. Beier, M. Rudy, K. Eren, J.I. Cervantes, B. Xu, F. Beuttenmueller, A. Wolny, C. Zhang, U. Koethe, F.A. Hamprecht, A. Kreshuk, Ilastik: interactive machine learning for (bio)image analysis, Nature Methods. 16 (2019) 1226 – 1232.

E. Chabanon, D. Mangin, C. Charcosset, Membranes and crystallisation processes: State of the art and prospects, J. Membr. Sci. 509 (2016) 57–67.

Y. Choi, G. Naidu, L.D. Nghiem, S. Lee, S. Vigneswaran, Membrnane distillation crystallisation for brine mining and zero liquid discharge: opportunities, challenges, and recent progress, Env. Sci. Water Res. & Technol. 5 (2019) 1202.

E. Curcio, E. Drioli, Membrane distillation and related operations – a review, Sep. Pu. Rev. 34 (2005) 35–86.

G. Di Profio, E. Curcio, E. Drioli, Supersaturation control and heterogeneous nucleation in membrane crystallizaers: facts and perspectives, Ind. Eng. Chem. Res. 49 (2010) 11878–11889.

A.R. Heath, P.D. Fawell, P.A. Bahri, J.D. Swift, Estimating average particle size by focused beam reflectance measurement, Part. Part. Syst. Charact. 19 (2002) 84–95.

X. Jiang, X Ruan, W. Xiao, D. Lu, G. He, A novel membrane distillation response technology for nucleation detection, metastable zone width measurement and analysis, Chem. Eng. Sci. 134 (2015) 671–680.

A. Jikazana, P. Moreno Campo, E.J. McAdam, Hydrodynamics (*Reynolds number*) determine scaling, nucleation and crystal growth kinetics in membrane distillation crystallisation, J. Membr. Sci. 685 (2023) 121909.

V. Karanikola, C. Boo, J. Rolf, M. Elimelech, Engineered slippery surface to mitigate gypsum scaling in membrane distillation for treatment of hypersaline industrial wastewaters, Environ. Sci. Technol. 52 (2018) 14362–14370.

J.W. Kim, J. Kim, K.-D. Lee, K.-K. Koo, Evaluation of nucleation rate by in-situ focused beam reflectance measurement in an unseeded batch cooling crystallisation, Crys. Res. Technol. 48 (2013) 1097–1105.

H. Marx, S. Kaps, B. Schultheis, M. Pfänder, Potassium sulphate – A precious by-product for solar salt works, Bull. Soc. Sea Water Sci. Jpn. 73 (2019) 89-93.

A. McLeod, P. Buzatu, O. Autin, B. Jefferson, E. McAdam, Controlling shell-side crystal nucleation in a gasi-liquid membrane contactor for simultaneous ammonium bicarbonate recovery and biogas upgrading, J. Membr. Sci. 473 (2015) 146 – 156.

A. Mersmann, M. Kind, Chemical Engineering Aspects f Precipitation from Solution, Chem. Eng. Technol. 11 (1988) 264 – 276.

N.A. Mitchell, P.J. Frawley, C.T. Ó'Ciardhá, Nucleation kinetics of paracetamol–ethanol solutions from induction time experiments using Lasentec FBRM®, J. Cryst. Growth 321 (2011) 91–99.

J. Mullin, C. Gaska, Potassium Sulphate Crystal Growth Rates in Aqueous Solution, J. Chem & Eng. Data, 18 (1973) 115 – 140.

J. Nývlt, Kinetics of nucleation in solutions, J. Cryst. Growth. 3, 4 (1968) 337 – 383.

A. Ouda, Y. Bajón Fernández, E. McAdam, Modifying supersaturation rate with membrane area can minimise scaling and improve control over crystal growth in membrane distillation crystallisation, J. Membr. Sci. 683 (2023) 121838.

F.M. Penha, G.P. Zago, Y.N. Nariyoshi, A. Bernardo, M.M. Seckler, Simultaneous crystallisation of NaCl and KCl from aqueous solution: Elementary phenomena and product characterisation, Cryst. Growth Des. 18 (2018) 1645-1656.

C. P. M. Roelands, J. H. ter Horst, H. J. M. Kramer, P. J. Jansens, Analysis of Nucleation Rate Measurements in Precipitation Processes, Cry. Gro. & Des. 6 (2006) 1380 – 1392.

I. Ruiz Salmon, P. Luis, Membrane crystallisation via membrane distillation, Chem. Eng. Process. Process Intensif. 123 (2017) 258–271.

K. Sangwal, On the linear and integral models for metastable zone width determined by solution cooling method, J. Cryst. Gro. 576 (2021) 126377.

C.M. Tun, A.G. Fane, J.T. Matheickal, R. Sheikholeslami, Membrane distillation crystallisation of concentrated salts-flux and crystal formation, J. Membr. Sci. 257 (2005) 144–155.

J. Ulrich, C. Strege, Some aspects of the importance of metastable zone width and nucleation in industrial crystallizers, J. Cryst. Growth 237 (2002) 2130–2135.

6 Discussion

The chapters of this thesis have presented a comprehensive framework for the recognition of essential factors and parameters that dictate crystallisation in MDCr. The use of aqueous salts with distinct crystal-liquid interfacial energy, have enabled the relevance of thermodynamics to membrane crystallisation to be characterised and differentiated from those factors such as temperature difference and hydrodynamics which modify supersaturation within the boundary layer to regulate the kinetics of crystallisation. The relevance of both thermodynamics and kinetics to crystal growth are also defined. The collective new knowledge can be used to provide a framework through which the extent of scaling, nucleation and crystal growth kinetics can be ascertained based on the physical characteristics of the salt and the boundary layer conditions set by mass and heat transfer processes. The outcomes therefore provide useful new knowledge for the design of batch or continuous MDCr designs for complex solutions, and can be extended to wider membrane technologies, or non-membrane technologies where scaling or crystallisation processes manifest as either a direct or indirect consequence of water processing (e.g. heat exchangers). The following themes are intended to extend this context and enrich the narrative of the thesis through synthesising outcomes to provide implications for membrane crystallisation and crystallisation control more generally.

6.1 How thermodynamic properties relate to crystallisation mechanisms in MDCr

According to the CNT theory, there is a cubic relationship between ΔG^* (activation energy) and interfacial free energy (Torrens-Serra et al., 2009). This means that salts with high interfacial energy need to reach greater saturation levels, which in turn causes them to enter the homogenous spectrum of the metastable zone width. While this outcome can be justified based on CNT, this contradicts the general membrane literature which consistently identifies high interfacial energy salts as the primary scalants (Darton et al., 2004; He et al., 2008; Rezai et al., 2018; Alkhatib et al., 2021). This is because researchers mistakenly conflate the roles of adhesive scaling and deposition, failing to distinguish between the two. In this study, we make it possible to distinguish between these mechanisms, through introducing two non-invasive detection techniques. This unique approach has permitted new evidence for scaling which is complimentary both to CNT and to the empirical study to scaling, thereby providing a unifying answer for how to establish the probability for scaling in any membrane system. It is generally also assumed due to the presence of the membrane, that crystallisation will follow a heterogeneous primary nucleation mechanism (Drioli

and Efrem, 2005; Tun et al., 2005; Wang et al., 2014). This is due to the theory for how a substrate can modify the crystal-liquid interfacial energy ($\Delta G = \Delta G_v + \Delta G_s$, Chapter 3) which reduces the supersaturation requirement to achieve primary nucleation. However, the conventional scalants (e.g. $CaSO_4$) possess a high crystal-liquid interfacial energy which sets a requirement for substantive supersaturation to be achieved (G_v) to surpass the critical Gibbs free energy requirement for nucleation; the consequence is that once this supersaturation is achieved, it is sufficient to bypass heterogeneous nucleation, toward homogeneous primary nucleation leading to no scaling (Chapter 1). In the case of membrane distillation, the membrane is hydrophobic which is characterised by a high-water contact angle. A high-water contact angle is also unlikely to significantly contribute toward the modification of the crystal liquid interfacial energy. However, reverse osmosis membranes possess a much lower water contact angle (<90°) which may make such materials more prone to scaling due to the possible reduction in supersaturation demanded for nucleation to commence. While further work is required to establish the translation of this understanding to more hydrophilic materials, the poor solubility of the identified scalants will inevitably lead to the requirement for conditions of elevated supersaturation, the consequence of which, based on this work is that scaling does not proceed via an adhesive growth mechanism (initiated by the membrane).

The misconception for the low interfacial energy salts being the scalants may arise from the ease with which the crystals formed in the bulk solution bind to the membrane following deposition, which poses challenges in its removal (Gryta, 2008). Conversely, salts with low crystal-liquid interfacial energy (e.g. NaCl) are more likely to nucleate at the membrane due to the limited supersaturation that can be created; the result is the formation of a scale that is more easily cleaned. This phenomenon can be attributed to the greater crystallite - water work of adhesion force (W_{23}) exhibited by salts with higher interfacial energy and the significantly lower W_{23} adhesion force of salts with lower interfacial energy. As W_{23} is reduced, the membrane becomes more attractive to the crystal resulting in a higher membrane – crystallite affinity (W_{12}) and a higher W_{12}/W_{23} ratio. The outcome is a stronger affinity between the crystal and the membrane, making it more difficult for the crystal to be removed from the membrane. The literature often assumes that it is the adhesion force which contributes toward the nucleation of scaling, while it actually describes the strength of the bond after the formation of scaling, between the crystallite and the membrane surface (Liu et al., 2024). This is corroborated within the materials literature in which the surface free energy analysis of scaling is reliant on both the crystal and crystal-liquid interfacial energy (Mersmann, 1990). This was observed within this thesis, where crystals could

be more easily separated from membranes scaled from high interfacial energy salts through the use of solvent washing compared to the scale produced from low interfacial energy salts. Further work, beyond the qualitative observations made within this thesis could be made to quantify these effects, therefore further extending and confirming understanding of the nucleation mechanisms, and adhesion behaviour of scaling. It has to be noted that the feed conditions used were laminar. By modifying the force balance acting on these particles in the flow through the use of hydrodynamics, it may be possible to mitigate the deposition of crystals by retaining the particles within the bulk suspension (Liu et al., 2022).

The extent of supersaturation is also determined by the solubility limit of the suspension, which is strongly correlated to temperature. Most salts mostly exhibit a positive solubility-temperature dependency, with few exceptions such as Na_2SO_4, Li_2SO_4 and $CaSO_4$ (above 32.4°C). In processes like MDCr where high temperature differences are used, the increase in heat and mass transfer processes enhance temperature polarisation. This leads to changes in the solubility limit and the solute concentration locally adjacent to the wall, increasing the probability for scaling through adhesive growth, contributing to a reduction in the critical Gibbs energy required for crystallisation (Chapter 3 & 4). While not well described, this scaling tendency which is dominated by thermal modification of the solubility limit rather than of the solute concentration, has also be observed elsewhere, such as for reverse osmosis (RO) (Liu et al., 2019; Matin et al., 2019), heat exchangers (Kapustenko et al., 2023) and in-pipe struvite formation in wastewater (Prot et al., 2021). The arising new knowledge within this thesis can therefore be transferred to these areas to improve diagnostics and scaling mitigation strategies.

6.2 How kinetics relate to crystallisation in MDCr

The literature to date proposes that the membrane surface can be used in crystallisation to decrease the surface free energy required for nucleation (ΔG_s), hence reducing the level of supersaturation needed to initiate crystallisation (Curcio et al., 2006; Erdemir et al., 2019). In principle, this favours heterogeneous primary nucleation, which in turn encourages the formation of scaling (Shirazi et al., 2010; Meng et al., 2015). This is emphasised on the more soluble salts where the high solubility leads to the development of only very low supersaturation in solution which can increase the probability for scaling, since the membrane is more likely to be of importance in the modification of the crystal-liquid interfacial energy to compensate for the low level of supersaturation. However, by modifying ΔT it is possible to increase supersaturation through adjusting the kinetics of crystallisation. As the concentration

rate of solution increases through an increase in ΔT, a higher supersaturation level is established within the boundary layer, shortening the induction time for bulk nucleation, increasing the nucleation rate. Even though this should result to crystallisation occurring within the upper region of the MSZW, where primary nucleation is more likely to occur by a homogeneous mechanism, resulting in less scaling, the contrary is happening when ΔT is increased. This is happening because while induction time is shorter for bulk nucleation, due to the higher supersaturation level that is reached, an equivalent (but higher) supersaturation level is developed that accelerates scaling, incurring shorter induction time and higher levels of growth. As a result, the difference in the induction between the onset of scaling and bulk nucleation increases with an increase in ΔT, causing higher scaling rates prior to nucleation. Scaling is therefore also kinetically controlled and is most severe in conditions that can be locally described as favouring homogeneous primary nucleation (Jikazana et al., 2023). A decrease in ΔT can therefore minimise scaling but will also limit control over nucleation kinetics which may be important for regulating properties of the crystal. To mitigate scaling at higher ΔT, to broaden where within the MSZW that MDCr can be operated, higher membrane area-to-volume ratio could be used. Increasing the membrane area in relation to the feed volume enables higher supersaturation rates to be achieved without modifying the boundary layer conditions. This permits greater nucleation rates to be established within higher regions of the MSZW without incurring scaling, as the concentration difference between the bulk and the boundary layer diminishes. Consequently, the probability of nucleation in the bulk solution becomes comparable, if not greater, than that on the membrane surface (Ouda et al., 2023). Therefore, by coupling high ΔTs with higher area-to-volume ratios, very high nucleation rates can be achieved without scaling.

6.3 Implications for application of MDCr to real brines

The primary focus of MDCr is to address the treatment of seawater. Brines consist of several salts with different solubilities and solubility-temperature relationships at varied concentrations. The fundamental reason why calcium sulphate ($CaSO_4$), calcium carbonate ($CaCO_3$), and barium sulphate ($BaSO_4$) are considered the primary scalants for seawater is that their initial concentrations are very close to their solubility limits (S≈1) (Shah et al., 2022; Poirier et al., 2023; Sabour and Ghorashi, 2024). Due to the high initial concentration of these salts, they are the first to undergo crystallisation. However, based on this work, since the membrane is not involved in the formation of adhesive scale by this group of poorly soluble salts, (Chapter 1), the optimal approach to mitigate scaling is to avoid the deposition of crystals formed within the bulk solution

by segregating the crystal phase before it contacts with the membrane with the use of a crystallizer or inline filtration process prior to the membranes.

To mitigate scaling from high solubility salts that are initially less saturated and crystallise at a later stage compared to the homogeneously nucleated salts, it is crucial to regulate their formation as well as their kinetics. This can be achieved by reducing ΔT in order to reduce transmembrane flux and temperature polarisation, hence minimising the concentration difference between the membrane and bulk solution which will favour nucleation in the bulk solution (Chapter 3). Simultaneously, the solution can also be pre-seeded with crystals, which can be used to control the level of available supersaturation, and enable control in the lower region of the MSZW ('growth only' zone), which exists between the solubility curve and the region where nucleation begins to dominate over growth (Threlfall and Coles, 2016) (Figure 6.1). By operating at supersaturation levels below the primary nucleation threshold, it is not possible to commence nucleation and therefore scale formation is minimised. Consequently, greater stability and longer term operation could be achieved; such an analogy can also be made to conditions in which primary nucleation is first favoured in the bulk solution, as the crystal phase once formed may be sufficient to reposition the system in the MSZW due to the desaturation of solution, dependent on the balance between the concentrating rate applied and the rate of desaturation fostered by the growth of the crystal phase. Further work could establish how optimisation of this balance can control the quality of the arising crystal phase, and whether it improves or diminishes it. This could serve as a tool to facilitate the promotion of membrane crystallisation as a viable technique for brine treatment.

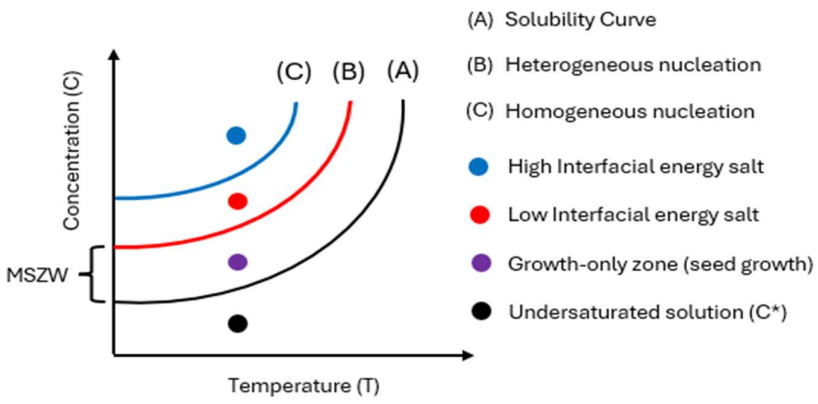

Figure 6.1 Connection between membrane-salt interfacial energy and metastable zone width of the solution.

6.4 Exploiting understanding for MDCr design

When low interfacial energy salts (scalants) are present, lower levels of TPC leads in reduced scaling and enhanced bulk nucleation. This is because the concentration of the solution between the membrane boundary layer and the bulk, which increases the amount of salt available in the bulk solution (Erdemir et al., 2019). By decreasing the temperature difference (ΔT) between the feed and permeate sides, the concentration gradient between the bulk solution and the membrane is reduced. This limits the formation of higher locally oversaturated regions on the membrane (Chapter 3). By simultaneously, increasing the membrane area-to-surface ratio, higher concentration rates are also imposed, pushing induction on higher supersaturation levels in the bulk solution. This modification does not affect the polarisation of the boundary layer and therefore does not alter the concentration gradient (Ouda et al., 2023). As such, the aim is to create conditions more favorable to homogeneous rather than heterogeneous nucleation. To further minimise temperature polarisation as a mechanism to mitigate scaling, more thermally efficient membranes such as PTFE (Chapter 3 & 4) or preferably alternative techniques, such as vacuum membrane distillation (VMD) should be used. VMD operates under reduced pressure conditions, effectively lowering the boiling point of the feed solution. This reduction facilitates similar transmembrane fluxes with smaller temperature differentials across the membrane. Additionally, VMD minimises convective heat transfer by utilising vacuum pressure instead of a cold solvent on the permeate side enhancing the efficiency of heat transfer. (Zhang et al., 2023; Dong et al., 2023; Gaspar et al., 2024). The result is a higher temperature polarisation coefficient which will contribute positively toward the mitigation of scaling.

In almost all circumstances, it is the deposition of crystals following bulk nucleation which leads to the suppression and ultimately the decline in flux. Systems level design should therefore consider how to retain and grow the crystal phase within the downstream crystalliser once nucleated by the membrane. This can be achieved by creating idealised conditions within the crystalliser, with modifications to upflow velocity, agitation, and hydraulic retention time to permit crystals to grow and settle inside the crystalliser, rather than being carried out of the system and towards the membrane in the recycle (Seckler, 2022). At the same time a reactor where the feed solution has to be prepared with the optimal operating conditions is needed (conditioning reactor). This can either be achieved by employing a single dual-purpose reactor that will be responsible for both crystallisation as well as conditioning in a sequential batch manner (Figure 6.2), or by utilising two distinct reactors for continuous operation, one dedicated to conditioning and the other to crystallisation (Figure 6.3). To prevent the crystals from reaching the membrane and maintain the continuity of the

process, an inline filter can also be installed to prevent carryover. The slower growth achieved through these adjustments allow for better control and ultimately result in a superior and more refined end product. As a result, creating higher purity crystals during crystallisation is economically vital due to its impact on market value, regulatory compliance, process efficiency, waste reduction, product performance, supply chain management, innovation, brand reputation, and competitive advantage.

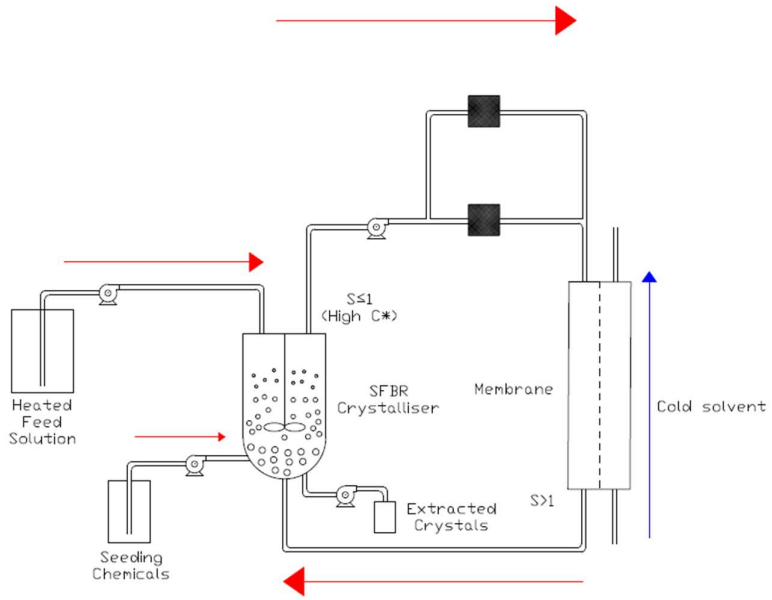

Figure 6.2 Proposed batch MDCr system

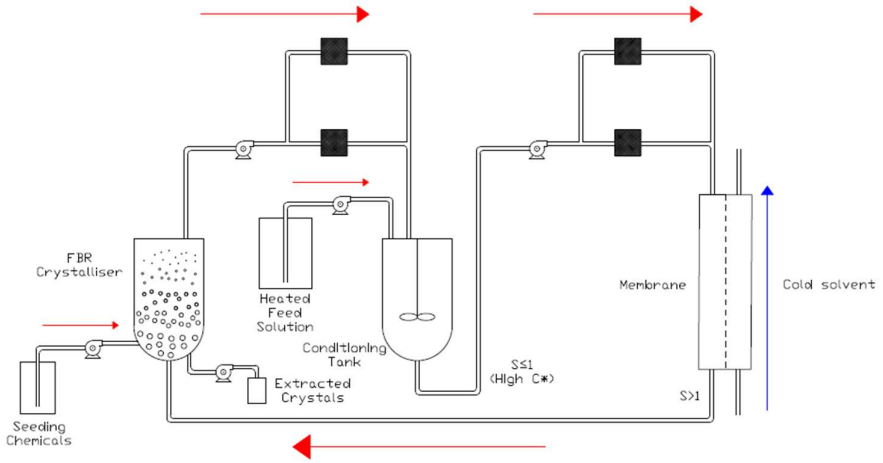

Figure 6.3 Proposed continuous MDCr system

6.5 References

A. Alkhatib, M. A. Ayari, A. H. Hawari, Fouling mitigation strategies for different foulants in membrane distillation, Chem. Eng. Proc. – Proc. Intens. 167 (2021) 108517.

E. Curcio, E. Fontananova, G. Di Profio, E. Drioli, Influence of the structural properties of poly(vinylidene fluoride) membranes on the heterogeneous nucleation rate of protein crystals, J. Phys. Chem. 110 (2006) 12438–12445.

T. Darton, U. Annunziata, F. del Vigo Pisano, S. Gallego, Membrane autopsy helps to provide solutions to operational problems, Desalination. 167(0) (2004) 239 – 245.

E. Drioli, C. Efrem, Membrane crystallisation in "Membrane Contactors: Fundamentals, Applications and Potentialities", Membr. Sci. Technol. 11 (2005) 254 – 272.

C. Dong, Y. Hang, L. Zhang, Slug flow-enhanced vacuum membrane distillation for seawater desalination: Flux improvement and anti-fouling effect, Sep. Pur. Technol. 320 (2023) 124178.

D. Erdemir, A. Lee, A. Myerson, Handbook of Industrial Crystallisation, Cambridge: Cambridge University Press, Chapter 3 (2019) 76 – 114.

J. Gaspar, G. Xue, A. Oztekin, Performance characteristics on up-scaling vacuum membrane distillation modules, Desalination. 569 (2024) 116994.

M. Gryta, Fouling in direct contact membrane distillation process, J. Membr. Sci. 325 (2008) 383 – 394.

F. He, H. Lee, L. Song, K. K. Sirkar, Potential for scaling by sparingly soluble salts in crossflow DCMD, J. Membr. Sci. 311(1-2) (2008) 68 – 80.

A. Jikazana, P. Campo, E.J. McAdam, Hydrodynamics (Reynolds number) determine scaling, nucleation and crystal growth kinetics in membrane distillation crystallisation, J. Membr. Sci. 685 (2023) 121909.

P. Kapustenko, J. J. Klemeš, O. Arsenyeva, Plate heat exchangers fouling mitigation effects in heating of water solutions: A review, Ren. and Sust. Ene. Rev., 179 (2023) 113283.

Q. Liu, G-R. Xu, R. Das, Inorganic scaling in reverse osmosis (RO) desalination: Mechanisms, monitoring, and inhibition strategies, Desalination, 468 (2019) 114065.

J. Liu, A. K. Albdoor, W. Lin, F. I. Hai, Z. Ma, Membrane fouling in direct contact membrane distillation for liquid desiccant regeneration: Effects of feed temperature and flow velocity, J. Membr. Sci. 642 (2022) 119936.

H. Liu, K. I. Jacob, Y. Wang, Scaling in membrane distillation (MD): Current state of art insight on mechanisms and Membrane design, Desalination. 581 (2024) 117539.

A. Matin, F. Rahman, H. Z. Shafi, S. M. Zubair, Scaling of reverse osmosis membranes used in water desalination: Phenomena, impact, and control; future directions, Desalination. 455 (2019) 135 – 157.

S. Meng, Y. Ye, J. Mansouri, V. Chen, Crystallisation behaviour of salts during membrane distillation with hydrophobic and superhydrophobic capillary membranes, J. Membr. Sci. 473 (2015) 165 – 176.
A. Mersmann, Calculation of interfacial energies, J. Cryst. Gro. 102 (1990) 841 – 847.
A. Ouda, Y. Bajón Fernández, E. McAdam, Modifying supersaturation rate with membrane area to volume ratio: Scaling reduction and improved crystal growth control in membrane distillation crystallisation, J. Membr. Sci. 683 (2023) 121838.
K. Poirier, M. Lotfi, K. Garg, K. Patchigolla, E. J. Anthony, N. H. Faisal, V. Mulgundmath, J. K. Sahith, P. Jadhawar, L. Koth, T. Morosuk, N. Al Mhanna, A comprehensive review of pre- and post-treatment approaches to achieve sustainable desalination for different water streams, Desalination. 566 (2023) 116944.
T. Prot, L. Korving, A.I. Dugulan, K. Goubitz, M.C.M. van Loosdrecht, Vivianite scaling in wastewater treatment plants: Occurrence, formation mechanisms and mitigation solutions, Water Res. 197 (2021) 117045.
M. Rezaei, D. M. Warsinger, J. H. Lienhard V, M. C. Duke, T. Matsuura, W. M. Samhaber, Wetting phenomena in membrane distillation: mechanisms, reversal, and prevention, Water Res. 139 (2018) 329 – 352.
S. M. J. S. Sabour, B. Ghorashi, A comprehensive review of major water desalination techniques and mineral extraction from saline water, Sep. Pur. Technol. 349 (2024) 127913.
M.M. Seckler, Crystallisation in Fluidized Bed Reactors: From Fundamental Knowledge to Full-Scale Applications, Crystals. 12 (2022) 1541.
K. M. Shah, I. H. Billinge, X. Chen, H. Fan, Y. Huang, R. K. Winton, N. Y. Yip, Drivers, challenges, and emerging technologies for desalination of high-salinity brines: A critical review, Desalination. 538 (2022) 115827.
S. Shirazi, C.-J. Lin, D. Chen, Inorganic fouling of pressure-driven membrane processes – a critical review, Desalination. 250(1) (2010) 236 – 248.
T. L. Threlfall, S. J. Coles, A perspective on the growth-only zone, the secondary nucleation threshold and crystal size distribution in solution crystallisation, Cryst. Eng. Comm. 18 (2016) 369 – 378.
J. Torrens-Serra, J. Rodriguez-Viejo, M.T. Clavaguera-Mora, Evaluation of the liquid-solid interfacial energy from crystallisation kinetic data, Scripta Materialis. 61 (2009) 879 – 882.
C.M. Tun, A.G. Fane, J.T. Matheickal, R. Sheikholeslami, Membrane distillation crystallisation of concentrated salts-flux and crystal formation, J. Membr. Sci. 257 (2005) 144 – 155.

L. Wang, B. Li, X. Gao, Q. Wang, J. Lu, Y. Wang, S. Wang, Study of membrane fouling in cross-flow vacuum membrane distillation, Sep. Purif. Technol. 122 (2014) 133 – 143.
Z. Zhang, N. Zhang, B. Xiang, Y. Yuan, P. E. Phelan, Numerical investigation on mass and heat transfer performance fr novel vacuum membrane distillation modules enanced by semicircular spacers, Int. J. of The. Sci., 187 (2023) 108165.

7 Conclusions and future work

7.1 Conclusions

The completed thesis utilizing classical nucleation theory, has established a comprehensive framework to establish a connection between the chemistry of the salt and the membrane properties with the two distinct mechanisms of crystallisation, and the expansion of scaling. The produced key conclusions are the following:

1. Using crystal-liquid interfacial energy, a framework was established for predicting nucleation and crystal growth kinetics, as well as the probability of adhesive scaling and crystal deposition.
2. As the supersaturation of the crystallisation induction grows in proportion to the solid-liquid interfacial tension of the salt, it approaches homogeneous nucleation relying less on the membrane for nucleation. This occurs as the elevated G_s, which is controlled by the interfacial energy generated by the membrane, is surpassed by the G_v of the system, which is governed by the nucleation kinetics.
3. The concurrent investigation of bulk nucleation and membrane scaling using the FBRM and the microscopic HD camera, supported by both calculated and practical nucleation rates obtained from the FBRM, provided additional evidence in favour of the theory positing two distinct scaling mechanisms: adhesive growth and crystal deposition.
4. The solubility – temperature dependency of salts has a substantial impact on their sensitivity to membranes. The fluctuation in salt concentration between the bulk and the membrane caused by polarisation phenomena, coupled with the salt's solubility – temperature dependency, exacerbates this effect and complicates the crystallisation process substantially more.
5. The temperature difference between the feed and permeate sides of the membrane distillation process, can be adjusted to influence the nucleation kinetics. By decreasing polarisation phenomena and reducing the concentration disparity between the membrane and the bulk solution, the membrane effect on the crystallisation is minimised, enhancing homogeneous nucleation.
6. In addition to enhanicing homogeneous nucleation, lowering the temperature differential between the feed and permeate increases nucleation rates and yields more crystals at a slower growth rate. As a result, purer and more stable crystals are formed, making them better suited for use in subsequent industrial applications.

7. Despite the presence of two distinct scaling mechanisms, the membrane contributes significantly in promoting scaling via heterogeneous nucleation in low interfacial energy salts. As a result, it was discovered that the lag time between scaling induction and bulk nucleation can greatly influence the extent of scaling and consequently, the longevity of the process.
8. As the lag time between heterogeneous and homogeneous nucleation is a critical factor in determining the extent of scaling, the initial concentration (C*) of the salt in the solution is of utmost importance as it decreases the MSZW, leading to shorter induction times and faster onset of homogeneous nucleation. This effect is most prominent in salts with a strong solubility – temperature dependency.

7.2 Future work

The subsequent areas for additional investigation were identified and are the following:

1. Manipulate hydrodynamic conditions on high interfacial energy salts to regulate the deposition of bulk nucleated crystals on the membrane, effectively eliminating membrane fouling due to shear effects. This would enable a membrane system to function more efficiently and for longer periods of time, lowering operational and maintenance expenses.
2. By employing a high-definition camera and imaging software, similar to the one utilised in this thesis, it is possible to estimate the scaling growth rate with higher precision. Consequently, the mass of the scaling can be determined and can be used to calculate the true saturation level of both the membrane and the bulk solution. Calculating the supersaturation with more accuracy allows us to have a better understanding of the nucleation and growth kinetics as well as be more precise of the effect of the membrane on the process.
3. During the research, it became apparent that the generated scaling migrates from the feed outlet (the colder side of the membrane) towards the feed inlet (the hotter side of the membrane). An investigation must be conducted to determine the impact of the thermodynamic and hydrodynamic conditions of the membrane distillation on the manner in which the scaling extension occurs in low interfacial energy salts. It would be intriguing to further expand on this work to compare the effect of salt chemistry via their temperature – solubility dependence. Understanding this scaling mechanism, allows us to implement ways to minimize the scaling extension on membranes.
4. Utilise the findings of this thesis to form homogeneous crystals and assess their purity levels to comprehend their potential for use in a variety of industries. That

would create additional financial incentives for the development and the installation of more crystallisation, membrane crystallisation or other membrane separation type technologies.

5. Given that crystals are formed at the nanoscale, it is critical to employ advanced imaging techniques at the nano-level to accurately distinguish between the two scaling mechanisms. Implementing more cutting-edge technologies provides us better understanding of the scaling and deposition processes, allowing us to be more precise in our understanding of the processes and adopt more targeted methods to minimise scaling and create processes with greater longevity.
6. Employ multiple salts in the system to investigate the impact of salt interactions on nucleation and scaling kinetics as well as their effect on the quality of the produced crystals, particularly the purity of the produced crystals, and the order of crystallisation such as simultaneous coprecipitation or staged nucleation.
7. Utilise the results of the thesis to design a crystallizer that has the required hydrodynamics, mixing, and potentially seeding conditions to effectively produce and retain the crystals within the crystallizer. If necessart, consider implementing in-line filtration prior to the membrane to ensure the successful development of a complete batch or continuous membrane crystallisation process.